A holistic approach to seismic waveform tomography of heterogeneous fractures: from geometric reconstruction to interfacial characterization

A DISSERTATION
SUBMITTED TO THE FACULTY OF THE GRADUATE SCHOOL
OF THE UNIVERSITY OF MINNESOTA
BY

Fatemeh Pourahmadian

IN PARTIAL FULFILLMENT OF THE REQUIREMENTS
FOR THE DEGREE OF
Doctor of Philosophy

Bojan B. Guzina and Joseph F. Labuz

August, 2016

Acknowledgements

I would like to express my sincere gratitude to my academic advisers Prof. Bojan Guzina and Prof. Joe Labuz for their extensive and continuous support during the course of this research. I am tremendously grateful to Prof. Guzina for fostering scientific rigor in this work and for offering me the liberty to experiment with new research areas beyond my educational background and capabilities, which without his help could not have come to a successful conclusion. This made my journey such a learning experience and all the more unique and exciting.

I would like to thank Prof. Houssem Haddar for his great guidance and insightful comments during the development of Chapter 4.

I have had a chance to work and interact with Dr. Sofia Mogilevskaya on a number of projects, and I would like to acknowledge our fruitful discussions that deepened my understanding of the boundary element formulation and integral equations.

I am indebted to Prof. Fioralba Cakoni and Prof. Guzina for providing me with the opportunity to experience an independent research with Irene De Teresa Trueba and in particular, for their encouragement and intellectual support beyond this thesis that steered me toward my future career.

I appreciate the efforts and the time of the committee members, namely Profs. Fadil Santosa, Stefano Gonella and Emmanuel Detournay.

A very special thanks goes to the my fellow graduate students at the Geomechanics group, in particular, to Roman Tokmashev and Ali Tarokh for their help and contribution to designing and conducting the laboratory experiments.

Warmest thanks must go to my family whose continuous love and encouragement made it possible to complete this dissertation.

The financial support provided by the Sommerfeld Fellowship, Daneshy Fellowship,

Dedication

To my parents who enabled me to pursue my dreams

Abstract

The primary focus of this thesis is on the development of a comprehensive analytical, computational, and experimental framework for (a) 3D seismic waveform tomography of partially-closed fractures, e.g. hydraulic fractures, and (b) reconstruction of their heterogeneous contact condition. Taking advantage of recent advancements in the theory of inverse scattering, the *analytical platform* is formulated as a novel 3-step approach where: (i) the fracture geometry Γ (which may be nonplanar and/or disconnected) is non-iteratively reconstructed without any prior knowledge about its interfacial condition via either the Generalized Linear Sampling Method (GLSM) or the method of Topological Sensitivity (TS); ii) given Γ, the fracture opening displacement (FOD) profile is computed from the integral equation relating FOD to the observed seismic data; and (iii) given Γ and FOD, the (normal and shear) specific stiffness profiles are resolved from the hypersingular boundary integral equation for a fracture with elastic contact condition. To cater for efficient numerical simulations, a *computational platform* is developed on the basis of a regularized boundary integral equation (BIE) method for elastic-wave scattering by heterogeneous fractures in 3D, which provided fertile ground for verifying and demonstrating the effectiveness of the 3-step inverse solution. The *experimental component* of this work makes use of the 3D Scanning Laser Doppler Vibrometer (SLDV) that is capable of remotely monitoring the triaxial motion waveforms (up to 1MHz) on the surface of rock specimens with 0.1mm spatial resolution and O(nm) displacement accuracy. In this setting, a set of plane-stress laboratory experiments is designed which allow for monitoring the full-field interaction of ultrasonic waves with stationary and advancing fractures in rock. The measured data are then used to: (1) non-parametrically expose the true contact law and its spatiotemporal variations along the surface of stationary and advancing fractures in rock, and (2) extract the linearized contact properties in terms of the (heterogeneous) distribution of shear and normal specific stiffness along the fracture. In turn, such high-fidelity results provide the *ground truth* toward validating the proposed inverse solution for the geometric reconstruction and interfacial characterization of fractures in rock by seismic waves.

Contents

List of Tables

List of Figures

xiii

Chapter 1

Introduction

Geometric and interfacial properties of fractures and related features (such as faults) in rock are the subject of critical importance to a wide spectrum of scientific and technological facets of our society including energy production from natural gas and geothermal resources [13, 163, 155], seismology [113], hydrogeology [62], environmental protection [131], and mining [79]. One particular quantity embodying the fracture's interfacial condition is the so-called (shear and normal) *specific stiffness*, relating the contact traction to the jump in displacement across the interface. Beyond its immediate relevance to the stress and thus stability analyses in rock masses [e.g. 62, 69], the fracture (or joint) specific stiffness has been shown to both (i) bear an intimate connection to the fracture's hydraulic properties [140, 163, 139], and (ii) serve as a precursor of shear failure in rock discontinuities [89]. In general, however, the fracture's response to given activation is equally driven by its *geometry*, which is not limited to the planar condition [e.g. 43, 21, 158]. Thus a holistic characterization of fractures in rock, that unveils both their geometric and mechanical characteristics, is a paramount.

Remote sensing of fractures. Unfortunately the direct access to a fracture surface in rock is, in most field situations, either non-existent or extremely limited (e.g. via isolated boreholes, shafts, or adits), which necessitates the use of remote sensing techniques. One powerful tool meeting such demand are *seismic waves* – thanks to the fact that they reflect and transmit, in a frequency-dependent fashion, off of displacement discontinuities across subsurface fractures [141, 62, 142, 3]. Traditionally, seismic waves have been used in the context of *acoustic emission* (AE) [106, 147] to monitor the

progression of evolving fractures via the detection of underlying microseismic events, whose energy – captured by the receivers – is used to describe the failure process. Such "passive" sensing approach is, however, ineffective when trying to either image in situ fractures or to assess the fracture's interfacial condition; further, questions are raised whether the AE events can in fact be used as a reliable precursor of a slip [78]. Another approach, motivating this research, is the concept of *active seismic sensing* applied to fracture identification. This approach, where the discontinuity is "illuminated" by an external seismic source, carries the potential of simultaneous fracture imaging and characterization thanks to aforementioned sensitivity of the reflected and refracted waves to the interfacial condition.

The need. Fractures' mechanical properties have been the subject of mounting attention across several fronts in geosciences [95, 89, 78, 113, 14, 74, 100], where the *spatial distribution* of the fracture's normal and shear specific stiffness emerged as the key question owing to its relevance to a number of subsurface phenomena. For instance, the inhomogeneity in interfacial contact conditions – due to e.g. variable distribution of normal stress [108] – is responsible for progressive failure along discontinuities that may occur well before the frictional resistance of the entire interface is surpassed [120]. This may lead to a catastrophic failure of dams, mines, tunnels and slopes [79, 71, 30, 149, 17], in particular when fractures show slip-weakening behavior [e.g. 76] while the underlying design is based upon *averaged* contact properties. Further, using direct-shear experiments, [89] showed that the onset of slip propagation along an interface can be identified via temporal variation of the fracture's shear specific stiffness. Accordingly, a detailed knowledge of the fracture's (linearized) mechanical properties may not only serve as an *early indicator* of the interfacial instability and failure, but may also help understand the mechanism of shallow earthquakes [93]. In the context of multiphase rock mechanics, experimental studies have shown [55, 131, 107, 91] that the ratio between the fracture's shear and normal specific stiffness, namely k_s/k_n [138] may exhibit significant variations in the field – which may affect the analyses of effective medium properties [e.g. 16] and studies on wave propagation through fractured media [144]. Furthermore, recent studies [14, 163] highlighted the importance of *seismically imaging* the k_s/k_n ratio owing to its connection with the hydraulic conductivity of a fracture network – which may further bear relevance to the development and management of enhanced geothermal

systems [e.g. 155].

The challenge. Recently, strides have been made [116, 117, 55, 163, 74, 170, 15, 134] toward the *simultaneous* reconstruction and interfacial characterization of fractures via *seismic waveform tomography.* So far the proposed methods, often reliant upon a rudimentary parameterization of the fracture geometry (e.g. planar fractures) and nonlinear minimization, entail a number of *impediments* including: (i) high computational cost [166]; (ii) sensitivity to the assumed parametrization resulting in multiple sets of "optimal" solutions and thus the ambiguity of such obtained subsurface information [163, 165]; (iii) computational instabilities requiring multiple stages of regularization [117], and iv) major restrictions in terms of the seismic sensing configuration [165, 74, 116, 15, 170], namely the location of sources and receivers relative to the (planar) fracture surface. One recent study aiming to mitigate such limitations can be found in [170] that makes use of focused Gaussian beams emitted from the surface source/receiver arrays to non-iteratively assess the orientation, spacing, and compliance of systems of parallel planar fractures.

Objectives. To help meet the challenge, the goal of this research is to establish a comprehensive analytical, computational, and experimental platform for the 3D reconstruction and interfacial characterization of arbitrarily-shaped fractures in rock by seismic waves. In particular, the focus is on developing a robust framework for the *seismic waveform tomography of heterogeneous fractures*, that is capable of resolving both their geometry and (linearized) contact condition without iterations.

Geometric reconstruction. Waveform tomography and in particular inverse obstacle scattering are essential to a broad spectrum of science and technology disciplines including geophysics [13, 113, 62, 131, 79], oceanography [125, 130], optics [18, 1], radiology [10, 154], aeronautics [47, 49], and non-destructive material testing [11, 159, 80]. In general the relationship between the wavefield scattered by an obstacle and its geometry (or physical characteristics) is nonlinear, which invites two overt solution strategies: (i) linearization via e.g. Born approximation and ray theory [32, 148], or ii) pursuit of the nonlinear minimization approach [164, 169, 101]. Over the past two decades, however, a number of *sampling methods* have emerged that both consider the nonlinear nature of the inverse problem and dispense with iterations. Commonly, these techniques deploy

an indicator functional that varies with spatial coordinates of the trial i.e. sampling point, and projects observations of the scattered field onto a functional space reflecting the "baseline" wave motion in a background medium. This indicator functional, designed to reach extreme values when the sampling point strikes the anomaly, accordingly provides a tomogram via its (thresholded) spatial distribution. Examples of such imaging paradigm include the Linear Sampling Method (LSM) [57, 122, 46, 11, 87], the Factorization Method (FM) [98, 40, 12, 52], the concept of Topological Sensitivity (TS) [92, 82, 23, 160, 75] and the subspace migration technique [129] in the context of extended (i.e. finite-sized) scatterers, as well as the time reversal method [136], the MUSIC algorithm [66, 127, 96], and the direct approach [7] as techniques catering for point-like targets. In general, the LSM and FM techniques are applicable to a wide class of interfacial conditions and inherently carry a superior localization property – potentially leading to high-fidelity geometric reconstruction of anomalies without prior knowledge of their boundary condition. These methods are, however, notably plagued by high sensitivity to measurement uncertainties. In contrast the TS approach, that is inherently robust to noisy data, fails to precisely recover (due to image smearing) the shape of a scatterer at long illuminating wavelengths. The subspace migration methods offer another alternative for a high-fidelity reconstruction, even from partial-aperture data, while requiring some *a priori* knowledge about the geometry of a discontinuity surface. In the context of seismic waveform tomography it should be noted that, among the aforementioned methods, the LSM and TS techniques have been applied to the problem of elastic-wave imaging of fractures with *homogeneous* i.e. traction-free boundary condition [42, 26].

Interfactial characterization. There is a growing interest spanning medical diagnosis, target recognition, seismology, and energy communities [47, 49, 117, 163, 131], in developing hybrid sensing schemes that are capable of both i) imaging the geometry of hidden anomalies, and (ii) distinguishing important features of their boundary condition, preferably in a non-iterative way. Existing studies on the waveform tomography of obstacles with unknown contact condition reflect two principal concerns, namely: (i) the effect of such lack of information on the quality of geometric reconstruction, and (ii) reliable retrieval of the key physical characteristics of such contact. The former aspect is of paramount importance, for instance, in imaging stress corrosion fractures [90] where

the crack extent may be underestimated due to interactions at its interface, leading to a catastrophic failure. As indicated earlier, some anomaly-indicator functionals – such as those featured by the FM [98] and LSM [49] are by design *less sensitive* to the boundary condition of a hidden anomaly. In particular, [40] demonstrates the capability of FM to reconstruct the shape of acoustic impedance cracks, while [47] elucidates that LSM is successful in imaging electromagnetic obstacles and cracks regardless of their boundary condition. Recent advancements on the recovery of boundary (or interfacial) conditions are, on the other hand, mostly *optimization-based* as proposed in the context of acoustic and electromagnetic inverse scattering. Hitherto, a variational method is proposed in [56] within the framework of the LSM to determine the essential supremum of the electrical impedance at the boundary of partially coated obstacles. More recently, [48] combined the LSM with iterative algorithms as a tool to expose the surface properties of obstacles from acoustic and electromagnetic data. In elastodynamics, [117] proposed a Fourier-based approach employing the reverse-time migration and wavefield extrapolation to retrieve the heterogeneous compliance of a planar interface under the premise of high illuminating wavenumber and absence of evanescent waves along the interface.

Inverse solution.   In light of the above developments [47, 48, 40, 11], the twin aim of seismic fracture reconstruction and characterization is pursued *sequentially* in that: (1) a focused effort is made toward *robust* shape reconstruction of subsurface fractures with unknown boundary condition, and (2) thus obtained geometric information is leveraged to *non-iteratively* identify the contact properties of germane interfaces. As described in the sequel, **Aim 1** is achieved via the development of an indicator map is that is (i) computed without iterations, (ii) agnostic with respect to the fracture's interfacial condition, (iii) robust against measurement errors, and (iv) flexible in terms of sensing parameters, e.g. the illumination frequency. This is accomplished by drawing from the inverse scattering theories and, in particular, by building upon the Factorization Method [98, 41] and the recently developed Generalized Linear Sampling Method (GLSM) [11, 12] which completes the theoretical foundation of its LSM predecessor. To provide an alternative pathway toward robust geometric reconstruction of subsurface fractures, the TS method [92, 82, 23, 160] is also adapted to cater for the geometric reconstruction of fractures regardless of their contact condition. As a first step toward theoretical justification of the TS approach – whose apparent success in solving a wide

variety of inverse scattering problems has been largely left without a proof, a theoretical study is performed in an idealized setting (assuming acoustic waves and convex anomalies) that, for the first time, rigorously establishes the TS as a tool for the precise reconstruction of sharp boundaries in the high-frequency regime. With such developments at hand, **Aim 2** is accomplished by computing suitable density maps over the recovered fracture surface on the basis of germane integral representation theorems. First, the fracture opening displacement (FOD) profile is computed (over the reconstructed discontinuity surface) from the integral equation relating FOD to the scattered i.e. observed seismic waveforms. Using this result, the (normal and shear) specific stiffness profiles are finally resolved from the *traction boundary integral equation*, likewise written for the recovered fracture surface.

Experimental developments. For completeness, a set of laboratory ultrasonic experiments is designed, in a *plane stress* setting, to: (a) explicitly reveal the geometry of stationary and propagating fractures in rock; (b) non-parametrically expose the true (traction-FOD) contact law and its spatiotemporal variations along the recovered fracture support, and (c) extract the linearized contact properties in terms of the distributions of shear and normal specific stiffness along the fracture. This is accomplished by remotely monitoring the *full-field* interaction of ultrasonic shear and compressional waved (propagating through granite specimens) with stationary and advancing fractures via a 3D Scanning Laser Doppler Vibrometer (SLDV). The latter sensing system is capable of remotely monitoring triaxial particle velocity, with frequencies up to 1MHz, over the surface of rock specimens with 0.1mm spatial resolution and O(nm) displacement accuracy. From a long-term perspective, the full-field, high-fidelity ultrasonic observations proposed in this thesis may not only help decipher the true physics of a fracture interface and shine light on the fidelity of linearized interface models in the context of seismic waves, but may also provide the *ground truth* toward validating a variety of inverse scattering solutions catering for the seismic reconstruction and characterization of fractures in rock.

Thesis organization. This dissertation is organized as a collection of self-contained, yet complementary papers:

Chapter 2 – published in *Proc. Roy. Soc. A* [85], shows theoretically why the topological sensitivity (TS) indicator works as a non-iterative tool for the waveform tomography

of impenetrable anomalies in the short wavelength regime. The analysis confirms previous numerical and experimental findings to this effect, that have so far eluded rigorous justification. While the simplifying assumptions of this work (acoustic waves, convex obstacles) do not explicitly cater for the seismic sensing of fracture surfaces, they nonetheless provide an analytical clarity that is necessary for theoretically supporting the success of elastodynamic TS fracture reconstruction shown in Chapter 3.

Chapter 3 – published in *Int. J. Solids Struct.* [134], adapts the TS to cater for 3D seismic imaging of partially-closed fractures. This study reveals that the TS indicator is capable of (i) accurately reconstructing curved fracture surfaces in the high-frequency regime; (ii) approximating the orientation of a fracture's unit normal even at lower frequencies, and (iii) providing qualitative information about the fracture's contact condition at virtually no added computational cost.

Chapter 4 – submitted to *Inverse Problems* [72], shows that the Generalized Linear Sampling Method (GLSM) – endowed with elements of the Factorization Method (FM) provides a fast, yet robust, platform for the 3D elastodynamic reconstruction of heterogeneous (and possibly dissipative) fracture surfaces from the scattered wavefield data. In particular, it is shown that the GLSM fracture indicator is characterized by *low sensitivity* to measurement errors – making it comparable in terms of robustness to the TS approach, while inheriting the *top-tier localization* property of the classical LSM, which virtually guarantees high-fidelity geometric fracture reconstruction over a wide range of excitation frequencies and fracture's (unknown) contact conditions.

Chapter 5 – to be submitted to *Inverse Problems*, combines the findings from Chapters 3 and 4 with a boundary integral representation of the scattered seismic field and the germane traction boundary integral equation (both written for the reconstructed fracture surface) to propose a unique *3-step approach* where the observed seismic waveforms are used to sequentially and non-iteratively reconstruct: (i) fracture geometry, (ii) fracture opening displacement profile, and (iii) heterogeneous specific stiffness in both shear and normal directions. The numerical results show a remarkable performance of the proposed scheme when dealing with both curved fractured surfaces and heterogeneous distributions of specific stiffness coefficients.

Chapter 6 – published in *Proc. 50th U.S. Rock Mech./Geomech. Symp.* [135], takes advantage of the Scanning Laser Doppler Vibrometer to monitor, in a non-contact

fashion, the full-field interaction of ultrasonic waves with stationary and advancing fractures in slab-like rock specimens. The proposed experimental procedure carries the potential of both (i) reconstructing the curvilinear and non-smooth fracture geometry, and (ii) point-wise identifying its true contact behavior, which can then be approximated in terms of customary linearized parameters of shear and normal specific stiffness.

Chapter 2

Why the inverse scattering by Topological Sensitivity may work

Stemming from the framework of shape optimization [150], the method of topological sensitivity (TS) [83, 75] has emerged as an effective tool for the waveform tomography of extended obstacles in acoustics [84, 50, 34], electromagnetism [111, 128], and elastodynamics [68, 54, 25]. Formally, the TS quantifies the leading-order perturbation of a given misfit functional when an infinitesimal scatterer is introduced at a sampling point in the reference domain – being imaged for obstacles. From the application viewpoint, the appeal of TS resides in its forthright computability as a bilinear form in terms of two (free and adjoint) forward solutions for the reference domain. Following the heuristic argument, this quantity is then used as *obstacle indicator* by identifying the support of its pronounced negative values with an anomaly.

Despite the mounting numerical [75, 38, 54, 25, 128] and experimental [67, 143, 160] evidence of the imaging capability of the method in a variety of sensing configurations, a *theoretical justification* of the TS as an obstacle indicator function *is still lacking*. So far, [68] established the analogy between the topological sensitivity and time reversal, while [27] elucidated the TS reconstruction of a) point-like anomalies, and b) extended weak anomalies in the sense of small material contrast (Born approximation) and/or low excitation frequency. Further, [5] explained how the TS discerns small acoustic obstacles, and established the underpinning stability and resolution analysis under
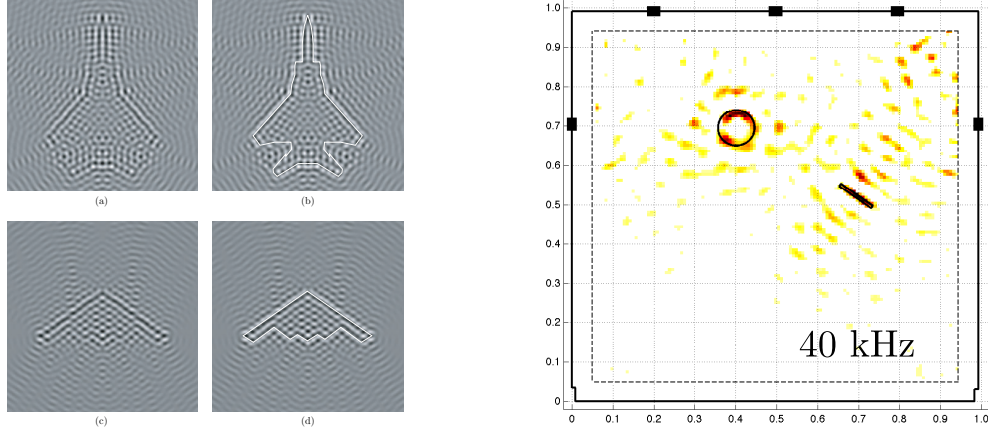
Figure 2.1: High-frequency performance of the TS indicator function as an obstacle imaging tool: 2D reconstruction of a fighter jet from scattered acoustic waves [75] (left), and elastodynamic TS map of a hole and a slit in a $1\,\mathrm{m} \times 1\,\mathrm{m}$ aluminum plate [160] (right).

medium and measurement perturbations. To date, however, the reported ability of TS to reconstruct obstacles of arbitrary (finite) size and contrast has eluded both physical understanding and rigorous justification. The problem is highlighted by the repeated observations [75, 54, 50, 160] that at higher frequencies, the usual reconstruction heuristics does not apply for the negative TS values tend to localize in a narrow region "*about the boundary*" of an anomaly [50] – rather than canvassing its support. Such behavior is illustrated in Fig. 2.1, which includes the application of TS to both synthetic data [75] and laboratory (ultrasonic) measurements [160].

In the spirit of Fig. 2.1, this chapter aims to *decipher the performance* of the TS indicator function as a tool for imaging anomalies in the high-frequency regime, where the germane wavelength is surpassed by the remaining length scales in the problem. It is assumed that the anomaly i.e. obstacle is convex and impenetrable (Dirichlet and Neumann), and that the measurements of the scattered field are taken over a sphere whose radius is large relative to the size of the interrogated region. In this setting, the formula for topological sensitivity is expressed as a pair of nested surface integrals: one taken over the boundary of a hidden obstacle, and the other over the measurement surface. Using multipole expansion, the latter integral is reduced to a set of antilinear forms featuring the Green's function and its gradient. The remaining expression is distilled by

evaluating the scattered field on the surface of an obstacle via Kirchhoff approximation, and pursuing the asymptotic expansion of the resulting Fourier integral. In this way the topological sensitivity is found to survive upon three asymptotic lynchpins, namely i) the near-boundary approximation for sampling points close to the "exposed" surface of an obstacle; ii) uniform expansions synthesizing the diffraction catastrophes for sampling points near caustic surfaces, lines, and points; and iii) non-uniform (stationary phase) approximation. Under the premise of a single illuminating (plane) wave, it is found that the distribution of topological sensitivity, while carrying hints about the shape of an anomaly via the near-boundary contribution, is controlled by the caustics. By way of the catastrophe theory and diffraction scaling laws, on the other hand, it is shown that in the case of the *full aperture* of illuminating wavefields, the topological sensitivity is asymptotically dominated by the (explicit) near-boundary term – which explains the evidenced imaging capabilities of this class of indicator functionals. This result further unveils the new reconstruction logic at short wavelengths where the *boundary* of an anomaly is obtained as a *zero level set* of the TS field separating its extreme negative and extreme positive values. From a practical point of view such paradigm allows, for the first time, size-accurate anomaly reconstruction without the use of an ad-hoc threshold parameter. The analysis is accompanied by numerical results and an application toward obstacle reconstruction to a recent set of experimental data [160].

2.1 Preliminaries

Consider the scattering of time-harmonic scalar waves by a convex impenetrable obstacle $D \subset \mathscr{B}_1 \subset \mathbb{R}^3$ (of either Dirichlet or Neumann type) with smooth boundary $S = \partial D$, where $\mathscr{B}_1$ is an open ball of radius R_1 centered at the origin. On denoting by $\tilde{u}$ the scattered field generated by the action of an incident field u^i on D, it is assumed that the total field

$$u(\boldsymbol{\xi}) \;=\; u^i(\boldsymbol{\xi}) \,+\, \tilde{u}(\boldsymbol{\xi}), \qquad \boldsymbol{\xi} \in \mathbb{R}^3 \backslash \overline{D},$$

is monitored over a closed measurement surface $\Gamma^{\mathrm{obs}} = \partial \mathscr{B}_2$, where $\mathscr{B}_2$ is an open ball of radius $R_2 = \alpha^{-1} R_1 \;\; (\alpha < 1)$ centered at the origin, see Fig. 2.2. The reference background medium is assumed to be homogeneous with wave speed c and mass density ρ.
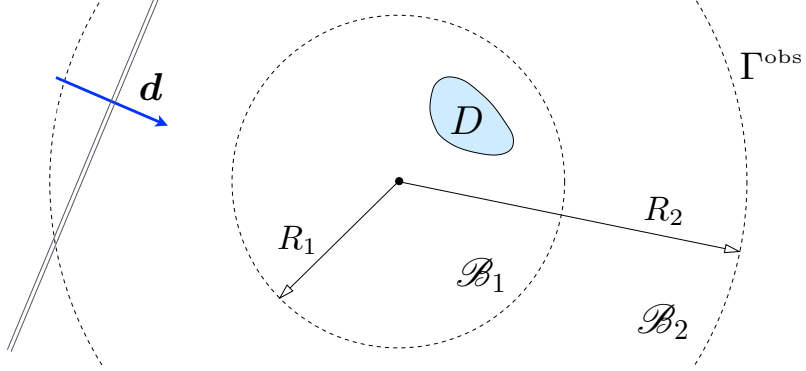
Figure 2.2: Convex obstacle $D \in \mathbb{R}^3$ illuminated by plane waves.

Sensory data. Writing the implicit time dependence as $e^{\mathrm{i}\omega t}$, the incident field is assumed in the form of a *plane wave*, $u^i = e^{-\mathrm{i}k\boldsymbol{\xi}\cdot\boldsymbol{d}}$, endowed with wavenumber $k = \omega/c$ and direction $\boldsymbol{d} \in \Omega$ where Ω is a unit sphere. For each $\boldsymbol{d}$, values of the total field u are collected over Γ^{obs}.

Cost functional. To provide the basis for obstacle reconstruction, consider the misfit functional

$$J(\mathscr{D},\beta,\gamma) \;=\; \int_{S^{\mathrm{obs}}} \varphi\left(v(\boldsymbol{\xi}), u(\boldsymbol{\xi}), \boldsymbol{\xi}\right) \; \mathrm{d}\Gamma_{\xi}, \tag{2.1}$$

computed for given $\boldsymbol{d}$, where $\mathscr{D}$, $\beta = \rho/\rho_{\mathrm{trial}}$ and $\gamma = c/c_{\mathrm{trial}}$ synthesize respectively the support and material characteristics of a *trial obstacle*; v is the total field generated by the action of u^i on $\mathscr{D}$, and φ is a distance function that is differentiable with respect to the real and imaginary parts of its first argument. Note that the trial scatterer is purposely assumed to be penetrable in an effort to make the analysis (via the adjustment of β and γ) applicable to both Dirichlet and Neumann obstacles. In what follows, φ is assumed to take the customary least-squares format

$$\varphi(v(\boldsymbol{\xi}), u(\boldsymbol{\xi}), \boldsymbol{\xi}) \;=\; \tfrac{1}{2} \, \overline{(v(\boldsymbol{\xi}) - u(\boldsymbol{\xi}))} \, (v(\boldsymbol{\xi}) - u(\boldsymbol{\xi})). \tag{2.2}$$

Green's function. For further reference, let

$$G(\boldsymbol{\xi}, \boldsymbol{x}) \;=\; \frac{e^{-\mathrm{i}kr}}{4\pi r}, \qquad G_{,n}(\boldsymbol{\xi}, \boldsymbol{x}) \;=\; \boldsymbol{n}\cdot\nabla G(\boldsymbol{\xi}, \boldsymbol{x}) \;=\; -\frac{e^{-\mathrm{i}kr}}{4\pi r^2}(1+\mathrm{i}kr)\, r_{,n}, \tag{2.3}$$

denote the fundamental solution for the free space $\mathbb{R}^3$ with wavenumber k, where $\boldsymbol{x}$

signifies the source location; $r = |\boldsymbol{\xi} - \boldsymbol{x}|$, and ∇G indicates differentiation with respect to *the first* argument.

Dimensional platform. In the sequel, all quantities are assumed to be dimensionless. This is accomplished by taking the radius of the inner sphere, the mass density of the background medium, and the sound speed in the background medium as the reference length, mass density and velocity. In this setting, one in particular has $R_1 = 1$ and $R_2 = \alpha^{-1}$.

2.1.1 Topological Sensitivity

Let $\mathscr{D} \subset \mathbb{R}^3$ contain the origin. As shown in [84] the formula for TS, stemming from the definition

$$J(\mathscr{D}_\epsilon, \beta, \gamma) \;=\; J(\emptyset, \beta, \gamma) \;+\; \mathsf{T}(\boldsymbol{x}^\circ, \beta, \gamma)|\mathscr{D}_\epsilon| \;+\; o(|\mathscr{D}_\epsilon|), \qquad \epsilon \to 0,$$

where $\mathscr{D}_\epsilon = \boldsymbol{x}^\circ + \epsilon \mathscr{D}$ is a vanishing obstacle nucleated at $\boldsymbol{x}^\circ$, can be written as

$$
\mathsf{T}(\boldsymbol{x}^\circ, \beta, \gamma) \;=\; \int_{S^{\mathrm{obs}}} \mathrm{Re}\, \Big[\varphi'(u^i(\boldsymbol{\xi}), u(\boldsymbol{\xi}), \boldsymbol{\xi}) \Big\{ (1{-}\beta)\, \nabla u^i(\boldsymbol{x}^\circ) \cdot \boldsymbol{A} \cdot \nabla G(\boldsymbol{x}^\circ, \boldsymbol{\xi})
$$
$$
-\; (1{-}\beta\gamma^2)\, k^2\, u^i(\boldsymbol{x}^\circ)\, G(\boldsymbol{x}^\circ, \boldsymbol{\xi}) \Big\} \Big]\, \mathrm{d}\Gamma_\xi, \qquad \boldsymbol{x}^\circ \in \mathscr{B}_1. \quad (2.4)
$$

Here, $\varphi'(u^i, u, \cdot) \;=\; \overline{u^i{-}u}$ signifies the derivative of φ with respect to its first argument; $\boldsymbol{A}$ is a second-order polarization tensor reflecting the shape $\mathscr{D}$ of an infinitesimal obstacle, and $\mathscr{B}_1$ contains the region that is sampled for anomalies. To expose the nature of (2.4), one may recall the integral representation of the scattered field

$$
-\tilde{u}(\boldsymbol{\xi}) \;=\; u^i(\boldsymbol{\xi}){-}u(\boldsymbol{\xi}) \;=\; \int_S \Big(u_{,n}(\boldsymbol{\zeta})\, G(\boldsymbol{\zeta}, \boldsymbol{\xi}) - u(\boldsymbol{\zeta})\, \boldsymbol{n}(\boldsymbol{\zeta}) \cdot \nabla G(\boldsymbol{\zeta}, \boldsymbol{\xi}) \Big) \mathrm{d}S_\zeta, \quad \mathbb{R}^3 \backslash \overline{D}, \;(2.5)
$$

where $\boldsymbol{n}$ is the unit *outward* normal on S and $f_{,n} = \boldsymbol{n} \cdot \nabla f$. Accordingly, (2.4) can be rewritten as

$$
\mathsf{T}(\boldsymbol{x}^\circ, \beta, \gamma) \;=\; -\mathrm{Re}\, \Big[(1{-}\beta)\, \nabla u^i(\boldsymbol{x}^\circ) \cdot \boldsymbol{A} \cdot \Big\{ \int_S \overline{u}_{,n}(\boldsymbol{\zeta}) \int_{\Gamma^{\mathrm{obs}}} \overline{G}(\boldsymbol{\xi}, \boldsymbol{\zeta})\, \nabla G(\boldsymbol{\xi}, \boldsymbol{x}^\circ)\, \mathrm{d}\Gamma_\xi\, \mathrm{d}S_\zeta
$$
$$
+\; \int_S \overline{u}(\boldsymbol{\zeta})\, \boldsymbol{n}(\boldsymbol{\zeta}) \cdot \int_{\Gamma^{\mathrm{obs}}} \nabla \overline{G}(\boldsymbol{\xi}, \boldsymbol{\zeta}) \otimes \nabla G(\boldsymbol{\xi}, \boldsymbol{x}^\circ)\, \mathrm{d}\Gamma_\xi\, \mathrm{d}S_\zeta \Big\} +
$$

$$+ (1-\beta\gamma^2)\, k^2\, u^i(\boldsymbol{x}^\circ) \bigg\{ \int_S \overline{u}_{,n}(\boldsymbol{\zeta}) \int_{\Gamma^{\mathrm{obs}}} \overline{G}(\boldsymbol{\xi},\boldsymbol{\zeta})\, G(\boldsymbol{\xi},\boldsymbol{x}^\circ)\, \mathrm{d}\Gamma_\xi\, \mathrm{d}S_\zeta$$

$$+ \int_S \overline{u}(\boldsymbol{\zeta})\, \boldsymbol{n}(\boldsymbol{\zeta}) \cdot \int_{\Gamma^{\mathrm{obs}}} \nabla\overline{G}(\boldsymbol{\xi},\boldsymbol{\zeta})\, G(\boldsymbol{\xi},\boldsymbol{x}^\circ)\, \mathrm{d}\Gamma_\xi\, \mathrm{d}S_\zeta \bigg\} \bigg], \quad (2.6)$$

due to the fact that $G(\boldsymbol{x},\boldsymbol{y}) = G(\boldsymbol{y},\boldsymbol{x})$ and $\nabla G(\boldsymbol{x},\boldsymbol{y}) = -\nabla G(\boldsymbol{y},\boldsymbol{x})$.

2.1.2 Approximation of the component integrals over Γ^{obs}

The purpose of this section is to reduce the TS formula (2.6) to a single, Fourier-type surface integral that is amenable to short-wavelength approximation.

2.1.2.1 The $\overline{G}\,G$ term

From (2.3), it follows that

$$
\begin{aligned}
\nabla^2 G(\boldsymbol{\xi},\boldsymbol{x}^\circ) \,+\, k^2\, G(\boldsymbol{\xi},\boldsymbol{x}^\circ) \,+\, \delta(\boldsymbol{\xi}-\boldsymbol{x}^\circ) &= 0, \\
\nabla^2 G(\boldsymbol{\xi},\boldsymbol{\zeta}) \,+\, k^2\, G(\boldsymbol{\xi},\boldsymbol{\zeta}) \,+\, \delta(\boldsymbol{\xi}-\boldsymbol{\zeta}) &= 0,
\end{aligned}
\qquad \boldsymbol{\xi} \in \mathbb{R}^3. \qquad (2.7)
$$

On multiplying (2.7a) and (2.7b) respectively by $\overline{G}(\boldsymbol{\xi},\boldsymbol{\zeta})$ and $\overline{G}(\boldsymbol{\xi},\boldsymbol{x}^\circ)$ and integrating by parts over $\mathscr{B}_2$, one finds by way of the divergence theorem that

$$\int_{\Gamma^{\mathrm{obs}}} G_{,n}(\boldsymbol{\xi},\boldsymbol{a})\, \overline{G}(\boldsymbol{\xi},\boldsymbol{b})\, \mathrm{d}\Gamma_\xi \;-\; \int_{\mathscr{B}_2} \nabla G(\boldsymbol{\xi},\boldsymbol{a}) \cdot \nabla\overline{G}(\boldsymbol{\xi},\boldsymbol{b})\, \mathrm{d}\mathscr{B}_\xi$$

$$+\; k^2 \int_{\mathscr{B}_2} G(\boldsymbol{\xi},\boldsymbol{a})\, \overline{G}(\boldsymbol{\xi},\boldsymbol{b})\, \mathrm{d}\mathscr{B}_\xi \;=\; -\overline{G}(\boldsymbol{a},\boldsymbol{b}), \qquad (\boldsymbol{a},\boldsymbol{b}) \in \{(\boldsymbol{x}^\circ,\boldsymbol{\zeta}),(\boldsymbol{\zeta},\boldsymbol{x}^\circ)\}, \qquad (2.8)$$

Thanks to (2.3), the subtraction of the complex conjugate of (2.8) with $(\boldsymbol{a},\boldsymbol{b}) = (\boldsymbol{\zeta},\boldsymbol{x}^\circ)$ from its companion yields

$$\int_{\Gamma^{\mathrm{obs}}} \overline{G}(\boldsymbol{\xi},\boldsymbol{\zeta})\, G(\boldsymbol{\xi},\boldsymbol{x}^\circ)\, [1 + E(\boldsymbol{\xi},\boldsymbol{x}^\circ,\boldsymbol{\zeta})]\, \mathrm{d}\Gamma_\xi \;=\; -\frac{1}{k}\, \mathrm{Im}(G(\boldsymbol{x}^\circ,\boldsymbol{\zeta})), \quad \boldsymbol{x}^\circ,\boldsymbol{\zeta} \in \mathscr{B}_1, \qquad (2.9)$$

where

$$E(\boldsymbol{\xi},\boldsymbol{x}^\circ,\boldsymbol{\zeta}) \;=\; \left[\frac{1}{2\mathrm{i}k}\left(\widehat{(\overline{\boldsymbol{\xi}-\boldsymbol{x}^\circ})} - \widehat{(\overline{\boldsymbol{\xi}-\boldsymbol{\zeta}})} \right) + \frac{1}{2}\left(\widehat{(\boldsymbol{\xi}-\boldsymbol{x}^\circ)} + \widehat{(\boldsymbol{\xi}-\boldsymbol{\zeta})} \right) \right] \cdot \boldsymbol{n}(\boldsymbol{\xi}) - 1,$$

noting that $\widehat{\boldsymbol{x}} = \boldsymbol{x}/|\boldsymbol{x}|$ and $\bar{\widehat{\boldsymbol{x}}} = \boldsymbol{x}/|\boldsymbol{x}|^2$. On recalling that $R_1 = 1$ and $R_2 = \alpha^{-1} > 1$, one finds via triangle inequality as

$$|E(\boldsymbol{\xi}, \boldsymbol{x}^\circ, \boldsymbol{\zeta})| \; < \; \frac{\alpha^2}{k(1-\alpha^2)} + \frac{\alpha^2}{2} + O(\alpha^4), \qquad \boldsymbol{\xi} \in \Gamma^{\text{obs}}, \quad \boldsymbol{x}^\circ, \boldsymbol{\zeta} \in \mathscr{B}_1.$$

When $k \geqslant O(1)$, (2.9) accordingly yields the Helmholtz-Kirchhoff identity

$$\int_{\Gamma^{\text{obs}}} \overline{G}(\boldsymbol{\xi}, \boldsymbol{\zeta})\, G(\boldsymbol{\xi}, \boldsymbol{x}^\circ)\, \mathrm{d}\Gamma_\xi \;\overset{\alpha^2}{=}\; -\frac{1}{k}\, \mathrm{Im}\big(G(\boldsymbol{x}^\circ, \boldsymbol{\zeta})\big), \qquad \boldsymbol{x}^\circ, \boldsymbol{\zeta} \in \mathscr{B}_1, \tag{2.10}$$

where " $\overset{\alpha^n}{=}$ " signifies approximation with an $O(\alpha^n)$ residual.

2.1.2.2 The $\overline{G}\,\nabla G$ and $\nabla\overline{G}\,G$ terms

On differentiating (2.9) with respect to $\boldsymbol{x}^\circ$, one obtains

$$-\int_{\Gamma^{\text{obs}}} \overline{G}(\boldsymbol{\xi}, \boldsymbol{\zeta})\, \nabla G(\boldsymbol{\xi}, \boldsymbol{x}^\circ)\, [1 + E(\boldsymbol{\xi}, \boldsymbol{x}^\circ, \boldsymbol{\zeta})]\, \mathrm{d}\Gamma_\xi + \int_{\Gamma^{\text{obs}}} \overline{G}(\boldsymbol{\xi}, \boldsymbol{\zeta})\, G(\boldsymbol{\xi}, \boldsymbol{x}^\circ)\, \nabla_{\boldsymbol{x}^\circ} E(\boldsymbol{\xi}, \boldsymbol{x}^\circ, \boldsymbol{\zeta})\, \mathrm{d}\Gamma_\xi$$

$$= \; -\frac{1}{k}\, \mathrm{Im}\big(\nabla G(\boldsymbol{x}^\circ, \boldsymbol{\zeta})\big), \quad \boldsymbol{x}^\circ, \boldsymbol{\zeta} \in \mathscr{B}_1, \tag{2.11}$$

where ∇G implies differentiation with respect to the first argument. To expose the magnitude of $\nabla_{\boldsymbol{x}^\circ} E$, it can be shown by the law of cosines that

$$|\nabla_{\boldsymbol{x}^\circ} E(\boldsymbol{\xi}, \boldsymbol{x}^\circ, \boldsymbol{\zeta})| \; < \; \frac{\alpha^2}{2k(1-\alpha)^2} + \frac{\alpha^2}{2(1-\alpha^2)} + O(\alpha^4), \qquad \boldsymbol{\xi} \in \Gamma^{\text{obs}}, \quad \boldsymbol{x}^\circ, \boldsymbol{\zeta} \in \mathscr{B}_1.$$

As a result, (2.11) can be rewritten as

$$\int_{\Gamma^{\text{obs}}} \overline{G}(\boldsymbol{\xi}, \boldsymbol{\zeta})\, \nabla G(\boldsymbol{\xi}, \boldsymbol{x}^\circ)\, \mathrm{d}\Gamma_\xi \;\overset{\alpha^2}{=}\; -\left[\mathrm{Re}(G(\boldsymbol{x}^\circ, \boldsymbol{\zeta})) + \frac{1}{kr}\, \mathrm{Im}(G(\boldsymbol{x}^\circ, \boldsymbol{\zeta}))\right] \widehat{(\boldsymbol{x}^\circ - \boldsymbol{\zeta})}, \qquad \boldsymbol{x}^\circ, \boldsymbol{\zeta} \in \mathscr{B}_1, \tag{2.12}$$

where $r = |\boldsymbol{x}^\circ - \boldsymbol{\zeta}|$. In a similar fashion, the differentiation of (2.9) with respect to $\boldsymbol{\zeta}$ yields

$$\int_{\Gamma^{\text{obs}}} \nabla\overline{G}(\boldsymbol{\xi}, \boldsymbol{\zeta})\, G(\boldsymbol{\xi}, \boldsymbol{x}^\circ)\, \mathrm{d}\Gamma_\xi \;\overset{\alpha^2}{=}\; \left[\mathrm{Re}(G(\boldsymbol{x}^\circ, \boldsymbol{\zeta})) + \frac{1}{kr}\, \mathrm{Im}(G(\boldsymbol{x}^\circ, \boldsymbol{\zeta}))\right] \widehat{(\boldsymbol{x}^\circ - \boldsymbol{\zeta})}, \qquad \boldsymbol{x}^\circ, \boldsymbol{\zeta} \in \mathscr{B}_1. \tag{2.13}$$

2.1.2.3 The $\nabla \overline{G} \otimes \nabla G$ term

To evaluate the second integral over Γ^{obs} in (2.6), one may differentiate (2.11) with respect to $\boldsymbol{\zeta}$ as

$$\int_{\Gamma^{\text{obs}}} \nabla G(\boldsymbol{\xi}, \boldsymbol{x}^{\circ}) \otimes \nabla \overline{G}(\boldsymbol{\xi}, \boldsymbol{\zeta}) \left[1 + E(\boldsymbol{\xi}, \boldsymbol{x}^{\circ}, \boldsymbol{\zeta})\right] d\Gamma_{\xi} - \int_{\Gamma^{\text{obs}}} \overline{G}(\boldsymbol{\xi}, \boldsymbol{\zeta}) \, \nabla G(\boldsymbol{\xi}, \boldsymbol{x}^{\circ}) \otimes \nabla_{\zeta} E(\boldsymbol{\xi}, \boldsymbol{x}^{\circ}, \boldsymbol{\zeta}) \, d\Gamma_{\xi}$$

$$- \int_{\Gamma^{\text{obs}}} G(\boldsymbol{\xi}, \boldsymbol{x}^{\circ}) \, \nabla_{\boldsymbol{x}^{\circ}} E(\boldsymbol{\xi}, \boldsymbol{x}^{\circ}, \boldsymbol{\zeta}) \otimes \nabla \overline{G}(\boldsymbol{\xi}, \boldsymbol{\zeta}) \, d\Gamma_{\xi} \;=\; \frac{1}{k} \, \text{Im}\big(\nabla\nabla G(\boldsymbol{x}^{\circ}, \boldsymbol{\zeta})\big), \quad \boldsymbol{x}^{\circ}, \boldsymbol{\zeta} \in \mathscr{B}_1, \tag{2.14}$$

noting that $\nabla_{\zeta} \nabla_{\boldsymbol{x}^{\circ}} E = \boldsymbol{0}$ due to the structure of the residual which permits decomposition $E(\boldsymbol{\xi}, \boldsymbol{x}^{\circ}, \boldsymbol{\zeta}) = E_1(\boldsymbol{\xi}, \boldsymbol{x}^{\circ}) + E_2(\boldsymbol{\xi}, \boldsymbol{\zeta})$. On the basis of (2.3), (2.9) and (2.12), (2.14) reduces to

$$\int_{\Gamma^{\text{obs}}} \nabla \overline{G}(\boldsymbol{\xi}, \boldsymbol{\zeta}) \otimes \nabla G(\boldsymbol{\xi}, \boldsymbol{x}^{\circ}) \, d\Gamma_{\xi} \;\overset{\alpha^2}{=}\; -\frac{1}{r}\left[\text{Re}(G(\boldsymbol{x}^{\circ}, \boldsymbol{\zeta})) + \frac{1}{kr}\text{Im}(G(\boldsymbol{x}^{\circ}, \boldsymbol{\zeta}))\right] \boldsymbol{I}$$

$$+ \frac{1}{r}\left[3\,\text{Re}(G(\boldsymbol{x}^{\circ}, \boldsymbol{\zeta})) + \Big(\frac{3}{kr} - kr\Big)\text{Im}(G(\boldsymbol{x}^{\circ}, \boldsymbol{\zeta}))\right]\widehat{(\boldsymbol{x}^{\circ} - \boldsymbol{\zeta})} \otimes \widehat{(\boldsymbol{x}^{\circ} - \boldsymbol{\zeta})}, \quad \boldsymbol{x}^{\circ}, \boldsymbol{\zeta} \in \mathscr{B}_1, \tag{2.15}$$

where $r = |\boldsymbol{x}^{\circ} - \boldsymbol{\zeta}|$ as before, and $\boldsymbol{I}$ is the second-order identity tensor.

2.2 High-frequency behavior of topological sensitivity

Consider the scattering of a plane wave, $u^i = e^{-ik\boldsymbol{x}\cdot\boldsymbol{d}}$, by convex impenetrable obstacle D as examined in Section 3.1. Next, let $\boldsymbol{n}$ signify the outward normal on $S = \partial D$; let $S^{\text{f}}(\boldsymbol{d}) = \{\boldsymbol{x} \in S : \boldsymbol{n}(\boldsymbol{x}) \cdot \boldsymbol{d} < 0\}$ be the "front" (i.e. illuminated) part of S, and denote by $S^{\text{b}}(\boldsymbol{d}) = \{\boldsymbol{x} \in S : \boldsymbol{n}(\boldsymbol{x}) \cdot \boldsymbol{d} \geqslant 0\}$ its "back" side. In what follows, the wavenumber is assumed to be large in the sense that $kL_{\min} \gg 1$, where $L_{\min}$ denotes the smallest characteristic length scale (e.g. minimum radius of curvature) of ∂D. Without loss of generality, the nucleating obstacle underpinning the definition of topological sensitivity is assumed to be ball-shaped [84], in which case

$$\boldsymbol{A} \;=\; 3(2 + \beta)^{-1} \boldsymbol{I}. \tag{2.16}$$

Dirichlet obstacle as a testbed. To provide specificity for the analysis, it is hereon assumed that D is *sound-soft*, i.e. of Dirichlet type. The case of a Neumann (sound-hard) obstacle is treated separately in Section 2.3.3. As it turns out, however, the latter developments draw heavily from the Dirichlet analysis – and in fact require only a minimal amount of additional deliberation.

2.2.1 Kirchhoff approximation

When the obstacle is sound-soft and $kL_{\min} \gg 1$, the physical optics (Kirchhoff) approximation [31] states that

$$u = 0 \quad \text{on} \quad S = \partial D, \qquad u_{,n} = \begin{cases} 2\, u^i_{,n} & \text{on} \quad S^{\mathrm{f}} \\ 0 & \text{on} \quad S^{\mathrm{b}} \end{cases}. \tag{2.17}$$

By virtue of (2.17), (2.6) reduces to

$$\begin{aligned} \mathsf{T}(\boldsymbol{x}^\circ, \beta, \gamma) &= -2\,\mathrm{Re}\Big[(1-\beta)\,\nabla u^i(\boldsymbol{x}^\circ)\cdot\boldsymbol{A}\cdot\int_{S^{\mathrm{f}}} \overline{u^i_{,n}}(\boldsymbol{\zeta}) \int_{\Gamma^{\mathrm{obs}}} \overline{G}(\boldsymbol{\xi},\boldsymbol{\zeta})\,\nabla G(\boldsymbol{\xi},\boldsymbol{x}^\circ)\,\mathrm{d}\Gamma_\xi\,\mathrm{d}S_\zeta \\ &\quad + (1-\beta\gamma^2)\,k^2\,u^i(\boldsymbol{x}^\circ)\int_{S^{\mathrm{f}}} \overline{u^i_{,n}}(\boldsymbol{\zeta}) \int_{\Gamma^{\mathrm{obs}}} \overline{G}(\boldsymbol{\xi},\boldsymbol{\zeta})\,G(\boldsymbol{\xi},\boldsymbol{x}^\circ)\,\mathrm{d}\Gamma_\xi\,\mathrm{d}S_\zeta\Big]. \end{aligned} \tag{2.18}$$

On recalling that $u^i = e^{-\mathrm{i}k\boldsymbol{x}\cdot\boldsymbol{d}}$ and substituting (2.10), (2.12) and (2.16) into (2.18), one finds that

$$\mathsf{T}(\boldsymbol{x}^\circ, \beta, \gamma) = 2k^2\,\mathrm{Im}\Big[\frac{3(1-\beta)}{2+\beta}\,(\mathrm{i}\,e^{-\mathrm{i}k\boldsymbol{x}^\circ\cdot\boldsymbol{d}})\,J_1 - (1-\beta\gamma^2)\,(e^{-\mathrm{i}k\boldsymbol{x}^\circ\cdot\boldsymbol{d}})\,J_2\Big], \tag{2.19}$$

where

$$\begin{aligned} J_1 &= \int_{S^{\mathrm{f}}} e^{\mathrm{i}k\boldsymbol{\zeta}\cdot\boldsymbol{d}}\left[\mathrm{Re}\big(G(\boldsymbol{x}^\circ,\boldsymbol{\zeta})\big) + \frac{1}{kr}\,\mathrm{Im}\big(G(\boldsymbol{x}^\circ,\boldsymbol{\zeta})\big)\right]\boldsymbol{d}\cdot\boldsymbol{n}(\boldsymbol{\zeta})\,\boldsymbol{d}\cdot\widehat{(\boldsymbol{x}^\circ - \boldsymbol{\zeta})}\,\mathrm{d}S_\zeta, \\ J_2 &= \int_{S^{\mathrm{f}}} e^{\mathrm{i}k\boldsymbol{\zeta}\cdot\boldsymbol{d}}\,\mathrm{Im}\big(G(\boldsymbol{x}^\circ,\boldsymbol{\zeta})\big)\,\boldsymbol{d}\cdot\boldsymbol{n}(\boldsymbol{\zeta})\,\mathrm{d}S_\zeta, \end{aligned} \tag{2.20}$$

and the $O(\alpha^2)$ approximation error stemming from (2.10) and (2.12) is tacit.

2.2.2 Contribution of non-degenerate stationary points

Consider first the high-frequency behavior of (2.19) when the sampling point $\boldsymbol{x}^\circ$ straddles the region of interest $\mathscr{B}_1$ *excluding* a "thin-shell" neighborhood of S^f, namely $\boldsymbol{x}^\circ \in \mathscr{B}_1 \backslash \mathscr{N}_\epsilon$, where

$$\mathscr{N}_\epsilon(\boldsymbol{d}) = \{\boldsymbol{x}\colon \boldsymbol{x} = \boldsymbol{\zeta} + \ell\boldsymbol{n}(\boldsymbol{\zeta}), \quad \boldsymbol{\zeta} \in S^\mathrm{f}(\boldsymbol{d}), \quad -\epsilon < \ell < \epsilon\}, \tag{2.21}$$

and $\epsilon = O(k^{-1})$ is a length scale to be specified later. In this setting, the analysis can be facilitated by recalling (2.3) and rewriting (2.19) as

$$
\begin{aligned}
J_1 \;=\; & \int_{S^\mathrm{f}} \frac{\boldsymbol{d}\cdot\boldsymbol{n}(\boldsymbol{\zeta})}{8\pi r}\Big(1+\frac{\mathrm{i}}{kr}\Big)\,\boldsymbol{d}\cdot\widehat{(\boldsymbol{x}^\circ - \boldsymbol{\zeta})}\, e^{\mathrm{i}k(\boldsymbol{\zeta}\cdot\boldsymbol{d}+r)}\,\mathrm{d}S_\zeta \;+ \\[2mm]
& \int_{S^\mathrm{f}} \frac{\boldsymbol{d}\cdot\boldsymbol{n}(\boldsymbol{\zeta})}{8\pi r}\Big(1-\frac{\mathrm{i}}{kr}\Big)\,\boldsymbol{d}\cdot\widehat{(\boldsymbol{x}^\circ - \boldsymbol{\zeta})}\, e^{\mathrm{i}k(\boldsymbol{\zeta}\cdot\boldsymbol{d}-r)}\,\mathrm{d}S_\zeta,
\end{aligned}
\tag{2.22}
$$

$$J_2 = \mathrm{i}\int_{S^\mathrm{f}} \frac{\boldsymbol{d}\cdot\boldsymbol{n}(\boldsymbol{\zeta})}{8\pi r}\, e^{\mathrm{i}k(\boldsymbol{\zeta}\cdot\boldsymbol{d}+r)}\,\mathrm{d}S_\zeta - \mathrm{i}\int_{S^\mathrm{f}} \frac{\boldsymbol{d}\cdot\boldsymbol{n}(\boldsymbol{\zeta})}{8\pi r}\, e^{\mathrm{i}k(\boldsymbol{\zeta}\cdot\boldsymbol{d}-r)}\,\mathrm{d}S_\zeta, \qquad r = |\boldsymbol{x}^\circ - \boldsymbol{\zeta}|.$$

To evaluate (2.22), one may invoke the parametrization of S^f in terms of curvilinear surface coordinates (η^1, η^2) as

$$\boldsymbol{\zeta} = \boldsymbol{\zeta}(\eta^1, \eta^2) \in S^\mathrm{f}, \quad \mathrm{d}S_\zeta = \sqrt{\det g_{pq}}\,\mathrm{d}S_\eta, \quad \mathrm{d}S_\eta = \mathrm{d}\eta^1\mathrm{d}\eta^2, \quad g_{pq} = \frac{\partial\boldsymbol{\zeta}}{\partial\eta^p}\frac{\partial\boldsymbol{\zeta}}{\partial\eta^q}, \quad p,q = 1,2,$$

where g_{pq} are the covariant components of the metric tensor, and $\partial\boldsymbol{\zeta}/\partial\eta^p$ is the unit tangent vector on S^f in the direction of η^p.

As examined in [31], the leading-order asymptotic behavior of (2.22) for large k is governed by the nature of the integrand in the neighborhood of three types of *critical points*, namely: i) the stationary points on S^f where $\nabla_\eta(\boldsymbol{\zeta}\cdot\boldsymbol{d}\pm r)$ vanishes; ii) the points on S^f where the integrand fails to be differentiable, and iii) all points on the closed curve ∂S^f – the boundary of S^f. By way of (2.21), $r \geqslant \epsilon > 0$ whereby the integrands in (2.22) are differentiable everywhere. One may also note that the latter *vanish* on ∂S^f due to multiplier $\boldsymbol{d}\cdot\boldsymbol{n}$. Following the analysis in [31], the leading contribution of ∂S^f to J_1 and J_2 can accordingly be shown (via integration by parts) to be $O(k^{-2})$ when k is large. In contrast, the contribution of a non-degenerate stationary point $\boldsymbol{\zeta}^* \in S^\mathrm{f}$ to a

two-dimensional Fourier integral

$$I \; = \; \int_{S^{\mathrm{f}}} f(\boldsymbol{\zeta})\, e^{\mathrm{i}k(\boldsymbol{\zeta}\cdot\boldsymbol{d}\pm r)} \,\mathrm{d}S_\eta, \qquad \boldsymbol{\zeta} = \boldsymbol{\zeta}(\eta^1,\eta^2), \qquad r = |\boldsymbol{\zeta}-\boldsymbol{x}^\circ|, \qquad (2.23)$$

can be computed via *non-uniform* asymptotic approximation [e.g. 152] as $O(k^{-1})$, namely

$$I^{\boldsymbol{\zeta}^*} \;\overset{k^{-2}}{=\!=}\; \frac{2\pi}{k}\, \frac{f(\boldsymbol{\zeta}^*)}{\sqrt{|\det A_{pq}|}}\, e^{\mathrm{i}k(\boldsymbol{\zeta}^*\cdot\boldsymbol{d}\pm r^*)+\mathrm{i}(\mathrm{sgn}\,A_{pq})\pi/4}, \qquad r^* = |\boldsymbol{\zeta}^*-\boldsymbol{x}^\circ|, \qquad (2.24)$$

where

$$A_{pq} \;=\; \frac{\partial^2(\boldsymbol{\zeta}\cdot\boldsymbol{d}\pm r)}{\partial\eta^p\partial\eta^q}\bigg|_{\boldsymbol{\zeta}=\boldsymbol{\zeta}^*}, \qquad p,q = 1,2, \qquad (2.25)$$

are the components of the Hessian matrix; $\det A_{pq} \neq 0$ by definition for simple stationary points, and $\mathrm{sgn}\,A_{pq} \in \{-2,0,2\}$ is the difference between the numbers of positive and negative eigenvalues of A_{pq}. Accordingly the portion of (2.22) due to non-degenerate stationary points can be computed, to the leading order, by summing the contributions of type (2.24).

Stationary points.

To evaluate (2.22) via the method of stationary phase [31], it is noted that

$$\nabla_\eta(\boldsymbol{\zeta}\cdot\boldsymbol{d}\pm r) = \boldsymbol{0} \quad\Longrightarrow\quad [\boldsymbol{d}\pm(\widehat{\boldsymbol{\zeta}-\boldsymbol{x}^\circ})]\cdot\frac{\partial\boldsymbol{\zeta}}{\partial\eta^p} \;=\; 0, \qquad \boldsymbol{\zeta}\in S^{\mathrm{f}}, \quad p=1,2. \qquad (2.26)$$

On denoting by $\boldsymbol{\zeta}^\pm \in S^{\mathrm{f}}$ the stationary point of $e^{\mathrm{i}k(\boldsymbol{\zeta}\cdot\boldsymbol{d}\pm r)}$, this implies that $\boldsymbol{d}\pm(\widehat{\boldsymbol{\zeta}^\pm-\boldsymbol{x}^\circ})$ must either vanish or be perpendicular to S^{f}. Making use of the inequality $\boldsymbol{d}\cdot\boldsymbol{n} < 0$, one finds from (2.26) that J_1 and J_2 feature two types of stationary points, namely

$$\begin{aligned} \boldsymbol{\zeta}_{\mathrm{I}}^\pm &= \boldsymbol{x}^\circ \mp r\,\boldsymbol{d} \\ \boldsymbol{\zeta}_{\mathrm{II}}^\pm &= \boldsymbol{x}^\circ \mp r\,[\boldsymbol{d}+2|\boldsymbol{d}\cdot\boldsymbol{n}|\,\boldsymbol{n}(\boldsymbol{\zeta}_{\mathrm{II}}^\pm)] \end{aligned}, \qquad \boldsymbol{\zeta}_{\mathrm{I/II}}^\pm \in S^{\mathrm{f}}(\boldsymbol{d}), \qquad r > 0. \qquad (2.27)$$

For a given sampling point, the stationary point of type I exists only if

$$\boldsymbol{x}^\circ \in \mathscr{L}^\pm, \qquad \mathscr{L}^\pm(\boldsymbol{d}) \;=\; \{\boldsymbol{x}\colon\, \boldsymbol{x} = \boldsymbol{\zeta}\pm\tau\,\boldsymbol{d}, \quad \boldsymbol{\zeta}\in S^{\mathrm{f}}(\boldsymbol{d}), \quad \tau > 0\}, \qquad (2.28)$$
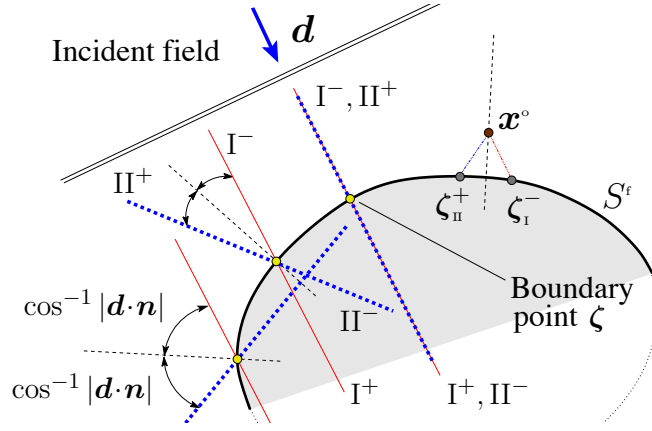
Figure 2.3: Loci of the sampling points, $\boldsymbol{x}^\circ$, for which given boundary point $\boldsymbol{\zeta} \in S^{\mathrm{f}}$ is the *stationary point* of type I (solid lines) and type II (thick dashed lines). The normal on S^{f} is indicated by a thin dashed line. On the right side of the diagram, also depicted is the unique critical point of type I and the nearest critical point of type II for $\boldsymbol{x}^\circ$ close to S^{f}.

and is *uniquely* determined by the projection of $\boldsymbol{x}^\circ$ along $\boldsymbol{d}$ on S^{f}. In light of the implicit specification of $\boldsymbol{\zeta}_{\mathrm{II}}^{\pm}$, on the other hand, integrals J_1 and J_2 may have *multiple* stationary points of type II. To provide further insight into (2.27), let

$$
\begin{aligned}
\mathrm{I}^{\pm} &= \{\boldsymbol{x}^\circ\colon\ \boldsymbol{x}^\circ = \boldsymbol{\zeta}_{\mathrm{I}}^{\pm} \pm r\,\boldsymbol{d}, \quad r > 0\}, \\
\mathrm{II}^{\pm} &= \{\boldsymbol{x}^\circ\colon\ \boldsymbol{x}^\circ = \boldsymbol{\zeta}_{\mathrm{II}}^{\pm} \pm r\,[\boldsymbol{d} + 2|\boldsymbol{d}\cdot\boldsymbol{n}|\,\boldsymbol{n}(\boldsymbol{\zeta}_{\mathrm{II}}^{\pm})], \quad r > 0\},
\end{aligned}
\tag{2.29}
$$

denote the loci of the sampling points for which *given* boundary point $\boldsymbol{\zeta} \in S^{\mathrm{f}}$ is the stationary point of (2.22). This is illustrated in Fig. 2.3 which shows that the I^- and II^+ loci emanate from S^{f} toward the exterior of D, while their I^+ and II^- counterparts extend (initially) from S^{f} toward the interior of D. One also may note that at the "apex" of S^{f}, where $\boldsymbol{n} = -\boldsymbol{d}$, locus I^- (resp. I^+) coincides with locus II^+ (resp. II^-). Such coalescence, however, does not pose special problems since each of the component integrals in (2.22) will have a stationary point of *either* type I or type II that in this case coincides with the apex of S^{f}.

Stationary point of type I. Recalling (2.28), the asymptotic behaviors of J_1 and J_2 entail the contribution of a unique stationary point $\boldsymbol{\zeta}_{\mathrm{I}}^{\pm}$ when $\boldsymbol{x}^\circ \in \mathscr{L}^{\pm}$, and no entries

of type $I^{\pm}$ otherwise. The results in Appendix A.1 show that in the former case

$$\det(A_{pq}) \;=\; \det g_{pq}\frac{(\boldsymbol{d}\cdot\boldsymbol{n})^2}{r^2} > 0, \qquad \mathrm{sgn}\,(A_{pq}) = \pm 2, \qquad \boldsymbol{\zeta} = \boldsymbol{\zeta}_{\mathrm{I}}^{\pm}, \quad \boldsymbol{x}^{\circ}\!\in \mathrm{I}^{\pm}. \quad (2.30)$$

Accordingly, the use of (2.24) in (2.22) and substitution into (2.19) yields the contribution of $\boldsymbol{\zeta}_{\mathrm{I}}^{\pm}$ to the topological sensitivity at $\boldsymbol{x}^{\circ}\!\in \mathrm{I}^{\pm}$ as

$$\mathsf{T}^{\mathrm{I}^{\pm}}(\boldsymbol{x}^{\circ},\beta,\gamma) \;\overset{k\gg 1}{=\joinrel=}\; \pm\frac{3(1-\beta)}{2(2+\beta)}\frac{1}{r}, \qquad r = |\boldsymbol{x}^{\circ}\!- \boldsymbol{\zeta}_{\mathrm{I}}^{\pm}|, \qquad \boldsymbol{x}^{\circ}\!\in \mathrm{I}^{\pm}\!\cap (\mathscr{B}_1\backslash\mathscr{N}_{\epsilon}). \quad (2.31)$$

where r is separated from zero thanks to (2.21).

Stationary point of type II^+. From the analysis in Appendix A and Appendix C, one finds that J_1 and J_2 feature a *unique* stationary point $\boldsymbol{\zeta}_{\mathrm{II}}^+$ when $\boldsymbol{x}^{\circ}\!\in \mathbb{R}^3\backslash\bar{\mathscr{L}}^+$, and no contributions of type II^+ otherwise. In this setting, (A4) demonstrates that

$$\det(A_{pq}) \;=\; \det g_{pq}\frac{4(\boldsymbol{d}\cdot\boldsymbol{n})^2}{\rho_1\rho_2 r^2}\,(r+r_1)(r+r_2) > 0,$$
$$\mathrm{sgn}\,(A_{pq}) = 2, \qquad \boldsymbol{\zeta} = \boldsymbol{\zeta}_{\mathrm{II}}^+, \qquad \boldsymbol{x}^{\circ}\!\in \mathrm{II}^+, \quad (2.32)$$

where $\rho_{1/2}$ are the principal radii of curvature of S^{f} at $\boldsymbol{\zeta}_{\mathrm{II}}^+$ while the roots $r_{1/2}$, given by (A5), are strictly positive. On the basis of (2.19), (2.22), (2.24) and (2.32), the contribution of stationary point $\boldsymbol{\zeta}_{\mathrm{II}}^+$ to the topological sensitivity at $\boldsymbol{x}^{\circ} \in \mathrm{II}^+$ can be computed as

$$\mathsf{T}^{\mathrm{II}^+}(\boldsymbol{x}^{\circ},\beta,\gamma) \;\overset{1}{=\joinrel=}\; \frac{k\sqrt{\rho_1\rho_2}}{\sqrt{(r+r_1)(r+r_2)}}\,\mathrm{Im}\left[e^{2ik(\boldsymbol{d}\cdot\boldsymbol{n})^2 r}\right]\left\{\frac{3(1-\beta)}{4(2+\beta)}\left(1-2(\boldsymbol{d}\cdot\boldsymbol{n})^2\right) - \frac{1-\beta\gamma^2}{4}\right\},$$
$$r = |\boldsymbol{x}^{\circ}\!- \boldsymbol{\zeta}_{\mathrm{II}}^+|, \qquad \boldsymbol{x}^{\circ}\!\in \mathrm{II}^+\!\cap (\mathscr{B}_1\backslash\mathscr{N}_{\epsilon}), \quad (2.33)$$

where $\boldsymbol{n} = \boldsymbol{n}(\boldsymbol{\zeta}_{\mathrm{II}}^+)$. A comparison between (2.31) and (2.33) immediately reveals that the stationary points of type $\mathrm{I}^{\pm}$ do not contribute to the leading asymptotic behavior of topological sensitivity; as a result, their $O(1)$ contribution is hereon ignored.

Stationary point of type II^-. With reference to Fig. 2.3 it is clear that, depending on $\boldsymbol{x}^{\circ}$, integrals J_1 and J_2 may feature *multiple* stationary points of type II^- according

to the second of (2.27). For this class of critical points, it is shown in Appendix A.1 that

$$\det(A_{pq}) = \det g_{pq} \frac{4(\boldsymbol{d}\cdot\boldsymbol{n})^2}{\rho_1\rho_2 r^2}(r-r_1)(r-r_2),$$

$$\operatorname{sgn}(A_{pq}) = \sum_{j=1}^{2} \operatorname{sign}(r - r_j), \qquad \boldsymbol{\zeta} = \boldsymbol{\zeta}_{\mathrm{II}}^-, \qquad \boldsymbol{x}^\circ \in \mathrm{II}^-,$$

(2.34)

where the nature of the roots $r_1 \geqslant r_2 > 0$ and their bounds are detailed in Appendix A.2 (see for instance Fig. 8.1). From (2.34) it is seen that the non-uniform asymptotic expansion (2.24) breaks down as $r \to r_{1/2}$, which in physical terms corresponds to $\boldsymbol{x}^\circ$ straddling a *caustic region* [152]. Appendix A.3 demonstrates that in this case the corank of A_{pq} approaches either 1 or 2, depending on $\boldsymbol{d}$ relative to the orthonormal basis $(\boldsymbol{a}_1, \boldsymbol{a}_2, \boldsymbol{n})$ – given by the principal directions and the outward normal to S^{f} at $\boldsymbol{\zeta}_{\mathrm{II}}^-$. On denoting by $\mathscr{C}_{\mathrm{II}} \subset \mathrm{II}^-$ the neighborhood of $r = r_{1/2}$ where (2.24) fails, the "minus" counterpart of (2.33) can be shown to read

$$\mathsf{T}^{\mathrm{II}^-}(\boldsymbol{x}^\circ, \beta, \gamma) \overset{1}{=} \frac{-k\sqrt{\rho_1\,\rho_2}}{\sqrt{|(r-r_1)(r-r_2)|}} \operatorname{Im}\left[e^{-2ik(\boldsymbol{d}\cdot\boldsymbol{n})^2 r + i(\operatorname{sgn} A_{pq} - 2)\pi/4}\right] \times$$

$$\times \left\{\frac{3(1-\beta)}{4(2+\beta)}\left(1-2(\boldsymbol{d}\cdot\boldsymbol{n})^2\right) - \frac{1-\beta\gamma^2}{4}\right\},$$

(2.35)

$$r = |\boldsymbol{x}^\circ - \boldsymbol{\zeta}_{\mathrm{II}}^-|, \qquad \boldsymbol{x}^\circ \in (\mathrm{II}^- \backslash \mathscr{C}_{\mathrm{II}}) \cap (\mathscr{B}_1 \backslash \mathscr{N}_\epsilon),$$

where $\boldsymbol{n} = \boldsymbol{n}(\boldsymbol{\zeta}_{\mathrm{II}}^-)$. In principle when $\boldsymbol{x}^\circ \in \mathrm{II}^- \backslash \mathscr{C}_{\mathrm{II}}$, the "mother" stationary pont $\boldsymbol{\zeta}_{\mathrm{II}}^-$ does not interact with its neighbors in the sense that nominally $\det A_{pq}(\boldsymbol{\zeta}_{\mathrm{II}}^-) = O(1)$. In contrast when $\boldsymbol{x}^\circ \in \mathscr{C}_{\mathrm{II}}$, $\det A_{pq}(\boldsymbol{p}) = O(k^{-\lambda})$ for some nominal $\lambda > 0$ – in which case the neighboring stationary points are sufficiently close to $\boldsymbol{\zeta}_{\mathrm{II}}^-$, and the germane interaction must be accounted for via uniform asymptotic expansion of (2.23) that is examined next.

2.2.3 Uniform TS approximation in the caustic region

To frame the above discussion in a formal setting, recall that for a given i.e. fixed obstacle shape, the *bifurcation set* [153] of the phase function

$$\phi(\eta^1, \eta^2) = \boldsymbol{\zeta} \cdot \boldsymbol{d} - r, \qquad \boldsymbol{\zeta} = \boldsymbol{\zeta}(\eta^1, \eta^2), \quad r = |\boldsymbol{\zeta} - \boldsymbol{x}^\circ|, \tag{2.36}$$

is given by

$$B_\phi = \left\{ (\boldsymbol{d}, \boldsymbol{x}^\circ) \in \Omega \times \mathbb{R}^3 : \ \nabla_\eta \phi = \boldsymbol{0}, \quad \det\left(\frac{\partial^2 \phi}{\partial \eta^p \partial \eta^q}\right) = 0, \quad \boldsymbol{\zeta} \in S^{\mathrm{f}}(\boldsymbol{d}) \right\}, \tag{2.37}$$

such that there exist at least two stationary points of ϕ whose distance vanishes as $(\boldsymbol{d}, \boldsymbol{x}^\circ) \to B_\phi$.

Lemma 2.2.1. *For the problem under consideration,*

$$B_\phi = \left\{ (\boldsymbol{d}, \boldsymbol{x}^\circ) \in \Omega \times \mathbb{R}^3 : \ \boldsymbol{x}^o \in \mathit{\Pi}^-, \quad |\boldsymbol{x}^o - \boldsymbol{\zeta}_{\mathit{II}}^-| = r_{1/2}, \quad \boldsymbol{\zeta}_{\mathit{II}}^- \in S^f(\boldsymbol{d}) \right\}, \tag{2.38}$$

where the loci $\mathit{\Pi}^-$ and affiliated caustic distances $r_{1/2}$ are specified respectively in (2.29) and (A5).

Proof. The claim is a direct consequence of i) definition (2.37); ii) the completeness of the set of stationary points given by (2.27), and iii) the fact that the only loci in (2.29) which permit singular Hessian of the phase function are those of of type II^-. □

Following [29], the interaction between stationary points should be considered as soon as their diminishing distance reaches $O(k^{-1/2})$ (a more precise condition will be established later). Hence when, given $\boldsymbol{d}$, the sampling point approaches the bifurcation set i.e. straddles the caustic region, the phase function is characterized by at least two *interacting* stationary points whose analysis warrants a uniform asymptotic treatment. In the context of (2.35) this neighborhood of interaction, as measured along ray II^-, is denoted by $\mathscr{C}_{\mathit{II}}$.

Elements of the catastrophe theory

The fundamental framework for the analysis of interacting (or coalescing) stationary points is provided by the catastrophe theory [156, 168], which is rooted in the notion of

structurally-stable bifurcations [153]. To facilitate the discussion, assume without loss of generality that the phase function has a critical point at $\eta^1 = \eta^2 = 0$ so that $\nabla\phi|_{\mathbf{0}} = \mathbf{0}$. In this setting the theory originates from the Morse Lemma and Splitting Lemma [e.g. 132], which guarantee the existence of a local diffeomorphism $(\eta^1, \eta^2) \to (\vartheta^1, \vartheta^2)$ in a neighborhood of the critical point such that

$$\mathrm{corank}\Big(\frac{\partial^2\phi}{\partial\eta^p\partial\eta^q}\Big)\Big|_{\mathbf{0}} = \begin{cases} 0 & \Rightarrow & \phi = \pm(\vartheta^1)^2 \pm (\vartheta^2)^2 + \phi_\circ, \\ 1 & \Rightarrow & \phi = \pm(\vartheta^1)^2 + \psi(\vartheta^2) + \phi_\circ, \\ 2 & \Rightarrow & \phi = \psi(\vartheta^1, \vartheta^2) + \phi_\circ, \end{cases} \tag{2.39}$$

where $\phi_\circ$ is a constant, ψ is a smooth function whose value and derivatives up to order two all vanish at the origin. The basic question regarding (2.39), whose first phase representation signifies the non-degenerate case examined in Section 2.2.2, deals with the order of degeneracy carried by function ψ. This issue is resolved via the concept of *codimension*, $\mathrm{cod}(\phi) = \mathrm{cod}(\psi)$, of the phase function that can be introduced as follows. Consider first the so-called Jacobian ideal of ϕ, given by $\Delta(\phi) = g_1 \partial\phi/\partial\vartheta_1 + g_2 \partial\phi/\partial\vartheta_2$ for arbitrary smooth functions $g_{1/2}$, and its formal Taylor series, $\jmath\Delta(\phi)$. With such definitions, the codimension of ϕ (assuming it is finite) can be written as

$$\mathrm{cod}(\phi) = \dim(H_2/\jmath\Delta(\phi)), \tag{2.40}$$

where H_2 is the space of all power series $\mathbb{R}^2 \to \mathbb{R}$ with zero constant term. In situations when $\jmath\Delta(\phi)$ is expressible in terms of monomials, $\mathrm{cod}(\phi)$ is simply the number of missing monomials relative to those in H_2. As examined in [153], the geometric implication of (2.40) is that a small perturbation of ϕ with codimension n can produce at most $n+1$ critical points in a neighborhood of $\eta^1 = \eta^2 = 0$. In contrast, infinite codimension is identified with structurally-unstable bifurcations that can be avoided via small perturbations of the phase function [157].

Perhaps the most powerful result of the catastrophe theory is that of *universal unfolding*, which encapsulates feasible perturbations of ϕ (assuming structural stability) and provides for a uniform asymptotic treatment of diffraction catastrophes in a neighborhood of the bifurcation set. For a phase function $\phi = \hat{\phi}(\vartheta^1, \vartheta^2)$ of finite codimension,

a universal unfolding can be written as

$$\jmath\hat{\phi}(\vartheta^1,\vartheta^2)\big|_{(\boldsymbol{d},\boldsymbol{x}^\circ)\in B_\phi} \;+\; \sum_{m=1}^{M} c_m(\boldsymbol{d},\boldsymbol{x}^\circ)\,h_m(\vartheta^1,\vartheta^2), \qquad M = \mathrm{cod}(\phi), \tag{2.41}$$

where c_m are the control parameters that vanish on B_ϕ, and h_m form a basis for H_2 modulo $\jmath\Delta(\hat{\phi})$. In the context of (2.39) it is noted that (2.40) and (2.41) apply equally to ψ, since ϕ and ψ by definition share the codimension and universal unfolding.

Diffraction scaling. On denoting by $\Psi(c_1,\ldots,c_M)$ the canonic Fourier integral with $k = 1$ and prototypical unfolding (2.41) of the phase function, the leading-order contribution of cognate critical point to (2.23) in the neighborhood of B_ϕ when $k \gg 1$ can be computed (up to an $O(1)$ multiplier) by way of *diffraction scaling* [29] as $k^\mu \Psi(k^{\sigma_1}c_1,\ldots,k^{\sigma_M}c_M)$, where μ is the so-called singularity index signifying the intensity of a caustic, c_m are k-independent, and $\sigma_m > 0$ are the measures of fringe spacings in the control directions c_m (see Appendix B – supplementary material – for details).

Asymptotic order of the uniform approximation

With reference to (2.39)–(2.41), Table 2.1 provides the complete list of elementary diffraction catastrophes with $\mathrm{cod}(\phi) < 4$ according to Thom's classification theorem [29, 153], including the respective universal unfoldings (where $(\vartheta^1, \vartheta^2)$ are replaced by (s,t)) and diffraction scaling parameters. Note that the diffraction catastrophes with $\mathrm{cod}(\phi) > 3$ have not been fully analyzed due to their complexity [29]. To aid the high-frequency evaluation of topological sensitivity, Appendix B (supplementary material) outlines the uniform asymptotic expansion of two-dimensional Fourier integral (2.23) for each featured type of diffraction catastrophe. The main result of this summary, listed in the last column of Table 2.1, is the (fractional) asymptotic order of the uniform expansion when applied to the TS formula (2.19). As a point of reference, one may recall that the non-uniform approximations of type II are $O(k)$, while those of type I are $O(1)$.

Global shape of a scatterer. Assuming structural stability, the type of catastrophe affiliated with given stationary point $\boldsymbol{\zeta}_{\mathrm{II}}^- \in S^{\mathrm{f}}$ as $|\boldsymbol{x}^\circ - \boldsymbol{\zeta}_{\mathrm{II}}^-| \to r_{1/2}$ i.e. $(\boldsymbol{d},\boldsymbol{x}^\circ) \to B_\phi$ depends on the local behavior of the phase function, and thus on the geometry of S^{f},

Table 2.1: Elementary diffraction catastrophes with codimension less than four and the asymptotic order of their contribution, T^c, to the topological sensitivity. Following Appendix B, the error of each approximation is at most $O(k^{1/2})$.

Catastrophe	corank	cod	universal unfolding	μ	$\sigma_m^{\min}$	$\mathsf{T}^c(\boldsymbol{x}^\circ, \cdot, \cdot)$
Fold	1	1	$\pm s^2 + t^3/3 + ct$	$1/6$	$2/3$	$O(k^{7/6})$
Cusp	1	2	$\pm s^2 + t^4 + c_2 t^2 + c_1 t$	$1/4$	$1/2$	$O(k^{5/4})$
Swallowtail	1	3	$\pm s^2 + t^5 + c_3 t^3 + c_2 t^2 + c_1 t$	$3/10$	$2/5$	$O(k^{13/10})$
Hyp. umbilic	2	3	$s^3 + t^3 + c_3 st + c_2 t + c_1 s$	$1/3$	$1/3$	$O(k^{4/3})$
Ell. umbilic	2	3	$s^3 - s t^2 + c_3(s^2 + t^2) + c_2 t + c_1 s$	$1/3$	$1/3$	$O(k^{4/3})$

in a neighborhood of $\boldsymbol{\zeta}_{\mathrm{II}}^-$. In Appendix A and Appendix B, the degeneracy of the Hessian matrix is examined in terms of the *second-order* properties of S^{f} (synthesized via the second fundamental form) at $\boldsymbol{\zeta} = \boldsymbol{\zeta}_{\mathrm{II}}^-$. In general, this type of analysis can be enriched by considering the *third- and higher-order* surface properties of $S = \partial D$ [29]. The principal result of this paper in terms of Lemma 2.3.5 and Lemma 2.3.6, however, applies *regardless* of this caveat – as long as the diffraction catastrophes affiliated with S do not exceed three in terms of their codimension.

2.2.4 TS approximation in the neighborhood of S^{f}

To complete the analysis, consider the case $\boldsymbol{x}^\circ \in \mathcal{N}_\epsilon$ where $\mathcal{N}_\epsilon$ is a thin-shell neighborhood of S^{f} given by (2.21). It is apparent from Fig. 2.3 that as $\boldsymbol{x}^\circ \to S^{\mathrm{f}}$ from the outside (resp. inside) there exist at least two stationary points, $\boldsymbol{\zeta}_{\mathrm{II}}^+$ and $\boldsymbol{\zeta}_{\mathrm{I}}^-$ (resp. $\boldsymbol{\zeta}_{\mathrm{II}}^-$ and $\boldsymbol{\zeta}_{\mathrm{I}}^+$), that merge at the normal projection of $\boldsymbol{x}^\circ$ onto S^{f}, denoted by $\boldsymbol{x}^\star$. Further when $\boldsymbol{x}^\circ \in S^{\mathrm{f}}$, the phase function in (2.22) assumes locally-conical shape and becomes non-differentiable at $r = 0$ i.e. $\boldsymbol{\zeta} = \boldsymbol{x}^\circ = \boldsymbol{x}^\star$, which is also the point where the non-exponential factors of integrands in J_1 and J_2 become singular. Under such circumstances, the asymptotic approximations developed in Sections 2.2.2–2.2.3 break down i.e. cease to represent the contribution of stationary points located in the vicinity of $\boldsymbol{x}^\star$. The purpose of this section is accordingly two-fold, namely to i) identify the length scale ϵ in (2.21) which preserves the validity of previously developed approximations, and ii) expose the asymptotic contribution of $\boldsymbol{x}^\star \in S^{\mathrm{f}}$ to the topological sensitivity (2.19) when $\boldsymbol{x}^\circ \in \mathcal{N}_\epsilon$.
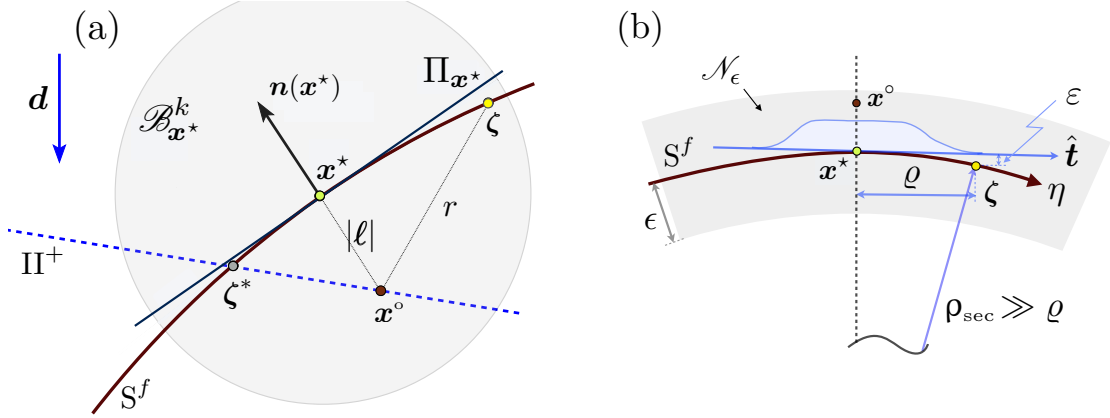
Figure 2.4: Sampling point $\boldsymbol{x}^\circ$ in a vicinity of the illuminated part, S^{f}, of the obstacle's boundary: (a) geometrical configuration, and (b) parameters in a generic normal section at $\boldsymbol{x}^\star$ used for computing the near-boundary approximation (ρ_{sec} is the sectional radius of curvature of S^{f}).

2.2.4.1 Extent of $\mathcal{N}_\epsilon$

With reference to Fig. 2.4(a), consider without loss of generality the situation where

$$\boldsymbol{x}^\circ \;=\; \boldsymbol{x}^\star - |\ell|\,\boldsymbol{n}(\boldsymbol{x}^\star), \qquad \ell \;=\; (\boldsymbol{x}^\circ - \boldsymbol{x}^\star)\!\cdot\!\boldsymbol{n}(\boldsymbol{x}^\star),$$

for some $\boldsymbol{x}^\star \in S^{\mathrm{f}}$ and small $|\ell|$, and let $\boldsymbol{\zeta}^* = \boldsymbol{\zeta}_{\mathrm{II}}^-$ denote the germane stationary point of type II. Next, recall the two-term extension [152] of the non-uniform approximation (2.24) which reads

$$\frac{2\pi}{k}\,\frac{e^{\mathrm{i}(\operatorname{sgn} A_{pq})\pi/4}}{\sqrt{|\det A_{pq}|}}\,e^{\mathrm{i}k\varphi(\boldsymbol{\zeta}^*)}\big(\mathrm{f}_0 + k^{-1}\mathrm{f}_1\big), \tag{2.42}$$

in terms of generic phase function $\varphi(\boldsymbol{\zeta})$, where $A_{pq} = \partial^2\varphi/(\partial\eta^p\partial\eta^q)$;

$$\mathrm{f}_0 \;=\; f(\boldsymbol{\zeta}^*), \quad \mathrm{f}_1 \;=\; 2\mathrm{i}\alpha^{-3}\big(2\mathrm{f}_0(\mathrm{p}_0 + \alpha\,\mathrm{p}_1) - 2\alpha\,\mathrm{p}_2 + \alpha^2\mathrm{p}_3\big), \quad \alpha \;=\; \det A_{pq}, \tag{2.43}$$

and

$$p_0 \;=\; 15\,(\varphi_{20}^3\,\varphi_{03}^2 \,+\, \varphi_{02}^3\,\varphi_{30}^2),$$

$$p_1 \;=\; \tfrac{3}{4}\varphi_{02}\,(2\varphi_{12}\varphi_{30} + \varphi_{21}^2) \,+\, \tfrac{3}{4}\varphi_{20}\,(2\varphi_{21}\varphi_{03} + \varphi_{12}^2) \,-$$
$$3(\varphi_{04}\varphi_{20}^2 + \varphi_{40}\varphi_{02}^2) \,-\, \varphi_{20}\varphi_{02}\varphi_{22},$$

$$p_2 \;=\; f_{10}\,(\varphi_{20}\varphi_{02}\varphi_{12} + 3\varphi_{30}\varphi_{02}^2) \,+\, f_{01}\,(\varphi_{02}\varphi_{20}\varphi_{21} + 3\varphi_{03}\varphi_{20}^2),$$

$$p_3 \;=\; f_{02}\varphi_{20} \,+\, f_{20}\varphi_{02}.$$

Here $g_{ij} = (i!\,j!)^{-1}\partial^{i+j}g(\boldsymbol{\zeta})/(\partial x^i \partial y^j)|_{\boldsymbol{\zeta}=\boldsymbol{\zeta}^*}$ for $g = \varphi, f$, and (x, y) are obtained by a local diffeomorphism from (η^1, η^2) so that $\partial^2\varphi/\partial x \partial y = 0$ at $\boldsymbol{\zeta} = \boldsymbol{\zeta}^*$.

In the context of (2.42), the idea behind exposing the characteristic length ϵ in (2.21) is to find a threshold value of $|\ell|$ beyond which $|k^{-1}\mathrm{f}_1/\mathrm{f}_0| = o(1)$. For brevity of exposition, the attention is hereon focused on applying (2.42) to the component of J_1 in (2.22) with phase function $\boldsymbol{\zeta}\cdot\boldsymbol{d} - r$, noting that the analysis of the remaining integrals in (2.22) yields the same result when $\boldsymbol{x}^\circ = \boldsymbol{x}^\star + \ell\boldsymbol{n}(\boldsymbol{x}^\star)$. To commence the analysis, let $|\ell| = |\boldsymbol{x}^\circ - \boldsymbol{x}^\star| = O(k^{-1})$, and let $\boldsymbol{x}^\star$ be located away from ∂S^{f} so that $\boldsymbol{\zeta}^*$ in Fig. 2.4(a) is contained within a ball $\mathscr{B}_{\boldsymbol{x}^\star}^k$ of radius $O(k^{-1})$ centered at $\boldsymbol{x}^\star$. In the high-frequency regime, one has $\rho_1 \geqslant \rho_2 \gg k^{-1}$, where ρ_1 and ρ_2 are the principal radii of curvature of S^{f} at $\boldsymbol{x}^\star$. As a result, S^{f} can be locally approximated (within $\mathscr{B}_{\boldsymbol{x}^\star}^k$) by its tangent plane, $\Pi_{\boldsymbol{x}^\star}$, drawn at $\boldsymbol{x}^\star$. As shown in Section 2.2.4.2, this treatment induces $O(k^{-2})$ error in the integration procedure.

To aid the application of (2.42), let the normal projection of $\boldsymbol{\zeta} \in S^{\mathrm{f}}$ on $\Pi_{\boldsymbol{x}^\star}$ be specified in terms of Cartesian coordinates (x, y) such that: i) $\boldsymbol{x}^\star$ is identified with the origin $(0, 0)$, and ii) x is parallel to the tangential component of $\boldsymbol{d}$, namely $\boldsymbol{d}_t = \boldsymbol{d} + |\boldsymbol{d}\cdot\boldsymbol{n}|\boldsymbol{n}(\boldsymbol{x}^\star)$. In this setting, the phase function can be approximated locally as

$$\boldsymbol{\zeta}\cdot\boldsymbol{d} - r \;\simeq\; \varphi(\boldsymbol{\zeta}), \quad \varphi \;=\; \boldsymbol{x}^\star\cdot\boldsymbol{d} \,+\, |\boldsymbol{d}_t|x \,-\, (\ell^2 + x^2 + y^2)^{1/2}, \quad \boldsymbol{\zeta} \in S^{\mathrm{f}} \cap \mathscr{B}_{\boldsymbol{x}^\star}^k, \quad (2.44)$$

for sufficiently large k. On computing the projection of the stationary point $\boldsymbol{\zeta}^*$ onto $\Pi_{\boldsymbol{x}^\star}$ as $(x^*, y^*) = (-\ell|\boldsymbol{d}_t|/d_n, 0)$ where $d_n = |\boldsymbol{d}\cdot\boldsymbol{n}(\boldsymbol{x}^\star)|$, the reduced phase function (2.44) can be expanded about (x^*, y^*) in Taylor series up to the fourth order to evaluate the necessary derivatives in (2.43). After treating in a similar way the multiplier of $\exp[\mathrm{i}k(\boldsymbol{\zeta}\cdot$

$\boldsymbol{d} - r)]$ in the first of (2.22), one finds that

$$\frac{f_1}{k\,f_0} = \frac{1}{8}\left|\frac{d_n}{k\ell}\right|(|k\ell| - \mathrm{i}\,d_n)^{-1}\left[d_n\,(15d_n^6 - 62d_n^4 + 87d_n^2 - 24) + \mathrm{i}\,|k\ell|\,(15d_n^6 - 46d_n^4 + 47d_n^2 - 8)\right],$$

from which it follows that $|k^{-1}f_1/f_0| \lesssim (2\pi)^{-1}$ for $|\ell| > 2\pi/k$. As a result, the second-order term in (2.42) can be neglected, i.e. (2.24) holds, for normal distances to S^{f} of at least *one wavelength*. One should bear in mind that, as the shadow region is approached when $\boldsymbol{x}^\star \to \partial S^{\mathrm{f}}$ i.e. $d_n \to 0$, the foregoing analysis ceases to apply for the distance between $\boldsymbol{\zeta}^*$ and $\boldsymbol{x}^\star$ exceeds $O(k^{-1})$, see Fig. 2.4(a). In this case, however, the situation is mitigated by the fact that the kernels in (2.22) are all proportional to d_n, which makes precise knowledge of the portal distance in this border region less relevant. Accordingly, the above threshold on $|\ell|$ is applied uniformly $\forall \boldsymbol{x}^\star \in S^{\mathrm{f}}$ by stipulating $\epsilon = O(k^{-1}) \geqslant 2\pi/k$ in (2.21).

2.2.4.2 Asymptotic expansion for $\boldsymbol{x}^{\mathrm{o}} \in \mathscr{N}_\epsilon$

In situations where the sampling point $\boldsymbol{x}^{\mathrm{o}}$ straddles the "near-boundary" region (2.21) with $\epsilon = O(k^{-1}) \geqslant 2\pi/k$, the method of stationary phase ceases to apply for critical points close to the normal projection, $\boldsymbol{x}^\star$, of $\boldsymbol{x}^{\mathrm{o}}$ on S^{f}. Further as $\boldsymbol{x}^{\mathrm{o}} \to \boldsymbol{x}^\star$, the normal projection itself becomes a critical point owing to the loss of differentiability of the integrands in (2.22) there. This section is devoted to computing asymptotically the contribution of $\boldsymbol{x}^\star \in S^{\mathrm{f}}$ (and its neighborhood) to $\mathsf{T}(\boldsymbol{x}^{\mathrm{o}}, \cdot, \cdot)$ when $\boldsymbol{x}^{\mathrm{o}} \in \mathscr{N}_\epsilon$.

It is well known that the topological sensitivity can be expressed as a bilinear form entailing two forward solutions for the reference domain, namely the incident field and the so-called adjoint field [e.g. 84]. In the context of Fig. 2.2, this guarantees that $\mathsf{T}(\boldsymbol{x}^{\mathrm{o}}, \cdot, \cdot)$ is in fact analytic for $\boldsymbol{x}^{\mathrm{o}} \in \mathscr{B}_1$. Indeed, the apparent singularities observed in (2.22) as $r \to 0$ (i.e. $\boldsymbol{x}^{\mathrm{o}} \to S^{\mathrm{f}}$) are the *artifact* of rearranging (2.20) to cater for the method of stationary phase, and can be dispensed with. Focusing on the component integral J_1 in (2.19), one finds from (2.3) and (2.20) that

$$J_1 = k\,e^{\mathrm{i}k\,\boldsymbol{x}^{\mathrm{o}}\cdot\boldsymbol{d}} \int_{S^{\mathrm{f}}} \frac{\boldsymbol{d}\cdot\boldsymbol{n}(\boldsymbol{\zeta})}{4\pi\,kr}\left[\cos(kr) - \frac{\sin(kr)}{kr}\right]\boldsymbol{d}\cdot(\widehat{\boldsymbol{x}^{\mathrm{o}} - \boldsymbol{\zeta}})\,e^{-\mathrm{i}k\,(\boldsymbol{x}^{\mathrm{o}} - \boldsymbol{\zeta})\cdot\boldsymbol{d}}\,\mathrm{d}S_\zeta, \qquad (2.45)$$

which is regular at $r = 0$. To analyze (2.45) when $\boldsymbol{x}^{\mathrm{o}} \in \mathscr{N}_\epsilon$, one may note that the

local behavior of the integrand is dominated by the term $(kr)^{-1}[\cos(kr) - \sin(kr)/kr]$, that vanishes at $kr = 0$ and reaches maximum (absolute) value at $kr \simeq 0.66$ i.e. $r = O(k^{-1})$. Thus, for sufficiently high k the contrbution of $\boldsymbol{x}^\star$ to J_1 can be evaluated by approximating S^{f} via its tangent plane $(\Pi_{\boldsymbol{x}^\star})$ as shown in Fig. 2.4(a).

To expose the error in computing the contribution of $\boldsymbol{x}^\star$ to J_1 via tangent-plane approximation, consider a generic normal section of S^{f} at $\boldsymbol{x}^\star$, and let $\hat{\boldsymbol{t}}$ denote the germane tangent vector as in Fig. 2.4(b) so that

$$
\begin{aligned}
r &= \sqrt{(\ell + \varepsilon)^2 + \varrho^2}, \qquad \ell = O(k^{-1}), \qquad \varrho = (\boldsymbol{x}^\circ - \boldsymbol{\zeta}) \cdot \hat{\boldsymbol{t}}, \\
\boldsymbol{x}^\circ - \boldsymbol{\zeta} &= (\ell + \varepsilon)\,\boldsymbol{n}(\boldsymbol{x}^\star) + \varrho \hat{\boldsymbol{t}}, \qquad \boldsymbol{n}(\boldsymbol{\zeta}) = \boldsymbol{n}(\boldsymbol{x}^\star) + \frac{2\varepsilon}{\varrho^2 + \varepsilon^2}\,(\varrho \hat{\boldsymbol{t}} - \varepsilon \boldsymbol{n}(\boldsymbol{x}^\star)).
\end{aligned}
\tag{2.46}
$$

Note that for $r = O(k^{-1})$, one has $\varrho = O(k^{-1})$ and $\varepsilon = O(k^{-2})$ under the premise of locally-constant radius of curvature. Accordingly, it follows from (2.45) and (2.46) that

$$
J_1 = J_1^\star + O(k^{-2}), \qquad J_1^\star = J_1|_{\varepsilon=0} = O(k^{-1}),
$$

in terms of the asymptotic contribution of $\boldsymbol{x}^\star$ to J_1, where $J_1^\star$ denotes the tangent-plane approximation obtained by setting $\varepsilon = 0$ in (2.46). On adopting the polar coordinate system (ϱ, θ) centered at $\boldsymbol{x}^\star$ so that direction $\boldsymbol{d}_t = \boldsymbol{d} - |\boldsymbol{d} \cdot \boldsymbol{n}|\boldsymbol{n}$ corresponds to $\theta = 0$, one finds that

$$
\begin{aligned}
J_1^\star = \frac{|\boldsymbol{d} \cdot \boldsymbol{n}|}{4\pi}\,e^{\mathrm{i}k\boldsymbol{x}^\star \cdot \boldsymbol{d}} \int_0^\infty \frac{k\varrho}{(kr_0)^2}\Big[\cos(kr_0) - \frac{\sin(kr_0)}{kr_0}\Big] \times \\
\times \int_0^{2\pi} \Big(|\boldsymbol{d} \cdot \boldsymbol{n}|k\ell + d_t \cos(\theta)k\varrho\Big) e^{\mathrm{i}d_t k\varrho \cos(\theta)}\,\mathrm{d}\theta\,\mathrm{d}\varrho,
\end{aligned}
\tag{2.47}
$$

where $\boldsymbol{n} = \boldsymbol{n}(\boldsymbol{x}^\star)$, $r_0 = \sqrt{\ell^2 + \varrho^2}$, $d_t = \sqrt{1 - |\boldsymbol{d} \cdot \boldsymbol{n}|^2}$, and the outer integral is extended to infinity via an implicit neutralizer function [e.g. 152]. The inner integral over θ can be computed in terms of Bessel functions of the first kind, reducing the outer integral to a pair of Hankel transforms

$$
J_1^\star = -\frac{|\boldsymbol{d} \cdot \boldsymbol{n}|}{2k}\,e^{\mathrm{i}k\boldsymbol{x}^\star \cdot \boldsymbol{d}} \Big\{|\boldsymbol{d} \cdot \boldsymbol{n}| \sin(k\ell) + d_t \Big[\mathrm{i}H_0(f_0; d_t) - |\boldsymbol{d} \cdot \boldsymbol{n}|\,k\ell\,H_1(f_1; d_t)\Big]\Big\}, \quad (2.48)
$$

where

$$H_\nu(f(\varrho); \tau) = \int_0^\infty f(\varrho)\, J_\nu(\tau\varrho)\, \sqrt{\tau\varrho}\, \mathrm{d}\varrho,$$

$$f_0 = \frac{\sin(kr_0)}{kr_0}\sqrt{k\,d_t\varrho}, \qquad f_1 = \frac{f_0}{k\,d_t\varrho}. \tag{2.49}$$

By way of the integral identities in [70], the leading-order contribution of $\boldsymbol{x}^\star$ to J_1 when $\boldsymbol{x}^\circ \in \mathscr{N}_\epsilon$ can accordingly be computed as

$$J_1^\star = -\frac{1}{2k}\, e^{\mathrm{i}k\boldsymbol{x}^\star \cdot \boldsymbol{d}}\left\{\mathrm{i}d_t^2\cos(|\boldsymbol{d}\cdot\boldsymbol{n}|k\ell) + |\boldsymbol{d}\cdot\boldsymbol{n}|^2\sin(|\boldsymbol{d}\cdot\boldsymbol{n}|k\ell)\right\}. \tag{2.50}$$

Recalling (2.20), the remaining integral in (2.19) can be evaluated in a similar fashion, yielding

$$J_2^\star = \frac{1}{2k}\, e^{\mathrm{i}k\boldsymbol{x}^\star \cdot \boldsymbol{d}}\cos(|\boldsymbol{d}\cdot\boldsymbol{n}|k\ell) \tag{2.51}$$

as the leading-order contribution of $\boldsymbol{x}^\star$ to J_2. On the basis of (2.19), (2.50) and (2.51), one finds

$$\mathsf{T}^\star(\boldsymbol{x}^\circ, \beta, \gamma) \overset{1}{=} \frac{k}{2}\sin(2k\ell|\boldsymbol{d}\cdot\boldsymbol{n}|)\left\{\frac{3(1-\beta)}{2+\beta}\left(1-2|\boldsymbol{d}\cdot\boldsymbol{n}|^2\right) - \left(1-\beta\gamma^2\right)\right\}, \qquad \boldsymbol{x}^\circ \in \mathscr{N}_\epsilon \tag{2.52}$$

to be the leading asymptotic contribution of $\boldsymbol{x}^\star$ to the topological sensitivity.

It is perhaps not surprising that the stationary phase approximations (2.33) and (2.35) share the *common multiplier* with (2.52), dependent on $|\boldsymbol{d}\cdot\boldsymbol{n}|$ and the trial material parameters of a vanishing obstacle, $\beta = \rho/\rho_{\mathrm{trial}}$ and $\gamma = c/c_{\mathrm{trial}}$. At this point, however, the choice of β and γ is left unspecified; their selection as it pertains to the reconstruction of a Dirichlet obstacle will be examined in Section 2.3.2.3, see also Section 2.3.4 for a unified discussion concerning Dirichlet and Neumann anomalies.

2.3   Imaging ability of the TS indicator function

From (2.4), it is seen that for $\boldsymbol{x}^\circ \in \mathscr{B}_1$ the topological sensitivity stems from a *bi-linear* form entailing two regular wave fields in the reference domain, namely the incident wave and the fundamental solution whose source is outside $\mathscr{B}_1$. As a result, the spatial distribution of TS is necessarily regular and generally characterized by wave-like fluctuations whose characteristic wavelength is π/k, i.e. half that of the illuminating wave. In this

setting, the key question is that of the conditions under which the most pronounced negative values of TS are localized in a narrow region "about the boundary" [50] of an obstacle.

2.3.1 Single plane-wave incidence

To provide an explicit platform for the analysis, the foregoing asymptotic developments (assuming the hidden anomaly to be of Dirichlet type) can be synthesized by writing

$$
\begin{aligned}
\mathsf{T}(\boldsymbol{x}^\circ, \beta, \gamma) \;\overset{k^\nu}{=}\;& 1_{\mathscr{N}_\epsilon(\boldsymbol{d})}(\boldsymbol{x}^\circ)\, \mathsf{T}^\star(\boldsymbol{x}^\circ, \beta, \gamma) \;+\; 1_{\tilde{B}_\phi}(\boldsymbol{d}, \boldsymbol{x}^\circ)\, \mathsf{T}^c(\boldsymbol{x}^\circ, \beta, \gamma) \\
& +\; 1_{\mathscr{G}(\boldsymbol{d})}(\boldsymbol{x}^\circ)\, \mathsf{T}^{\mathrm{II}^+}(\boldsymbol{x}^\circ, \beta, \gamma) \;+\; \sum \mathsf{T}^{\mathrm{II}^-}(\boldsymbol{x}^\circ, \beta, \gamma), \quad \boldsymbol{x}^\circ \in \mathscr{B}_1, \quad \boldsymbol{d} \in \Omega
\end{aligned}
\tag{2.53}
$$

where $\nu \leqslant 1/2$; $1_M(m)$ is the characteristic function equalling 1 for $m \in M$ and 0 otherwise; recalling Fig. 2.5, $\mathscr{N}_\epsilon$ is a thin-shell neighborhood of S^{f} given by (2.21); $\tilde{B}_\phi \supset B_\phi$ is a neighborhood of the bifurcation set (2.37) where the non-uniform approximation fails; and, as shown in Appendix C (supplementary material), $\mathscr{G}(\boldsymbol{d}) = \mathbb{R}^3 \backslash \bar{\mathscr{L}}^+(\boldsymbol{d})$ where $\mathscr{L}^+$ is a semi-infinite cylindrical domain given by (2.28). From (2.33), (2.35), (2.52) and Table 2.1, one finds that

$$
\mathsf{T}^\star = O(k), \qquad \mathsf{T}^c = O(k^\alpha), \quad \tfrac{7}{6} \leqslant \alpha \leqslant \tfrac{4}{3}, \qquad \mathsf{T}^{\mathrm{II}^\pm} = O(k).
\tag{2.54}
$$
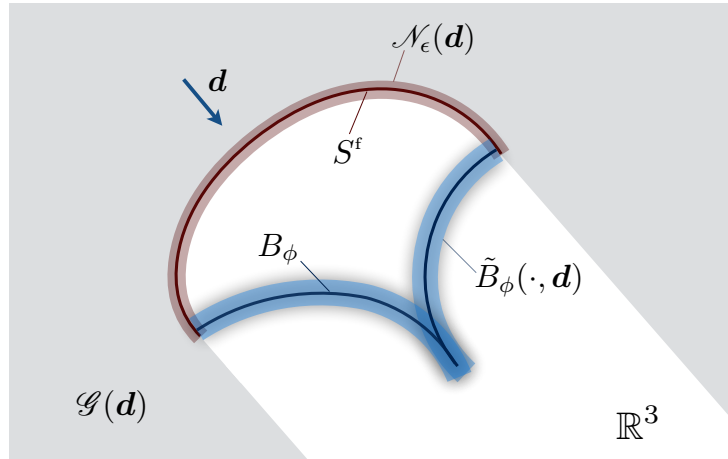
Figure 2.5: Schematics of the sets $\mathscr{N}_\epsilon$, $\tilde{B}_\phi$ and $\mathscr{G}$ featured in (2.53).

Note that for given $\boldsymbol{d}$, the contributions of type $\mathsf{T}^\star$, T^c and $\mathsf{T}^{\mathrm{II}^+}$ are *unique* due respectively to: i) the uniqueness of the normal projection of $\boldsymbol{x}^\circ \in \mathscr{N}_\epsilon$ on S^{f}, ii) premise that the hidden obstacle is convex with smooth boundary, and iii) geometrical grounds elaborated in Appendix C. In contrast $\mathsf{T}(\boldsymbol{x}^\circ, \beta, \gamma)$ may include the contribution of *multiple* isolated stationary points of type II^-, as indicated by the summation symbol before $\mathsf{T}^{\mathrm{II}^-}$. In the context of (2.53) one should also mention that for $\boldsymbol{x}^\circ \in \mathscr{N}_\epsilon$, the contribution of critical points within distance $O(k^{-1})$ from $\boldsymbol{x}^\star$ – accounted for via $\mathsf{T}^\star$ – is implicitly excluded when computing T^c and $\mathsf{T}^{\mathrm{II}^\pm}$.

From (2.54) it is readily seen that the near-boundary contribution is $O(k)$ i.e. commensurate with the non-uniform approximation, yet *subpar in order* relative to the asymptotic contribution of diffraction catastrophes summarized in Table 2.1. Accordingly the high-frequency distribution of topological sensitivity is, under the premise of single plane-wave incidence, asymptotically dominated by the caustics.

2.3.2 Full source aperture

To expose the imaging ability of the TS indicator function, consider the full source aperture companion of (2.4), namely

$$\breve{\mathsf{T}}(\boldsymbol{x}^\circ, \beta, \gamma) \;=\; \int_\Omega \mathsf{T}(\boldsymbol{x}^\circ, \beta, \gamma)\, \mathrm{d}\Omega_{\boldsymbol{d}}\,, \tag{2.55}$$

where the integration is performed over the direction $\boldsymbol{d}$ of incident plane wave, Ω is the unit sphere, and the dependence of T on $\boldsymbol{d}$ is implicit.

Proposition 2.3.1. *For given $\boldsymbol{x}^\circ \in \mathscr{B}_1$, every boundary point $\boldsymbol{\zeta} \in S$ becomes stationary point of type II for some unique incident direction $\boldsymbol{d} = \boldsymbol{d}^*(\boldsymbol{x}^\circ, \boldsymbol{\zeta})$ provided that $\widehat{(\boldsymbol{\zeta} - \boldsymbol{x}^\circ)} \cdot \boldsymbol{n}(\boldsymbol{\zeta}) \neq 0$.*

Proof. From (2.27) one finds that for stationary points of type II, $\boldsymbol{d}^*$ must satisfy

$$\hat{\boldsymbol{r}}^\pm \;=\; \mp[\boldsymbol{d}^* + 2|\boldsymbol{d}^* \cdot \boldsymbol{n}|\, \boldsymbol{n}(\boldsymbol{\zeta}_{\mathrm{II}}^\pm)]\,, \qquad \hat{\boldsymbol{r}}^\pm \;=\; \widehat{\boldsymbol{\zeta}_{\mathrm{II}}^\pm - \boldsymbol{x}^\circ}\,, \tag{2.56}$$

subject to the condition $\boldsymbol{d}^* \cdot \boldsymbol{n}(\boldsymbol{\zeta}_{\mathrm{II}}^\pm) < 0$ to ensure $\boldsymbol{\zeta}_{\mathrm{II}}^\pm \in S^{\mathrm{f}}(\boldsymbol{d}^*)$. A contraction of (2.56)
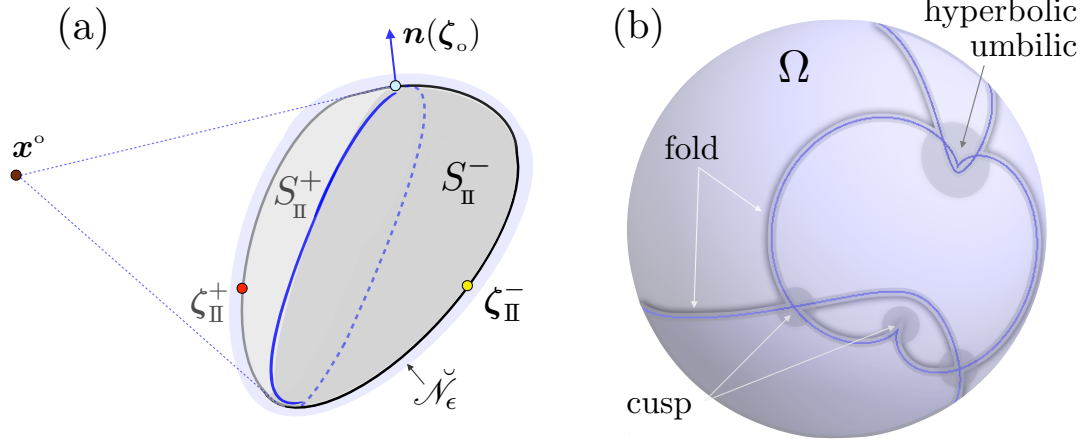
Figure 2.6: Schematics of the sets $S_{\mathrm{II}}^{\pm} \subset S$ and $B_\phi \subset \Omega$ for given $\boldsymbol{x}^\circ \in \mathscr{B}_1$: (a) Loci of the stationary points of type $\mathrm{II}^\pm$ when $\boldsymbol{d}$ spans Ω, and (b) bifurcation set $B_\phi(\boldsymbol{d}, \boldsymbol{x}^\circ)$ on the unit sphere, solid lines, surrounded by a narrow region $\tilde{B}_\phi$ (shaded area) where the non-uniform approximation fails.

with $\boldsymbol{n}(\boldsymbol{\zeta}_{\mathrm{II}}^{\pm})$ yields $\boldsymbol{d}^* \cdot \boldsymbol{n}(\boldsymbol{\zeta}_{\mathrm{II}}^{\pm}) = \pm\, \hat{\boldsymbol{r}}^{\pm} \cdot \boldsymbol{n}(\boldsymbol{\zeta}_{\mathrm{II}}^{\pm})$, whereby

$$\boldsymbol{d}^*(\boldsymbol{x}^\circ, \boldsymbol{\zeta}) \;=\; \sigma\,[\boldsymbol{I} - 2\boldsymbol{n} \otimes \boldsymbol{n}(\boldsymbol{\zeta})]\hat{\boldsymbol{r}}, \quad \hat{\boldsymbol{r}} \;=\; \widehat{\boldsymbol{\zeta} - \boldsymbol{x}^\circ}, \quad \sigma \;=\; \mathrm{sign}(\boldsymbol{n} \cdot \hat{\boldsymbol{r}}), \quad \sigma \neq 0. \quad (2.57)$$

Here $\boldsymbol{\zeta} \in S$ is a stationary point of type II for pair $(\boldsymbol{x}^\circ, \boldsymbol{d}^*)$, and $[\boldsymbol{I} - 2\boldsymbol{n} \otimes \boldsymbol{n}]$ is an (orthogonal) reflection matrix. The uniqueness of $\boldsymbol{d}^*$ is then verified by contradiction noting that $\boldsymbol{n}(\boldsymbol{\zeta})$ is single-valued. $\qquad\square$

Remark 1. *The uniqueness of $\boldsymbol{d}^*$ ceases at boundary points $\boldsymbol{\zeta}_o \in S$ where $\hat{\boldsymbol{r}} \cdot \boldsymbol{n}(\boldsymbol{\zeta}_o) = 0$. In particular, (2.56) demonstrates each $\boldsymbol{\zeta}_o$ is a stationary point of type $\mathrm{II}^\pm$ when $\boldsymbol{d}^* = \mp \hat{\boldsymbol{r}}$. Their leading-order contribution to $\check{\mathsf{T}}$, however, can be neglected since the slowly-varying components of the Fourier integrals in (2.20) vanish there due to the fact that $\boldsymbol{d}^* \cdot \boldsymbol{n}(\boldsymbol{\zeta}_o) = \hat{\boldsymbol{r}} \cdot \boldsymbol{n}(\boldsymbol{\zeta}_o) = 0$.*

Remark 2. *For $\boldsymbol{x}^\circ \in D$, one has $\hat{\boldsymbol{r}} \cdot \boldsymbol{n} \geqslant 0 \;\; \forall \boldsymbol{\zeta} \in S$. As a result, the stationarity type of every boundary point $\boldsymbol{\zeta}$ when $\boldsymbol{d} = \boldsymbol{d}^*(\boldsymbol{x}^\circ, \boldsymbol{\zeta})$ is II^-. When $\boldsymbol{x}^\circ \in \mathscr{B}_1 \backslash \overline{D}$, on the other hand, the boundary S of a Dirichlet obstacle can be split into subsets $S_{\mathrm{II}}^{\pm}(\boldsymbol{x}^\circ) = \{\boldsymbol{\zeta} \in S : \boldsymbol{d} = \boldsymbol{d}^*(\boldsymbol{x}^\circ, \boldsymbol{\zeta}) \rightarrow \boldsymbol{\zeta} = \boldsymbol{\zeta}_{\mathrm{II}}^{\pm}\}$, separated by a closed curve that is the locus of points $\boldsymbol{\zeta}_o$ where $\boldsymbol{d}^* \cdot \boldsymbol{n}(\boldsymbol{\zeta}_o) = 0$ (see Fig. 2.6(a)). When $\boldsymbol{x}^\circ \in \overline{D}$, these two subsets degenerate to $S_{\mathrm{II}}^+ = \emptyset$ and $S_{\mathrm{II}}^- = S$.*

Remark 3. *For given $\boldsymbol{x}^{\circ} \in \mathscr{B}_1$, the bifurcation set $B_{\phi}(\boldsymbol{d}, \boldsymbol{x}^{\circ})$ on the unit sphere spanned by $\boldsymbol{d}$ is a union of smooth curves and points where such curves join, intersect, or terminate as indicated in Fig. 2.6(b). Since $dim(\Omega) = 2$, the only diffraction catastrophe affiliated with the* curves *in B_{ϕ} is of type fold ($cod(\phi) = 1$), while the higher-order catastrophes ($cod(\phi) > 1$) appear as* points *[29] on Ω. In general, B_{ϕ} is contained within an open neighborhood $\tilde{B}_{\phi}$ where the non-uniform approximation fails, see also Fig. 2.5 for the schematics of $\tilde{B}_{\phi}$ in the physical space. On denoting by*

$$\boldsymbol{c} = \{c_m(\boldsymbol{d}, \boldsymbol{x}^{\circ}), \quad m = 1, ..., cod(\phi)\}$$

the minimal control space describing given diffraction catastrophe (see Section 2.2.3), B_{ϕ} and $\tilde{B}_{\phi}$ can be formally specified as the level set *$|\boldsymbol{c}| = 0$ and* neighborhood *$|\boldsymbol{c}| < k^{-\upsilon}$, where $\upsilon > 0$ is a catastrophe-specific scaling parameter to be specified later. For completeness, it is noted that B_{ϕ} is* closed *for the assumption to the contrary would require $cod(\phi) = 0$ [65]. In the context of (2.57) relating (for given $\boldsymbol{x}^{\circ}$) $\boldsymbol{d} = \boldsymbol{d}^*$ to the stationary point(s) $\boldsymbol{\zeta} \in S$, the subset of S corresponding to $\tilde{B}_{\phi}$ is hereon denoted by $\tilde{S}_{\phi}$.*

In light of the above remarks, one may observe that a *discrete* set of critical points contributing to $\mathsf{T}(\boldsymbol{x}^{\circ}, \beta, \gamma)$ in the case of a single incident wave, see (2.53), transitions in the course of full-aperture illumination into a *continuous* set S of all boundary points contributing to $\check{\mathsf{T}}(\boldsymbol{x}^{\circ}, \beta, \gamma)$. This suggests the possibility of a change of variable which remarkably facilitates the analysis. To introduce the idea, suppose that $\boldsymbol{x}^{\circ} \in \mathscr{B}_1 \backslash \{\mathscr{N}_{\epsilon} \cup D\}$ and consider the integral of $\mathsf{T}^{\mathrm{II}^+}$ with respect to $\boldsymbol{d}$ as it contributes to (2.55). Next, recall that (2.57) provides the map relating $\boldsymbol{d} = \boldsymbol{d}^*$ to the solid angle of a boundary point with respect to $\boldsymbol{x}^{\circ}$, namely $\hat{\boldsymbol{r}}$. This map is *one-to-one* on account of the uniqueness of $\boldsymbol{\zeta}_{\mathrm{II}}^+$, see Appendix C. It is then straightforward to transform $\hat{\boldsymbol{r}}$ to $\boldsymbol{\zeta} \in S_{\mathrm{II}}^+$ (see Fig. 2.6) using the solid angle property $\mathrm{d}\Omega_{\hat{\boldsymbol{r}}} = \sigma(\hat{\boldsymbol{r}} \cdot \boldsymbol{n}/r^2) \, \mathrm{d}S_{\boldsymbol{\zeta}}$, whereby

$$\int_{\Omega} 1_{\mathscr{G}(\boldsymbol{d})}(\boldsymbol{x}^{\circ}) \, \mathsf{T}^{\mathrm{II}^+}(\boldsymbol{x}^{\circ}, \beta, \gamma) \, \mathrm{d}\Omega_{\boldsymbol{d}} = -\int_{S_{\mathrm{II}}^+} \mathsf{T}^{\mathrm{II}^+}(\boldsymbol{x}^{\circ}, \beta, \gamma) \, \frac{\hat{\boldsymbol{r}} \cdot \boldsymbol{n}}{r^2} \, \mathrm{d}S_{\boldsymbol{\zeta}}, \qquad r = |\boldsymbol{x}^{\circ} - \boldsymbol{\zeta}|. \quad (2.58)$$

When $\boldsymbol{x}^{\circ} \in \mathscr{N}_{\epsilon} \backslash \overline{D}$, on the other hand, $\boldsymbol{\zeta}_{\mathrm{II}}^+ \in \mathscr{B}_{\boldsymbol{x}^{\star}}^k$ and its contribution is computed via $\mathsf{T}^{\star}$, see Section 2.2.4. Hence $\mathscr{B}_{\boldsymbol{x}^{\star}}^k \cap S$ must be excluded from S_{II}^+ in computing (2.58) via the concept of Van der Corput neutralizers [e.g. 39, 31]. This tool is implicitly used in all cases where partitioning of the domain of integration is in order.

The same change of variable can be applied to the integral over $\sum \mathsf{T}^{\mathrm{II}^-}$ in (2.53) with respect to $\boldsymbol{d}$. In this case, however, (2.57) is not one-to-one – which signifies the multiplicity of $\boldsymbol{\zeta}_{\mathrm{II}}^-$ and thus inherently accounts for the summation over $\mathsf{T}^{\mathrm{II}^-}$.

Corollary 1. *By way of (2.53), (2.55) and relationship* $|\hat{\boldsymbol{r}}\cdot\boldsymbol{n}| = |\boldsymbol{d}^*\cdot\boldsymbol{n}|$, *the full-aperture distribution* $\check{\mathsf{T}}$ *can be recast as*

$$\check{\mathsf{T}}(\boldsymbol{x}^o, \beta, \gamma) \overset{k^\nu}{=} \mathbb{1}_{\check{\mathcal{N}}_\epsilon}(\boldsymbol{x}^o) \int_\Omega \mathsf{T}^\star \, \mathrm{d}\Omega_{\boldsymbol{d}} \;+\; \int_{\tilde{B}_\phi} \mathsf{T}^c \, \mathrm{d}\Omega_{\boldsymbol{d}} \;+\; \int_{S^\pm} \frac{|\boldsymbol{d}^*\cdot\boldsymbol{n}|}{r^2} \mathsf{T}^{\mathrm{II}\pm} \mathrm{d}S_\zeta, \qquad (2.59)$$

where $\nu \leqslant 1/2$; $\boldsymbol{d}^*$ *solves (2.57);* $\check{\mathcal{N}}_\epsilon = \cup_{\boldsymbol{d}\in\Omega}\mathcal{N}_\epsilon(\boldsymbol{d})$ *is the "full-aperture" neighborhood of S constructed from (2.21);* $\mathsf{T}^\star = 0$ *for* $\boldsymbol{d}\cdot\boldsymbol{n}(\boldsymbol{x}^\star) > 0$;

$$S^\pm \;=\; S_{\mathrm{II}}^\pm \setminus \{\mathbb{1}_{\check{\mathcal{N}}_\epsilon}(\boldsymbol{x}^o) \mathscr{B}_{\boldsymbol{x}^\star}^k \cup \tilde{S}_\phi\}, \qquad (2.60)$$

and $\mathscr{B}_{\boldsymbol{x}^\star}^k$ *is a ball of radius* $O(k^{-1})$ *centered at the normal projection* $\boldsymbol{x}^\star$ *of* $\boldsymbol{x}^o$ *on S, see Fig. 2.4(a). Geometrically, the respective support of* $\mathsf{T}^\star, \mathsf{T}^c$ *and* $\mathsf{T}^\pm$ *in (2.59) can be described as unit hemisphere, a small neighborhood of the bifurcation set* B_ϕ *on the unit sphere, and the boundary of the scatterer excluding its subsets contributing to* $\mathsf{T}^\star$ *and* T^c.

2.3.2.1 Contribution of non-degenerate stationary points

Proposition 2.3.2. *The contribution of isolated stationary points to* $\check{\mathsf{T}}$ *in (2.59) scales as*

$$\int_{S^\pm} \frac{|\boldsymbol{d}^*\cdot\boldsymbol{n}|}{r^2} \mathsf{T}^{\mathrm{II}\pm} \, \mathrm{d}S_\zeta \;=\; O(k^\alpha), \qquad 0 \leqslant \alpha \leqslant \tfrac{1}{3} \qquad (2.61)$$

for sufficiently large k, assuming the codimension of phase singularities in the featured integral not to exceed three.

Proof. By way of (2.33) and (2.35), the left-hand side of (2.61) can be rewritten as a Fourier integral

$$k \, \mathrm{Im}\left[\int_{S^\pm} F^\pm(\boldsymbol{\zeta}) \, e^{\pm 2\mathrm{i}kr|\boldsymbol{d}^*\cdot\boldsymbol{n}|^2} \, \mathrm{d}S_\zeta \right], \qquad |\boldsymbol{d}^*\cdot\boldsymbol{n}| \;=\; |(\widehat{\boldsymbol{\zeta} - \boldsymbol{x}^o})\cdot\boldsymbol{n}(\boldsymbol{\zeta})|, \qquad (2.62)$$

where $S^\pm$ is such that $r > 2\pi k^{-1}$ thanks to (2.60), and

$$k \int_{S^\pm} |F^\pm(\boldsymbol{\zeta})|\, \mathrm{d}S_{\boldsymbol{\zeta}} \;=\; O(k).$$

In this setting, the leading asymptotic behavior of (2.62) is governed by critical points of the phase function $r|\boldsymbol{d}^*{\cdot}\boldsymbol{n}|^2$ which satisfy

$$2|\boldsymbol{d}^*{\cdot}\boldsymbol{n}| \left[\sigma\boldsymbol{n} - \frac{|\boldsymbol{d}^*{\cdot}\boldsymbol{n}|}{2}(\widehat{\boldsymbol{\zeta}-\boldsymbol{x}^\circ}) + \frac{\boldsymbol{d}^*{\cdot}\boldsymbol{a}_1}{\rho_1}r\boldsymbol{a}_1 + \frac{\boldsymbol{d}^*{\cdot}\boldsymbol{a}_2}{\rho_2}r\boldsymbol{a}_2 \right]\cdot\frac{\partial\boldsymbol{\zeta}}{\partial\eta^p} \;=\; \boldsymbol{0}, \qquad (2.63)$$

where $\sigma = \mathrm{sign}(\boldsymbol{n}{\cdot}\hat{\boldsymbol{r}})$ and $\rho_{1/2}$ are the principal radii of curvature of $S^\pm$ at $\boldsymbol{\zeta}$. From the definition of $S^\pm$ in (2.60), the relevant roots of (2.63) are

$$|(\widehat{\boldsymbol{\zeta}-\boldsymbol{x}^\circ}){\cdot}\boldsymbol{n}(\boldsymbol{\zeta})| \;=\; 1, \qquad (2.64)$$

which can be interpreted as the normal projection of $\boldsymbol{x}^\circ$ on S. Over S^+, the solution of (2.64) is unique due to the convexity and smoothness of S, whereby the phase function in this case possesses a single isolated stationary point. From (2.24), one accordingly finds that the integral over S^+ in (2.61) scales as $O(1)$.

On the other hand, the normal projection of $\boldsymbol{x}^\circ$ on S^- is generally not unique. In this case, it can be shown via (2.60) and (2.63) that the Hessian of $r|\boldsymbol{d}{\cdot}\boldsymbol{n}|^2$ becomes singular at a critical point $\boldsymbol{\zeta} \in S^-$ solving (2.64) only if

$$|\boldsymbol{\zeta} - \boldsymbol{x}^\circ| \;=\; \rho_{1/2}(\boldsymbol{\zeta}). \qquad (2.65)$$

Making an appeal to the analysis in Section 2.2.3 and Appendix B, one subsequently finds that the integral over S^- in (2.61), on accounting for catastrophes where (2.64) and (2.65) both hold, may include contributions of orders shown in Table 2. $\qquad\square$

Table 2.2: Leading-order contribution in (2.61) of the critical points over S^- to $\check{\mathsf{T}}(\boldsymbol{x}^\circ, \cdot, \cdot)$

Catastrophe of $r|\boldsymbol{d}^*{\cdot}\boldsymbol{n}|^2$	None	Fold	Cusp	Swallowtail	Hyperbolic umbilic	Elliptic umbilic
Contribution	$O(1)$	$O(k^{1/6})$	$O(k^{1/4})$	$O(k^{3/10})$	$O(k^{1/3})$	$O(k^{1/3})$

2.3.2.2 Contribution of diffraction catastrophes

Proposition 2.3.3. *For sufficiently large k, the contribution of caustics to* $\widecheck{\mathsf{T}}$ *in (2.59) behaves as*

$$\int_{\tilde{B}_\phi} \mathsf{T}^c \; d\Omega_{\boldsymbol{d}} \;\; = \;\; O(k^\alpha), \qquad \tfrac{1}{4} \leqslant \alpha \leqslant \tfrac{2}{3}. \tag{2.66}$$

Proof. The idea behind establishing (2.66) is to expose the vanishing support, $|\tilde{B}_\phi|$, of a region on the unit sphere where the non-uniform approximation fails – indicated by the shaded area in Fig. 2.6(b). In particular as $\boldsymbol{d}$ (for given $\boldsymbol{x}^\circ$) leaves $\tilde{B}_\phi \subset \Omega$, special functions involved in describing the diffraction catastrophes, formally denoted by

$$\Psi(k^{\sigma_1} c_1, \ldots, k^{\sigma_M} c_M), \qquad M = \mathrm{cod}(\phi) < 4 \tag{2.67}$$

(see Section 2.2.3 and Appendix B), approach their large-argument asymptotics [123] due to growing magnitude, $|\boldsymbol{c}| = (c_1^2 + \cdots + c_M^2)^{1/2}$, of the featured minimal control space. This in turn reduces the germane *uniform* approximation to either its non-uniform counterpart, or zero – on the dark side of some caustics (e.g. fold) due to absence of real stationary points [152]. On denoting $b_m = k^{\sigma_m} c_m$, such transition in (2.67) occurs when $(b_1^2 + \cdots + b_M^2)^{1/2} = O(1)$, see Fig. 14 in Appendix B as an example. Accordingly, one obtains

$$|\boldsymbol{c}| \;\; \leqslant \;\; O(k^{-\sigma_m^{\min}}), \qquad \sigma_m^{\min} \;\; = \;\; \min\{\sigma_1, \ldots, \sigma_M\} > 0 \tag{2.68}$$

as a *sufficient condition* for estimating the extent of $\tilde{B}_\phi$, where $\sigma_m^{\min}$ are given in Table 2.1.

The next step in the analysis is to establish (for given $\boldsymbol{x}^\circ$) a *linearized* relationship between $|\boldsymbol{c}|$ and $\mathrm{dist}(\boldsymbol{d}, B_\phi)$ on the unit sphere, in a small neighborhood of the bifurcation set. In the context of Fig. 2.6(b), it is recalled that the fold caustics $(\mathrm{cod}(\phi) = 1)$ translate into smooth non-intersecting curves in $B_\phi \subset \Omega$, while the catastrophes of higher codimension are projected as points in B_ϕ. In this setting, $\mathrm{dist}(\boldsymbol{d}, B_\phi)$ is identified as the normal spherical distance to a curve (resp. spherical distance to a point) when $\mathrm{cod}(\phi) = 1$ (resp. $\mathrm{cod}(\phi) > 1$). On writing the sought relationship as $|\boldsymbol{c}| = V \cdot \mathrm{dist}(\boldsymbol{d}, B_\phi)$, one

finds from (2.68) that

$$\tilde{B}_\phi \;=\; \{ \boldsymbol{d} \in \Omega : \; \mathrm{dist}(\boldsymbol{d}, B_\phi) \leqslant V^{-1} O(k^{-\sigma_m^{\min}}) \} \tag{2.69}$$

for sufficiently large k, noting that $V > 0$ since the bifurcation set $B_\phi \subset \Omega$ is *closed* (see Remark 3).

To estimate V, consider first a *fold* bifurcation point $\boldsymbol{d}^\circ \in B_\phi$ for given $\boldsymbol{x}^\circ$, and let $\boldsymbol{\zeta}^* \in S$ denote the affiliated critical point on the boundary of the scatterer. In this case $\boldsymbol{c} = c$, and the Hessian of ϕ is of corank one. On account of the Splitting Lemma (2.39) and Taylor expansion of $\phi(\boldsymbol{\zeta})$ about $\boldsymbol{\zeta}^*$, there exist local surface coordinates (σ, τ) such that

$$\phi(\boldsymbol{\zeta})\big|_{\boldsymbol{d}^\circ} \;\simeq\; \phi_\circ + \tfrac{1}{2} \phi_\circ^{(2)} \sigma^2 + \tfrac{1}{6} \phi_\circ''' \tau^3,$$

$$\phi_\circ^{(2)} = \frac{\partial^2 \phi}{\partial \sigma^2}\bigg|_{\boldsymbol{\zeta}^*}, \quad \phi_\circ''' = \frac{\partial^3 \phi}{\partial \tau^3}\bigg|_{\boldsymbol{\zeta}^*}, \quad \boldsymbol{\zeta} \simeq \boldsymbol{\zeta}^* + \sigma\, \hat{\boldsymbol{s}} + \tau\, \hat{\boldsymbol{t}} \tag{2.70}$$

where $\phi_\circ = \phi(\boldsymbol{\zeta}^*)$; $\phi_\circ^{(2)}$ and $\phi_\circ'''$ are $O(1)$, and $(\hat{\boldsymbol{s}}, \hat{\boldsymbol{t}})$ are the unit vectors tangent to (σ, τ) at $\boldsymbol{\zeta}^*$, used to describe $\boldsymbol{\zeta}$ to the leading order. The objective is to find the variation in c due to infinitesimal perturbation $\mathrm{d}\boldsymbol{d} \perp \boldsymbol{d}^\circ$. Using (2.70) and definition $\phi = \boldsymbol{\zeta} \cdot \boldsymbol{d} - r$ where $r = |\boldsymbol{x}^\circ - \boldsymbol{\zeta}|$, one finds

$$\phi(\boldsymbol{\zeta})\big|_{\boldsymbol{d}^\circ + \mathrm{d}\boldsymbol{d}} \;\simeq\; \tilde{\phi}_\circ + \tfrac{1}{2} \phi_\circ^{(2)} \sigma^2 + (\mathrm{d}\boldsymbol{d} \cdot \hat{\boldsymbol{s}}) \sigma + \tfrac{1}{6} \phi_\circ''' \tau^3 + (\mathrm{d}\boldsymbol{d} \cdot \hat{\boldsymbol{t}}) \tau,$$

$$\tilde{\phi}_\circ = \phi_\circ + \mathrm{d}\boldsymbol{d} \cdot \boldsymbol{\zeta}^*. \tag{2.71}$$

By considering the *fold* universal unfolding as in Table 2.1, one finds from (2.71) via mapping $t = (|\phi_\circ'''|/2)^{1/3} \tau$ that

$$|c| \;=\; \left| \tfrac{1}{2} \phi_\circ''' \right|^{-\frac{1}{3}} |\mathrm{d}\boldsymbol{d} \cdot \hat{\boldsymbol{t}}|.$$

When $\mathrm{d}\boldsymbol{d}$ is parallel to $\boldsymbol{d}^\circ \times \hat{\boldsymbol{t}}$, c remains zero to the leading order. This shows $\boldsymbol{d}^\circ \times \hat{\boldsymbol{t}}$ is *tangent* to the fold curve at $\boldsymbol{d}^\circ \in B_\phi$. Subsequently, the width of a stripe-like region $\tilde{B}_\phi$ surrounding B_ϕ is exposed by considering $\mathrm{d}\boldsymbol{d}$ in the plane containing $\boldsymbol{d}^\circ$ and $\hat{\boldsymbol{t}}$, which

yields

$$|\mathrm{d}\boldsymbol{d}\!\cdot\!\hat{\boldsymbol{t}}| = |\mathrm{d}\boldsymbol{d}|\sqrt{|\boldsymbol{d}^{\circ}\!\cdot\!\boldsymbol{n}|^2 + \sin(\vartheta)^2(1-|\boldsymbol{d}^{\circ}\!\cdot\!\boldsymbol{n}|^2)} \geqslant |\mathrm{d}\boldsymbol{d}|\,|\boldsymbol{d}^{\circ}\!\cdot\!\boldsymbol{n}| \;\Rightarrow\; V \geqslant \left|\tfrac{1}{2}\phi_{\circ}'''\right|^{-\frac{1}{3}}|\boldsymbol{d}^{\circ}\!\cdot\!\boldsymbol{n}|, \tag{2.72}$$

where $|\mathrm{d}\boldsymbol{d}| = \mathrm{dist}(\boldsymbol{d}, B_{\phi})$, $\boldsymbol{n} = \boldsymbol{n}(\boldsymbol{\zeta}^*)$, and ϑ is the angle between $\hat{\boldsymbol{t}}$ and the plane containing $\boldsymbol{d}^{\circ}$ and $\boldsymbol{n}$. From (2.69), (2.72) and Table 2.1, one finds an upper-bound estimate

$$|\tilde{B}_{\phi}|_{\mathrm{cod}(\phi)=1} = O(|\boldsymbol{d}^{\circ}\!\cdot\!\boldsymbol{n}|^{-1}k^{-\sigma_m^{\min}}) = O(|\boldsymbol{d}^{\circ}\!\cdot\!\boldsymbol{n}|^{-1}k^{-2/3}). \tag{2.73}$$

Note that the integrands (2.22) underpinning T^c scale with $|\boldsymbol{d}^{\circ}\!\cdot\!\boldsymbol{n}|$, so that the situations of widening $\tilde{B}_{\phi}$ when $|\boldsymbol{d}^{\circ}\!\cdot\!\boldsymbol{n}| \to 0$ pose no problem in terms of the contribution of the fold catastrophes to (2.66).

From (2.72), it is seen that the sole situation precluding $V = O(1)$ is $|\boldsymbol{d}^{\circ}\boldsymbol{n}(\boldsymbol{\zeta}^*)| \ll 1$. Following (A8) this requires that the distance between $\boldsymbol{x}^{\circ}$ and the critical point, $|\boldsymbol{x}^{\circ}\!-\!\boldsymbol{\zeta}^*|$, behaves as $O(|\boldsymbol{d}^{\circ}\!\cdot\!\boldsymbol{n}|^{\pm 1})$, see also Fig. 8.1. Due to the regularity of S, however, catastrophes with $\mathrm{cod}(\phi) > 1$ cannot occur arbitrarily close to S, while the sampling points where $|\boldsymbol{x}^{\circ} - \boldsymbol{\zeta}^*| \gg 1$ are outside of $\mathscr{B}_1$. As a result, $V = O(1)$ for higher-codimension catastrophes and consequently

$$|\tilde{B}_{\phi}|_{\mathrm{cod}(\phi)>1} = O(k^{-2\sigma_m^{\min}}), \tag{2.74}$$

where $\sigma_m^{\min}$ are given in Table 2.1, and factor 2 in the exponent arises from the fact that $\tilde{B}_{\phi}|_{\mathrm{cod}(\phi)>1}$ assembles the neighborhoods of *isolated points*, see Fig. 2.6(b). The claim (2.66) then immediately follows from the scaling of T^c in Table 2.1, (2.22), (2.73), and (2.74). □

2.3.2.3 Contribution of nearby critical points for $\boldsymbol{x}^{\circ} \in \check{\mathscr{N}}_{\epsilon}$

Proposition 2.3.4. *For $\boldsymbol{x}^{\circ} \in \check{\mathscr{N}}_{\epsilon}$, the contribution of nearby critical points to $\check{\mathsf{T}}$ in (2.59) is given by*

$$\int_{\Omega} \mathsf{T}^{\star}\,\mathrm{d}\Omega_{\boldsymbol{d}} \;\overset{1}{=}\; \frac{\pi k}{(k\ell)^3}\left\{\frac{3(1-\beta)}{2+\beta}\big(k\ell\cos(k\ell)-\sin(k\ell)\big)^2 - (1-\beta\gamma^2)\,(k\ell)^2\sin(k\ell)^2\right\} \tag{2.75}$$

for sufficiently large k, *where* $\ell = (\boldsymbol{x}^o - \boldsymbol{x}^\star) \cdot \boldsymbol{n}(\boldsymbol{x}^\star)$ *is the signed normal distance between* $\boldsymbol{x}^o$ *and the boundary of the scatterer.*

Proof. The single-incident-wave expression for $\mathsf{T}^\star(\boldsymbol{x}^o, \cdot, \cdot)$, given by (2.52), is explicit and permits direct integration with respect to $\boldsymbol{d}$. Recall that $\mathsf{T}^\star = 0$ for $\boldsymbol{d} \cdot \boldsymbol{n}(\boldsymbol{x}^\star) \geqslant 0$ thanks to (2.17), whereby the effective integration support in (2.75) is a hemisphere. By taking $-\boldsymbol{n}(\boldsymbol{x}^\star)$ as the zenith direction of the spherical coordinate system describing Ω, it is evident from (2.52) that $\mathsf{T}^\star$ is exclusively a function of the zenith angle $|\boldsymbol{d}\boldsymbol{n}(\boldsymbol{x}^\star)| = \cos\theta$ and $k\ell$ so that

$$\int_\Omega \mathsf{T}^\star \, \mathrm{d}\Omega_{\boldsymbol{d}} \;\; = \;\; \int_0^{2\pi} \int_0^{\pi/2} [\mathsf{T}^\star](\cos\theta, k\ell) \, \sin\theta \, \mathrm{d}\theta \, \mathrm{d}\varphi \;\; = \;\; 2\pi \int_0^1 [\mathsf{T}^\star](\tau, k\ell) \, \mathrm{d}\tau, \quad (2.76)$$

resulting immediately in (2.75). $\qquad\qquad\qquad\qquad\qquad\qquad\qquad\qquad\qquad\qquad\qquad\square$

Remark 4. *In the context of (2.75), a natural question arises as to the suitable choice of trial obstacle parameters,* $\beta = \rho/\rho_{trial}$ *and* $\gamma = c/c_{trial}$, *when attempting to reconstruct a Dirichlet obstacle. Formally, sound-soft boundary condition is recovered by setting* $\beta \to \infty$ *which requires separate treatment [84, 68] of the small-obstacle perturbation that is not covered by (2.6). Nonetheless, the foregoing analysis can be applied toward the reconstruction of a Dirichlet obstacle by setting* $\beta\gamma^2 \gg 1$ *in the sense that (2.75) is well approximated by* $\pi k \beta\gamma^2 \sin(k\ell)^2/(k\ell)$. *This is shown in Fig. 2.7(a) which plots (2.75) versus normal distance to the boundary assuming* $\beta = 10$ *and* $\gamma = 1$. *As can be seen from the diagram, the leading contribution of* $\mathsf{T}^\star$ *to* $\check{\mathsf{T}}$ *in such case (i) crosses zero at the boundary of a Dirichlet obstacle, and (ii) attains extreme negative (resp. positive) value at its first peak inside (resp. outside) the obstacle, at a normal distance of* $|k\ell| < \pi/2$ *from the boundary. For future reference, Fig. 2.7(b) plots the corresponding distribution of (2.75) assuming* $\beta = 0$, *i.e. the vanishing obstacle to be of Neumann type.*

The foregoing developments are now concluded with *the main result* of this work.

Theorem 2.3.5. *For a convex Dirichlet obstacle D and sufficiently large k, the full-source-aperture distribution of TS (2.59) behaves as*

$$\check{\mathsf{T}}(\boldsymbol{x}^o, \beta, \gamma) \overset{k^\alpha}{=} 1_{\check{\mathscr{N}}_\epsilon}(\boldsymbol{x}^o) \, \frac{\pi k}{(k\ell)^3} \left\{ \frac{3(1-\beta)}{2+\beta} \big(k\ell\cos(k\ell) - \sin(k\ell)\big)^2 - (1-\beta\gamma^2)\,(k\ell)^2 \sin(k\ell)^2 \right\}$$
$$(2.77)$$

under the premise of diffraction catastrophes with codimension less than four, where $\alpha \leqslant 2/3$, $\check{\mathscr{N}_\epsilon}$ *is a 2ϵ-thick shell (for some $\epsilon = O(k^{-1}) \geqslant 2\pi/k$) with mid-plane ∂D, and* $\ell = (\boldsymbol{x}^o - \boldsymbol{x}^\star) \cdot \boldsymbol{n}(\boldsymbol{x}^\star)$ *is the signed normal distance between $\boldsymbol{x}^o$ and ∂D.*

Proof. The claim is a direct consequence of Propositions 2.3.2, 2.3.3 and 2.3.4. $\qquad\square$
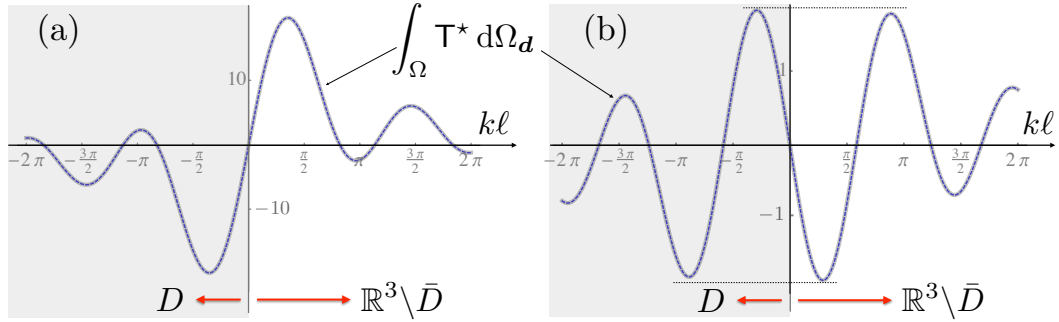
Figure 2.7: Contribution of $\mathsf{T}^\star(\boldsymbol{x}^o, \beta, \gamma)$ to $\check{\mathsf{T}}$ versus normal distance to the boundary of a Dirichlet obstacle: (a) local variation assuming $\beta = 10$ and $\gamma = 1$, and (b) variation assuming $\beta = 0$.

2.3.3 Neumann obstacle

For a sound-hard obstacle, the physical optics approximation [31] reads

$$u = \begin{cases} 2\,u^i & \text{on} \quad S^{\mathrm{f}} \\ 0 & \text{on} \quad S^{\mathrm{b}} \end{cases}, \qquad u_{,n} = 0 \quad \text{on} \quad S = \partial D. \tag{2.78}$$

Applying this condition with $u^i = e^{-ik\boldsymbol{x}\cdot\boldsymbol{d}}$ to (2.6), followed by the use of (2.13) and (2.15) to address the component integrals over Γ^{obs}, results in a TS formula for Neumann obstacle that is structurally similar to (2.19). In particular, the kernel in the "sound-hard" counterpart of (2.19) can be shown to (i) feature the identical phase function $\boldsymbol{\zeta}\cdot\boldsymbol{d} \pm r$, (ii) remain regular as $\boldsymbol{x}^o \to S^{\mathrm{f}}$, and (iii) vanish on ∂S^{f}. The end result of the analysis is given by the following statement.

Theorem 2.3.6. *For a convex Neumann obstacle D and sufficiently large k, the full-source-aperture distribution of TS behaves as*

$$\check{\mathsf{T}}(\boldsymbol{x}^o, \beta, \gamma) \overset{k^\alpha}{=} 1_{\check{\mathscr{N}}_\epsilon}(\boldsymbol{x}^o) \, \frac{-\pi\, k}{(k\ell)^3} \left\{ \frac{3(1-\beta)}{2+\beta} \big(k\ell\cos(k\ell) - \sin(k\ell)\big)^2 - (1-\beta\gamma^2)\,(k\ell)^2 \sin(k\ell)^2 \right\}$$

$$(2.79)$$

under the premise of diffraction catastrophes with codimension less than four, where $\alpha \leqslant 2/3$, $\check{\mathscr{N}}_\epsilon$ is a 2ϵ-thick shell (for some $\epsilon = O(k^{-1}) \geqslant 2\pi/k$) with mid-plane ∂D, and $\ell = (\boldsymbol{x}^o - \boldsymbol{x}^\star)\cdot\boldsymbol{n}(\boldsymbol{x}^\star)$ is the signed normal distance between $\boldsymbol{x}^o$ and ∂D.

Proof. Claim (2.79) is established by the steps analogous to those entailed in the proof of (2.77). $\qquad\square$

2.3.4 Reconstruction scheme

A comparison between (2.77) and (2.79) reveals that for (β, γ) fixed, the leading-order distribution of $\check{\mathsf{T}}$ simply *changes sign* when the boundary condition on the surface of a hidden anomaly is changed from Dirichlet to Neumann type. Accordingly, the counterpart of Fig. 2.7 for a Neumann obstacle is obtained via reflection of the featured diagrams about the $k\ell$-axis. This opens two distinct avenues toward the high-frequency reconstruction of impenetrable obstacles:

Algorithm 1. When the nature of a hidden obstacle D is known beforehand, (i) compute $\check{\mathsf{T}}(\boldsymbol{x}^o, \beta, \gamma)$ with commensurate trial parameters ($\beta\gamma \gg 1$ for Dirichlet type, $\beta = 0$ for Neumann type) and (ii) reconstruct ∂D as the *(innermost) zero level set* of $\check{\mathsf{T}}$ separating its extreme negative and extreme positive values. For each obstacle type, extreme $\check{\mathsf{T}}$-values immediately enclosed by the reconstruction are *negative.*

Algorithm 2. Compute $\check{\mathsf{T}}(\boldsymbol{x}^o, \beta, \gamma)$ with $\beta\gamma \gg 1$ and reconstruct the boundary of a hidden obstacle, ∂D, as the *zero level set* of $\check{\mathsf{T}}$ separating its extreme negative and extreme positive values. When the extreme $\check{\mathsf{T}}$-values to the *inside* of the reconstruction are negative (resp. positive), the impenetrable obstacle is of Dirichlet (resp. Neumann) type.

Recalling Fig. 2.7, Algorithm 2 is generally preferred due the to the facts that (a) the obstacle type is *revealed* rather than required as prior information, and (b) setting

$\beta\gamma \gg 1$ allows for *better localization* of the extreme $\check{\mathsf{T}}$-values near ∂D than $\beta = 0$. In particular (b) results in Algorithm 1 imposing an additional qualifier ("innermost") on the zero level set, for the variation of $\check{\mathsf{T}}|_{\beta=0}$ with $k\ell$ – deployed in the Neumann case – features four (instead of two) peaks that are commensurate in magnitude, see Fig. 2.7.

2.4 Numerical results

A numerical experiment is devised to illustrate the performance of TS as an imaging tool in the high-frequency regime. The sensing arrangement, reflecting the framework adopted in Section 3.1, is shown in Fig. 3.1(a) where D is an ellipsoidal anomaly with semi-axes $(0.2, 0.08, 0.8)$. In what follows, the TS distribution is computed in the obstacle's mid-section Π perpendicular to its major axis, assuming incident plane waves with $k = 300$ (wavelength $\lambda = 0.021$) propagating in direction $\boldsymbol{d}\,\|\Pi$. It is noted that the ellipsoid's minimum radius of curvature is $0.032 \sim 1.5\lambda$.

In this case, the computation of TS is facilitated by two critical observations: i) for $\boldsymbol{x}^\circ$ within the square "patch" shown in Fig. 3.1(a), the critical points on S^{f} are confined to $S^{\mathrm{f}}\cap\Pi$, and ii) the germane catastrophes are of either type fold or cusp, i.e. $\mathrm{cod}(\phi) \leqslant 2$. Note, however, that the caustics of higher codimension may occur in out-of-plane situations – when either $\boldsymbol{d}\nparallel\Pi$ or $\boldsymbol{x}^\circ\notin\Pi$ – see Fig. 3.1(b) for an example projection of the bifurcation set $B_\phi(\boldsymbol{d}, \boldsymbol{x}^\circ)$ on Ω.
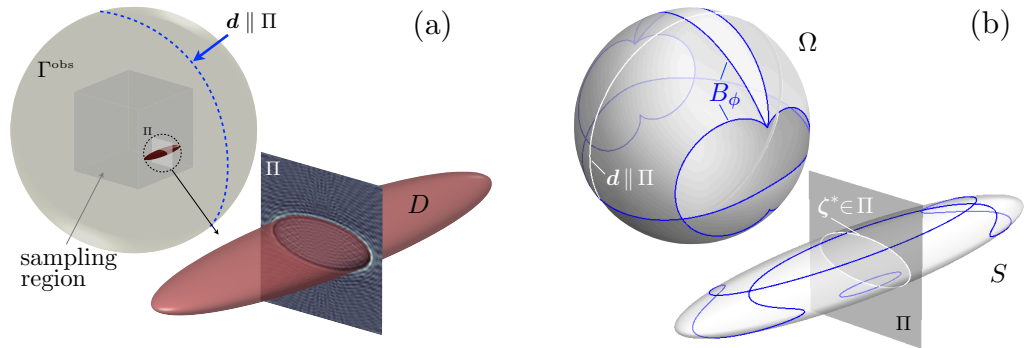
Figure 2.8: Example problem: (a) sensing configuration, and (b) bifurcation set $B_\phi(\boldsymbol{d}, \boldsymbol{x}^\circ) \subset \Omega$ with affiliated critical points $\boldsymbol{\zeta}^* \in S$ (dark curves) for the sampling point $\boldsymbol{x}^\circ = \boldsymbol{p}$ shown in Fig. 2.9(b). Loci $\boldsymbol{d}\,\|\Pi$ and matching $\boldsymbol{\zeta}^*$ are shown in white.
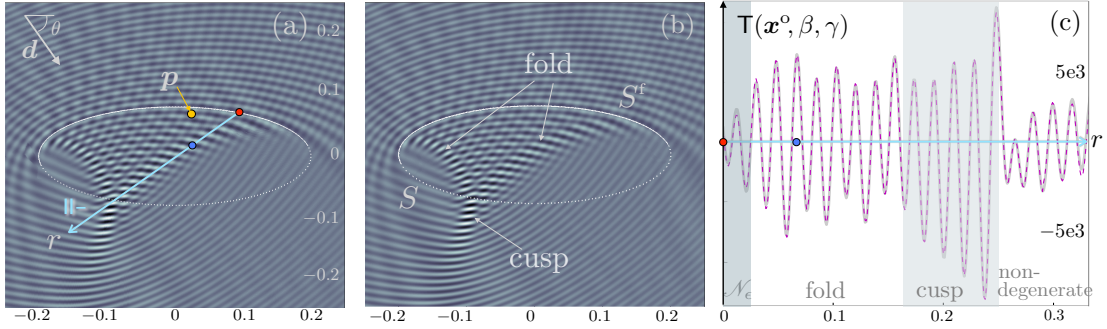
Figure 2.9: Distribution of $\mathsf{T}(\boldsymbol{x}^{\mathrm{o}}, 20, 1)$ in the Π-plane for $\boldsymbol{d} \| \Pi$ and $\theta = 0.35\pi$: (a) numerical integration, (b) high-frequency approximation, and (c) comparison along example ray Π^- (solid line - numerics, dashed line - asymptotics).

2.4.1 Single plane-wave incidence

With the aid of the high-frequency approximations described in Section 2.2 and Appendix B, the TS field (2.53) is computed via the following steps: i) the 0.5×0.5 square computational domain within Π (see Fig. 3.1(a)) is discretized by 10^6 pixels, nearly 42 per wavelength; ii) the boundary curve $S^{\mathrm{f}}(\boldsymbol{d}) \cap \Pi$ is split into 10^4 segments centered at $\boldsymbol{\zeta}^n$, $n = \overline{1, 10^4}$; and iii) starting from $\boldsymbol{\zeta}^1$, the contribution of $\boldsymbol{\zeta}^n$ to (2.53) is computed (via either near-boundary, uniform, or non-uniform approximation) along rays $\Pi^\pm \in \Pi$, and accordingly used to "paint" the pixels. In doing so, the use is made of the Van der Corput neutralizers [31] to prevent double-counting of individual contributions. Assuming the ellipsoidal anomaly to be of Dirichlet type, the resulting TS map is shown in Fig. 2.9(a), which clearly reflects the presence of fold- and cusp-type caustics. For completeness, Fig. 2.9(b) plots the corresponding diagram obtained via "brute-force" numerical integration of (2.20), while Fig. 2.9(c) compares the two estimates along example ray Π^-. As can be seen from the latter panel, the (i) near-boundary, (ii) Airy, (iii) Pearcey and (iv) non-uniform approximations smoothly transition into one another and overlap with the numerical solution.

2.4.2 Partial and full source aperture

As demonstrated by Fig. 2.9, the TS map due to single incident $\boldsymbol{d}$ is dominated by the caustics, and reveals little about the geometry of a hidden anomaly. In such a context,
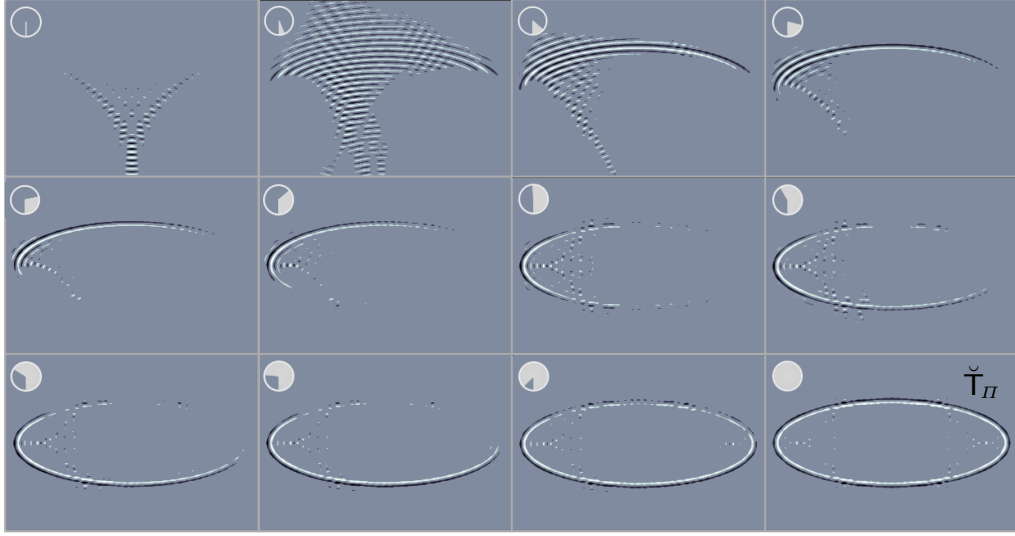
Figure 2.10: Imaging of a Dirichlet anomaly by $\mathsf{T}(\boldsymbol{x}^\circ, 20, 1)$: evolution of TS with increasing (in-plane) source aperture.

it is of interest to integrate $\mathsf{T}(\boldsymbol{x}^\circ, \beta, \gamma)$ with respect to $\boldsymbol{d} \, \| \, \Pi$, i.e. with respect to the *in-plane* angle of incidence θ shown in Fig. 2.9(a). On denoting for brevity $\breve{\mathsf{T}}_\Pi = \int_\Pi \mathsf{T} \, \mathrm{d}\Omega_{\boldsymbol{d}}$, it can be shown by following the analysis in Section 2.3.2 that the contributions of $\mathsf{T}^\star$, T^c and $\mathsf{T}^{\Pi^\pm}$ to $\breve{\mathsf{T}}_\Pi$ behave respectively as $O(k)$, $O(k^\alpha)$ and $O(k^\mu)$, where $\alpha \leqslant 3/4$ and $\mu \leqslant 3/4$ due to the fact that the codimension of catastrophes in the example does not exceed two. Such reconstruction ability of $\breve{\mathsf{T}}_\Pi$ is illustrated in Fig. 2.10 which plots the evolution of TS (assuming Dirichlet anomaly) with increasing *in-plane* aperture, noting that (i) the bright sector of the unit circle in each panel depicts the source aperture, (ii) the TS distributions are thresholded at 45%, and (iii) the bottom right panel plots $\breve{\mathsf{T}}_\Pi$.

For completeness, the reconstruction of a Dirichlet obstacle via $\breve{\mathsf{T}}_\Pi(\boldsymbol{x}^\circ, 20, 1)$ is compared in Fig. 2.11 to that of a Neumann anomaly by $\breve{\mathsf{T}}_\Pi(\boldsymbol{x}^\circ, 0, \gamma)$. Here the left, middle, and right panels plot respectively $\breve{\mathsf{T}}_\Pi$, thresholded $\breve{\mathsf{T}}_\Pi$, and example near-boundary variation of $\breve{\mathsf{T}}_\Pi$ (along the indicated normal) versus the contribution of $\mathsf{T}^\star$ only. Note that the featured images are obtained by adopting *Algorithm 1*, which samples each anomaly with physically-compatible vanishing obstacle. As can be seen from Fig. 2.11(e), this leads to apparent "smearing" in the case of a Neumann obstacle. In contrast, its image obtained via *Algorithm 2*, i.e. using $\breve{\mathsf{T}}_\Pi(\boldsymbol{x}^\circ, 20, 1)$ as a sampling tool, is given by the

negative of Fig. 2.11(b) and thus better localized.

To provide the *full-source-aperture* counterpart of the result in Fig 2.11(c) – computed at boundary point $\boldsymbol{x}^\star = (0.178, 0.036, 0)$, Fig. 2.12 compares the analytical expression (2.77) with a numerical estimate of $\check{\mathsf{T}} \equiv \check{\mathsf{T}}_\Omega$, obtained via quadrature and superposition of (2.20) for 512 incident plane-wave directions, uniformly distributed over Ω. For generality, the comparison is made at both in-plane boundary point $\boldsymbol{x}^\star = (0.178, 0.036, 0)$ (left panel), and its out-of-plane companion $\boldsymbol{x}^\star = (0.114, 0.046, 0.470)$ (right panel). Irrespective of the boundary point, the numerical result closely follows (2.77) at both $k = 300$ and $k = 600$, showing visibly better agreement in the latter case.

For the sake of completeness, the high-frequency reconstruction of an onion-shaped (asymmetric) Dirichlet obstacle by TS is shown in Fig. 2.13, where the full source aperture is given by the unit sphere. The reconstructed obstacle and its projections are shown in dark blue. To facilitate the comparison, the contours enclosing the boundary of the *true scatterer* are displayed in bright blue in each projection plane.

To conclude the study, *Algorithm 1* is applied to identify the boundary of a circular hole in an aluminum plate from the recent set of *elastodynamic* experiments [160]. In this case the wave motion, governed by the two-dimensional Navier equations, is induced in a *bounded* domain shown in Fig. 2.14(a) and monitored along its top and side edges. The incident waves are generated by a piezoelectric transducer, placed sequentially at five locations indicated in the diagram, such that the ratio of the illuminating wavelength to the hole diameter is 0.85. Thus, the testing configuration is incompatible with the present analysis in several aspects, including (i) dimensionality of the problem, (ii) type of the governing equation, (iii) geometry of the anomaly-free domain, (iv) probing wavelength, and (v) aperture of the illuminating sources. Nonetheless the reconstruction of a circular hole in panel (c), obtained by applying *Algorithm 1* to the TS distribution [160] showin in panel (b), is rather satisfactory.
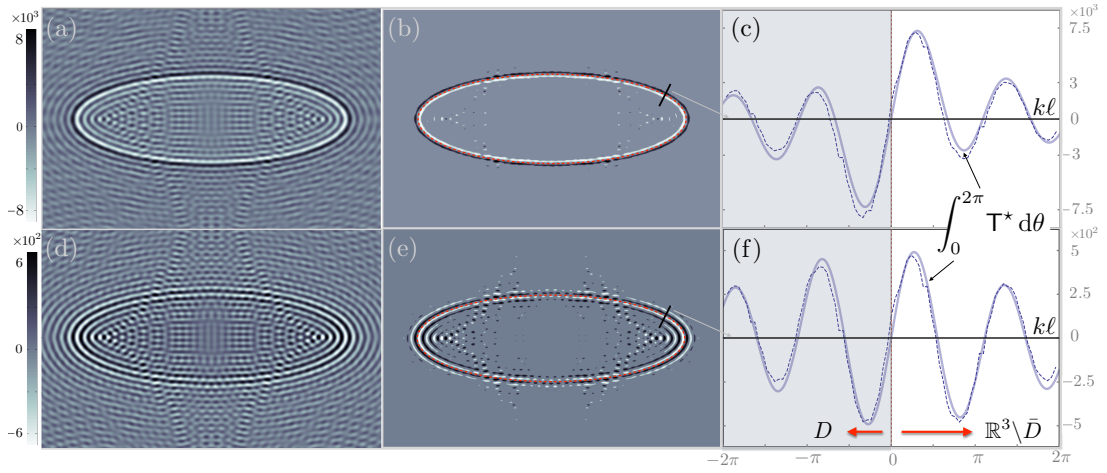
Figure 2.11: Distribution of $\check{\mathsf{T}}_\Pi(\boldsymbol{x}^\circ, \beta, \gamma)$ for a Dirichlet obstacle probed by ($\beta = 20, \gamma = 1$) (top row), and Neumann obstacle sampled by ($\beta = 0, \gamma$) (bottom row): full variation (left), thresholded distribution (middle), and example near-boundary variation (right). The thin dashed line in panels (b) and (e) traces $S \cap \Pi$.
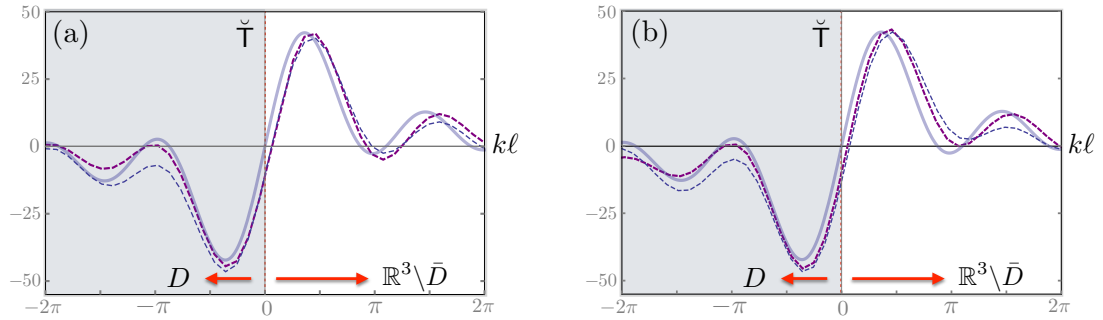
Figure 2.12: Near-boundary variation of $\check{\mathsf{T}}(\boldsymbol{x}^\circ, 20, 1)$ at $\boldsymbol{x}^\star = (0.178, 0.036, 0)$ (left panel) and $\boldsymbol{x}^\star = (0.114, 0.046, 0.470)$ (right panel): analytical solution (2.3.5) (solid line) versus the numerical result for $k = 300$ (thin dashed line) and $k = 600$ (thick dashed line). The true anomaly is of Dirichlet type.
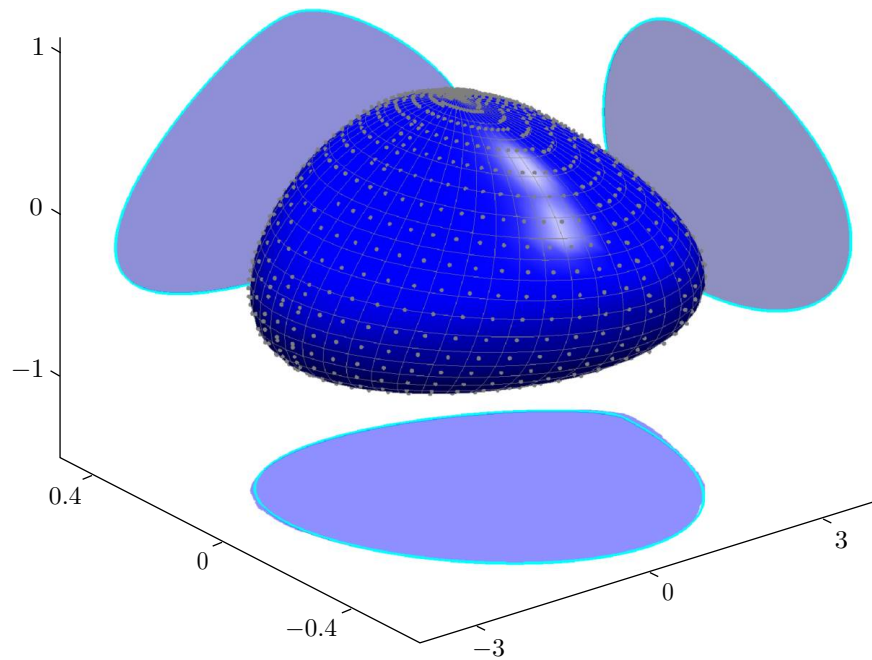
Figure 2.13: High-frequency 3D reconstruction of an onion-shaped Dirichlet obstacle by Topological Sensitivity.
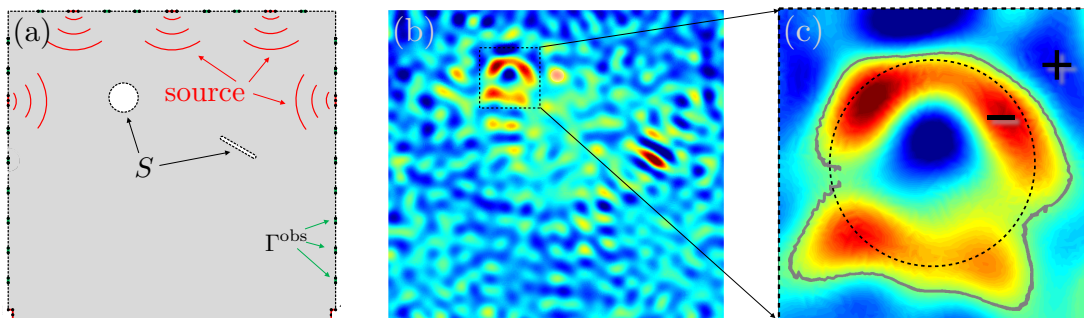
Figure 2.14: Elastodynamic experiment in [160]: (a) testing setup, (b) five-sources TS field, and (c) true boundary (dashed circle) versus its reconstruction (solid irregular line) obtained via Algorithm 1.

Chapter 3

Elastodynamic TS imaging and characterization of fractures with specific stiffness

In this chapter, a TS sensing platform is developed for the inverse scattering of time-harmonic elastic waves by fractures with unknown geometry and contact condition in $\mathbb{R}^3$. Considering the *small-amplitude* elastic waves – commonly used for seismic imaging and non-destructive evaluation, interactions between the two faces of a fracture – due to e.g. the presence of asperities, fluid, or proppant, are described by the Schoenberg's *linear* slip model [145]. This framework can be interpreted as a linearization of the interfacial behavior about the elastostatic equilibrium state [133] prior to elastic-wave excitation, which gives rise to linear (normal and shear) specific stiffnesses k_n and k_s. Here it is worth noting that strong correlations are reported in the literature [163, 55, 4, 139] between (k_s, k_n) and surface roughness, residual stress, fluid viscosity (if present at the interface), intact material properties, fracture connectivity, and excitation frequency.

In this vein, the proposed TS sensing algorithm entails *point-wise interrogation* of the subsurface volume by *infinitesimal fissures* endowed with trial (shear and normal) *specific stiffnesses* κ_s and κ_n. To this end, the germane TS formula is derived in terms of the trial coefficient pair (κ_s, κ_n) and expressed in closed form. Simulations demonstrate that, irrespective of the contact condition at the interface of a hidden fracture, the

TS indicator function is capable of (i) approximating its location and (ii) identifying the (average) normal vector to the fracture surface without iterations. In the higher frequency range, the numerical results also demonstrate that the TS is capable of *high-fidelity geometric reconstruction* – an observation that is consistent with the theoretical developments presented in Chapter 2. On the basis of such geometrical information and available sensory data in the "low frequency" regime of illumination, it is further shown (via asymptotic analysis) that by certain *trial* choices of (κ_s, κ_n), the ratio between the *true* shear and normal specific stiffness, k_s/k_n, along the recovered (fracture) interface can be qualitatively identified. This provides a valuable insight into the fracture's interfacial condition at virtually no additional cost – beyond the computational effort required for its geometric reconstruction.

Here it is worth mentioning that seismic sensing of the specific stiffness ratio k_s/k_n has recently come under the spotlight in hydraulic fracturing, petroleum migration, and Earth's Critical Zone studies [100, 13]. By way of laboratory experiments [55, 131, 16], it is specifically shown that k_s/k_n – often approximated as either one (dry contact) or zero (isolated fluid-filled fracture) – can deviate significantly from such canonical estimates, having fundamental ramifications on the analysis of the effective moduli and wave propagation in fractured media. A recent study [13, 163] on the production from the Cotton Valley tight gas reservoir, using shear-wave splitting data, further highlights the importance of monitoring k_s/k_n during hydraulic fracturing via the observations that: (a) the correlation between proppant introduction and dramatic increase in k_s/k_n can be used as a tool to directly image the proppant injection process; (b) the ratio k_s/k_n provides a means to discriminate between newly created, old mineralized and proppant-filled fractures, and (c) k_s/k_n may be used to monitor the evolving hydraulic conductivity of an induced fracture network and subsequently assess the success of drilling and stimulation strategies.

3.1   Preliminaries

Consider the scattering of time-harmonic elastic waves by a smooth fracture surface $\Gamma \subset \mathscr{B}_1 \subset \mathbb{R}^3$ (see Fig. 3.1) under the premise of a linear, but otherwise generic, contact condition between its faces $\Gamma^\pm$. For instance the fracture may be partially closed (due
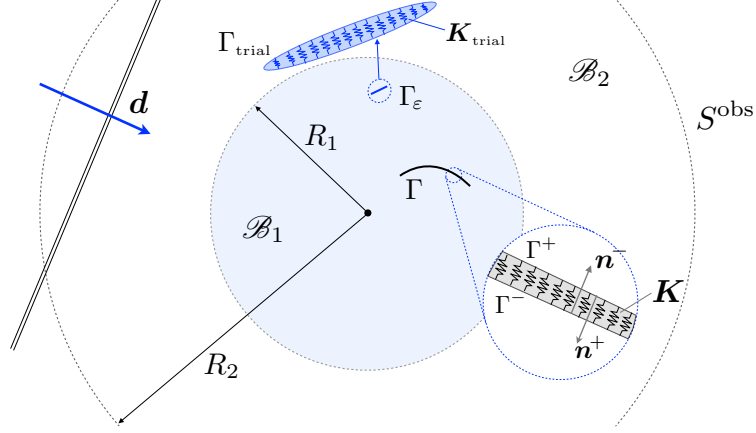
Figure 3.1: Illumination of a hidden fracture $\Gamma \in \mathbb{R}^3$ with specific stiffness $\boldsymbol{K}$ by a plane (P- or S-) incident wave propagating in direction $\boldsymbol{d}$, where the induced wavefield is monitored over S^{obs}.

to surface asperities), fluid-filled, or traction free. Here, $\mathscr{B}_1$ is a ball of radius R_1 – containing the sampling region i.e. the search domain for hidden fractures. The action of an *incident plane wave* $\boldsymbol{u}^i$ on Γ results in the scattered field $\tilde{\boldsymbol{u}}$ – observed in the form of the total field

$$\boldsymbol{u}(\boldsymbol{\xi}) \;=\; \boldsymbol{u}^i(\boldsymbol{\xi}) \,+\, \tilde{\boldsymbol{u}}(\boldsymbol{\xi}), \qquad \boldsymbol{\xi} \in S^{\mathrm{obs}}, \tag{3.1}$$

over a closed measurement surface $S^{\mathrm{obs}} = \partial \mathscr{B}_2$, where $\mathscr{B}_2$ is a ball of radius $R_2 \gg R_1$ centered at the origin. The reference i.e. "background" medium is assumed to be elastic, homogeneous, and isotropic with mass density ρ, shear modulus μ, and Poisson's ratio ν.

Dimensional platform For simplicity, all quantities in the sequel are rendered *dimensionless* by taking ρ, μ, and R_1 (see Fig. 3.1) as the reference scales for mass density, elastic modulus, and length, respectively – which amounts to setting $\rho = \mu = R_1 = 1$ [20].

Sensory data In what follows, the time-dependent factor $e^{\mathrm{i}\omega t}$ will be made implicit, where ω denotes the frequency of excitation. With such premise, the incident wavefield can be written as $\boldsymbol{u}^i(\boldsymbol{\xi}) = \boldsymbol{b}\, e^{-\mathrm{i}k\boldsymbol{\xi}\cdot\boldsymbol{d}}$ where $k = \omega/c$ signifies the wavenumber; c is the

relevant (compressional or shear) wave speed; $\boldsymbol{b} \in \Omega$ is the polarization vector, and $\boldsymbol{d} \in \Omega$ specifies the direction of propagation of the incident plane wave, noting that Ω stands for a unit sphere. For each incident plane wave specified via pair $(\boldsymbol{b}, \boldsymbol{d})$, values of the total field $\boldsymbol{u}(\boldsymbol{\xi})$ are collected over S^{obs}.

Governing equations With the above assumptions in place, the scattered field $\tilde{\boldsymbol{u}}(\boldsymbol{\xi})$ can be shown to satisfy the field equation and interfacial condition

$$
\begin{aligned}
\nabla \cdot [\boldsymbol{C} : \nabla \tilde{\boldsymbol{u}}](\boldsymbol{\xi}) + \omega^2 \tilde{\boldsymbol{u}}(\boldsymbol{\xi}) &= \boldsymbol{0}, && \boldsymbol{\xi} \in \mathbb{R}^3 \backslash \Gamma, \\
\tilde{\boldsymbol{t}}^{\pm}(\boldsymbol{\xi}) &= \mp \, \boldsymbol{K}(\boldsymbol{\xi}) \, [\![\tilde{\boldsymbol{u}}]\!](\boldsymbol{\xi}) - \boldsymbol{t}_f^{\pm}(\boldsymbol{\xi}), && \boldsymbol{\xi} \in \Gamma^{\pm},
\end{aligned}
\tag{3.2}
$$

complemented by the Kupradze radiation conditions [2] at infinity. Here, $\mathbb{R}^3 \backslash \Gamma$ denotes the unbounded domain surrounding Γ; $[\![\tilde{\boldsymbol{u}}]\!] = [\![\boldsymbol{u}]\!] = \boldsymbol{u}^+ - \boldsymbol{u}^-$ signifies the fracture opening displacement (FOD) on Γ; $\tilde{\boldsymbol{t}}^{\pm} = \boldsymbol{n}^{\pm} \cdot \boldsymbol{C} : \nabla \tilde{\boldsymbol{u}}^{\pm}$ where $\boldsymbol{n}^{\pm}$ is the unit normal on $\Gamma^{\pm}$ (see Fig. 3.1); $\boldsymbol{K}(\boldsymbol{\xi})$ is a symmetric, positive-definite matrix of the specific stiffness coefficients; $\boldsymbol{t}_f^{\pm} = \boldsymbol{n}^{\pm} \cdot \boldsymbol{C} : \nabla \boldsymbol{u}^i$ denotes the free-field traction on $\Gamma^{\pm}$, and $\boldsymbol{C}$ is the (dimensionless) fourth-order elasticity tensor

$$
\boldsymbol{C} = 2\Big[\boldsymbol{I}_4^{sym} + \frac{\nu}{1 - 2\nu} \boldsymbol{I}_2 \otimes \boldsymbol{I}_2 \Big],
$$

in which $\boldsymbol{I}_2$ and $\boldsymbol{I}_4^{sym}$ stand respectively for the second-order and symmetric fourth-order identity tensors. Following the usual convention [36], the *unsigned* tractions and normals on a generic surface S (e.g. $\boldsymbol{t}_f, \boldsymbol{n}$) are referred to S^- and affiliated normal $\boldsymbol{n}^-$ where applicable.

Here it is noted that $\boldsymbol{K}$, which accounts for the interaction between Γ^+ and Γ^- due to e.g. surface asperities, fluid, or proppant at the fracture interface, may exhibit arbitrary spatial variations along Γ in terms of its normal and shear components. In light of the fact that the primary focus of this work is "low" frequency sensing where the illuminating wavelength exceeds most (if not all) characteristic length scales of a fracture – de facto resulting in the spatial averaging of its properties, it is for simplicity assumed that the normal and shear specific stiffness are both *constant* across Γ [145, 138, 137].

More specifically, it is hereon assumed that

$$\boldsymbol{K}(\boldsymbol{\xi}) \;=\; \boldsymbol{K} \;=\; k_n(\boldsymbol{n} \otimes \boldsymbol{n}) \,+\, k_s \sum_{\beta=1}^{2} (\boldsymbol{e}_\beta \otimes \boldsymbol{e}_\beta), \qquad \boldsymbol{\xi} \in \Gamma, \tag{3.3}$$

where $(\boldsymbol{e}_1, \boldsymbol{e}_2, \boldsymbol{n})$ constitute an orthonormal basis on Γ; $k_s = \text{const.}$ (resp. $k_n = \text{const.}$) is the *dimensionless* shear (resp. normal) specific stiffness, and $\otimes$ signifies the tensor product.

Cost functional   For the purposes of solving the inverse problem the cost functional is, assuming given incident wavefield $\boldsymbol{u}^i$, defined as

$$J(\Gamma_{\text{trial}}) \;=\; \int_{S^{\text{obs}}} \varphi\left(\boldsymbol{v}, \boldsymbol{u}^{\text{obs}}, \boldsymbol{\xi}\right) \mathrm{d}S_{\boldsymbol{\xi}}, \tag{3.4}$$

in terms of the least-squares misfit density

$$\varphi(\boldsymbol{v}, \boldsymbol{u}^{\text{obs}}, \boldsymbol{\xi}) \;=\; \tfrac{1}{2} \, \overline{\left(\boldsymbol{v}(\boldsymbol{\xi}) - \boldsymbol{u}^{\text{obs}}(\boldsymbol{\xi})\right)} \cdot \boldsymbol{W}(\boldsymbol{\xi}) \cdot \left(\boldsymbol{v}(\boldsymbol{\xi}) - \boldsymbol{u}^{\text{obs}}(\boldsymbol{\xi})\right), \tag{3.5}$$

where $\boldsymbol{u}^{\text{obs}}$ are the observations of $\boldsymbol{u}|_{S^{\text{obs}}}$ (say polluted by noise); $\boldsymbol{v}$ is the simulation of $\boldsymbol{u}$ computed for trial fracture Γ_{trial}, and $\boldsymbol{W}$ is a suitable (positive definite) weighting matrix, e.g. data covariance operator.

3.2   Topological sensitivity for a fracture with specific stiffness

On recalling (3.4) and denoting

$$\Gamma_\varepsilon \;=\; \boldsymbol{\xi}^\circ \,+\, \varepsilon\, \Gamma_{\text{trial}}, \qquad \boldsymbol{\xi}^\circ \in \mathscr{B}_1, \tag{3.6}$$

where Γ_{trial} contains the origin, the topological sensitivity (TS) of the featured cost functional can be defined as the leading-order term in the expansion of $J(\Gamma_\varepsilon)$ with respect to the vanishing (trial) fracture size as $\varepsilon \to 0$ [26]. In what follows, Γ_{trial} is taken as a *penny-shaped* fracture of unit radius with normal $\boldsymbol{n}'$, shear specific stiffness κ_s, and

normal specific stiffness κ_n, whereby its stiffness matrix can be expressed as

$$\boldsymbol{K}_{\text{trial}} = \kappa_n(\boldsymbol{n}' \otimes \boldsymbol{n}') + \kappa_s \sum_{\beta=1}^{2}(\boldsymbol{e}'_\beta \otimes \boldsymbol{e}'_\beta), \qquad (3.7)$$

with reference to the local orthonormal basis $(\boldsymbol{e}'_1, \boldsymbol{e}'_2, \boldsymbol{n}')$. Here it is worth recalling that the true $(\boldsymbol{K})$ and trial $(\boldsymbol{K}_{\text{trial}})$ stiffness matrices are both described with respect to the same dimensional platform where $\mu = \rho = R_1 = 1$. Hereon, the stiffness matrix affiliated with an *infinitesimal* trial scatterer Γ_ε according to (3.6) is denoted by $\boldsymbol{K}_\varepsilon$ – whose relationship with $\boldsymbol{K}_{\text{trial}}$ is to be determined.

On the basis of the above considerations, the topological sensitivity $\mathsf{T}(\boldsymbol{\xi}^\circ; \boldsymbol{n}', \kappa_n, \kappa_s)$ is obtained from the expansion

$$J(\Gamma_\varepsilon) = J(\emptyset) + f(\varepsilon)\,\mathsf{T}(\boldsymbol{\xi}^\circ; \boldsymbol{n}', \kappa_n, \kappa_s) + o(f(\varepsilon)) \quad \text{as} \quad \varepsilon \to 0, \qquad (3.8)$$

where $f(\varepsilon) \to 0$ with diminishing ε, see also [151, 77, 82, 37]. Thanks to the fact that the trial scattered field $\tilde{\boldsymbol{v}}(\boldsymbol{\xi}) = \boldsymbol{v}(\boldsymbol{\xi}) - \boldsymbol{u}^i(\boldsymbol{\xi})$ due to Γ_ε vanishes as $\varepsilon \to 0$, (3.4) can be conveniently expanded in terms of $\boldsymbol{v}$ about $\boldsymbol{u}^i$, see [36]. As a result (3.8) can be rewritten, to the leading order, as

$$J(\Gamma_\varepsilon) - J(\emptyset) \simeq \int_{S^{\text{obs}}} \frac{\partial\varphi}{\partial\boldsymbol{v}}(\boldsymbol{u}^i, \boldsymbol{u}^{\text{obs}}, \boldsymbol{\xi}) \cdot \tilde{\boldsymbol{v}}(\boldsymbol{\xi})\, \mathrm{d}S_{\boldsymbol{\xi}} = f(\varepsilon)\,\mathsf{T}(\boldsymbol{\xi}^\circ; \boldsymbol{n}', \kappa_n, \kappa_s). \qquad (3.9)$$

Adjoint field approach At this point, one may either differentiate (3.5) at $\boldsymbol{v} = \boldsymbol{u}^i$ and seek the asymptotic behavior of $\tilde{\boldsymbol{v}}(\boldsymbol{\xi})$ over S^{obs}, or follow the adjoint field approach [e.g. 36, 22] which transforms the domain of integration in (3.9) from S^{obs} to Γ_ε – and leads to a compact representation of the TS formula. The essence of the latter method, adopted in this study, is to interpret the integral in (3.9) through Graffi's reciprocity identity [2] between the trial scattered field $\tilde{\boldsymbol{v}}(\boldsymbol{\xi})$ and the so-called adjoint field $\hat{\boldsymbol{u}}(\boldsymbol{\xi})$, whose governing equations read

$$\tilde{\boldsymbol{v}} : \begin{cases} \nabla\cdot[\boldsymbol{C}:\nabla\tilde{\boldsymbol{v}}](\boldsymbol{\xi}) + \omega^2\,\tilde{\boldsymbol{v}}(\boldsymbol{\xi}) = \boldsymbol{0}, & \boldsymbol{\xi} \in \mathbb{R}^3\backslash\Gamma_\varepsilon \\[2mm] \tilde{\mathbf{t}}^{\pm}(\boldsymbol{\xi}) = \mp\boldsymbol{K}_\varepsilon\,[\![\tilde{\boldsymbol{v}}]\!](\boldsymbol{\xi}) - \boldsymbol{t}_f^{\pm}(\boldsymbol{\xi}), & \boldsymbol{\xi} \in \Gamma_\varepsilon^{\pm} \end{cases},$$

$$\hat{\boldsymbol{u}}: \begin{cases} \nabla\!\cdot\ + \omega^2\,\hat{\boldsymbol{u}}(\boldsymbol{\xi}) = \boldsymbol{0}, \quad \boldsymbol{\xi} \in \mathbb{R}^3 \\ [\![\hat{\boldsymbol{t}}]\!](\boldsymbol{\xi}) = \dfrac{\partial\varphi}{\partial\boldsymbol{v}}(\boldsymbol{u}^i, \boldsymbol{u}^{\text{obs}}, \boldsymbol{\xi}), \qquad \boldsymbol{\xi} \in S^{\text{obs}} \end{cases}, \tag{3.10}$$

subject to the Kupradze radiation condition at infinity. Here $\hat{\boldsymbol{t}}$ and $\tilde{\boldsymbol{t}}$ denote respectively the adjoint- and scattered-field tractions; $[\![\tilde{\boldsymbol{v}}]\!] = \tilde{\boldsymbol{v}}^+ - \tilde{\boldsymbol{v}}^-$ is the crack opening displacement on Γ_ε, and

$$[\![\hat{\boldsymbol{t}}]\!](\boldsymbol{\xi}) = \lim_{\eta\to 0} \boldsymbol{n}(\boldsymbol{\xi})\!\cdot\!\boldsymbol{C}\!\cdot\!\big(\nabla\hat{\boldsymbol{u}}(\boldsymbol{\xi} - \eta\boldsymbol{n}) - \nabla\hat{\boldsymbol{u}}(\boldsymbol{\xi} + \eta\boldsymbol{n})\big), \qquad \boldsymbol{\xi} \in S^{\text{obs}} \tag{3.11}$$

denotes the jump in adjoint-field tractions across S^{obs} with outward normal $\boldsymbol{n}$. Note that the adjoint field is defined over the intact reference domain, whereby $\hat{\boldsymbol{u}}$ is continuous $\forall\boldsymbol{\xi} \in \mathscr{B}_1$ and consequently $\hat{\boldsymbol{t}}^\pm = \mp\hat{\boldsymbol{t}}$ on $\Gamma_\varepsilon^\pm$. As a result, application of the reciprocity identity over $\mathbb{R}^3\backslash\Gamma_\varepsilon$ can be shown to reduce (3.9) to

$$\mathsf{T}(\boldsymbol{\xi}^\circ; \boldsymbol{n}', \kappa_n, \kappa_s) = \big(f(\varepsilon)\big)^{-1}\int_{\Gamma_\varepsilon} \hat{\boldsymbol{t}}(\boldsymbol{\xi}) \cdot [\![\tilde{\boldsymbol{v}}]\!](\boldsymbol{\xi})\,\mathrm{d}S_{\boldsymbol{\xi}}. \tag{3.12}$$

3.2.1 Asymptotic analysis

Considering the trial scattered field $\tilde{\boldsymbol{v}}(\boldsymbol{\xi})$, the leading-order contribution of the FOD is sought on the boundary of the vanishing crack ($\boldsymbol{\xi} \in \Gamma_\varepsilon$) as $\varepsilon \to 0$. For problems involving kinematic discontinuities such as that investigated here, it is convenient to deploy the traction BIE framework [33] as the basis for the asymptotic analysis, namely

$$\begin{aligned} \boldsymbol{t}_f(\boldsymbol{\xi}) - \boldsymbol{K}_\varepsilon\!\cdot\![\![\tilde{\boldsymbol{v}}]\!](\boldsymbol{\xi}) = {} & \boldsymbol{n}'\!\cdot\!\boldsymbol{C} : \fint_{\Gamma_\varepsilon} \boldsymbol{\Sigma}(\boldsymbol{\xi}, \boldsymbol{x}, \omega) : \boldsymbol{D}_{\boldsymbol{x}}[\![\tilde{\boldsymbol{v}}]\!](\boldsymbol{x})\,\mathrm{d}S_{\boldsymbol{x}} \\ & - \rho\omega^2\,\boldsymbol{n}'\!\cdot\!\boldsymbol{C} : \int_{\Gamma_\varepsilon} \boldsymbol{U}(\boldsymbol{\xi}, \boldsymbol{x}, \omega)\!\cdot\!\big([\![\tilde{\boldsymbol{v}}]\!] \otimes \boldsymbol{n}'\big)(\boldsymbol{x})\,\mathrm{d}S_{\boldsymbol{x}}, \qquad \boldsymbol{\xi} \in \Gamma_\varepsilon, \end{aligned} \tag{3.13}$$

where, assuming the Einstein summation convention over repeated indexes,

$$\boldsymbol{U} = U_i^k(\boldsymbol{\xi}, \boldsymbol{x}, \omega)\,\boldsymbol{e}_k \otimes \boldsymbol{e}_i, \qquad \boldsymbol{\Sigma} = \Sigma_{ij}^k(\boldsymbol{\xi}, \boldsymbol{x}, \omega)\,\boldsymbol{e}_k \otimes \boldsymbol{e}_i \otimes \boldsymbol{e}_j;$$

$U_i^k(\boldsymbol{\xi}, \boldsymbol{x}, \omega)$ and $\Sigma_{ij}^k(\boldsymbol{\xi}, \boldsymbol{x}, \omega)$ (given in F) denote respectively the elastodynamic *displacement* and *stress* fundamental solution due to point force acting at $\boldsymbol{x} \in \mathbb{R}^3$ in direction k;

$\fint$ signifies the Cauchy-principal-value integral, and $\boldsymbol{D_x}$ is the *tangential* differential operator [33] on Γ_ε given by

$$\boldsymbol{D_x}(\boldsymbol{f}) = D_{kl}(f_m)\,\boldsymbol{e}_l \otimes \boldsymbol{e}_m \otimes \boldsymbol{e}_k, \qquad D_{kl}(f_m) = n'_k f_{m,l} - n'_l f_{m,k}, \tag{3.14}$$

such that $n'_k = n'_k(\boldsymbol{x})$ and $f_{m,k} = \partial f_m / \partial x_k$ in the global coordinate frame.

Scaling considerations   Motivated by (3.6), a change of variable $\boldsymbol{x} = \boldsymbol{\xi}^\circ + \varepsilon \bar{\boldsymbol{x}}$ is introduced where $\boldsymbol{x} \in \Gamma_\varepsilon$ and $\bar{\boldsymbol{x}} \in \Gamma_{\text{trial}}$, resulting in the scaling relations

$$\mathrm{d}S_{\boldsymbol{x}} \; = \; \varepsilon^2\,\mathrm{d}S_{\bar{\boldsymbol{x}}}, \qquad \boldsymbol{D_x}(\cdot) \; = \; \varepsilon^{-1}\boldsymbol{D_{\bar{x}}}(\cdot), \qquad \boldsymbol{t}_f(\boldsymbol{\xi}) \; = \; \boldsymbol{t}_f(\boldsymbol{\xi}^\circ) + O(\varepsilon), \quad \boldsymbol{\xi} \in \Gamma_\varepsilon, \tag{3.15}$$

when $\varepsilon \to 0$. In this setting, the elastodynamic fundamental tensors in (3.13) are known to have the asymptotic behavior

$$\begin{aligned}
\boldsymbol{\Sigma}(\boldsymbol{\xi}, \boldsymbol{x}, \omega) \; &= \; \varepsilon^{-2}\,\breve{\boldsymbol{\Sigma}}(\bar{\boldsymbol{\xi}}, \bar{\boldsymbol{x}}) + O(1), \\
\boldsymbol{U}(\boldsymbol{\xi}, \boldsymbol{x}, \omega) \; &= \; \varepsilon^{-1}\,\breve{\boldsymbol{U}}(\bar{\boldsymbol{\xi}}, \bar{\boldsymbol{x}}) + O(1), \qquad \bar{\boldsymbol{x}}, \bar{\boldsymbol{\xi}} \in \Gamma_{\text{trial}},
\end{aligned} \tag{3.16}$$

in which $\breve{\boldsymbol{U}}(\bar{\boldsymbol{\xi}}, \bar{\boldsymbol{x}})$ and $\breve{\boldsymbol{\Sigma}}(\bar{\boldsymbol{\xi}}, \bar{\boldsymbol{x}})$ signify the displacement and stress tensors associated with the Kelvin's *elastostatic* fundamental solution [33]. Moreover, introducing the change of variable $\boldsymbol{\xi} = \boldsymbol{\xi}^\circ + \varepsilon\bar{\boldsymbol{\xi}}$ in the boundary condition in (3.10) affiliated with $\tilde{\boldsymbol{v}}(\boldsymbol{\xi})$ yields the rescaled contact condition at $\bar{\boldsymbol{\xi}} \in \Gamma_{\text{trial}}$ as

$$\bar{\boldsymbol{t}}^\pm(\bar{\boldsymbol{\xi}}) \; = \; \mp \varepsilon\,\boldsymbol{K}_\varepsilon [\![\bar{\boldsymbol{v}}]\!](\bar{\boldsymbol{\xi}}) \; - \; \bar{\boldsymbol{t}}_f^\pm(\bar{\boldsymbol{\xi}}), \qquad \bar{\boldsymbol{\xi}} \in \Gamma_{\text{trial}}^\pm, \tag{3.17}$$

where $\bar{\boldsymbol{v}}(\bar{\boldsymbol{\xi}})$ is the trial scattered field $\tilde{\boldsymbol{v}}(\boldsymbol{\xi})$ recast in terms of $\bar{\boldsymbol{\xi}}$ so that

$$[\![\bar{\boldsymbol{v}}]\!](\bar{\boldsymbol{\xi}}) \; := \; [\![\tilde{\boldsymbol{v}}]\!](\boldsymbol{\xi}^\circ + \varepsilon\bar{\boldsymbol{\xi}}), \qquad \bar{\boldsymbol{\xi}} \in \Gamma_{\text{trial}}, \tag{3.18}$$

while $\bar{\boldsymbol{t}}(\bar{\boldsymbol{\xi}}) = \boldsymbol{n}' \cdot \boldsymbol{C} : \nabla\bar{\boldsymbol{v}}(\bar{\boldsymbol{\xi}})$ and $\bar{\boldsymbol{t}}_f(\bar{\boldsymbol{\xi}}) = \boldsymbol{n}' \cdot \boldsymbol{C} : \nabla\bar{\boldsymbol{u}}^i(\bar{\boldsymbol{\xi}})$ (with $\nabla = \nabla_{\bar{\xi}}$ and $\bar{\boldsymbol{u}}^i(\bar{\boldsymbol{\xi}}) = \boldsymbol{u}^i(\boldsymbol{\xi})$) are the associated tractions written in terms of $\bar{\boldsymbol{\xi}}$. In light of (3.7) and (3.10), (3.17) reveals the sought relationship between $\boldsymbol{K}_\varepsilon$ and $\boldsymbol{K}_{\text{trial}}$ as

$$\boldsymbol{K}_\varepsilon \; = \; \varepsilon^{-1}\boldsymbol{K}_{\text{trial}} \; = \; \frac{\kappa_n}{\varepsilon}(\boldsymbol{n}' \otimes \boldsymbol{n}') + \frac{\kappa_s}{\varepsilon}\sum_{\beta=1}^{2}(\boldsymbol{e}'_\beta \otimes \boldsymbol{e}'_\beta). \tag{3.19}$$

Following the logic of earlier works [e.g. 26, 24, 36], the asymptotic behavior of a vanishing scattered field $[\![\bar{\boldsymbol{v}}]\!](\bar{\boldsymbol{\xi}})$ as $\varepsilon \to 0$ can be exposed by substituting (3.15), (3.16) and (3.19) into (3.13) which yields

$$
\begin{aligned}
\boldsymbol{t}_f(\boldsymbol{\xi}^\circ) \; - \; \varepsilon^{-1} \boldsymbol{K}_{\text{trial}} \cdot [\![\bar{\boldsymbol{v}}]\!](\bar{\boldsymbol{\xi}}) \; &= \\
&= \; \varepsilon^{-1} \boldsymbol{n}' \cdot \boldsymbol{C} : \oint_{\Gamma_{\text{trial}}} \check{\boldsymbol{\Sigma}}(\bar{\boldsymbol{\xi}}, \bar{\boldsymbol{x}}) : \boldsymbol{D}_{\bar{\boldsymbol{x}}} [\![\bar{\boldsymbol{v}}]\!](\bar{\boldsymbol{x}}) \, \mathrm{d}S_{\bar{\boldsymbol{x}}} \; + \; O(\varepsilon), \quad \bar{\boldsymbol{\xi}} \in \Gamma_{\text{trial}},
\end{aligned}
\tag{3.20}
$$

and seeking the balance of the featured leading terms [121]. To solve (3.20), consider a representation of the fracture opening displacement as

$$
[\![\bar{\boldsymbol{v}}]\!](\bar{\boldsymbol{\xi}}) \; \simeq \; \varepsilon^{\mathrm{a}} \, \sigma_{ij}^{f}(\boldsymbol{\xi}^\circ) \, [\![\boldsymbol{V}]\!]^{ij}(\bar{\boldsymbol{\xi}}), \qquad \bar{\boldsymbol{\xi}} \in \Gamma_{\text{trial}}, \tag{3.21}
$$

where σ_{ij}^{f} are the components of the free-field stress tensor $\boldsymbol{\sigma}_f = \boldsymbol{C} : \nabla \boldsymbol{u}^i$, and $[\![\boldsymbol{V}]\!]^{ij}$ ($i, j = 1, 2, 3$) are canonical solutions to be determined. On recalling that the free-field traction $\boldsymbol{t}_f = \boldsymbol{n}' \cdot \boldsymbol{\sigma}_f$ in (3.20) is independent of ε, one immediately finds that $\mathrm{a} = 1$ in (3.21) which reduces (3.20) to

$$
\begin{aligned}
\tfrac{1}{2} \boldsymbol{n}' \cdot (\boldsymbol{e}_i \otimes \boldsymbol{e}_j + \boldsymbol{e}_j \otimes \boldsymbol{e}_i) \; - \; \boldsymbol{K}_{\text{trial}} \cdot [\![\boldsymbol{V}]\!]^{ij}(\bar{\boldsymbol{\xi}}) \; &= \\
&= \; \boldsymbol{n}' \cdot \boldsymbol{C} : \oint_{\Gamma_{\text{trial}}} \check{\boldsymbol{\Sigma}}(\bar{\boldsymbol{\xi}}, \bar{\boldsymbol{x}}) : \boldsymbol{D}_{\bar{\boldsymbol{x}}} [\![\boldsymbol{V}]\!]^{ij}(\bar{\boldsymbol{x}}) \, \mathrm{d}S_{\bar{\boldsymbol{x}}}, \quad \bar{\boldsymbol{\xi}} \in \Gamma_{\text{trial}}.
\end{aligned}
\tag{3.22}
$$

By analogy to the BIE formulation for an exterior (traction-free) crack problem in *elastostatic* [e.g. 33, 22] one recognizes that, for given pair (i, j), integral equation (3.22) governs the fracture opening displacement $[\![\boldsymbol{V}]\!]^{ij}$ due to tractions $\mp \tfrac{1}{2} \boldsymbol{n}' \cdot (\boldsymbol{e}_i \otimes \boldsymbol{e}_j + \boldsymbol{e}_j \otimes \boldsymbol{e}_i)$ applied to the faces $\Gamma_{\text{trial}}^{\pm}$ of a "unit" fracture Γ_{trial} with interfacial stiffness $\boldsymbol{K}_{\text{trial}}$ in an infinite elastic solid (recall that $\boldsymbol{n}'^{\pm} = \mp \boldsymbol{n}'$). Owing to the symmetry of $[\![\boldsymbol{V}]\!]^{ij}$ with respect to i and j, (3.22) can accordingly be affiliated with six canonical elastostatic problems in $\mathbb{R}^3$.

The TS formula   Having $[\![\tilde{\boldsymbol{v}}]\!]$ characterized to the leading order, one finds from (3.12), (3.15) (3.18) and (3.21) that $f(\varepsilon) = \varepsilon^3$ and consequently

$$
\begin{aligned}
\mathsf{T}(\boldsymbol{\xi}^\circ; \boldsymbol{n}', \kappa_n, \kappa_s) \; &= \; \boldsymbol{\sigma}_f(\boldsymbol{\xi}^\circ) : \boldsymbol{A} : \hat{\boldsymbol{\sigma}}(\boldsymbol{\xi}^\circ), \\
\boldsymbol{A} \; &= \; \boldsymbol{e}_i \otimes \boldsymbol{e}_j \otimes \left(\int_{\Gamma_{\text{trial}}} [\![\boldsymbol{V}]\!]^{ij}(\bar{\boldsymbol{x}}) \, \mathrm{d}S_{\bar{\boldsymbol{x}}} \right) \otimes \boldsymbol{n}',
\end{aligned}
\tag{3.23}
$$

where $\hat{\boldsymbol{\sigma}} = \boldsymbol{C} : \nabla\hat{\boldsymbol{u}}$ denotes the adjoint-field stress tensor, and $\boldsymbol{A}$ is the so-called *polarization tensor* – independent of $\boldsymbol{\xi}^\circ$ and ω – whose evaluation is examined next.

3.2.2 Elastic polarization tensor

In prior works on the topological sensitivity [e.g. 6, 86, 24, 128], relevant polarization tensors were calculated analytically thanks to the available closed-form solutions for certain (2D and 3D) elastostatic exterior problems – e.g. those for a penny-shaped crack, circular hole, and spherical inclusion in an infinite solid. To the authors' knowledge, however, analytical solution to (3.22) is unavailable. As a result, numerical evaluation of $[\![\boldsymbol{V}]\!]^{ij}$ and thus $\boldsymbol{A}$ is pursued within a BIE framework [126, 33]. On recalling the definition of Γ_{trial} and the dimensional platform established in Sec. 3.1, the computation is effected assuming i) penny-shaped fracture of unit radius $\Lambda = 1$, ii) unbounded elastic medium $\mathbb{R}^3$ with unit shear modulus and mass density ($\mu = 1$, $\rho = 1$), and iii) various combinations between the trial fracture parameters (κ_s, κ_n) and the Poisson's ratio ν of the elastic solid.

To solve (3.22) for given $\Gamma_{\text{trial}} \in \mathbb{R}^3$, A BIE computational platform is developed on the basis of the regularized *traction* boundary integral equation [33] where the featured weakly-singular integrals are evaluated via suitable mapping techniques [126]. Without loss of generality, it is assumed that the origin of $\bar{\boldsymbol{\xi}}$ coincides with the center of a penny-shaped fracture surface, and that $\boldsymbol{n}' = \bar{\boldsymbol{e}}_3$ (see Fig. 8.6). A detailed account of the adopted BIE framework, including the regularization and parametrization specifics, is provided in G.

To validate the computational developments, Fig. 3.2(a) compares the numerically-obtained nontrivial components of $[\![V_k]\!]^{i3}$ with their analytical counterparts along the line of symmetry in Γ_{trial} assuming traction-free interfacial conditions ($\kappa_n = \kappa_s = 0$) and $\nu = 0.35$. Here is noted that, thanks to the problem symmetries, the variation of $[\![V_1]\!]^{13}$ equals that of $[\![V_2]\!]^{23}$ along the $\bar{\xi}_1$-axis i.e. the line of symmetry. To illustrate the influence of $\boldsymbol{K}_{\text{trial}}$ on the result, Fig. 3.2(b) shows the effect of shear specific stiffness κ_s (assuming $\kappa_n = 0$) on the tangential fracture opening displacement $[\![V_1]\!]^{13}$; a similar behavior is also observed concerning the effect of κ_n on the normal opening component $[\![V_3]\!]^{33}$.

Structure of the polarization tensor Before proceeding further, it is useful to observe from (3.23) that only the part of $\boldsymbol{A}$ with minor symmetries enters the computation of T thanks to the symmetry of $\boldsymbol{\sigma}_f$ and $\hat{\boldsymbol{\sigma}}$. Further, as shown in [8, 26], properties of the effective polarization tensor (hereon denoted by $\boldsymbol{A}^{\mathrm{eff}}$) can be extended to include the major symmetry. With reference to the local basis $(\bar{\boldsymbol{e}}_1, \bar{\boldsymbol{e}}_1, \bar{\boldsymbol{e}}_3 = \boldsymbol{n}')$, on the other hand, one finds that: i) $[\![\boldsymbol{V}]\!]^{\alpha\beta} = 0$ $(\alpha, \beta = 1, 2)$ due to a trivial forcing term in (3.22); ii) $[\![\boldsymbol{V}]\!]^{33} \propto \bar{\boldsymbol{e}}_3$ owing to the symmetry (about the $\bar{\xi}_3 = 0$ plane) of the boundary value problem for a penny-shaped fracture in $\mathbb{R}^3$ solved by (3.22), and iii) $[\![\boldsymbol{V}]\!]^{\alpha 3} \cdot \bar{\boldsymbol{e}}_3 = [\![\boldsymbol{V}]\!]^{3\alpha} \cdot \bar{\boldsymbol{e}}_3 = 0$ due to the anti-symmetry of the germane boundary value problem about the $\bar{\xi}_3 = 0$ plane – combined with the axial symmetry of Γ_{trial} about the $\bar{\xi}_3$-axis. A substitution of these findings immediately verifies that $[\![\boldsymbol{V}]\!]^{3\alpha}$ and $[\![\boldsymbol{V}]\!]^{\alpha 3}$ are independent of κ_n, whereas $[\![\boldsymbol{V}]\!]^{33}$ does not depend on κ_s. Note, however, that the above arguments are predicated upon the diagonal structure of $\boldsymbol{K}_{\mathrm{trial}}$ according to (3.3). As a result, one finds that the effective polarization tensor, superseding $\boldsymbol{A}$ in (3.23), permits representation

$$
\begin{aligned}
\boldsymbol{A}^{\mathrm{eff}} \;=\; & \alpha_s(\kappa_s, \nu) \sum_{\beta=1}^{2} (\bar{\boldsymbol{e}}_3 \otimes \bar{\boldsymbol{e}}_\beta + \bar{\boldsymbol{e}}_\beta \otimes \bar{\boldsymbol{e}}_3) \otimes (\bar{\boldsymbol{e}}_3 \otimes \bar{\boldsymbol{e}}_\beta + \bar{\boldsymbol{e}}_\beta \otimes \bar{\boldsymbol{e}}_3) \;+ \\
& + \; \alpha_n(\kappa_n, \nu)\, (\bar{\boldsymbol{e}}_3 \otimes \bar{\boldsymbol{e}}_3 \otimes \bar{\boldsymbol{e}}_3 \otimes \bar{\boldsymbol{e}}_3).
\end{aligned}
\tag{3.24}
$$

To evaluate the dependency of α_s and α_n on their arguments, $\boldsymbol{A}$ is evaluated numerically according to (3.23) for various triplets $(\nu, \kappa_s, \kappa_n)$. On deploying the Matlab optimization toolbox, the coefficients $\alpha_s(\kappa_s, \nu)$ and $\alpha_n(\kappa_n, \nu)$ are found to be rational functions of their arguments, identified as

$$
\alpha_s(\kappa_s, \nu) \;=\; \frac{4(1 - \nu^2)}{3(2 - \nu)(\kappa_s \Lambda + \nu + 1)}, \qquad \alpha_n(\kappa_n, \nu) \;=\; \frac{8(1 - \nu)(2\nu + 1)}{3(\kappa_n \Lambda + 2\nu + 1)}, \tag{3.25}
$$

where the implicit scaling parameter, $\Lambda = 1$, is retained to facilitate the forthcoming application of (21) to penny-shaped fractures of non-unit radius. Assuming $\nu = 0.35$, the behavior of α_s and α_n according to (3.25) is plotted in Fig. 3.2(c) versus the germane specific stiffness, with the corresponding numerical values included as dots. For completeness, a comparison between (3.25) and the BIE-evaluated values of α_s and α_n is provided in Fig. 3.3 for a range Poisson's ratios, $\nu \in [0.05, 0.45]$.
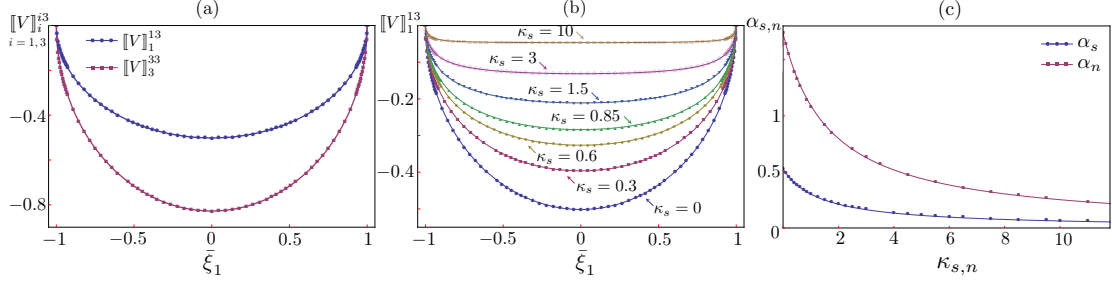
Figure 3.2: Dependence of the crack opening displacement $[\![V]\!]^{ij}$ and coefficients of the effective polarization tensor $\boldsymbol{A}^{\mathrm{eff}}$ on the specific stiffnesses, κ_s and κ_n, of a trial fracture assuming $\nu = 0.35$: (a) analytical values (solid lines) *vs.* numerical values (dots) of the FOD along $(\bar{\xi}_1, 0, 0)$ for a traction-free crack; (b) evolution of the shear FOD $[\![V_1]\!]^{13}$ with increasing k_s, and (c) proposed variation (solid lines) *vs.* numerical variation (dots) of α_n and α_n versus the relevant specific stiffness.

From (3.24), it is seen that the interfacial condition on Γ_{trial} has no major effect on the *structure* of the polarization tensor. This may explain the observation from numerical experiments (Section 3.4) that by using a traction-free trial crack ($\kappa_s = \kappa_n = 0$) in (3.24), the *geometrical* characteristics of a hidden fracture – its location, normal vector and, in the case of high excitation frequencies, its shape – can be reconstructed regardless of the assumed interfacial condition. Nonetheless, a trial crack with interacting surfaces introduces two new parameters (κ_s and κ_n) to the reconstruction scheme, whereby further information on the hidden fracture's interfacial condition may be extracted. In this vein, it can be shown that the first-order topological sensitivity (3.23) is, for given $\boldsymbol{\xi}^\circ$, a monotonic function of κ_n, κ_s; accordingly, precise contact conditions on Γ (the true fracture) cannot be identified separately via e.g. a TS-based minimization procedure. In principle, such information could be retrieved by pursuing a higher-order TS scheme [e.g. 35] which is beyond the scope of this study. As shown in the sequel, however, the present (first-order) TS sensing framework is capable of qualitatively *identifying the ratio* between the specific shear and normal stiffnesses on Γ – an item that is strongly correlated with the hydro-mechanical properties (e.g. hydraulic conductivity) of the fracture interface [131], and thus potentially of great interest in hydraulic fracturing applications [e.g 16, 163].
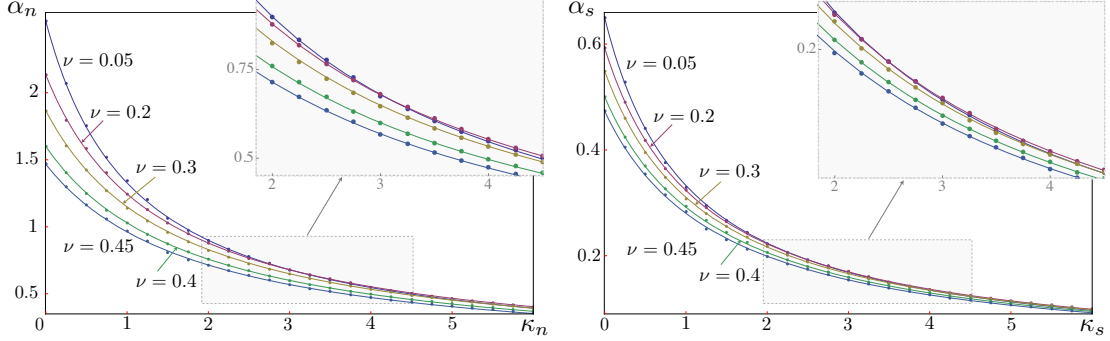
Figure 3.3: Performance of the formulas (3.25) describing $\alpha_n(\kappa_n, \nu)$ and $\alpha_s(\kappa_s, \nu)$ in the $(\nu, \kappa_s, \kappa_n)$-space: numerical values (dots) *vs.* proposed expressions (solid lines).

3.3 Qualitative identification of the fracture's interfacial condition

In this section, an ability of the TS indicator function (3.23) to qualitatively characterize the interfacial condition of *nearly-planar fractures* is investigated in the *"low" frequency regime* where the illuminating wavelength $2\pi/k$, controlled by wavenumber k, exceeds – by at least 2-3 times – the characteristic size of Γ i.e. the maximum extent associated with the fracture geometry such as diameter or length. Such limitations are introduced to facilitate the asymptotic analysis where the true (finite) fracture is approximated as being penny-shaped. The proposed analysis naturally extends to arbitrary-shaped, near-flat fractures by assuming a diagonal, *to the leading order*, interfacial stiffness matrix and the FOD profile proposed in [73] to calculate the relevant polarization tensor required in the asymptotic approximation of the scattered field due to Γ. In the approach, it is also assumed that the fracture location and normal vector to its surface are identified via an initial TS reconstruction performed using a traction-free trial crack ($\kappa_s = \kappa_n = 0$) as described in Section 3.4. As shown there, however, the latter geometric reconstruction is not limited to a particular frequency range.

On recalling the least-squares distance function φ in (3.5) and the leading-order perturbation of $J(\emptyset)$ in (3.9), the TS may be rewritten as

$$\varepsilon^3 \, \mathsf{T}(\boldsymbol{\xi}^\circ; \boldsymbol{n}', \kappa_n, \kappa_s) = -\mathrm{Re}\Big[\int_{S^{\mathrm{obs}}} \tilde{\boldsymbol{u}}^*(\boldsymbol{\xi}) \cdot \tilde{\boldsymbol{v}}(\boldsymbol{\xi}) \, \mathrm{d}S_{\boldsymbol{\xi}} \Big], \tag{3.26}$$

where $(\cdot)^*$ signifies complex conjugation and $-\tilde{\boldsymbol{u}}^*(\boldsymbol{\xi}) = \partial\varphi(\boldsymbol{v}, \boldsymbol{u}^{\text{obs}}, \boldsymbol{\xi})/\partial\boldsymbol{v}|_{\boldsymbol{v}=\boldsymbol{u}^i}$, noting that $\tilde{\boldsymbol{u}} = \boldsymbol{u} - \boldsymbol{u}^i$ is the scattered field due to Γ, see (3.1). Given the fact that the hidden fracture is separated from the observation surface, the scattered field on S^{obs} can be expressed via a displacement boundary integral representation as

$$\tilde{\boldsymbol{u}}(\boldsymbol{\xi}) = \int_{\Gamma} (\llbracket\tilde{\boldsymbol{u}}\rrbracket(\boldsymbol{x}) \otimes \boldsymbol{n}) : \boldsymbol{\Sigma}(\boldsymbol{\xi}, \boldsymbol{x}, \omega) \, \mathrm{d}S_{\boldsymbol{x}}, \qquad \boldsymbol{\xi} \in S^{\text{obs}}. \tag{3.27}$$

Small crack asymptotics Consider the testing configuration as in Fig. 3.1, and let Γ with interfacial stiffness (3.3) be illuminated by a "low-frequency" plane wave $\boldsymbol{u}^i = \boldsymbol{b}\, e^{-ik\boldsymbol{\xi}\cdot\boldsymbol{d}}$ in that $kL \ll 1$, where $2L$ is the characteristic size of Γ, normalized by the radius of the sampled domain (see Sec. 3.1). With such premise and hypothesis that $2L < R_1 = 1 \ll R_2$ made earlier (recall that R_2 is the radius of S^{obs}), the hidden fracture can – in situations of predominantly flat geometry and an $O(1)$ aspect ratio – be approximated as a penny-shaped fracture of finite radius L. In this setting (3.27) can be expanded, utilizing the developments from Section 3.2, as

$$\tilde{\boldsymbol{u}}(\boldsymbol{\xi}) \simeq \left(\int_{\Gamma} (\llbracket\tilde{\boldsymbol{u}}\rrbracket(\boldsymbol{x}) \otimes \boldsymbol{n}) \, \mathrm{d}S_{\boldsymbol{x}} \right) : \boldsymbol{\Sigma}(\boldsymbol{\xi}, \boldsymbol{z}, \omega) \simeq L^3 \boldsymbol{\sigma}^f(\boldsymbol{z}) : \boldsymbol{A}^{\Gamma} : \boldsymbol{\Sigma}(\boldsymbol{\xi}, \boldsymbol{z}, \omega), \qquad \boldsymbol{\xi} \in S^{\text{obs}}, \tag{3.28}$$

where $\boldsymbol{z}$ (to be determined) is an indicator of the fracture location, and $\boldsymbol{A}^{\Gamma}$ is its effective (low-frequency) polarization tensor given by

$$\boldsymbol{A}^{\Gamma} = \sum_{\beta=1}^{2} \varsigma_s (\boldsymbol{n} \otimes \boldsymbol{e}_{\beta} + \boldsymbol{e}_{\beta} \otimes \boldsymbol{n}) \otimes (\boldsymbol{n} \otimes \boldsymbol{e}_{\beta} + \boldsymbol{e}_{\beta} \otimes \boldsymbol{n}) + \varsigma_n (\boldsymbol{n} \otimes \boldsymbol{n} \otimes \boldsymbol{n} \otimes \boldsymbol{n}). \tag{3.29}$$

Here $\boldsymbol{n}$ is the normal on Γ; $(\boldsymbol{e}_1, \boldsymbol{e}_2, \boldsymbol{n})$ make an orthonormal basis, and

$$\varsigma_s(k_s, \nu) = \frac{4(1 - \nu^2)}{3(2 - \nu)(k_s L + \nu + 1)}, \qquad \varsigma_n(k_n, \nu) = \frac{8(1 - \nu)(2\nu + 1)}{3(k_n L + 2\nu + 1)}, \tag{3.30}$$

where k_s and k_n are the shear and normal specific stiffness of the true fracture according to (3.3), see also (3.7) and (3.25). On taking without loss of generality $(\boldsymbol{e}_1, \boldsymbol{e}_2, \boldsymbol{n})$ as the basis of the global coordinate system, (3.28) can be rewritten in component form as

$$\tilde{u}_j(\boldsymbol{\xi}) = L^3 \left[4\varsigma_s(k_s, \nu) \Sigma_{3\beta}^j(\boldsymbol{\xi}, \boldsymbol{z}, \omega) \sigma_{3\beta}^f(\boldsymbol{z}) + \varsigma_n(k_n, \nu) \Sigma_{33}^j(\boldsymbol{\xi}, \boldsymbol{z}, \omega) \sigma_{33}^f(\boldsymbol{z}) \right], \qquad \boldsymbol{\xi} \in S^{\text{obs}}, \tag{3.31}$$

where $\beta = 1, 2$ and the summation is assumed over repeated indexes as before.

Assuming that the location and (average) normal on Γ are identified beforehand, one may set $\boldsymbol{n}' = \boldsymbol{n}$ and $\boldsymbol{\xi}^{\circ} = \boldsymbol{z}$ in (3.26) and expand the scattered field due to vanishing *trial* fracture $\Gamma_\varepsilon = \boldsymbol{\xi}^{\circ} + \varepsilon \Gamma_{\text{trial}}$ in an analogous fashion as

$$\tilde{v}_j(\boldsymbol{\xi}) \;=\; \varepsilon^3 \left[4\alpha_s(\kappa_s, \nu) \, \Sigma_{3\beta}^j(\boldsymbol{\xi}, \boldsymbol{z}, \omega) \, \sigma_{3\beta}^f(\boldsymbol{z}) + \alpha_n(\kappa_n, \nu) \, \Sigma_{33}^j(\boldsymbol{\xi}, \boldsymbol{z}, \omega) \, \sigma_{33}^f(\boldsymbol{z}) \right], \qquad \boldsymbol{\xi} \in S^{\text{obs}}, \tag{3.32}$$

On substituting (3.31) and (3.32) into (3.26), the leading-order TS contribution in the low-frequency regime is obtained as

$$\mathsf{T}(\boldsymbol{z}, \kappa_n, \kappa_s) \;\simeq\; -L^3 \left[\alpha_n \varsigma_n Q_1(\boldsymbol{z}) \;+\; (\alpha_s \varsigma_n + \alpha_n \varsigma_s) Q_2(\boldsymbol{z}) \;+\; \alpha_s \varsigma_s Q_3(\boldsymbol{z}) \right], \tag{3.33}$$

where

$$Q_1(\boldsymbol{z}) \;=\; |\sigma_{33}^f(\boldsymbol{z})|^2 \int_{S^{\text{obs}}} [\Sigma_{33}^{j*} \Sigma_{33}^j](\boldsymbol{\xi}, \boldsymbol{z}, \omega) \, \mathrm{d}S_{\boldsymbol{\xi}},$$

$$Q_2(\boldsymbol{z}) \;=\; 4 \operatorname{Re}\left\{ [\sigma_{33}^{f*} \sigma_{3\beta}^f](\boldsymbol{z}) \int_{S^{\text{obs}}} [\Sigma_{33}^{j*} \Sigma_{3\beta}^j](\boldsymbol{\xi}, \boldsymbol{z}, \omega) \, \mathrm{d}S_{\boldsymbol{\xi}} \right\}, \tag{3.34}$$

$$Q_3(\boldsymbol{z}) \;=\; 16 \operatorname{Re}\left\{ [\sigma_{3\alpha}^{f*} \sigma_{3\beta}^f](\boldsymbol{z}) \int_{S^{\text{obs}}} [\Sigma_{3\alpha}^{j*} \Sigma_{3\beta}^j](\boldsymbol{\xi}, \boldsymbol{z}, \omega) \, \mathrm{d}S_{\boldsymbol{\xi}} \right\},$$

where $(\cdot)^*$ indicates complex conjugation, $\alpha, \beta = 1, 2$, and $j = 1, 2, 3$ as before. With reference to F, integration of the anti-linear forms, featuring components of the fundamental stress tensor, over S^{obs} can be performed analytically by approximating the distance $r = |\boldsymbol{\xi} - \boldsymbol{z}|$, $\boldsymbol{\xi} \in S^{\text{obs}}$ in (F1) and (F2) to the leading order as $r = R_2$. As a result, the behavior of (3.34) can be approximated as

$$Q_1 \simeq \frac{|\sigma_{33}^f(\boldsymbol{z})|^2}{4\pi R_2^2} \left[\tfrac{1}{5} \mathrm{X}_2 + \tfrac{4}{3} \operatorname{Re}(\mathrm{X}_3) + |B_5(R_2)|^2 \right], \quad Q_2 = O\left(\frac{1}{R_2^3} \right) \simeq 0,$$

$$Q_3 \simeq \frac{4}{\pi R_2^2} [\sigma_{3\beta}^{f*} \sigma_{3\beta}^f](\boldsymbol{z}) \left[\tfrac{1}{15} \mathrm{X}_2 + \tfrac{2}{3} |B_4(R_2)|^2 \right], \tag{3.35}$$

owing to the initial premise of "far field" sensing (namely $R_2 \gg 1$ within the adopted dimensional platform), where $B_4(\cdot)$, $B_5(\cdot)$, X_2 and X_3 are given by (F2) and (F6) in F along with the calculation details.

A remarkable outcome of the analysis is that the coefficient Q_2 describing the mixed term in (3.35) vanishes to the leading order, whereby the TS structure *decouples* and

may be perceived as a superposition of the normal and shear contributions. Specifically, (3.33) becomes

$$\mathsf{T}(\boldsymbol{z}; \boldsymbol{n}, \kappa_n, \kappa_s) \simeq -L^3 \left(\alpha_n(\kappa_n, \nu) \varsigma_n Q_1(\boldsymbol{z}) + \alpha_s(\kappa_s, \nu) \varsigma_s Q_3(\boldsymbol{z}) \right), \tag{3.36}$$

where ς_n and ς_s are given by (3.30). On account of (3.36) and the limiting behavior of α_n (resp. α_s) as a function of the trial interface parameter κ_n (reps. κ_s) in (3.25), the ratio between the shear and normal specific stiffness (k_s/k_n) of a hidden fracture can be qualitatively identified via the following procedure.

Interface characterization scheme With reference to the last paragraph of Section 3.2, it is hereon assumed that the fracture location is identified beforehand from the low-frequency scattered field data as

$$\boldsymbol{z} = \arg \min_{\boldsymbol{\xi}^\circ} \mathsf{T}(\boldsymbol{\xi}^\circ; \boldsymbol{n}'(\boldsymbol{\xi}^\circ), 0, 0), \tag{3.37}$$

where, for each sampling point, $\boldsymbol{n}'(\boldsymbol{\xi}^\circ)$ is the optimal unit normal (minimizing T at that point) as described in [26]. In this setting the *effective* normal to a hidden fracture, $\boldsymbol{n}$, is obtained by averaging $\boldsymbol{n}'(\boldsymbol{\xi}^\circ)$ over a suitable neighborhood of $\boldsymbol{z}$. Here it is for completeness noted that the spatial variation of $\boldsymbol{n}'(\boldsymbol{\xi}^\circ)$ provides a clue whether the hidden fracture is nearly-planar and thus amenable to the proposed treatment, see the low-frequency results in Figs. 3.7 and 3.6 as an example.

In the vicinity of $\boldsymbol{z}$, the TS characterization of the fracture's interfacial condition is performed using two (vanishing) trial fractures: one allowing for the FOD in the normal direction only by assuming $(\kappa_s, \kappa_n) = (\infty, 0)$, and the other restricting the FOD to tangential directions via $(\kappa_s, \kappa_n) = (0, \infty)$. The resulting TS fields are then normalized by the relevant components of $\boldsymbol{\sigma}_f(\boldsymbol{z})$ according to (3.34). Thanks to the limits $\lim_{\kappa_s \to \infty} \alpha_s = 0$ and $\lim_{\kappa_n \to \infty} \alpha_n = 0$, this leads to the respective indicator functionals

$$\mathsf{T}_1(\boldsymbol{\xi}^\circ) = \frac{1}{|\sigma_{33}^f(\boldsymbol{z})|^2} \mathsf{T}(\boldsymbol{\xi}^\circ; \boldsymbol{n}, 0, \infty) \simeq -\frac{L^3 \varsigma_n}{4\pi R_2^2} \alpha_n(0, \nu) \left[\tfrac{1}{5} \mathrm{X}_2 + \tfrac{4}{3} \mathrm{Re}(\mathrm{X}_3) + |B_5(R_2)|^2 \right],$$

$$\mathsf{T}_2(\boldsymbol{\xi}^\circ) \;=\; \frac{1}{[\sigma_{3\beta}^{f*}\,\sigma_{3\beta}^{f}](\boldsymbol{z})}\,\mathsf{T}(\boldsymbol{\xi}^\circ;\boldsymbol{n},\infty,0) \;\simeq\; -\,\frac{4L^3\varsigma_s}{\pi R_2^2}\,\alpha_s(0,\nu)\Big[\tfrac{1}{15}\mathrm{X}_2 + \tfrac{2}{3}|B_4(R_2)|^2\Big],$$

$$(3.38)$$

were $\boldsymbol{\xi}^\circ$ is in a neighborhood of $\boldsymbol{z}$. In practical terms, the latter is identified as a ball (centered at $\boldsymbol{z}$) whose radius is a fraction of the germane (compressional or shear) wavelength. On the basis of (3.38), one can identify three distinct interface scenarios:

1. The situation where k_s and k_n are of the same order of magnitude (e.g. traction-free crack), in which case $[\mathsf{T}_1/\mathsf{T}_2](\boldsymbol{\xi}^\circ) = O(1)$ regardless of ν. This is verified in Fig. 3.4, where the ratio $\mathsf{T}_1/\mathsf{T}_2$ is plotted against R_2 – scaled by the shear wavelength $\lambda_s = 2\pi c_s/\omega$ – for various Poisson's ratios and two "extreme" sets of interfacial stiffnesses, namely $k_\star = 0.1$ and $k_\star = 10$ ($\star = s, n$). In the context of the proposed characterization scheme, Fig. 3.8(a) plots the spatial distribution of T_1 and T_2 in a neighborhood of a traction-free fracture. As can be seen from the display, the fracture is visible from both panels, which suggests that k_s and k_n are comparable in magnitude.

2. The limiting case $k_s \ll k_n$ that, in the context of energy applications, corresponds to a hydraulically-isolated fracture [55, 131, 16]. Under such circumstances one has $\mathsf{T}_1(\boldsymbol{\xi}^\circ) \ll \mathsf{T}_2(\boldsymbol{\xi}^\circ)$, which can be verified by letting $\varsigma_n \to 0$ in (3.30). This behavior is shown in Fig. 3.8(b), where a hidden fracture with $(k_s, k_n) = (2, 100)$ is visible in the distribution of T_2, but not in that of T_1. Note that the image of a fracture is notably smeared due to the use of low-frequency excitation, as postulated by the interface characterization scheme.
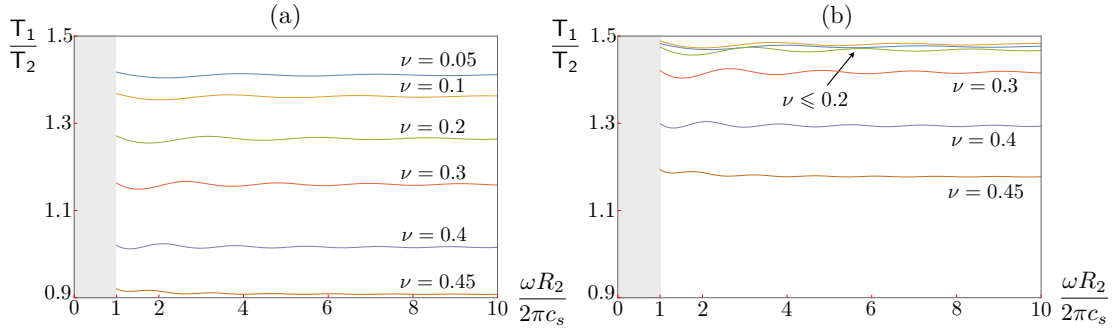
Figure 3.4: Ratio $[\mathsf{T}_1/\mathsf{T}_2](\boldsymbol{z})$ *vs.* the radius of S^{obs}, measured in shear wavelengths, assuming the fracture specific stiffnesses as (a) $k_s = k_n = 0.1$, and (b) $k_s = k_n = 10$.

3. The case when the fracture surface is under small normal pressure and the effect of surface roughness is significant, namely $k_s \gg k_n$. Here $\mathsf{T}_1(\boldsymbol{\xi}^\circ) \gg \mathsf{T}_2(\boldsymbol{\xi}^\circ)$ due to the fact that $\lim_{k_s \to \infty} \varsigma_s = 0$ thanks to (3.30). This is illustrated in Fig. 3.8(c), where the fracture with $(k_s, k_n) = (100, 2)$ appears in the distribution of T_1 only, suggesting that its interfacial stiffness according to (3.3) is dominated by the shear component k_s.

Here it is worth noting that the above TS scheme for *qualitative identification* of the ratio k_s/k_n is non-iterative, and shines light on an important contact parameter at virtually no computational surcharge – beyond the effort needed to image the fracture. In particular, since the (low-frequency) free and adjoint fields are precomputed toward initial estimation of the fracture location $\boldsymbol{z}$ and effective normal vector $\boldsymbol{n}$, they can be re-used to compute T_1 and T_2 via (3.23), (3.24), (3.25) and (3.38), wherein the only variable is the effective polarization tensor $\boldsymbol{A}^{\text{eff}}$ – describing trial fractures with different interfacial condition.

Illumination by multiple incident waves In many situations the imaging ability of a TS indicator functional can be improved by deploying multiple illuminating wavefields, which in the context of this study translates into multiple directions $\boldsymbol{d}$ of plane-wave incidence. In this case the "fortified" TS functional can be written as

$$\breve{\mathsf{T}} \;=\; \int_{\Omega_{\boldsymbol{d}}} \mathsf{T}|_{\boldsymbol{d}} \cdot \mathrm{w}(\boldsymbol{d}) \; \mathrm{d}S_{\boldsymbol{d}}, \tag{3.39}$$

which superimposes (in a weighted fashion) the TS distributions for incident plane waves spanning a given subset, $\Omega_{\boldsymbol{d}}$, of the unit sphere. In the context of (3.33) and (3.34), the only $\boldsymbol{d}$-dependent items are the components of the free-field stress tensor $\boldsymbol{\sigma}_f$. As a result, the criteria deduced from (3.38) remain valid under the premise of multiple incident-wave illumination provided that the free-field terms

$$[\sigma_{33}^{f*} \sigma_{33}^{f}], \quad [\sigma_{33}^{f*} \sigma_{3\beta}^{f}], \quad [\sigma_{3\alpha}^{f*} \sigma_{3\beta}^{f}],$$

in (3.34) are replaced respectively by

$$\int_{\Omega_{\boldsymbol{d}}} [\sigma_{33}^{f*} \sigma_{33}^{f}]_{\boldsymbol{d}} \, \mathrm{d}S_{\boldsymbol{d}}, \quad \int_{\Omega_{\boldsymbol{d}}} [\sigma_{33}^{f*} \sigma_{3\beta}^{f}]_{\boldsymbol{d}} \, \mathrm{d}S_{\boldsymbol{d}}, \quad \int_{\Omega_{\boldsymbol{d}}} [\sigma_{3\alpha}^{f*} \sigma_{3\beta}^{f}]_{\boldsymbol{d}} \, \mathrm{d}S_{\boldsymbol{d}}.$$

Comment   It is well known [55] that the fracture specific stiffness, quantified in terms of k_s and k_n, is strongly correlated with both i) the state of stress at the interface (prior to illumination), and ii) the frequency of excitation (due to presence of surface asperities). Under the premise of long illuminating wavelength – exceeding the fracture extent, however, the dependence of seismically-identified k_s and k_n on frequency is expected to be mild due to separation in scales between the probing wavelength and the characteristic length representing the asperities. With such caveats, the ensuing set of numerical results are based on *synthetic data* computed, via a boundary integral equation approach, for a fracture with *a priori* specified i.e. fixed k_s and k_n. The main idea is to examine whether (at a given frequency and given state of stress) the TS approach is capable of non-iteratively sensing the fracture's *apparent* contact law – an information that, given the reconstruction at multiple frequencies, could possibly be deployed to shine light of the physics of a fracture interface – including e.g. its roughness, presence of proppant, and hydraulic condition.

3.4   Numerical results

A set of numerical experiments is devised to illustrate the performance of the TS for elastic-wave imaging of fractures and qualitative characterization of their interfacial condition. To this end the BIE computational platform, described in G, is used to generate the synthetic data ($\boldsymbol{u}^{\mathrm{obs}}$) for the inverse problem. While the main focus of the study is on the low-frequency sensing as mandated by the characterization scheme, the results also include the TS reconstruction examples at intermediate-to-high frequencies, motivating future research in this area. The sensing setup, reflecting the assumptions made in Section 2, is shown in Fig. 3.5 where the "true" fracture Γ is either i) a penny-shaped crack with diameter $L = 0.7$ and normal $\boldsymbol{n} = (0, -1/\sqrt{2}, 1/\sqrt{2})$ – see Fig. 3.5(a), or ii) a cylindrical crack of length $L = 0.7$ and radius $R = 0.35$ shown in Fig. 3.5(b). The shear modulus, mass density, and Poisson's ratio of the background medium are taken as $\mu = 1$, $\rho = 1$ and $\nu = 0.35$, whereby the shear and compressional wave speeds read $c_s = 1$ and $c_p = 2.08$, respectively. The elastodynamic field produced by the action of illuminating (P- or S-) plane wave, propagating in direction $\boldsymbol{d}$, on Γ is measured over S^{obs} – taken as the surface of a *cube* with side 3.5 centered at the origin. This was
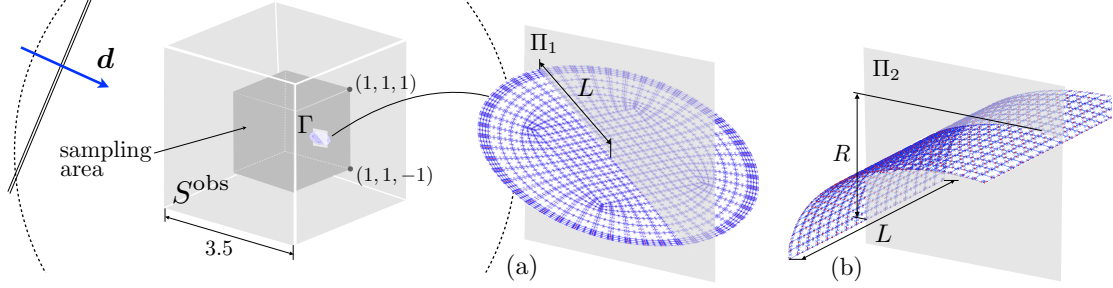
Figure 3.5: Model problem: (a) sensing configuration with an embedded penny shaped fracture, and (b) with non-planar scatterer i.e. cylindrical fracture.

done to investigate the robustness of the interface characterization scheme developed in Section 3.3 with respect to the simplifying assumptions used to derive (3.33)–(3.35), namely the premise that S^{obs} is a *sphere*. On the adopted observation surface, the density of sensing points is chosen to ensure at least four sensors per shear wavelength. In what follows, the TS is computed inside a sampling cube of side 2 centered at the origin; its spatial distribution is plotted either in three dimensions, or in the mid-section Π_1 (resp. Π_2) of the penny-shaped (resp. cylindrical) fracture shown in Fig. 3.5. In the spirit of an effort to test the robustness of the adopted simplifying assumptions, it is noted that the ratio between the radii of spheres circumscribing the sensing area and the sampling region is $R_2/R_1 = 1.75 \not\gg 1$.

Low-frequency TS reconstruction Consider first the case of an "isolated fluid-filled" planar fracture shown in Fig. 3.5(a), whose specific stiffnesses are given by $(k_s, k_n) = (2, 100)$. To geometrically identify the fracture, the region of interest is illuminated by twelve P- and S- incident waves propagating in directions $\boldsymbol{d} \in \{(\pm1, 0, 0), (0, \pm1, 0), (0, 0, \pm1)\}$, while assuming $(\kappa_s, \kappa_n) = (0, 0)$ for the (vanishing) trial fracture. The illuminating frequency is taken as $\omega = 4$, whereby the ratio between the probing shear wavelength $\lambda_s = 2\pi c_s/\omega \simeq 1.6$ and fracture diameter, L, is approximately 2.2. For each incident wave and each sampling point, the optimal normal vector $\boldsymbol{n}'(\boldsymbol{\xi}^\circ)$ is estimated by evaluating $\mathsf{T}(\boldsymbol{\xi}^\circ; \boldsymbol{n}' = [\cos(\theta_i)\cos(\phi_j), \sin(\theta_i)\cos(\phi_j), \sin(\phi_j)], 0, 0)$ for trial pairs $(\theta_i, \phi_j) \in [0, 2\pi] \times [0, \pi]$ and choosing the pair that minimizes $\mathsf{T}(\boldsymbol{\xi}^\circ; \cdot)$. Thus

obtained TS distributions are superimposed as

$$\check{\mathsf{T}}(\boldsymbol{\xi}^{\circ}; \boldsymbol{n}', 0, 0) = |\min_{\boldsymbol{\xi}^{\circ}} \check{\mathsf{T}}|^{-1} \sum_{n=1}^{12} \mathsf{T}(\boldsymbol{\xi}^{\circ}; \boldsymbol{n}', 0, 0)|_{(\boldsymbol{b}_n, \boldsymbol{d}_n)},$$

resulting in a composite indicator function whose spatial distribution shown in Fig. 3.7(a). In this setting, the fracture is geometrically identified via a region where $\check{\mathsf{T}}$ attains its most pronounced negative values, see Fig. 3.7(b). To provide a more complete insight into the performance of the approach, Fig. 3.7(c) plots the distribution of point-optimal unit normal $\boldsymbol{n}'(\boldsymbol{\xi}^{\circ})$ over the reconstructed region. For the purposes of interface characterization, the fracture location $\boldsymbol{z}$ is identified according to (3.37), while its effective normal $\boldsymbol{n}'$ is computed by averaging $\boldsymbol{n}'(\boldsymbol{\xi}^{\circ})$ over the reconstructed volume in Fig. 3.7(b).
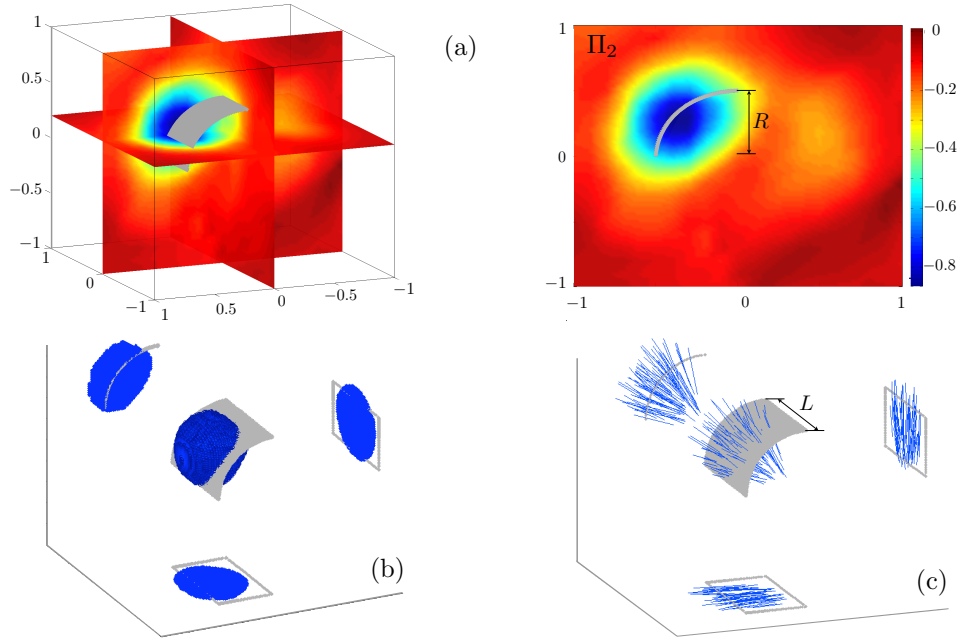
Figure 3.6: Low-frequency reconstruction of a cylindrical fracture with $(k_s, k_n) = (4, 4)$: (a) composite TS distribution $\check{\mathsf{T}}(\boldsymbol{\xi}^{\circ}; \boldsymbol{n}', 0, 0)$ in three dimensions, and in the fracture mid-section Π_2; (b) region containing the most pronounced negative TS values: $-1 \leqslant \check{\mathsf{T}} \leqslant -0.6$, and (c) point-optimal normal vector $\boldsymbol{n}'(\boldsymbol{\xi}^{\circ})$ plotted over the true fracture surface Γ.
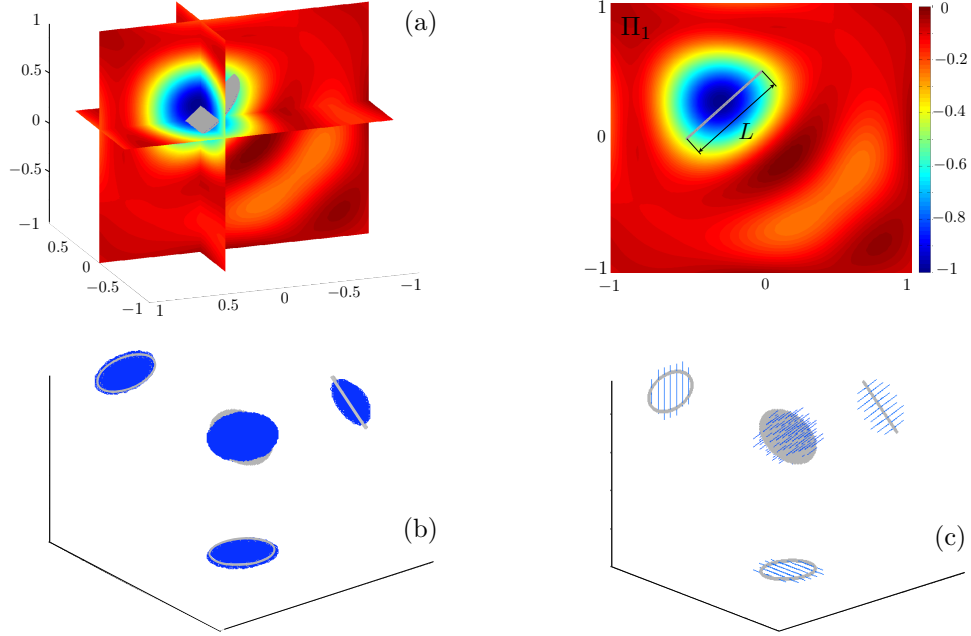
Figure 3.7: Low-frequency reconstruction of an "isolated fluid-filled" planar fracture with $(k_s, k_n) = (2, 100)$: (a) composite TS distribution $\check{\mathsf{T}}(\boldsymbol{\xi}^\circ; \boldsymbol{n'}, 0, 0)$ in three dimensions, and in the fracture mid-section Π_1; (b) region containing the most pronounced negative TS values: $-1 \leqslant \check{\mathsf{T}} \leqslant -0.6$, and (c) point-optimal normal vector $\boldsymbol{n'}(\boldsymbol{\xi}^\circ)$ plotted over the true fracture surface Γ.

For completeness, the above-described geometrical identification procedure is next applied to the cylindrical fracture in Fig. 3.5(b), assuming the "true" specific stiffnesses as $(k_s, k_n) = (4, 4)$ and setting the excitation frequency to $\omega = 5$. In this case, the wavelength-to-fracture-size ratio can be computed as $\lambda_s/L \simeq 1.8$. The resulting distributions of $\check{\mathsf{T}}$ and point-optimal normal $\boldsymbol{n'}$ are shown in Fig. 3.6, from which one can observe that i) the method performs similarly for both planar an non-planar fractures, and ii) the reconstruction procedure is apparently not sensitive to the nature of the interfacial condition in terms of k_s and k_n.

Interface characterization With reference to Fig. 3.5(a), the characterization of a penny-shaped fracture with three distinct interface scenarios is considered, namely: i) the traction-free crack i.e. $k_n = k_s = 0$, ii) isolated fluid-filled fracture with $(k_s, k_n) = (2, 100)$, and iii) fracture with rough surfaces under insignificant normal stress [146],
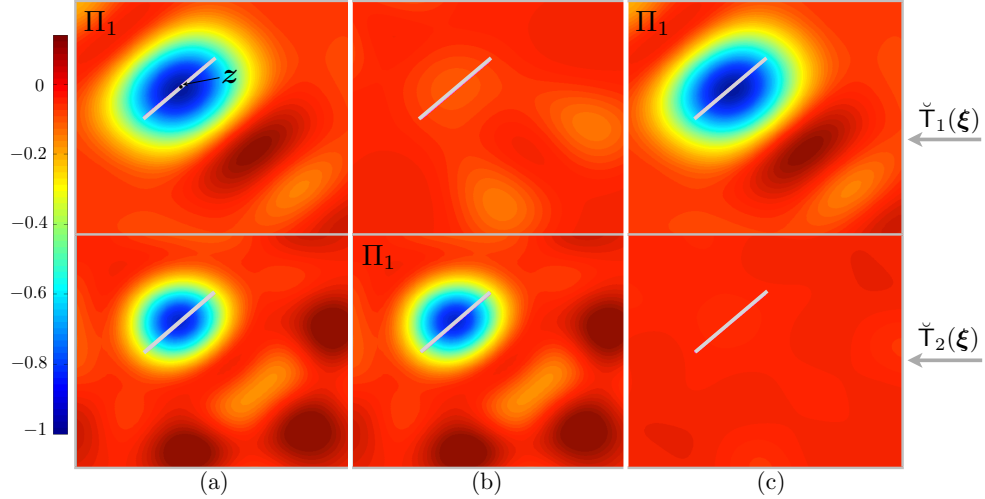
Figure 3.8: Spatial distribution of $\check{\mathsf{T}}_1$ (top panels) versus $\check{\mathsf{T}}_2$ (bottom panels), in the mid-section of a penny-shaped fracture, whose interface is (a) traction-free ($k_s = k_n = 0$), (b) isolated fluid-filled ($k_s = 2, k_n = 100$), and (c) of significant surface roughness and under low normal stress ($k_s = 100, k_n = 2$).

simulated by setting $(k_s, k_n) = (100, 2)$. In all cases, the interface characterization is carried out at $\omega = 5$ i.e. $\lambda_s/L \simeq 1.8$ using twelve incident (P- and S-) waves as described earlier. Next, to identify the contact condition, the "test" indicator functions

$$\check{\mathsf{T}}_1(\boldsymbol{\xi}^\circ) \;=\; |\check{\mathsf{T}}_{\mathrm{m}}|^{-1} \, \frac{\sum_{\mathrm{n}=1}^{12} \mathsf{T}(\boldsymbol{\xi}^\circ; \boldsymbol{n}, 0, 50)\big|_{(\boldsymbol{b}_{\mathrm{n}}, \boldsymbol{d}_{\mathrm{n}})}}{\sum_{\mathrm{n}=1}^{12} |\sigma_{33}^f(\boldsymbol{z})|_{(\boldsymbol{b}_{\mathrm{n}}, \boldsymbol{d}_{\mathrm{n}})}^2} ,$$

$$\check{\mathsf{T}}_2(\boldsymbol{\xi}^\circ) \;=\; |\check{\mathsf{T}}_{\mathrm{m}}|^{-1} \, \frac{\sum_{\mathrm{n}=1}^{12} \mathsf{T}(\boldsymbol{\xi}^\circ; \boldsymbol{n}, 50, 0)\big|_{(\boldsymbol{b}_{\mathrm{n}}, \boldsymbol{d}_{\mathrm{n}})}}{\sum_{\mathrm{n}=1}^{12} \big[\sigma_{3\beta}^{f*} \sigma_{3\beta}^f\big](\boldsymbol{z})\big|_{(\boldsymbol{b}_{\mathrm{n}}, \boldsymbol{d}_{\mathrm{n}})}} ,$$

are computed on the basis of (3.38), where $\check{\mathsf{T}}_{\mathrm{m}} = \min\{\min_{\boldsymbol{\xi}^\circ} \check{\mathsf{T}}_1, \min_{\boldsymbol{\xi}^\circ} \check{\mathsf{T}}_2\}$.

The resulting distributions of $\check{\mathsf{T}}_1$ and $\check{\mathsf{T}}_2$ for all three scenarios are plotted in Fig. 3.8, using a common color scale, over the fracture's mid-section Π_1. From the display, it is clear that $\check{\mathsf{T}}_1(\boldsymbol{\xi}^\circ)/\check{\mathsf{T}}_2(\boldsymbol{\xi}^\circ) = O(1)$, $\check{\mathsf{T}}_1(\boldsymbol{\xi}^\circ) \ll \check{\mathsf{T}}_2(\boldsymbol{\xi}^\circ)$, and $\check{\mathsf{T}}_1(\boldsymbol{\xi}^\circ) \gg \check{\mathsf{T}}_2(\boldsymbol{\xi}^\circ)$ respectively for the "true" interfacial conditions according to i), ii) and iii). These results indeed support the claim of the preliminary characterization scheme that, at long illumination wavelengths, the interfacial condition of nearly-planar fractures can be *qualitatively*

assessed at virtually no computational cost - beyond what is needed to identify the fracture geometrically.

TS reconstruction at higher frequencies Clearly, the geometrical information in Figs. 3.7(b) and 3.6(b), obtained with $\lambda_s/L \sim 2$, does not carry sufficient detail to accurately reconstruct the fracture surface in 3D from the scattered elastic waves. To help mitigate the drawback, the forward scattering problem is recomputed at a higher frequency, namely $\omega = 20$ for which $\lambda_s/L \simeq 0.45$. In doing so, the number of incident elastodynamic fields is increased so that *twenty* plane waves of each (P- and S-) type, propagating in directions $\{\boldsymbol{d}_n \in \Omega,\ n = 1, 2, ..., 20\}$ – evenly distributed over the unit sphere Ω – participate in the TS evaluation. The resulting "high-frequency" behavior of the composite indicator function

$$\check{\mathsf{T}}(\boldsymbol{\xi}^\circ; \boldsymbol{n}', 0, 0) \;=\; |\min_{\boldsymbol{\xi}^\circ} \check{\mathsf{T}}|^{-1} \sum_{n=1}^{40} \mathsf{T}(\boldsymbol{\xi}^\circ; \boldsymbol{n}', 0, 0)|_{(\boldsymbol{b}_n, \boldsymbol{d}_n)},$$

is shown in Figs. 3.9 and 3.10 for the cases of penny-shaped fracture and cylindrical fracture, respectively (see Fig. 3.5). The featured results are consistent with the recent findings in acoustics and elastodynamics [75, 160, 85] which demonstrate that, at higher illumination frequencies, pronounced negative values of TS tend to localize in a narrow region *tracing the boundary* of a scatterer. However, in the present case $\check{\mathsf{T}}$ also exhibits a notable sensitivity to the fracture's interfacial condition; in particular, for the traction-free crack in Fig. 3.9(a), extreme negative values of the TS are localized in the vicinity of the *crack tip*, whereas in the case of fractures with interfacial stiffness – Fig. 3.9(b) and Fig. 3.10 – the TS exposes the *entire fracture surface*. These initial results suggest that at shorter wavelengths, the TS experiences a different type of sensitivity to the fracture interfacial condition, which may lead to a more detailed identification of the fracture's specific stiffnesses. Given a sensory data set that includes the scattered field measurements at both long and short wavelengths, one may consider a staggered approach where i) high-frequency data are deployed to more precisely evaluate the fracture geometry, including its location $\boldsymbol{z}$ and effective normal $\boldsymbol{n}$; ii) low-frequency observations are used as in Section 3.3 to qualitatively identify the interfacial condition, and iii) additional information is obtained on the fracture's interface thanks to the dependence

of the high-frequency TS thereon. Such developments, however, require high-frequency asymptotics of the scattered field due to a fracture with specific stiffness – a topic that is beyond the scope of this study.
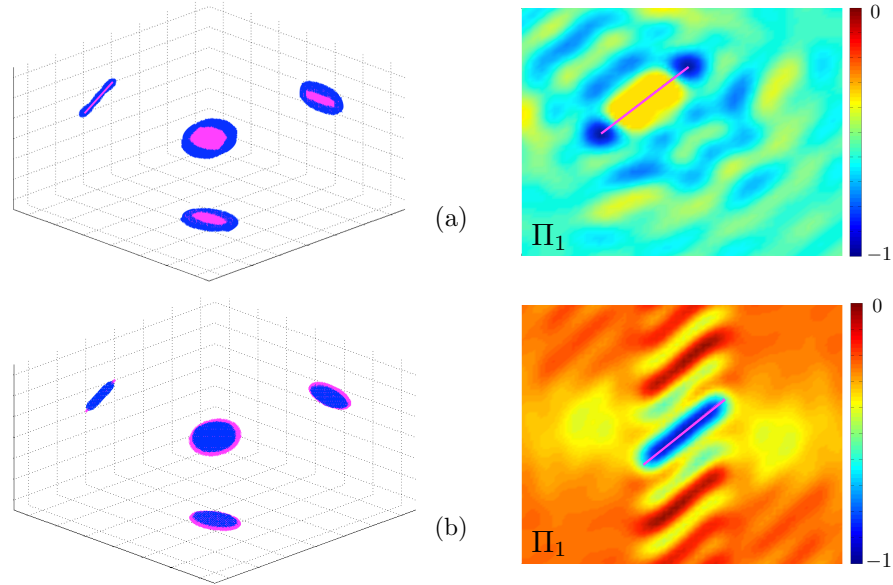
Figure 3.9: "High"-frequency $(\lambda_s/L \simeq 0.45)$ TS reconstruction of a penny-shaped fracture whose interfacial condition is (a) traction-free $(k_s = k_n = 0)$, and (b) isolated fluid-filled $(k_s = 2, k_n = 100)$.
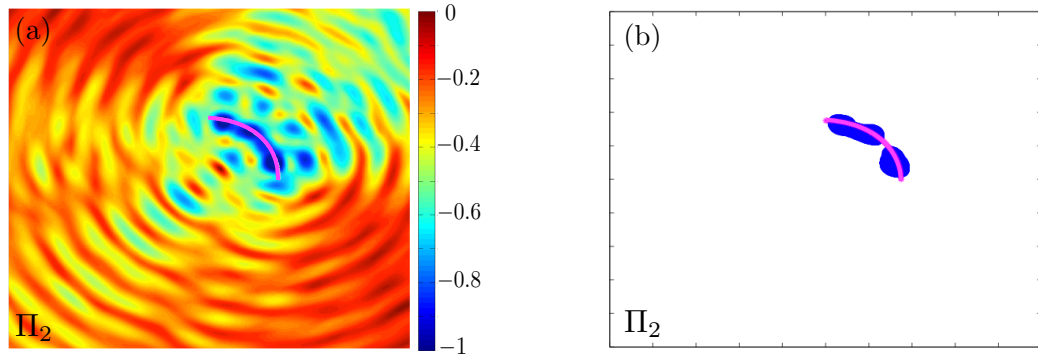
Figure 3.10: "High"-frequency $(\lambda_s/L \simeq 0.45)$ TS reconstruction of a cylindrical fracture with $k_n = k_s = 4$: (a) distribution of $\check{\mathsf{T}}$ in the fracture's mid-section, and (b) corresponding $\check{\mathsf{T}}$ map thresholded at 70%.

Chapter 4

Generalized Linear Sampling Method for elastic-wave sensing of heterogeneous fractures

This work aims to develop a non-iterative, full-waveform approach to 3D seismic imaging of fractures with non-trivial – generally heterogeneous and dissipative – interfacial condition, e.g. hydraulic fractures, on the basis of the Linear Sampling Method [57]. To this end, the sought indicator map – targeting *geometric* fracture reconstruction – is preferably (i) agnostic with respect to the fracture's interfacial condition, (ii) robust against measurement errors, and (iii) flexible in terms of sensing parameters, e.g. the illumination frequency. This is pursued by drawing from the theories of inverse scattering [47, 58] and, in particular, by building upon the Factorization Method (FM) [98, 41] and the recently developed Generalized Linear Sampling Method (GLSM) [11, 12] which completes the theoretical foundation of its LSM predecessor. First, the inverse problem is formulated in the frequency domain where the *illuminating wavefield* is described by the elastic Herglotz wave function [64] with its inherent compressional (P) and shear (S) wave components. On characterizing the induced *scattered wavefield* in terms of its far-field P- and S-wave patterns [109], the far-field operator F is then defined as a map from the Herglotz densities to the far-field observations of the scattered field. The

75

GLSM indicator functional is introduced as in [12] on the basis of (a) a custom factorization of the far-field operator, and (b) a sequence of approximate solutions to the LSM integral equation, seeking Herglotz densities whose far-field pattern matches that of the point-load solution radiating from a (trial) *sampling point.* The latter sequence is essentially a set of penalized least-squares misfit functionals – aimed at producing nearby solutions to the LSM equation, where the penalty term is constructed using a factorization component of F. Minimizing this class of cost functionals in their most general form requires an optimization procedure, i.e. iterations [12]. In the proposed approach, the latter difficulty is eluded by establishing the applicability of the $F_\sharp$-factorization method [98, 41] – as a suitable candidate for (a). This is accomplished thanks to the admissibility condition on the fracture's (linearized) contact parameters, obtained through the well-posedness analysis of the forward scattering problem. In this setting, it is shown that the use of $F_\sharp$-factorization gives rise to a sequence of *convex* GLSM cost functionals whose minimizers can be computed without iterations. Such minimizer is then used to construct a robust fracture indicator, whose performance is illustrated through a set of numerical experiments. For completeness, the results of the GLSM reconstruction are compared to those obtained by the classical linear sampling method (LSM).

4.1   Problem statement

With reference to Fig. 4.1(a), consider the elastic-wave sensing of a partially closed fracture $\Gamma \subset \mathbb{R}^3$ embedded in a homogeneous, isotropic, elastic solid endowed with mass density ρ and Lamé parameters μ and λ. The fracture is characterized by a heterogeneous contact condition synthesizing the spatially-varying nature of its rough and/or multi-phase interface. Next, let Ω denote the unit sphere centered at the origin. For a given triplet of vectors $\boldsymbol{d} \in \Omega$ and $\boldsymbol{q}_p, \boldsymbol{q}_s \in \mathbb{R}^3$ such that $\boldsymbol{q}_p \parallel \boldsymbol{d}$ and $\boldsymbol{q}_s \perp \boldsymbol{d}$, the obstacle is illuminated by a combination of compressional and shear plane waves

$$\boldsymbol{u}^{\mathrm{f}}(\boldsymbol{\xi}) \;=\; \boldsymbol{q}_p e^{\mathrm{i}k_p \boldsymbol{\xi} \cdot \boldsymbol{d}} \;+\; \boldsymbol{q}_s e^{\mathrm{i}k_s \boldsymbol{\xi} \cdot \boldsymbol{d}} \tag{4.1}$$

propagating in direction $\boldsymbol{d}$, where k_p and $k_s = k_p\sqrt{(\lambda+2\mu)/\mu}$ denote the respective wave numbers. The interaction of $\boldsymbol{u}^{\mathrm{f}}$ with Γ gives rise to the scattered field $\boldsymbol{v} \in H^1_{\mathrm{loc}}(\mathbb{R}^3 \backslash \Gamma)^3$,
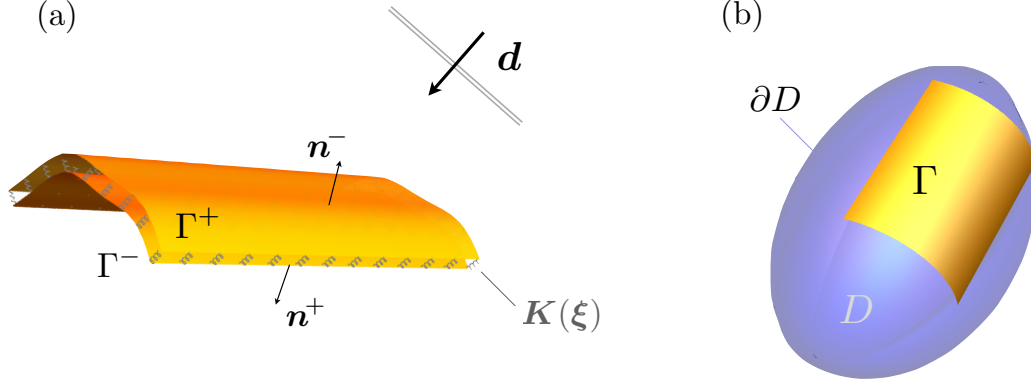
Figure 4.1: Direct scattering problem. The fracture boundary Γ is arbitrarily extended to a piecewise smooth, simply connected, closed surface ∂D of a bounded domain D.

solving

$$
\begin{aligned}
\nabla\!\cdot\!(\boldsymbol{C}\!:\!\nabla\boldsymbol{v}) + \rho\omega^2\boldsymbol{v} &= \boldsymbol{0} && \text{in} \quad \mathbb{R}^3\backslash\Gamma, \\
\boldsymbol{n}\cdot\boldsymbol{C}\!:\!\nabla\boldsymbol{v} &= \mathscr{L}(\llbracket\boldsymbol{v}\rrbracket) - \boldsymbol{t}^{\mathrm{f}} && \text{on} \quad \Gamma,
\end{aligned}
\tag{4.2}
$$

where $\omega^2 = k_s^2\mu/\rho$ is the frequency of excitation; $\llbracket\boldsymbol{v}\rrbracket = [\boldsymbol{v}^+ - \boldsymbol{v}^-]$ is the jump in $\boldsymbol{v}$ across Γ, hereon referred to as the fracture opening displacement (FOD);

$$
\boldsymbol{C} = \lambda\,\boldsymbol{I}_2\otimes\boldsymbol{I}_2 + 2\mu\,\boldsymbol{I}_4
\tag{4.3}
$$

is the fourth-order elasticity tensor; $\boldsymbol{I}_m\,(m=2,4)$ denotes the mth-order symmetric identity tensor; $\boldsymbol{t}^{\mathrm{f}} = \boldsymbol{n}\cdot\boldsymbol{C}\!:\!\nabla\boldsymbol{u}^{\mathrm{f}}$ is the free-field traction vector; $\boldsymbol{n} = \boldsymbol{n}^-$ is the unit normal on Γ, and $\mathscr{L} : H^{1/2}(\Gamma)^3 \to H^{-1/2}(\Gamma)^3$ represents a heterogeneous bijective contact law over the fracture surface, physically relating the displacement jump to surface traction. In many practical situations, the fracture's contact law is *linearized* about a dynamic equilibrium state as

$$
\mathscr{L}(\llbracket\boldsymbol{v}\rrbracket) = \boldsymbol{K}(\boldsymbol{\xi})\llbracket\boldsymbol{v}\rrbracket, \qquad \boldsymbol{\xi}\in\Gamma,
\tag{4.4}
$$

where $\boldsymbol{K} = \boldsymbol{K}(\boldsymbol{\xi})$ is a *symmetric* (due to reciprocity considerations) and possibly *complex-valued* matrix of specific stiffness coefficients.

Remark 5. *In what follows, the analysis is based on the linear contact condition (4.4)*

over Γ. Under the premise of bijectivity, most of the ensuing developments (except for the $F_\sharp$ factorization method) can be adapted to handle nonlinear contact laws; such extension, however, is beyond the scope of this study.

The formulation of the direct scattering problem can now be completed by requiring that $\boldsymbol{v}$ satisfies the Kupradze radiation condition at infinity [104]. On uniquely decomposing the scattered field into an irrotational part and a solenoidal part as $\boldsymbol{v} = \boldsymbol{v}^p + \boldsymbol{v}^s$ where

$$\boldsymbol{v}^p = \frac{1}{k_s^2 - k_p^2}(\Delta + k_s^2)\boldsymbol{v}, \qquad \boldsymbol{v}^s = \frac{1}{k_p^2 - k_s^2}(\Delta + k_p^2)\boldsymbol{v}, \tag{4.5}$$

the Kupradze condition can be stated as

$$\frac{\partial \boldsymbol{v}^p}{\partial r} - \mathrm{i}k_p \boldsymbol{v}^p = o(r^{-1}) \quad \text{and} \quad \frac{\partial \boldsymbol{v}^s}{\partial r} - \mathrm{i}k_s \boldsymbol{v}^s = o(r^{-1}) \qquad \text{as } r := |\boldsymbol{\xi}| \to \infty, \tag{4.6}$$

uniformly with respect to $\hat{\boldsymbol{\xi}} := \boldsymbol{\xi}/r$.

Dimensional platform. In what follows, all quantities are rendered *dimensionless* by taking ρ, μ, and R – the characteristic size of a region sampled for fractures – as the respective scales for mass density, elastic modulus, and length – which amounts to setting $\rho = \mu = \mathsf{R} = 1$ [20].

Function spaces. To assist the ensuing analysis, the fracture surface Γ is arbitrarily extended, as shown in Fig. 4.1(b), to a piecewise smooth, simply connected, closed surface ∂D of a bounded domain D such that the normal vector $\boldsymbol{n}$ to the fracture surface Γ coincides with the outward normal vector to ∂D – likewise denoted by $\boldsymbol{n}$. We also assume that Γ is an open set (relative to ∂D) with positive surface measure. Following [114], we define

$$\begin{aligned} H^{\pm\frac{1}{2}}(\Gamma) &:= \{f|_\Gamma : \ f \in H^{\pm\frac{1}{2}}(\partial D)\}, \\ \tilde{H}^{\pm\frac{1}{2}}(\Gamma) &:= \{f \in H^{\pm\frac{1}{2}}(\partial D) : \ \mathrm{supp}(f) \subset \overline{\Gamma}\}, \end{aligned} \tag{4.7}$$

and recall that $H^{-1/2}(\Gamma)$ and $\tilde{H}^{-1/2}(\Gamma)$ are respectively the dual spaces of $\tilde{H}^{1/2}(\Gamma)$ and

$H^{1/2}(\Gamma)$. Accordingly, the following embeddings hold

$$\tilde{H}^{\frac{1}{2}}(\Gamma) \subset H^{\frac{1}{2}}(\Gamma) \subset L^2(\Gamma) \subset \tilde{H}^{-\frac{1}{2}}(\Gamma) \subset H^{-\frac{1}{2}}(\Gamma). \tag{4.8}$$

Remark 6. *In the context of fracture mechanics, it is well known that $[\![\boldsymbol{v}]\!](\boldsymbol{\xi}) \to \boldsymbol{0}$ continuously as $\Gamma \ni \boldsymbol{\xi} \to \partial\Gamma$ (typically as d^α, $0 < \alpha \leqslant \frac{1}{2}$ [162] where d is a normal distance to $\partial\Gamma$ when $\partial\Gamma$ is smooth), which lends credence to the assumption $[\![\boldsymbol{v}]\!] \in \tilde{H}^{1/2}(\Gamma)^3$ used hereon.*

4.2 Well-posedness of the forward scattering problem

Serving as a prerequisite for the inverse scattering analysis, this section investigates the well-posedness of the direct scattering problem (4.2)–(4.6). Let $R > 0$ be sufficiently large so that the ball B_R of radius R contains Γ, and consider the Dirichlet-to-Neumann operator $\mathscr{T}_R : H^{1/2}(\partial B_R)^3 \to H^{-1/2}(\partial B_R)^3$ associated with the scattering problem in $\mathbb{R}^3 \backslash B_R$. Formally, one has

$$\mathscr{T}_R(\boldsymbol{\varphi})(\boldsymbol{\xi}) := \hat{\boldsymbol{\xi}} \cdot \boldsymbol{C} : \nabla\mathbf{u}_{\boldsymbol{\varphi}}(\boldsymbol{\xi}), \qquad \boldsymbol{\xi} \in \partial B_R,$$

where $\mathbf{u}_{\boldsymbol{\varphi}} \in H^1_{\mathrm{loc}}(\mathbb{R}^3 \backslash B_R)^3$ is the unique radiating solution, satisfying (4.6), of

$$
\begin{aligned}
\nabla \cdot (\boldsymbol{C} : \nabla\mathbf{u}_{\boldsymbol{\varphi}}) + \rho\omega^2\mathbf{u}_{\boldsymbol{\varphi}} &= \boldsymbol{0} & &\text{in} \quad \mathbb{R}^3 \backslash B_R, \\
\mathbf{u}_{\boldsymbol{\varphi}} &= \boldsymbol{\varphi} & &\text{on} \quad \partial B_R.
\end{aligned}
\tag{4.9}
$$

The scattering problem (4.2)–(4.6) can now be equivalently written in terms of $\boldsymbol{v} \in H^1(B_R \backslash \Gamma)^3$ as

$$
\begin{aligned}
\nabla \cdot (\boldsymbol{C} : \nabla\boldsymbol{v}) + \rho\omega^2\boldsymbol{v} &= \boldsymbol{0} & &\text{in} \quad \mathbb{R}^3 \backslash \Gamma, \\
\boldsymbol{n} \cdot \boldsymbol{C} : \nabla\boldsymbol{v} &= \boldsymbol{K} \cdot [\![\boldsymbol{v}]\!] - \boldsymbol{t}^{\mathrm{f}} & &\text{on} \quad \Gamma, \\
\boldsymbol{n} \cdot \boldsymbol{C} : \nabla\boldsymbol{v} &= \mathscr{T}_R(\boldsymbol{v}) & &\text{on} \quad \partial B_R,
\end{aligned}
\tag{4.10}
$$

where $\boldsymbol{n}(\boldsymbol{\xi}) = \hat{\boldsymbol{\xi}}$ on ∂B_R. This problem can be written variationally in terms of

$\boldsymbol{v} \in H^1(\mathscr{B}_2 \backslash \Gamma)^3$ as

$$-\rho\omega^2 \int_{\mathscr{B}_2\backslash\Gamma} \overline{\boldsymbol{w}} \cdot \boldsymbol{v} \, \mathrm{d}V_{\boldsymbol{\xi}} \;+\; \int_{\mathscr{B}_2\backslash\Gamma} \nabla\overline{\boldsymbol{w}} : \boldsymbol{C} : \nabla\boldsymbol{v} \, \mathrm{d}V_{\boldsymbol{\xi}} \;+\; \langle \boldsymbol{K} \cdot [\![\boldsymbol{v}]\!], [\![\boldsymbol{w}]\!] \rangle_{\Gamma} \; - $$

$$\langle \mathscr{T}_R(\boldsymbol{v}), \boldsymbol{w} \rangle_{\partial B_R} \;=\; \int_{\Gamma} \overline{[\![\boldsymbol{w}]\!]} \cdot \boldsymbol{t}^{\mathrm{f}} \, \mathrm{d}S_{\boldsymbol{\xi}}, \qquad \forall \boldsymbol{w} \in H^1(\mathscr{B}_2\backslash\Gamma)^3, \tag{4.11}$$

where $\langle \cdot, \cdot \rangle_{\Gamma}$ and $\langle \cdot, \cdot \rangle_{\partial B_R}$ denote respectively the $\langle H^{-1/2}(\Gamma)^3, \tilde{H}^{1/2}(\Gamma)^3 \rangle$ and $\langle H^{-1/2}(\partial B_R)^3, H^{1/2}(\partial B_R)^3 \rangle$ *duality products* that extend L^2 inner products. For simplicity, we will also use a short-hand notation for the vector norms where e.g. $\| \cdot \|_{H^{1/2}(\Gamma)^3}$ is written as $\| \cdot \|_{H^{1/2}(\Gamma)}$ and so on. In this setting, the analysis of the forward scattering problem is based on the following properties of the Dirichlet-to-Neumann operator $\mathscr{T}_R$ (see also [44]).

Lemma 4.2.1. *There exists a bounded, non-negative and self-adjoint operator* $\mathscr{T}_R^0 :$ $H^{1/2}(\partial B_R)^3 \to H^{-1/2}(\partial B_R)^3$ *such that* $\mathscr{T}_R + \mathscr{T}_R^0 : H^{1/2}(\partial B_R)^3 \to H^{-1/2}(\partial B_R)^3$ *is compact. Moreover,*

$$\Im \langle \mathscr{T}_R(\boldsymbol{\varphi}), \boldsymbol{\varphi} \rangle_{\partial B_R} > 0 \qquad \forall \boldsymbol{\varphi} \in H^{1/2}(\partial B_R)^3 : \; \boldsymbol{\varphi} \neq 0. \tag{4.12}$$

Proof. Let $R_\circ > R$ and $\boldsymbol{\varphi}, \boldsymbol{\psi} \in H^{1/2}(\partial B_R)^3$. Multiplying the first equation in (4.9) by $\overline{\mathbf{u}_{\boldsymbol{\psi}}}$ and integrating by parts on $B_{R_\circ} \backslash B_R$ yields

$$\langle \mathscr{T}_R(\boldsymbol{\varphi}), \boldsymbol{\psi} \rangle_{\partial B_R} \;=\; \rho\omega^2 \int_{B_{R_\circ}\backslash B_R} \overline{\mathbf{u}_{\boldsymbol{\psi}}} \cdot \mathbf{u}_{\boldsymbol{\varphi}} \, \mathrm{d}V_{\boldsymbol{\xi}} \;- $$

$$\int_{B_{R_\circ}\backslash B_R} \nabla\overline{\mathbf{u}_{\boldsymbol{\psi}}} : \boldsymbol{C} : \nabla\mathbf{u}_{\boldsymbol{\varphi}} \, \mathrm{d}V_{\boldsymbol{\xi}} \;+\; \int_{\partial B_{R_\circ}} \overline{\mathbf{u}_{\boldsymbol{\psi}}} \cdot \boldsymbol{t}(\boldsymbol{\varphi}) \, \mathrm{d}S_{\boldsymbol{\xi}},$$

where $\boldsymbol{t}(\boldsymbol{\varphi})(\boldsymbol{\xi}) := \hat{\boldsymbol{\xi}} \cdot \boldsymbol{C} : \nabla\mathbf{u}_{\boldsymbol{\varphi}}(\boldsymbol{\xi})$ for $\boldsymbol{\xi} \in \partial B_{R_\circ}$. Using the well-posedness of (4.9) and the Riesz representation theorem, we define $\mathscr{T}_R^0$ by

$$\left\langle \mathscr{T}_R^0(\boldsymbol{\varphi}), \boldsymbol{\psi} \right\rangle_{\partial B_R} := \int_{B_{R_\circ}\backslash B_R} \nabla\overline{\mathbf{u}_{\boldsymbol{\psi}}} : \boldsymbol{C} : \nabla\mathbf{u}_{\boldsymbol{\varphi}} \, \mathrm{d}V_{\boldsymbol{\xi}}.$$

On demonstrating that $\|(\mathscr{T}_R + \mathscr{T}_R^0)(\boldsymbol{\varphi})\|_{H^{-1/2}(\Gamma)} \leqslant C(\|\mathbf{u}_{\boldsymbol{\varphi}}\|_{L^2(B_{R_\circ}\backslash B_R)} + \|\boldsymbol{t}(\boldsymbol{\varphi})\|_{L^2(\partial B_{R_\circ})})$ for some constant $C > 0$ independent of $\boldsymbol{\varphi}$, the compactness of $\mathscr{T}_R + \mathscr{T}_R^0$ then follows from the compactness of mapping $\boldsymbol{\varphi} \to \mathbf{u}_{\boldsymbol{\varphi}}$ (resp. $\boldsymbol{\varphi} \to \boldsymbol{t}(\boldsymbol{\varphi})$) from $H^{1/2}(\partial B_R)$

into $L^2(B_{R_\circ}\backslash B_R)$ (resp. $L^2(\partial B_{R_\circ})$) thanks to the compact embedding of $H^1(B_{R_\circ}\backslash B_R)$ into $L^2(B_{R_\circ}\backslash B_R)$ and the standard regularity results for scattering problems [114], which can be recovered from the boundary integral representation of $\mathbf{u}_{\boldsymbol{\varphi}}$ in $\mathbb{R}^3\backslash B_R$ in terms of boundary data on ∂B_R. As shown in H, the sign of the imaginary part of $\mathscr{T}_R$ is a consequence of the asymptotic behavior of $\mathbf{u}_{\boldsymbol{\varphi}}$ at infinity [104] which implies

$$
\begin{aligned}
\Im\left\langle\mathscr{T}_R(\boldsymbol{\varphi}),\boldsymbol{\varphi}\right\rangle_{\partial B_R} &= \Im\lim_{R_\circ\to\infty}\int_{\partial B_{R_\circ}}\overline{\mathbf{u}_{\boldsymbol{\varphi}}}\cdot\mathbf{t}(\boldsymbol{\varphi})\,\mathrm{d}S_{\boldsymbol{\xi}} \\
&= \lim_{R_\circ\to\infty}\int_{\partial B_{R_\circ}}\left\{k_p(\lambda+2\mu)|\mathbf{u}_{\boldsymbol{\varphi}}^{\mathrm{p}}|^2 + k_s\mu|\mathbf{u}_{\boldsymbol{\varphi}}^{\mathrm{s}}|^2\right\}\,\mathrm{d}S_{\boldsymbol{\xi}}.
\end{aligned}
\tag{4.13}
$$

The sign-definiteness of the imaginary part is a consequence of the Rellich lemma [58] applied to $\mathbf{u}_{\boldsymbol{\varphi}}^{\mathrm{p}}$ and $\mathbf{u}_{\boldsymbol{\varphi}}^{\mathrm{s}}$, which requires that $\mathbf{u}_{\boldsymbol{\varphi}}=\mathbf{u}_{\boldsymbol{\varphi}}^{\mathrm{p}}+\mathbf{u}_{\boldsymbol{\varphi}}^{\mathrm{s}}=0$ whenever $\Im\left\langle\mathscr{T}_R(\boldsymbol{\varphi}),\boldsymbol{\varphi}\right\rangle_{\partial B_R}=0$. $\qquad\square$

Theorem 4.2.2. *Assume that $\boldsymbol{t}^f\in H^{-1/2}(\Gamma)^3$ and that $\boldsymbol{K}\in L^\infty(\Gamma)^{3\times 3}$ is symmetric such that $\Im\boldsymbol{K}\leqslant\boldsymbol{0}$ on Γ, i.e. that $\overline{\boldsymbol{\theta}}\cdot\Im\boldsymbol{K}(\boldsymbol{\xi})\cdot\boldsymbol{\theta}\leqslant 0$, $\forall\boldsymbol{\theta}\in\mathbb{C}^3$ and a.e. on Γ. Then problem (4.11) has a unique solution that continuously depends on $\boldsymbol{t}^f\in H^{-1/2}(\Gamma)^3$.*

Proof. Since $\boldsymbol{t}^{\mathrm{f}}\in H^{-1/2}(\Gamma)$, the antilinear form $\int_\Gamma\overline{[\![\boldsymbol{w}]\!]}\cdot\boldsymbol{t}^{\mathrm{f}}\,\mathrm{d}S_{\boldsymbol{\xi}}$ may be understood as a duality pairing $\langle\cdot,\cdot\rangle_\Gamma$. The continuity of this form comes from the continuity of the trace mapping $\boldsymbol{w}\to[\![\boldsymbol{w}]\!]$ from $H^1(\mathscr{B}_2\backslash\Gamma)^3$ into $\tilde{H}^{1/2}(\Gamma)^3$.

On the basis of the adopted dimensional platform i.e. $\rho=\mu=1$ (see Section 4.1), the sesquilinear form on the left hand side of (4.11) can be decomposed into a coercive part

$$
\begin{aligned}
\mathrm{A}(\boldsymbol{v},\boldsymbol{w}) &= \int_{\mathscr{B}_2\backslash\Gamma}\overline{\boldsymbol{w}}\cdot\boldsymbol{v}\,dV_{\boldsymbol{\xi}} + \int_{\mathscr{B}_2\backslash\Gamma}\nabla\overline{\boldsymbol{w}}:\boldsymbol{C}:\nabla\boldsymbol{v}\,dV_{\boldsymbol{\xi}} + \\
&\quad + \left\langle\mathscr{T}_R^0(\boldsymbol{v}),\boldsymbol{w}\right\rangle_{\partial B_R}, \qquad\forall\boldsymbol{w}\in H^1(\mathscr{B}_2\backslash\Gamma)^3,
\end{aligned}
\tag{4.14}
$$

and a compact part

$$
\begin{aligned}
\mathrm{B}(\boldsymbol{v},\boldsymbol{w}) &= -(1+k_s^2)\int_{\mathscr{B}_2\backslash\Gamma}\overline{\boldsymbol{w}}\cdot\boldsymbol{v}\,dV_{\boldsymbol{\xi}} + \left\langle\boldsymbol{K}\cdot[\![\boldsymbol{v}]\!],[\![\boldsymbol{w}]\!]\right\rangle_\Gamma - \\
&\quad - \left\langle(\mathscr{T}_R+\mathscr{T}_R^0)(\boldsymbol{v}),\boldsymbol{w}\right\rangle_{\partial B_R}, \qquad\forall\boldsymbol{w}\in H^1(\mathscr{B}_2\backslash\Gamma)^3.
\end{aligned}
\tag{4.15}
$$

The coercivity of $\mathrm{A}(\boldsymbol{v},\boldsymbol{w})$ follows from the Korn inequality [114] and the non negative

sign of $\mathscr{T}_R^0$ (Lemma 4.2.1). Now, in order to prove that the antilinear form B defines a compact perturbation of $A(\boldsymbol{v}, \boldsymbol{w})$, one may observe that

$$|\mathrm{B}(\boldsymbol{v}, \boldsymbol{w})| \;\leqslant\; \mathrm{c}_2 \left\{ \|\boldsymbol{v}\|_{L^2(\mathscr{B}_2\backslash\Gamma)} \|\boldsymbol{w}\|_{L^2(\mathscr{B}_2\backslash\Gamma)} \;+\; \|[\![\boldsymbol{v}]\!]\|_{L^2(\Gamma)} \|[\![\boldsymbol{w}]\!]\|_{L^2(\Gamma)} \right\} \;+$$
$$\|(\mathscr{T}_R + \mathscr{T}_R^0)(\boldsymbol{v})\|_{H^{-1/2}(\partial B_R)} \|\boldsymbol{w}\|_{H^{1/2}(\partial B_R)}$$

for a constant c_2 independent of $\boldsymbol{v}$ and $\boldsymbol{w}$. The claim then follows from Lemma 4.2.1, the compact embedding of $H^1(\mathscr{B}_2\backslash\Gamma)$ into $L^2(\mathscr{B}_2\backslash\Gamma)$ and the compactness of the trace operator $\boldsymbol{v} \to [\![\boldsymbol{v}]\!]$ as an application from $H^1(\mathscr{B}_2\backslash\Gamma)$ into $L^2(\Gamma)$ where the latter comes from the compact embedding of $\tilde{H}^{1/2}(\Gamma)$ into $L^2(\Gamma)$.

Problem (4.11) is then of Fredholm type, and is therefore well-posed as soon as the uniqueness of a solution is guaranteed. Assume that $\boldsymbol{t}^{\mathrm{f}} = 0$. Then

$$\Im \left\langle \mathscr{T}_R(\boldsymbol{v}), \boldsymbol{v} \right\rangle_{\partial B_R} \;=\; \left\langle \Im \boldsymbol{K} \cdot [\![\boldsymbol{v}]\!], [\![\boldsymbol{v}]\!] \right\rangle_\Gamma \;\leqslant\; 0$$

by premise of the Theorem. Thanks to Lemma 4.2.1, this requires that $\boldsymbol{v} = \boldsymbol{0}$ on ∂B_R and thus $\boldsymbol{v} = \boldsymbol{0}$ in $\mathscr{B}_2\backslash\Gamma$ by the unique continuation principle. $\qquad\square$

4.3   Elements of the inverse scattering solution

This section is devoted to the introduction of the *far-field operator* – relevant to the scattering problem (4.2), and the derivation of its first and second factorizations. In the sequel, we assume that the hypotheses of Theorem 4.2.2 hold.

Elastic Herglotz wave function.   For given density $\boldsymbol{g} \in L^2(\Omega)^3$, we consider the unique decomposition

$$\boldsymbol{g} \;:=\; \boldsymbol{g}_p \oplus \boldsymbol{g}_s \tag{4.16}$$

such that $\boldsymbol{g}_p(\boldsymbol{d}) \,\|\, \boldsymbol{d}$ and $\boldsymbol{g}_s(\boldsymbol{d}) \perp \boldsymbol{d}$, $\boldsymbol{d} \in \Omega$. In dyadic notation, one has

$$\boldsymbol{g}_p(\boldsymbol{d}) := (\boldsymbol{d} \otimes \boldsymbol{d}) \cdot \boldsymbol{g}(\boldsymbol{d}) \quad \text{and} \quad \boldsymbol{g}_s(\boldsymbol{d}) := (\boldsymbol{I} - \boldsymbol{d} \otimes \boldsymbol{d}) \cdot \boldsymbol{g}(\boldsymbol{d}). \tag{4.17}$$

Next, we define the elastic Herglotz wave function [64] as

$$\mathbf{u}_{\boldsymbol{g}}(\boldsymbol{\xi}) \;:=\; \int_\Omega \boldsymbol{g}_p(\boldsymbol{d}) \, e^{\mathrm{i}k_p \boldsymbol{d}\cdot\boldsymbol{\xi}} \, \mathrm{d}S_{\boldsymbol{d}} \;+\; \int_\Omega \boldsymbol{g}_s(\boldsymbol{d}) \, e^{\mathrm{i}k_s \boldsymbol{d}\cdot\boldsymbol{\xi}} \, \mathrm{d}S_{\boldsymbol{d}}, \qquad \boldsymbol{\xi} \in \mathbb{R}^3 \tag{4.18}$$

in terms of the compressional and shear wave densities $\boldsymbol{g}_p$ and $\boldsymbol{g}_s$.

The far-field pattern. As shown in [109], any scattered wave $\boldsymbol{v} \in H^1_{\text{loc}}(\mathbb{R}^3\backslash\Gamma)^3$ solving (4.2)-(4.6) has the asymptotic expansion

$$\boldsymbol{v}(\boldsymbol{\xi}) = \frac{e^{\mathrm{i}k_p r}}{4\pi(\lambda+2\mu)r}\,\boldsymbol{v}_p^\infty(\hat{\boldsymbol{\xi}}) + \frac{e^{\mathrm{i}k_s r}}{4\pi\mu r}\,\boldsymbol{v}_s^\infty(\hat{\boldsymbol{\xi}}) + O(r^{-2}) \quad \text{as} \quad r := |\boldsymbol{\xi}| \to \infty, \quad (4.19)$$

where $\hat{\boldsymbol{\xi}}$ is the unit direction of observation, while $\boldsymbol{v}_p^\infty$ and $\boldsymbol{v}_s^\infty$ denote respectively the far-field patterns of $\boldsymbol{v}^p$ and $\boldsymbol{v}^s$ – see (4.5), which satisfy $\boldsymbol{v}_p^\infty \parallel \hat{\boldsymbol{\xi}}$ and $\boldsymbol{v}_s^\infty \perp \hat{\boldsymbol{\xi}}$. In this setting, we define the far-field pattern of $\boldsymbol{v}$ by

$$\boldsymbol{v}^\infty := \boldsymbol{v}_p^\infty \oplus \boldsymbol{v}_s^\infty. \quad (4.20)$$

By way of the integral representation theorem in elastodynamics [33] and the far-field expansion of the elastodynamic fundamental stress tensor (see I), one can show that if $\boldsymbol{v} \in H^1_{\text{loc}}(\mathbb{R}^3\backslash\Gamma)^3$ satisfies (4.2)-(4.6), then

$$\begin{aligned}
\boldsymbol{v}_p^\infty(\hat{\boldsymbol{\xi}}) &= -\,\mathrm{i}k_p\hat{\boldsymbol{\xi}} \int_\Gamma \left\{ \lambda\,[\![\boldsymbol{v}]\!]\cdot\boldsymbol{n} + 2\mu(\boldsymbol{n}\cdot\hat{\boldsymbol{\xi}})\,[\![\boldsymbol{v}]\!]\cdot\hat{\boldsymbol{\xi}} \right\} e^{-\mathrm{i}k_p\hat{\boldsymbol{\xi}}\cdot\boldsymbol{x}}\,\mathrm{d}S_{\boldsymbol{x}}, \\
\boldsymbol{v}_s^\infty(\hat{\boldsymbol{\xi}}) &= -\,\mathrm{i}k_s\hat{\boldsymbol{\xi}} \times \int_\Gamma \left\{ \mu([\![\boldsymbol{v}]\!]\times\hat{\boldsymbol{\xi}})(\boldsymbol{n}\cdot\hat{\boldsymbol{\xi}}) + \mu(\boldsymbol{n}\times\hat{\boldsymbol{\xi}})([\![\boldsymbol{v}]\!]\cdot\hat{\boldsymbol{\xi}}) \right\} e^{-\mathrm{i}k_s\hat{\boldsymbol{\xi}}\cdot\boldsymbol{x}}\,\mathrm{d}S_{\boldsymbol{x}}.
\end{aligned} \quad (4.21)$$

The far-field operator.

Definition 1. *We define the far-field operator $F : L^2(\Omega)^3 \to L^2(\Omega)^3$ by*

$$F(\boldsymbol{g}) = \boldsymbol{v}_{g_\Omega}^\infty, \quad (4.22)$$

where $\boldsymbol{v}_{g_\Omega}^\infty$ is the far-field pattern (4.20) of $\boldsymbol{v} \in H^1_{\text{loc}}(\mathbb{R}^3\backslash\Gamma)^3$ solving (4.2)-(4.6) with data $\boldsymbol{u}^f = \mathbf{u}_{\boldsymbol{g}}$, see (4.18).

When the contact law $\mathcal{L}([\![\boldsymbol{v}]\!])$ on Γ is linear as in (4.4), the far-field operator can be expressed as a linear integral operator. To examine this case, consider an incident plane wave (4.1) propagating in direction $\boldsymbol{d} \in \Omega$ with amplitude $\boldsymbol{q} = \boldsymbol{q}_p \oplus \boldsymbol{q}_s$, and denote the induced far-field pattern (4.20) by $\boldsymbol{v}_{\boldsymbol{q}}^\infty(\boldsymbol{d},\cdot) = \boldsymbol{v}_{\boldsymbol{q}_p}^\infty \oplus \boldsymbol{v}_{\boldsymbol{q}_s}^\infty$. Next, let us define the far-field

kernel $\boldsymbol{W}^\infty(\boldsymbol{d}, \hat{\boldsymbol{\xi}}) \in \mathbb{C}^{6\times 6}$ so that

$$\boldsymbol{W}^\infty(\boldsymbol{d}, \hat{\boldsymbol{\xi}}) \cdot \boldsymbol{q} \; := \; \boldsymbol{v}_{\boldsymbol{q}}^\infty(\boldsymbol{d}, \hat{\boldsymbol{\xi}}). \tag{4.23}$$

Then one easily verifies that

$$F(\boldsymbol{g})(\hat{\boldsymbol{\xi}}) \; = \; \int_\Omega \boldsymbol{W}^\infty(\boldsymbol{d}, \hat{\boldsymbol{\xi}}) \cdot \boldsymbol{g}(\boldsymbol{d}) \; \mathrm{d}S_{\boldsymbol{d}}. \tag{4.24}$$

Lemma 4.3.1. *The far-field kernel* $\boldsymbol{W}^\infty(\boldsymbol{d}, \hat{\boldsymbol{\xi}})$ *satisfies the reciprocity identity*

$$\boldsymbol{W}^\infty(\boldsymbol{d}, \hat{\boldsymbol{\xi}}) \; = \; \overline{\boldsymbol{W}^{\infty*}}(-\hat{\boldsymbol{\xi}}, -\boldsymbol{d}), \qquad \forall \boldsymbol{d}, \hat{\boldsymbol{\xi}} \in \Omega. \tag{4.25}$$

Proof. See J. $\qquad\square$

4.4 Key properties for the application of sampling methods

Factorization of the far-field operator F**.** Consider the Herglotz operator $\mathscr{H}: L^2(\Omega)^3 \to H^{-1/2}(\Gamma)^3$ given by

$$\mathscr{H}(\boldsymbol{g}) \; := \; \boldsymbol{n} \cdot \boldsymbol{C} : \nabla \mathbf{u}_{\boldsymbol{g}} \qquad \text{on} \quad \Gamma, \tag{4.26}$$

where $\mathbf{u}_{\boldsymbol{g}}$ is the Herglotz wave function (4.18). Next, define $\mathscr{G}: H^{-1/2}(\Gamma)^3 \to L^2(\Omega)^3$ as the map taking the traction vector $\boldsymbol{t}^\mathrm{f}$ over Γ to the far-field pattern, $\boldsymbol{v}^\infty$, of $\boldsymbol{v} \in H^1_{\mathrm{loc}}(\mathbb{R}^3 \backslash \Gamma)^3$ satisfying (4.2)-(4.6). Then from Definition 1, the far-field operator (4.22) becomes

$$F \; = \; \mathscr{G}\mathscr{H}. \tag{4.27}$$

Lemma 4.4.1. *With reference to decomposition* (4.20)*, the adjoint Herglotz operator* $\mathscr{H}^*: \tilde{H}^{1/2}(\Gamma)^3 \to L^2(\Omega)^3$ *takes the form*

$$\mathscr{H}^*(\boldsymbol{a})(\hat{\boldsymbol{\xi}}) \; = \; -\left(\mathrm{i}k_p\, \hat{\boldsymbol{\xi}} \int_\Gamma \{\lambda(\boldsymbol{a}\cdot\boldsymbol{n}) + 2\mu\,(\boldsymbol{n}\cdot\hat{\boldsymbol{\xi}})(\boldsymbol{a}\cdot\hat{\boldsymbol{\xi}})\}\, e^{-\mathrm{i}k_p\hat{\boldsymbol{\xi}}\cdot\boldsymbol{y}} \; dS_{\boldsymbol{y}} \right.$$
$$\left. \oplus \mathrm{i}k_s\, \hat{\boldsymbol{\xi}} \times \int_\Gamma \{\mu\,(\boldsymbol{a} \times \hat{\boldsymbol{\xi}})(\boldsymbol{n}\cdot\hat{\boldsymbol{\xi}}) + \mu\,(\boldsymbol{n} \times \hat{\boldsymbol{\xi}})(\boldsymbol{a}\cdot\hat{\boldsymbol{\xi}})\}\, e^{-\mathrm{i}k_s\hat{\boldsymbol{\xi}}\cdot\boldsymbol{y}} \; dS_{\boldsymbol{y}} \right). \tag{4.28}$$

Proof. see K. $\qquad\square$

On the basis of (4.21) and (4.28), map $\mathscr{G}$ can be further decomposed as $\mathscr{G} = \mathscr{H}^* T$ where the middle operator $T\colon H^{-1/2}(\Gamma)^3 \to \tilde{H}^{1/2}(\Gamma)^3$ is given by

$$T(\boldsymbol{t}^{\mathrm{f}})(\boldsymbol{\xi}) \; := \; [\![\boldsymbol{v}(\boldsymbol{\xi})]\!], \qquad \boldsymbol{\xi} \in \Gamma \tag{4.29}$$

such that $\boldsymbol{v} \in H^1_{\mathrm{loc}}(\mathbb{R}^3\backslash\Gamma)^3$ satisfies (4.2)-(4.6) or equivalently (4.11). Thanks to this new decomposition of $\mathscr{G}$, a second factorization of $F\colon L^2(\Omega)^3 \to L^2(\Omega)^3$ is obtained as

$$F \; = \; \mathscr{H}^* T \mathscr{H}, \tag{4.30}$$

which provides the key ingredient for the ensuing analysis.

Properties of the Herglotz operator $\mathscr{H}$.

Lemma 4.4.2. *Operator $\mathscr{H}^* : \tilde{H}^{1/2}(\Gamma)^3 \to L^2(\Omega)^3$ in Lemma 4.4.1 is compact and injective.*

Proof. Integral operator $\mathscr{H}^*$ has a smooth kernel and is therefore compact from $\tilde{H}^{1/2}(\Gamma)^3$ into $L^2(\Omega)^3$. Next, suppose that there exists $\boldsymbol{a} \in \tilde{H}^{1/2}(\Gamma)^3$ such that $\mathscr{H}^*(\boldsymbol{a}) = \boldsymbol{0}$. On the basis of (4.19), (4.21) and (4.28), one finds that $\mathscr{H}^*$ is nothing else but the far-field operator stemming from the double-layer potential

$$\boldsymbol{V}(\boldsymbol{a})(\boldsymbol{\xi}) \; = \; \int_\Gamma \boldsymbol{a}(\boldsymbol{y})\!\cdot\!\boldsymbol{T}(\boldsymbol{\xi},\boldsymbol{y})\,\mathrm{d}S_{\boldsymbol{y}}, \qquad \boldsymbol{T}(\boldsymbol{\xi},\boldsymbol{y}) \; = \; \boldsymbol{n}(\boldsymbol{y})\!\cdot\!\boldsymbol{\Sigma}(\boldsymbol{\xi},\boldsymbol{y}), \qquad \boldsymbol{\xi} \in \mathscr{B}_2\backslash\Gamma, \tag{4.31}$$

where $\boldsymbol{\Sigma}(\boldsymbol{\xi},\boldsymbol{y})$ is the (third-order) elastodynamic fundamental stress tensor, see I. Thanks to definition (4.19), the vanishing far-field pattern of $\boldsymbol{V}(\boldsymbol{a})$ implies, by the Rellich Lemma and the unique continuation principle, that $\boldsymbol{V}(\boldsymbol{a}) = \boldsymbol{0}$ in $\mathbb{R}^3\backslash\Gamma$. Owing to the fundamental jump property of double-layer potentials by which $[\![\boldsymbol{V}]\!] = \boldsymbol{a}$, one obtains $\boldsymbol{a} = \boldsymbol{0}$ which guarantees the injectivity of $\mathscr{H}^*$. $\qquad\square$

One additional property that is needed for the analysis of the sampling methods is the densness of the range of $\mathscr{H}^*$, i.e. the injectivity of $\mathscr{H}$. Unfortunately the latter cannot be guaranteed in general, and one needs to impose this property as an assumption on Γ and ω.

Assumption 1. *We assume that Γ and ω are such that the Herglotz operator $\mathscr{H}$: $L^2(\Omega)^3 \to H^{-1/2}(\Gamma)^3$ is injective, i.e. that $\mathscr{H}^*: \tilde{H}^{1/2}(\Gamma)^3 \to L^2(\Omega)^3$ has a dense range.*

The following lemma indicates why we expect that for a given fracture geometry Γ, Assumption 1 holds for all $\omega > 0$ possibly excluding a discrete set of values without finite accumulation points.

Lemma 4.4.3. *Assume that Γ contains $M \geqslant 1$ (possibly disjoint) analytic surfaces $\Gamma_m \subset \Gamma$, $m = 1, \ldots M$, and consider the unique analytic continuation ∂D_m of Γ_m identifying "interior" domain $D_m \subset \mathbb{R}^3$. Then Assumption 1 holds as soon as for any such m, $\omega > 0$ is not a "Neumann" eigenfrequency of the Navier equation in D_m, i.e. as long as every function $\mathbf{u} \in H^1(D_m)^3$ satisfying*

$$
\begin{aligned}
\nabla \cdot (\boldsymbol{C} : \nabla \mathbf{u}) + \rho \omega^2 \mathbf{u} &= \mathbf{0} && \text{in } D_m, \\
\boldsymbol{n} \cdot \boldsymbol{C} : \nabla \mathbf{u} &= \mathbf{0} && \text{on } \partial D_m
\end{aligned}
\tag{4.32}
$$

vanishes identically in D_m. Further if D_m is bounded, the real eigenfrequencies of (4.32) form a discrete set.

Proof. Let Γ_m denote the mth analytic piece of Γ. Recalling (4.18) and invoking the analyticity of $\boldsymbol{n} \cdot \boldsymbol{C} : \nabla \mathbf{u}_g$ with respect to the surface coordinates on ∂D_m, we deduce that if $\boldsymbol{n} \cdot \boldsymbol{C} : \nabla \mathbf{u}_g = \mathbf{0}$ on $\Gamma_m \subset \partial D_m$ then

$$
\boldsymbol{n} \cdot \boldsymbol{C} : \nabla \mathbf{u}_g = \mathbf{0} \quad \text{on } \partial D_m.
$$

This means that $\mathbf{u}_g = \mathbf{0}$ in D_m since ω is not a "Neumann" eigenvalue of the Navier equation in D_m. The unique continuation principle then implies that $\mathbf{u}_g = \mathbf{0}$ in $\mathbb{R}^3$. Accordingly, we deduce that the Herglotz density vanishes, i.e. that $\boldsymbol{g} = \mathbf{0}$ as in the scalar case [58]. The proof of discreteness of the set of real eigenfrequencies characterizing (4.32) when D_m is bounded can be found in [104], Chapter 7, Theorem 1.4. $\qquad\square$

Properties of the middle operator T.

Lemma 4.4.4. *Operator $T: H^{-1/2}(\Gamma)^3 \to \tilde{H}^{1/2}(\Gamma)^3$ in (4.29) is bounded and satisfies*

$$
\Im \langle \boldsymbol{\varphi}, T\boldsymbol{\varphi} \rangle_\Gamma < 0 \qquad \forall \boldsymbol{\varphi} \in H^{-1/2}(\Gamma)^3 : \ \boldsymbol{\varphi} \neq \mathbf{0}.
\tag{4.33}
$$

Proof. The boundedness of T stems from the well-posedness of problem (4.11) and classical trace theorems. Next, let $\boldsymbol{\varphi} \in H^{-1/2}(\Gamma)^3$ and consider $\boldsymbol{v}$ satisfying (4.11) with $\boldsymbol{t}^{\mathrm{f}} = \boldsymbol{\varphi}$. Taking $\boldsymbol{w} = \boldsymbol{v}$ in (4.11) we get

$$\Im \langle \boldsymbol{\varphi}, T\boldsymbol{\varphi} \rangle_\Gamma \;=\; \langle \Im \boldsymbol{K} \cdot [\![\boldsymbol{v}]\!], [\![\boldsymbol{v}]\!] \rangle_\Gamma - \Im \langle \mathscr{T}_R(\boldsymbol{v}), \boldsymbol{v} \rangle_{\partial B_R}. \tag{4.34}$$

By virtue of (4.34), the claim of the theorem follows immediately from Lemma 4.2.1 and the earlier hypothesis that $\Im \boldsymbol{K} < 0$. $\qquad\square$

Lemma 4.4.5. *Operator $T\colon H^{-1/2}(\Gamma)^3 \to \tilde{H}^{1/2}(\Gamma)^3$ can be decomposed into a compact part T_c and a coercive and self-adjoint part T_o such that $T = \mathsf{T}_c + \mathsf{T}_o$. The coercive part $\mathsf{T}_o\colon H^{-1/2}(\Gamma)^3 \to \tilde{H}^{1/2}(\Gamma)^3$ is defined by*

$$\mathsf{T}_o(\boldsymbol{\varphi}) \;:=\; [\![\boldsymbol{u}^o]\!] \quad on \;\; \Gamma, \tag{4.35}$$

where $\boldsymbol{u}^o \in H^1(\mathscr{B}_2 \backslash \Gamma)$ is a solution to

$$A(\boldsymbol{u}^o, \boldsymbol{w}) = \langle \boldsymbol{\varphi}, [\![\boldsymbol{w}]\!] \rangle_\Gamma \qquad \forall \boldsymbol{w} \in H^1(\mathscr{B}_2 \backslash \Gamma)^3, \tag{4.36}$$

with A being the coercive sesquilinear form given by (4.14).

Proof. We first observe from (4.14) that

$$\begin{aligned}
\nabla \cdot (\boldsymbol{C} : \nabla \boldsymbol{u}^o) - \boldsymbol{u}^o &= \boldsymbol{0} && in \quad \mathscr{B}_2 \backslash \Gamma, \\
\boldsymbol{n} \cdot \boldsymbol{C} : \nabla \boldsymbol{u}^o &= -\boldsymbol{\varphi} && on \quad \Gamma, \\
\boldsymbol{n} \cdot \boldsymbol{C} : \nabla \boldsymbol{u}^o &= \mathscr{S}_R(\boldsymbol{u}^o) && on \quad \partial B_R,
\end{aligned} \tag{4.37}$$

where $\mathscr{S}_R\colon H^{1/2}(\partial B_R)^3 \to H^{-1/2}(\partial B_R)^3$ is a Dirichlet-to-Neumann operator, $\mathscr{S}_R(\boldsymbol{\psi}) := \boldsymbol{n} \cdot \boldsymbol{C} : \nabla \mathbf{u}_\psi$, stemming from the *elastostatic problem* in $B_{R_\circ} \backslash B_R$ with Dirichlet data $\mathbf{u}_\psi = \boldsymbol{\psi}$ on ∂B_R and homogeneous "Neumann" data $\boldsymbol{n} \cdot \boldsymbol{C} : \nabla \mathbf{u}_\psi = \boldsymbol{0}$ on $\partial B_{R_\circ}$.

Using standard trace theorems for vector fields with square-integrable divergence [118], one finds that

$$\begin{aligned}
\|\boldsymbol{\varphi}\|_{H^{-\frac{1}{2}}(\Gamma)} = \|\boldsymbol{n} \cdot \boldsymbol{C} : \nabla \boldsymbol{u}^o\|_{H^{-\frac{1}{2}}(\Gamma)} &\leqslant \|\boldsymbol{n} \cdot \boldsymbol{C} : \nabla \boldsymbol{u}^o\|_{H^{-\frac{1}{2}}(\partial D)} \leqslant \\
&\leqslant c \left(\|\nabla \cdot (\boldsymbol{C} : \nabla \boldsymbol{u}^o)\|_{L^2(D)} + \|(\boldsymbol{C} : \nabla \boldsymbol{u}^o)\|_{L^2(D)} \right),
\end{aligned} \tag{4.38}$$

for a positive constant c independent from $\boldsymbol{u}^\circ$. Thanks to the first equation in (4.37) we then deduce

$$\|\boldsymbol{\varphi}\|_{H^{-\frac{1}{2}}(\Gamma)} \;\leqslant\; c_1 \,\|\boldsymbol{u}^\circ\|_{H^1(D)}$$

for some $c_1 > 0$ independent from $\boldsymbol{u}^\circ$. On taking $\boldsymbol{w} = \boldsymbol{u}^\circ$ in (4.36), deploying the coercivity of A, and recalling from (4.14) that $\Im A(\boldsymbol{v}, \boldsymbol{v}) = 0$, we find

$$\langle \boldsymbol{\varphi}, \mathsf{T}_\circ \boldsymbol{\varphi} \rangle_\Gamma = A(\boldsymbol{u}^\circ, \boldsymbol{u}^\circ) \geqslant c_2 \,\|\boldsymbol{\varphi}\|^2_{H^{-\frac{1}{2}}(\Gamma)} \tag{4.39}$$

for a positive constant c_2 independent from $\boldsymbol{\varphi}$, which establishes the coercivity of $\mathsf{T}_\circ$. The self-adjointness of $\mathsf{T}_\circ$ follows immediately from that of A.

To complete the argument, consider the compactness of $\mathsf{T}_c \colon H^{-1/2}(\Gamma)^3 \to \tilde{H}^{1/2}(\Gamma)^3$, given by

$$\mathsf{T}_c(\boldsymbol{\varphi}) \;=\; [\![\boldsymbol{v}^c]\!], \quad \boldsymbol{v}^c \,=\, \boldsymbol{v} - \boldsymbol{u}^\circ \quad \text{on } \Gamma$$

where $\boldsymbol{v}$ solves (4.11). On subtracting (4.36) from (4.11) with $\boldsymbol{t}^{\mathrm{f}} = \boldsymbol{\varphi}$, one finds that

$$A(\boldsymbol{v}^c, \boldsymbol{w}) \;=\; -B(\boldsymbol{v}, \boldsymbol{w}) \qquad \forall \boldsymbol{w} \in H^1(\mathscr{B}_2 \backslash \Gamma)^3,$$

where A is coercive while B, given by (4.15), is compact on $H^1(\mathscr{B}_2 \backslash \Gamma)^3$. As a result, the induced mapping $\boldsymbol{v} \to \boldsymbol{v}^c$ from $H^1(\mathscr{B}_2 \backslash \Gamma)^3$ into $H^1(\mathscr{B}_2 \backslash \Gamma)^3$ is *compact*, whereby the compactness of T_c follows directly from the continuity of $\boldsymbol{v} \in H^1(\mathscr{B}_2 \backslash \Gamma)^3$ with respect to $\boldsymbol{\varphi} \in H^{-\frac{1}{2}}(\Gamma)^3$ and the trace theorem. $\qquad\square$

Lemma 4.4.6. *Operator* $T \colon H^{-1/2}(\Gamma)^3 \to \tilde{H}^{1/2}(\Gamma)^3$ *has a bounded (and thus continuous) inverse.*

Proof. The idea is to show that T, given by (4.29), is injective and Fredholm of index zero. The second claim follows immediately from Lemma 4.4.5. To demonstrate the injectivity of (4.29), one may recall a double-layer potential representation of elastodynamic fields solving (4.2)-(4.6) which demonstrates that for any $\boldsymbol{\varphi} \in H^{-1/2}(\Gamma)$, one has

$$\boldsymbol{v}(\boldsymbol{\varphi})(\boldsymbol{\xi}) \;=\; \int_\Gamma T(\boldsymbol{\varphi}) \cdot \boldsymbol{T}(\boldsymbol{\xi}, \boldsymbol{y}) \, \mathrm{d}S_{\boldsymbol{y}}, \qquad \boldsymbol{T}(\boldsymbol{\xi}, \boldsymbol{y}) \;=\; \boldsymbol{n}(\boldsymbol{y}) \cdot \boldsymbol{\Sigma}(\boldsymbol{\xi}, \boldsymbol{y}), \qquad \boldsymbol{\xi} \in \mathbb{R}^3 \backslash \Gamma,$$

where $[\![\boldsymbol{v}]\!] = T(\boldsymbol{\varphi})$ on Γ thanks to the fundamental property of double-layer potentials. Thus, on assuming that there exists $\boldsymbol{\varphi} \in H^{-1/2}(\Gamma)$ so that $T(\boldsymbol{\varphi}) = \boldsymbol{0}$, one finds that $\boldsymbol{v} = \boldsymbol{0}$ in $\mathbb{R}^3 \backslash \Gamma$ and consequently, by the second of (4.2) and trace theorems, that $\|\boldsymbol{\varphi}\|_{H^{-1/2}(\Gamma)} = \|\boldsymbol{n} \cdot \boldsymbol{C} : \nabla \boldsymbol{v}\|_{H^{-1/2}(\Gamma)} = 0.$ $\hfill\square$

Lemma 4.4.7. *Operator $T \colon H^{-1/2}(\Gamma)^3 \to \tilde{H}^{1/2}(\Gamma)^3$ is coercive, i.e. there exists constant $c > 0$ independent of $\boldsymbol{\varphi}$ such that*

$$|\langle \boldsymbol{\varphi}, T(\boldsymbol{\varphi}) \rangle| \ \geqslant \ c \, \|\boldsymbol{\varphi}\|_{H^{-\frac{1}{2}}(\Gamma)}^2, \qquad \forall \boldsymbol{\varphi} \in H^{-1/2}(\Gamma)^3. \tag{4.40}$$

Proof. Lemma 4.4.4 demonstrates that the duality product $\langle \boldsymbol{\varphi}, T(\boldsymbol{\varphi}) \rangle \in \mathbb{C} \setminus (-\infty, \infty)$ for all nonzero $\boldsymbol{\varphi} \in H^{-1/2}(\Gamma)^3$. Due to Lemma 4.4.5, on the other hand, decomposition $T = \mathsf{T}_c + \mathsf{T}_o$ exists where T_c is compact and T_o is such that $\langle \boldsymbol{\varphi}, \mathsf{T}_o(\boldsymbol{\varphi}) \rangle \in \mathbb{R}$ satisfies the coercivity condition (4.39) $\forall \boldsymbol{\varphi} \in H^{-1/2}(\Gamma)^3$. With such results in place, claim (4.49) follows immediately by Lemma 1.17 in [98]. $\hfill\square$

4.5 Application of sampling methods

4.5.1 Linear sampling method (LSM)

The essential idea behind the LSM [46] and also the factorization method (FM) [41] for geometrical obstacle reconstruction stems from the particular nature of an approximate solution, $\boldsymbol{g} = \boldsymbol{g}_p \oplus \boldsymbol{g}_s$, to the far-field equation

$$F\boldsymbol{g} \ = \ \boldsymbol{\Phi}_L^\infty, \qquad F \ = \ \mathscr{G}\mathscr{H} \ = \ \mathscr{H}^* T \mathscr{H}, \tag{4.41}$$

where $\boldsymbol{\Phi}_L^\infty$ is the far-field pattern of a trial radiating field, see Definition 2. In this setting, the behavior of $\boldsymbol{g}$ in the sampling region is exposed by characterizing the range of $\mathscr{G}$ or $\mathscr{H}^*$, which then forms the basis for approximating the characteristic function of a scatterer. This section presents an adaptation of the key LSM results for the problem of elastic-wave imaging of heterogeneous fractures, which provides a foundation for the GLSM developments in Section 4.5.3.

Definition 2. *With reference to (4.28), for every admissible FOD profile $\boldsymbol{a} \in \tilde{H}^{1/2}(L)$ specified over a smooth, non-intersecting trial fracture $L \subset \mathscr{B}_2$, the induced far-field pattern $\boldsymbol{\Phi}_L^\infty \colon \tilde{H}^{1/2}(L) \to L^2(\Omega)^3$ is given by*

$$\boldsymbol{\Phi}_L^\infty(\boldsymbol{a})(\hat{\boldsymbol{\xi}}) \;=\; -\left(\mathrm{i}k_p\,\hat{\boldsymbol{\xi}} \int_L \left\{ \lambda(\boldsymbol{a}\cdot\boldsymbol{n}) + 2\mu(\boldsymbol{n}\cdot\hat{\boldsymbol{\xi}})(\boldsymbol{a}\cdot\hat{\boldsymbol{\xi}}) \right\} e^{-\mathrm{i}k_p\hat{\boldsymbol{\xi}}\cdot\boldsymbol{y}} \; dS_{\boldsymbol{y}} \right.$$
$$\left. \oplus \; \mathrm{i}k_s\,\hat{\boldsymbol{\xi}} \times \int_L \left\{ \mu(\boldsymbol{a}\times\hat{\boldsymbol{\xi}})(\boldsymbol{n}\cdot\hat{\boldsymbol{\xi}}) + \mu(\boldsymbol{n}\times\hat{\boldsymbol{\xi}})(\boldsymbol{a}\cdot\hat{\boldsymbol{\xi}}) \right\} e^{-\mathrm{i}k_s\hat{\boldsymbol{\xi}}\cdot\boldsymbol{y}} \; dS_{\boldsymbol{y}} \right). \tag{4.42}$$

and $\boldsymbol{n}$ is the unit normal on L.

Remark 7. *On the basis of Definition 2, one may interpret the LSM reconstruction philosophy as follows. Let $\mathsf{L} \subset \mathbb{R}^3$ (containing the origin) denote a reference fracture surface whose characteristic size is small relative to the length scales describing the forward scattering problem, and let $L = \boldsymbol{z} + \mathsf{R}\mathsf{L}$ where $\boldsymbol{z} \in \mathbb{R}^3$ and $\mathsf{R} \in U(3)$ is a unitary rotation matrix. Given an admissible FOD profile $\boldsymbol{a} \in \tilde{H}^{1/2}(\mathsf{L})$, solving the far-field equation (4.41) over a grid of trial pairs $(\boldsymbol{z}, \mathsf{R})$ sampling $\mathbb{R}^3 \times U(3)$ is simply an effort to probe the far-field kernel (4.23) – through synthetic rearrangement of the illuminating plane waves – for fingerprints in terms of $\boldsymbol{\Phi}_L^\infty$. As shown by Theorems 4.5.2, 4.5.7 and 4.5.9, such fingerprint is found in the data if and only if $L \subset \Gamma$. Otherwise, the norm of any approximate solution to (4.41) can be made arbitrarily large, which then provides a criterion for reconstructing Γ.*

Theorem 4.5.1. *Assume that ω is not a "Neumann" eigenvalue of the Navier equation (4.32) for some m, and that $\boldsymbol{K}^{-1} \in L^\infty(\Gamma)$. Then for every smooth and non-intersecting trial crack $L \subset \mathscr{B}_2$ and some FOD profile $\boldsymbol{a}(\boldsymbol{\xi}) \in \tilde{H}^{1/2}(L)$, one has*

$$\boldsymbol{\Phi}_L^\infty \in Range(\mathscr{H}^*) \quad \Longleftrightarrow \quad L \subset \Gamma.$$

Proof. Consider the following:

- If $L \subset \Gamma$, then $\tilde{H}^{1/2}(L)^3 \subset \tilde{H}^{1/2}(\Gamma)^3$. By extending the domain of $\boldsymbol{a} \in \tilde{H}^{1/2}(L)^3$ from L to Γ through zero padding, one immediately obtains $\boldsymbol{\Phi}_L^\infty \in Range(\mathscr{H}^*)$ thanks to (4.28) and (4.42).

- Assume that $L \not\subset \Gamma$ and that $\boldsymbol{\Phi}_L^\infty \in Range(\mathscr{H}^*)$. Then there exists $\boldsymbol{b} \in \tilde{H}^{1/2}(\Gamma)^3$

such that

$$\mathbf{\Phi}_L^\infty(\boldsymbol{b})(\hat{\boldsymbol{\xi}}) \;=\; -\Big(ik_p\hat{\boldsymbol{\xi}} \int_\Gamma \big\{ \lambda(\boldsymbol{b}\cdot\boldsymbol{n}) + 2\mu(\boldsymbol{n}\cdot\hat{\boldsymbol{\xi}})(\boldsymbol{b}\cdot\hat{\boldsymbol{\xi}}) \big\} e^{-ik_p\hat{\boldsymbol{\xi}}\cdot\boldsymbol{y}} \,\mathrm{d}S_{\boldsymbol{y}}$$

$$\oplus\; ik_s\hat{\boldsymbol{\xi}} \times \int_\Gamma \big\{ \mu(\boldsymbol{b}\times\hat{\boldsymbol{\xi}})(\boldsymbol{n}\cdot\hat{\boldsymbol{\xi}}) + \mu(\boldsymbol{n}\times\hat{\boldsymbol{\xi}})(\boldsymbol{b}\cdot\hat{\boldsymbol{\xi}}) \big\} e^{-ik_s\hat{\boldsymbol{\xi}}\cdot\boldsymbol{y}} \,\mathrm{d}S_{\boldsymbol{y}} \Big),$$

associated with the layer potential

$$\mathbf{\Phi}_\Gamma(\boldsymbol{\xi}) \;=\; \int_\Gamma \boldsymbol{b}(\boldsymbol{y})\cdot\boldsymbol{T}(\boldsymbol{\xi},\boldsymbol{y})\,\mathrm{d}S_{\boldsymbol{y}}, \quad \boldsymbol{T}(\boldsymbol{\xi},\boldsymbol{y}) \;=\; \boldsymbol{n}(\boldsymbol{y})\cdot\boldsymbol{\Sigma}(\boldsymbol{\xi},\boldsymbol{y}), \quad \boldsymbol{\xi}\in\mathscr{B}_2\backslash\Gamma. \quad (4.43)$$

On the other hand, owing to Definition 2 of $\mathbf{\Phi}_L^\infty(\hat{\boldsymbol{\xi}})$, potential $\mathbf{\Phi}_\Gamma(\boldsymbol{\xi})$ should coincide with

$$\mathbf{\Psi}_L(\boldsymbol{\xi}) \;=\; \int_L \boldsymbol{a}(\boldsymbol{y})\cdot\boldsymbol{T}(\boldsymbol{\xi},\boldsymbol{y})\,\mathrm{d}S_{\boldsymbol{y}}, \qquad \boldsymbol{\xi}\in\mathscr{B}_2\backslash L, \qquad\qquad (4.44)$$

over $\boldsymbol{\xi}\in\mathscr{B}_2\backslash(L\cup\Gamma)$. Now, let $\Gamma\not\ni\boldsymbol{\xi}^\circ\in L$ and let $\mathscr{B}_\epsilon$ be a small ball centered at $\boldsymbol{\xi}^\circ$ such that $\mathscr{B}_\epsilon\cap\Gamma=\emptyset$. In this case $\mathbf{\Phi}_\Gamma$ is analytic in $\mathscr{B}_\epsilon$, while $\mathbf{\Psi}_L$ has a singularity at $\boldsymbol{\xi}^\circ\in\mathscr{B}_\epsilon$ – which by contradiction completes the proof.

$$\square$$

On the basis of the above result, one arrives at the following statement which inspires most of the LSM-based indicator functionals.

Theorem 4.5.2. *Under the assumptions of Lemma 4.4.3 and Theorem 4.5.1,*

- *If $L\subset\Gamma$, there exists a Herglotz density vector $\boldsymbol{g}_\epsilon^L\in L^2(\Omega)^3$ such that $\|F\boldsymbol{g}_\epsilon^L - \mathbf{\Phi}_L^\infty\|_{L^2(\Omega)}\leqslant\epsilon$ and $\limsup_{\epsilon\to0}\|\mathscr{H}\boldsymbol{g}_\epsilon^L\|_{H^{-1/2}(\Gamma)}<\infty$.*

- *If $L\not\subset\Gamma$, then $\forall\boldsymbol{g}_\epsilon^L\in L^2(\Omega)^3$ such that $\|F\boldsymbol{g}_\epsilon^L - \mathbf{\Phi}_L^\infty\|_{L^2(\Omega)}\leqslant\epsilon$, one has $\lim_{\epsilon\to0}\|\mathscr{H}\boldsymbol{g}_\epsilon^L\|_{H^{-1/2}(\Gamma)}=\infty$.*

Proof. Let us first assume $L\subset\Gamma$, whereby $\mathbf{\Phi}_L^\infty\in Range(\mathscr{H}^*)$ thanks to Theorem 4.5.1. Then, by definition, there exists $\boldsymbol{a}^L\in\overline{Range(T)}$ such that $\mathscr{H}^*\boldsymbol{a}^L = \mathbf{\Phi}_L^\infty$. By invoking Lemma 4.4.6 on the boundedness i.e. continuity of T^{-1} and Lemma 4.4.2 which (by the injectivity of $\mathscr{H}^*$) guarantees the range denseness of $\mathscr{H}$, one finds that $\forall\epsilon>0$, $\exists\boldsymbol{g}_\epsilon^L\in L^2(\Omega)^3$ such that $\|T^{-1}\boldsymbol{a}^L - \mathscr{H}\boldsymbol{g}_\epsilon^L\|_{H^{-1/2}(\Gamma)}\leqslant\epsilon$.

Thanks to (i) the continuity of $\mathscr{H}^*T$ and (ii) the fact that $\boldsymbol{a}^L \in \tilde{H}^{1/2}(\Gamma)^3$, this establishes the first part of the claim.

Next, consider the case where $L \not\subset \Gamma$ and consequently $\boldsymbol{\Phi}_L^\infty \notin Range(\mathscr{H}^*)$ by Theorem 4.5.1. Then, thanks to Lemma 4.4.3 which implies the range denseness of $\mathscr{H}^*$, for every $\epsilon > 0$ and some regularization parameter $\alpha = \alpha(\epsilon)$ $(\lim_{\epsilon \to 0} \alpha = 0)$, a nearby solution $\boldsymbol{a}_\epsilon^L \in \tilde{H}^{1/2}(\Gamma)^3$ can be built e.g. via Tikhonov regularization [102] such that $\| \boldsymbol{\Phi}_L^\infty - \mathscr{H}^* \boldsymbol{a}_\epsilon^L \|_{L^2(\Omega)} \leqslant \epsilon$ and $\lim_{\epsilon \to 0} \| \boldsymbol{a}_\epsilon^L \|_{\tilde{H}^{1/2}(\Gamma)} = \infty$ – due to the compactness of $\mathscr{H}^*$ established in Lemma 4.4.2. At this point, the same argument as in the first part of the proof – deploying the continuity of T^{-1} and the range denseness of $\mathscr{H}$ – can be used to establish the second claim.

$\square$

4.5.2 Factorization method (FM)

To facilitate the ensuing developments, we recall elements of the factorization method [98] as they pertain to our inverse problem.

Definition 3. *The self-adjoint operator $F_\sharp \colon L^2(\Omega)^3 \to L^2(\Omega)^3$ is defined by*

$$F_\sharp := |\Re F| + \Im F, \tag{4.45}$$

where $F \colon L^2(\Omega)^3 \to L^2(\Omega)^3$ is given by (4.24), and

$$\Re F = \tfrac{1}{2}(F + F^*), \qquad \Im F = \tfrac{1}{2\mathrm{i}}(F - F^*). \tag{4.46}$$

Remark 8. *In line with decomposition (4.30) of the far-field operator F, there exists factorization*

$$F_\sharp = \mathscr{H}^* T_\sharp \mathscr{H} \tag{4.47}$$

of (4.45), where the middle operator $T_\sharp \colon H^{-1/2}(\Gamma)^3 \to \tilde{H}^{1/2}(\Gamma)^3$ is given by

$$T_\sharp := \Re T (Q^+ - Q^-) + \Im T; \tag{4.48}$$

Q^+ and Q^- are bounded projectors such that $Q^+ + Q^- = I$; $Q^+ - Q^-$ is an isomorphism, and Q^- has a finite rank. See Theorem 2.15 in [98] for derivation.

Theorem 4.5.3. *Under the assumptions of Theorem 4.5.1, operator $F_\sharp$ in (4.45) has the following properties:*

- *Operator $F_\sharp$ is positive.*

- *The ranges of $\mathscr{H}^*\colon \tilde{H}^{1/2}(\Gamma)^3 \to L^2(\Omega)^3$ and $F_\sharp^{1/2}\colon L^2(\Omega)^3 \to L^2(\Omega)^3$ coincide.*

- $\boldsymbol{\Phi}_L^\infty \in Range(F_\sharp^{1/2}) \quad \Longleftrightarrow \quad L \subset \Gamma.$

Proof. The first two claims follow directly from Theorem 2.15 in [98], its extended version (Theorem 3.2) in [41], Lemma 4.4.2 Lemma 4.4.4, and Lemma 4.4.5. With such result in place, the last claim is immediately established by Theorem 4.5.1. □

Lemma 4.5.4. *Operator $T_\sharp\colon H^{-1/2}(\Gamma)^3 \to \tilde{H}^{1/2}(\Gamma)^3$ in the factorization (4.47) has the following properties:*

- *$T_\sharp$ has a bounded (and thus continuous) inverse.*

- *$T_\sharp$ is selfadjoint and is positively coercive, i.e. there exists a constant $c > 0$ independent of $\boldsymbol{\varphi}$ so that*

$$\left(\boldsymbol{\varphi}, T_\sharp(\boldsymbol{\varphi})\right)_{H^{-\frac{1}{2}}(\Gamma)} \;\geqslant\; c\,\|\boldsymbol{\varphi}\|_{H^{-\frac{1}{2}}(\Gamma)}^2, \qquad \forall \boldsymbol{\varphi} \in H^{-1/2}(\Gamma)^3. \qquad (4.49)$$

Proof. See Appendix A in [41] and the proof of Theorem 2.15, part E in [98]. □

On the basis of Theorem 4.5.2, one sees that $F_\sharp^{1/2}$ can be used to characterize Γ from the far-field measurements. In what follows, it is in particular shown that the GLSM cost functionals based on $F_\sharp$ (i) are convex, (ii) have closed-form minimizers, and (iii) enable fast and robust reconstruction of Γ – especially when the data (and thus the far-field operator) are contaminated by noise.

4.5.3 Generalized Linear Sampling Method (GLSM)

Theorem 4.5.2 of the linear sampling method poses two fundamental challenges in that: i) the featured anomaly indicator $\| \mathscr{H} \boldsymbol{g}_\epsilon^L \|_{H^{-1/2}(\Gamma)}$ inherently depends on the unknown fracture support Γ, and ii) construction of the Herglotz density vector $\boldsymbol{g}_\epsilon^L \in L^2(\Omega)^3$ is implicit in the theorem [12]. Conventionally, these issues are addressed by replacing $\|\mathscr{H} \boldsymbol{g}_\epsilon^L\|_{H^{-1/2}(\Gamma)}$ with $\|\boldsymbol{g}_\epsilon^L\|_{L^2(\Omega)}$ which is, in turn, computed by way of Tikhonov regularization [102]. Such treatment, however, has proven to be particularly sensitive to perturbations in the data due to e.g. measurement errors.

To help meet the challenge, the GLSM takes advantage of the second factorization (4.30) of the far-field operator and the mathematical properties of its components to properly construct a *stable* approximate solution to the far-field equation (4.41). This is accomplished through a *sequence* of penalized least-squares problems where the principal ingredient of the penalty term is $\|\mathscr{H} \boldsymbol{g}_\epsilon^L\|_{H^{-1/2}(\Gamma)}$, reformulated in a computable way in terms of the far-field operator F. More specifically, by invoking factorizations (4.30) and (4.47), one may observe that

$$
\begin{aligned}
(\boldsymbol{g}_\epsilon^L, F\boldsymbol{g}_\epsilon^L)_{L^2(\Omega)} &= \langle \mathscr{H} \boldsymbol{g}_\epsilon^L, T\mathscr{H}\boldsymbol{g}_\epsilon^L \rangle_\Gamma, \\
(\boldsymbol{g}_\epsilon^L, F_\sharp\boldsymbol{g}_\epsilon^L)_{L^2(\Omega)} &= \langle \mathscr{H} \boldsymbol{g}_\epsilon^L, T_\sharp \mathscr{H}\boldsymbol{g}_\epsilon^L \rangle_\Gamma, \qquad \forall \boldsymbol{g}_\epsilon^L \in L^2(\Omega)^3
\end{aligned}
$$

where $(\cdot,\cdot)_{L^2(\Omega)} := (\cdot,\cdot)_{L^2(\Omega)^3}$ denotes the usual L^2 inner product on Ω. Then, thanks to the coercivity of the middle operator T (see Lemma 4.4.7), quantity $|(\boldsymbol{g}_\epsilon^L, F\boldsymbol{g}_\epsilon^L)_{L^2(\Omega)}|$ – which is computable without prior knowledge of Γ – may be safely substituted for $\|\mathscr{H} \boldsymbol{g}_\epsilon^L\|^2_{H^{-1/2}(\Gamma)}$ in constructing a penalty term for the GLSM cost functional. Similarly, the positive coercivity $T_\sharp$ (See Lemma 4.5.4) and factorization (4.47) of $F_\sharp$ demonstrate that $|(\boldsymbol{g}_\epsilon^L, F_\sharp\boldsymbol{g}_\epsilon^L)_{L^2(\Omega)}| = \| F_\sharp^{1/2}\boldsymbol{g}_\epsilon^L \|^2$ may serve as a replacement for $\|\mathscr{H} \boldsymbol{g}_\epsilon^L\|^2_{H^{-1/2}(\Gamma)}$, giving birth to a *convex* GLSM cost functional whose minimizer can be computed without iterations. This shines light on the GLSM approach to elastodynamic reconstruction of heterogeneous fractures, whose specificities are presented next.

GLSM cost functional.

- *Unperturbed (noise-free) operators.* Let $\alpha > 0$ be a regularization parameter, and consider the far-field pattern $\boldsymbol{\Phi}_L^\infty \in L^2(\Omega)^3$ as in Definition 2. Then the GLSM

cost functional is defined by a sequence of penalized least-squares misfit functionals $J_\alpha(\boldsymbol{\Phi}_L^\infty; \cdot)\colon L^2(\Omega)^3 \to \mathbb{R}$, namely

$$J_\alpha(\boldsymbol{\Phi}_L^\infty; \boldsymbol{g}) := \|F\boldsymbol{g} - \boldsymbol{\Phi}_L^\infty\|^2 + \alpha\,\|F_\sharp^{\frac{1}{2}}\boldsymbol{g}\|^2, \qquad \boldsymbol{g} \in L^2(\Omega)^3, \tag{4.50}$$

whose minimizers $\boldsymbol{g}_\alpha^L \in L^2(\Omega)^3$ can be computed *non-iteratively* by solving

$$F^*(F\boldsymbol{g}_\alpha^L - \boldsymbol{\Phi}_L^\infty) + \alpha(F_\sharp^{\frac{1}{2}})^*F_\sharp^{\frac{1}{2}}\,\boldsymbol{g}_\alpha^L = \boldsymbol{0}. \tag{4.51}$$

For completeness, a more general form $\mathscr{J}_\alpha(\boldsymbol{\Phi}_L^\infty; \cdot)\colon L^2(\Omega)^3 \to \mathbb{R}$ of the GLSM cost functional, namely

$$\mathscr{J}_\alpha(\boldsymbol{\Phi}_L^\infty; \boldsymbol{g}) := \|F\boldsymbol{g} - \boldsymbol{\Phi}_L^\infty\|^2 + \alpha\,|(\boldsymbol{g}, F\boldsymbol{g})|, \qquad \boldsymbol{g} \in L^2(\Omega)^3, \tag{4.52}$$

is also considered. Note that (4.52) does not demand $F_\sharp$ to be applicable (see Theorem 4.5.3), and thus may cater for a wider class of contact laws, $\mathscr{L}[\![\boldsymbol{v}]\!]$, over the fracture surface in (4.2).

Remark 9. *In general,* $\mathscr{J}_\alpha(\boldsymbol{\Phi}_L^\infty; \boldsymbol{g})$ *does not have a minimizer; however, one may define*

$$j_\alpha(\boldsymbol{\Phi}_L^\infty) := \inf_{\boldsymbol{g}\in L^2(\Omega)^3}\mathscr{J}_\alpha(\boldsymbol{\Phi}_L^\infty; \boldsymbol{g}).$$

Thanks to the range denseness of F (see Lemma 4.5.6), one has that $j_\alpha \to 0$ as $\alpha \to 0$. Accordingly, an optimized nearby solution can be constructed by following the algorithm described in [12].

- *Perturbed operators.* When the measurements are contaminated with noise (e.g. sensing errors, fluctuations in the medium properties), one has to deal with noisy operators F^δ and $F_\sharp^\delta$ satisfying

$$\|F^\delta - F\| \leqslant \delta, \qquad \|F_\sharp^\delta - F_\sharp\| \leqslant \delta, \tag{4.53}$$

where $\delta > 0$ is a measure of perturbation in data – independent of F and $F_\sharp$. Assuming that F^δ and $F_\sharp^\delta$ are compact, a regularized version $J_\alpha^\delta(\boldsymbol{\Phi}_L^\infty; \cdot)\colon L^2(\Omega)^3 \to \mathbb{R}$ of the GLSM cost functional is defined in spirit of the Tikhonov regularization

method as

$$J_\alpha^\delta(\mathbf{\Phi}_L^\infty; \boldsymbol{g}) \; := \; \|F^\delta \boldsymbol{g} \, - \, \mathbf{\Phi}_L^\infty\|^2 \, + \, \alpha \, (\, \|(F_\sharp^\delta)^{\frac{1}{2}} \boldsymbol{g}\|^2 \, + \, \delta \, \|\boldsymbol{g}\|^2), \qquad \boldsymbol{g} \in L^2(\Omega)^3.$$
(4.54)

Note that J_α^δ is again convex and that its minimizer $\boldsymbol{g}_{\alpha,\delta}^L \in L^2(\Omega)^3$ solves the linear system

$$F^{\delta*}(F^\delta \boldsymbol{g}_{\alpha,\delta}^L \, - \, \mathbf{\Phi}_L^\infty) \; + \; \alpha \, (\, (F_\sharp^\delta)^{\frac{1}{2}*}(F_\sharp^\delta)^{\frac{1}{2}} \boldsymbol{g}_{\alpha,\delta}^L \, + \, \delta \, \boldsymbol{g}_{\alpha,\delta}^L) \; = \; \mathbf{0}.$$
(4.55)

In this vein, the (regularized) cost functional affiliated with the general form (4.52) may be recast as

$$\mathscr{J}_\alpha^\delta(\mathbf{\Phi}_L^\infty; \boldsymbol{g}) \; := \; \|F^\delta \boldsymbol{g} \, - \, \mathbf{\Phi}_L^\infty\|^2 \, + \, \alpha \, (\, |(\boldsymbol{g}, F^\delta \boldsymbol{g})| \, + \, \delta \, \|\boldsymbol{g}\|^2), \qquad \boldsymbol{g} \in L^2(\Omega)^3.$$
(4.56)

Remark 10. *In (4.54) and (4.56), δ signifies both a measure of perturbation in F and a regularization parameter that, along with α, is designed to create a robust fracture indicator functional via a sequence of the GLSM minimizers (see the proof of Theorem 4.5.9).*

With the above definitions in place, the main GLSM theorems are based on the following lemmas.

Lemma 4.5.5. *Operator $\mathscr{G} = \mathscr{H}^*T \colon H^{-1/2}(\Gamma)^3 \to L^2(\Omega)^3$ is compact over $H^{-1/2}(\Gamma)^3$.*

Proof. The claim follows immediately from Lemmas 4.4.2 and 4.4.4 establishing, respectively, the compactness of $\mathscr{H}^*$ and the boundedness of T. $\qquad\qquad \square$

Lemma 4.5.6. *The far-field operator $F \colon L^2(\Omega)^3 \to L^2(\Omega)^3$ is injective, compact and, under the assumptions of Lemma 4.4.3, has a dense range.*

Proof. Injectivity. Let $F(\boldsymbol{g}) = \mathbf{0}$. Then, recalling the factorization $F = \mathscr{H}^*T\mathscr{H}$ and the injectivity of $\mathscr{H}^*$ and T (due respectively to Lemma 4.4.3 and Lemma 4.4.6), one finds that $\mathscr{H}(\boldsymbol{g}) := \boldsymbol{n} \cdot \boldsymbol{C} \colon \nabla \mathbf{u}_{\boldsymbol{g}} = \mathbf{0}$ on Γ. Under the assumptions of Lemma 4.4.3, this requires that $\mathbf{u}_{\boldsymbol{g}} = \mathbf{0}$ in $\mathbb{R}^3$, i.e. that $\boldsymbol{g} = \mathbf{0}$ which establishes the first claim.

Compactness. The compactness of F follows immediately from the compactness of $\mathscr{H}^*$ – and thus that of $\mathscr{H}$ (Lemma 4.4.2), and the boundedness of T (Lemma 4.4.4).

Range densenes. This claim is conveniently verified by establishing the injectivity of F^*. To this end, recall (4.24) and consider the L^2-inner product

$$\big(F(\boldsymbol{g}),\boldsymbol{a}\big)_{L^2(\Omega)} \;=\; \int_\Omega \bar{\boldsymbol{a}}(\hat{\boldsymbol{\xi}})\cdot\boldsymbol{v}^\infty_{g_\Omega}(\hat{\boldsymbol{\xi}})\,\mathrm{d}S_{\hat{\boldsymbol{\xi}}} \;=\; \int_\Omega \boldsymbol{g}(\boldsymbol{d})\cdot\overline{\int_\Omega \boldsymbol{W}^{\infty*}(\boldsymbol{d},\hat{\boldsymbol{\xi}})\cdot\boldsymbol{a}(\hat{\boldsymbol{\xi}})\,\mathrm{d}S_{\hat{\boldsymbol{\xi}}}}\;\mathrm{d}S_{\boldsymbol{d}}, \quad (4.57)$$

where $\boldsymbol{a}\in L^2(\Omega)^3$. Thanks to the reciprocity identity (4.25), inner product (4.57) exposes the adjoint far-field operator as

$$\begin{aligned}
F^*(\boldsymbol{a})(\boldsymbol{d}) \;&=\; \int_\Omega \boldsymbol{W}^{\infty*}(\boldsymbol{d},\hat{\boldsymbol{\xi}})\cdot\boldsymbol{a}(\hat{\boldsymbol{\xi}})\,\mathrm{d}S_{\hat{\boldsymbol{\xi}}} \;=\; \\
&=\; \overline{\int_\Omega \boldsymbol{W}^\infty(\hat{\boldsymbol{\xi}},-\boldsymbol{d})\cdot\overline{\boldsymbol{a}}(-\hat{\boldsymbol{\xi}})\,\mathrm{d}S_{\hat{\boldsymbol{\xi}}}} \;=\; \overline{F}(\tilde{\boldsymbol{a}})(-\boldsymbol{d}), \quad \boldsymbol{d}\in\Omega,
\end{aligned} \qquad (4.58)$$

where $\tilde{\boldsymbol{a}}(\hat{\boldsymbol{\xi}}):=\overline{\boldsymbol{a}}(-\hat{\boldsymbol{\xi}})$ on Ω. Owing to the injectivity of F, one finds from (4.58) that setting $F^*(\boldsymbol{a})=\boldsymbol{0}$ necessitates $\tilde{\boldsymbol{a}}=\boldsymbol{0}$ and thus $\boldsymbol{a}=\boldsymbol{0}$. $\qquad\square$

We are now in position to establish the main result of the GLSM approach, given by Theorem 4.5.7 and Theorem 4.5.9, catering for the elastodynamic reconstruction of heterogeneous fractures.

Theorem 4.5.7. *Consider the GLSM cost functional $\mathfrak{J}_\alpha$ unifying (4.50) and (4.52) with unperturbed operators F^δ and $F_\sharp^\delta$, namely*

$$\mathfrak{J}_\alpha(\boldsymbol{\Phi}_L^\infty;\boldsymbol{g}) \;:=\; \|F\boldsymbol{g}-\boldsymbol{\Phi}_L^\infty\|^2_{L^2(\Omega)} \;+\; \alpha\,|(\boldsymbol{g},B\boldsymbol{g})|, \qquad \boldsymbol{g}\in L^2(\Omega)^3, \qquad (4.59)$$

where $\alpha>0$ and B, denoting either F or $F_\sharp$, admits the factorization

$$B \;=\; \mathscr{H}^*\mathfrak{T}\mathscr{H}, \qquad \mathfrak{T} \;=\; T,T_\sharp. \qquad (4.60)$$

Since $\mathfrak{J}_\alpha\geqslant 0$, define the infimum

$$\mathfrak{j}_\alpha(\boldsymbol{\Phi}_L^\infty) \;:=\; \inf_{\boldsymbol{g}\in L^2(\Omega)^3}\mathfrak{J}_\alpha(\boldsymbol{\Phi}_L^\infty;\boldsymbol{g}),$$

and let $\boldsymbol{g}_\alpha^L \in L^2(\Omega)^3$ denote a nearby solution such that

$$\mathfrak{J}_\alpha(\boldsymbol{\Phi}_L^\infty; \boldsymbol{g}_\alpha^L) \ \leqslant\ \mathrm{j}_\alpha(\boldsymbol{\Phi}_L^\infty) + \mu\alpha,$$

$\mu > 0$ being a constant independent of α. Then,

$$\boldsymbol{\Phi}_L^\infty \in Range(\mathscr{H}^*) \ \Longleftrightarrow\ \Big\{ \limsup_{\alpha\to 0} |(\boldsymbol{g}_\alpha^L, B\boldsymbol{g}_\alpha^L)| < \infty \ \Longleftrightarrow\ \liminf_{\alpha\to 0} |(\boldsymbol{g}_\alpha^L, B\boldsymbol{g}_\alpha^L)| < \infty \Big\}.$$

Proof. See the proof of Theorem 3 in [12], synthesized in L using present notation. $\square$

Lemma 4.5.8. *Consider the regularized GLSM cost functional $\mathfrak{J}_\alpha^\delta$ unifying (4.54) and (4.56) with perturbed operators F^δ and $F_\sharp^\delta$, namely*

$$\mathfrak{J}_\alpha^\delta(\boldsymbol{\Phi}_L^\infty; \boldsymbol{g}) \ :=\ \|F^\delta \boldsymbol{g} - \boldsymbol{\Phi}_L^\infty\|^2 \ +\ \alpha\big(|(\boldsymbol{g}, B^\delta \boldsymbol{g})| + \delta\|\boldsymbol{g}\|^2\big), \qquad \boldsymbol{g} \in L^2(\Omega)^3 \quad (4.61)$$

where $\alpha, \beta > 0$ and B^δ denotes either F^δ or $F_\sharp^\delta$. Assuming that B^δ is compact, $\mathfrak{J}_\alpha^\delta$ has a minimizer $\boldsymbol{g}_{\alpha,\delta}^L \in L^2(\Omega)^3$ satisfying

$$\lim_{\alpha\to 0} \limsup_{\delta\to 0} \mathfrak{J}_\alpha^\delta(\boldsymbol{\Phi}_L^\infty; \boldsymbol{g}_{\alpha,\delta}^L) \ =\ 0. \tag{4.62}$$

Proof. Existence of a minimizer. For any $\alpha, \delta > 0$ and $\boldsymbol{\Phi}_L^\infty \in L^2(\Omega)^3$ given by (4.42), any sequence $(\boldsymbol{g}^n)$ constructed to minimize $\mathfrak{J}_\alpha^\delta$ is bounded in $L^2(\Omega)^3$, and thus weakly convergent to some $\boldsymbol{g}_{\alpha,\delta}^L \in L^2(\Omega)^3$. Thanks to the lower semi-continuity of a norm with respect to the weak convergence and the postulated compactness of B^δ, one has

$$\mathfrak{J}_\alpha^\delta(\boldsymbol{\Phi}_L^\infty; \boldsymbol{g}_{\alpha,\delta}^L) \ \leqslant\ \liminf_{n\to\infty} \mathfrak{J}_\alpha^\delta(\boldsymbol{\Phi}_L^\infty; \boldsymbol{g}^n) \ \leqslant\ \inf_{\boldsymbol{g}\in L^2(\Omega)^3} \mathfrak{J}_\alpha^\delta(\boldsymbol{\Phi}_L^\infty; \boldsymbol{g}), \tag{4.63}$$

which proves that $\boldsymbol{g}_{\alpha,\delta}^L$ is a minimizer of $\mathfrak{J}_\alpha^\delta(\boldsymbol{\Phi}_L^\infty; \boldsymbol{g})$ in $L^2(\Omega)^3$.

Limiting behavior. Let us first observe from (4.53), (4.59) and (4.61) that

$$\mathfrak{J}_\alpha^\delta(\boldsymbol{\Phi}_L^\infty; \boldsymbol{g}) \leqslant \mathfrak{J}_\alpha(\boldsymbol{\Phi}_L^\infty; \boldsymbol{g}) + \delta\big\{2\alpha\|\boldsymbol{g}\|^2 + \delta\|\boldsymbol{g}\|^2 + 2\|F\boldsymbol{g} - \boldsymbol{\Phi}_L^\infty\|\,\|\boldsymbol{g}\|\big\}, \quad \forall \boldsymbol{g} \in L^2(\Omega)^3. \tag{4.64}$$

For any $\delta > 0$ (α fixed), on can chose $\boldsymbol{g}_{\alpha,\delta}$ such that $|\mathfrak{J}_\alpha(\boldsymbol{\Phi}_L^\infty; \boldsymbol{g}_{\alpha,\delta}) - \mathrm{j}_\alpha(\boldsymbol{\Phi}_L^\infty)| \leqslant \delta$. Then

by the definition of $\boldsymbol{g}_{\alpha,\delta}^L$ one finds via triangle inequality that

$$\mathfrak{I}_\alpha^\delta(\boldsymbol{\Phi}_L^\infty; \boldsymbol{g}_{\alpha,\delta}^L) \;\leqslant\; \mathfrak{I}_\alpha^\delta(\boldsymbol{\Phi}_L^\infty; \boldsymbol{g}_{\alpha,\delta}) \;\leqslant\;$$
$$\leqslant\; \mathfrak{j}_\alpha(\boldsymbol{\Phi}_L^\infty) + \delta\{1 + 2\alpha\|\boldsymbol{g}_{\alpha,\delta}\|^2 + \delta\|\boldsymbol{g}_{\alpha,\delta}\|^2 + 2\|F\boldsymbol{g}_{\alpha,\delta} - \boldsymbol{\Phi}_L^\infty\|\,\|\boldsymbol{g}_{\alpha,\delta}\|\}.$$

The proof of (4.62) is now completed by noting that (i) given α, the term inside the brackets is bounded for any δ, and (ii) $\lim\limits_{\alpha\to 0} \mathfrak{j}_\alpha = 0$. $\qquad\square$

Theorem 4.5.9. *Under the assumptions of Theorem 4.5.7 and an additional hypothesis that B^δ (denoting either F^δ or $F_\sharp^\delta$) is compact, one has*

$$\boldsymbol{\Phi}_L^\infty \in Range(\mathscr{H}^*) \quad\Longleftrightarrow\quad \Big\{ \limsup_{\alpha\to 0}\limsup_{\delta\to 0}\big(|(\boldsymbol{g}_{\alpha,\delta}^L, B^\delta \boldsymbol{g}_{\alpha,\delta}^L)| + \delta\|\boldsymbol{g}_{\alpha,\delta}^L\|^2\big) < \infty$$
$$\Longleftrightarrow\quad \liminf_{\alpha\to 0}\liminf_{\delta\to 0}\big(|(\boldsymbol{g}_{\alpha,\delta}^L, B^\delta \boldsymbol{g}_{\alpha,\delta}^L)| + \delta\|\boldsymbol{g}_{\alpha,\delta}^L\|^2\big) < \infty\Big\},$$

where $\boldsymbol{g}_{\alpha,\delta}^L$ is a minimizer of the perturbed GLSM cost functional (4.61) *in the sense of* (4.62).

Proof. See the proof of Theorem 5 in [12], also summarized in L. $\qquad\square$

4.5.3.1 The GLSM criteria for imaging heterogeneous fractures

On the basis of Theorem 4.5.9, a robust GLSM-based criterion for the elastic-wave reconstruction of heterogeneous fractures can be designed as

$$I^{\mathscr{G}}(L) \;:=\; \frac{1}{\sqrt{|(\boldsymbol{g}_{\alpha,\delta}^L, B^\delta \boldsymbol{g}_{\alpha,\delta}^L)| + \delta\|\boldsymbol{g}_{\alpha,\delta}^L\|^2}}, \qquad B^\delta \;=\; F^\delta, F_\sharp^\delta, \qquad (4.65)$$

where $\boldsymbol{g}_{\alpha,\delta}^L$ is a minimizer of (4.61) in the sense of (4.62). In this setting, it is particularly instructive to focus on the case where $B^\delta = F_\sharp^\delta$, since $\boldsymbol{g}_{\alpha,\delta}^L$ in this case can be obtained *non-iteratively* by explicitly solving (4.55). Accordingly, the GLSM indicator functional used is the sequel is taken as

$$I^{\mathscr{G}_\sharp}(L) \;=\; \frac{1}{\sqrt{\|(F_\sharp^\delta)^{\frac{1}{2}}\boldsymbol{g}_{\alpha,\delta}^L\|^2 + \delta\|\boldsymbol{g}_{\alpha,\delta}^L\|^2}}. \qquad (4.66)$$

For future reference, let us also recall the classical LSM/FM solution $\boldsymbol{g}_\epsilon^L \in L^2(\Omega)^3$ (see Theorem 4.5.2) obtained by way of Tikhonov regularization [102], namely

$$\boldsymbol{g}_\epsilon^L \; := \; \min_{\boldsymbol{g} \in L^2(\Omega)^3} \big\{ \| F^\delta \boldsymbol{g} \, - \, \boldsymbol{\Phi}_L^\infty \|^2 + \beta \| \boldsymbol{g} \|^2 \big\}, \tag{4.67}$$

where β is a regularization parameter computable by the Morozov discrepancy principle.

Remark 11. *It is worth noting that the GLSM characterization of Γ from the far-field data (via the range of F) is deeply rooted in geometrical considerations, so that the fracture indicator functionals (4.65) and (4.66) may exhibit only a minor dependence on its heterogeneous contact condition – given by the distribution of $\boldsymbol{K}$ on Γ. This behavior can be traced back to Remark 7, where the opening displacement profile $\boldsymbol{a} \in \tilde{H}^{1/2}(L)$ – intimately related to the interface law – is deemed arbitrary (within the constraints of admissibility). This quality makes the GLSM imaging paradigm particularly attractive in situations where the fracture's contact law is unknown beforehand, which opens up possibilities for the sequential geometrical reconstruction and interfacial characterization of partially-closed fractures.*

4.6 Computational treatment and results

To illustrate the theoretical developments, this section examines the performance of (4.66) through a set of numerical experiments and compares the results of the GLSM reconstruction to those obtained by two alternative approaches, namely the linear sampling method (LSM) [46] and the method of topological sensitivity (TS) [134]. In what follows the synthetic sensory data, namely the far-field patterns (4.21) over the unit sphere, are generated by way of an elastodynamic boundary integral method [134].

Testing configuration. The sensing setup, shown in Fig. 4.2, features a "true" cylindrical fracture Γ of length $L = 0.7$ and radius $R = 0.35$. The fracture is endowed with a piecewise-constant ("zebra") distribution of interfacial stiffness $\boldsymbol{K}(\boldsymbol{\xi})$ on Γ, alternating between $\boldsymbol{K}_1$ and $\boldsymbol{K}_2$, where

$$\boldsymbol{K}_1 \; = \; (1 - 0.25\mathrm{i}) \, \boldsymbol{n} \otimes \boldsymbol{n} \; + \; (4 - 2\mathrm{i}) \, \boldsymbol{e}_1 \otimes \boldsymbol{e}_1 \; + \; (4 - 2\mathrm{i}) \, \boldsymbol{e}_2 \otimes \boldsymbol{e}_2, \qquad \boldsymbol{K}_2 \; = \; \boldsymbol{0}$$

in terms of the orthonormal basis $(\boldsymbol{e}_1, \boldsymbol{e}_2, \boldsymbol{n})$ shown in the figure. The shear modulus,
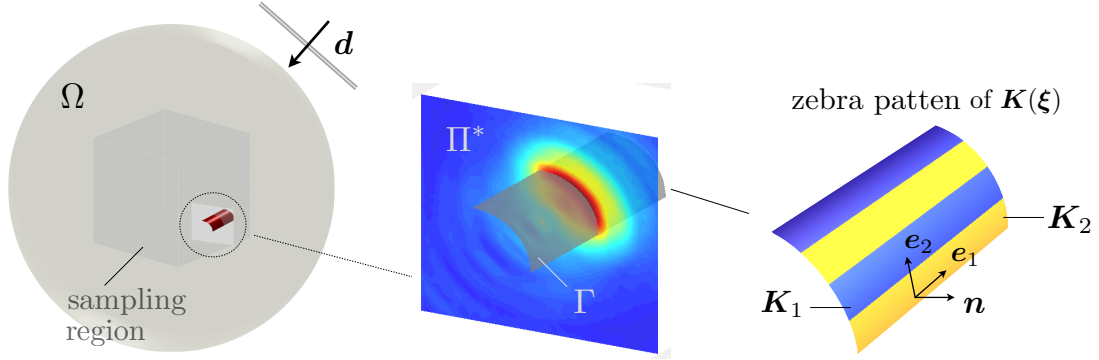
Figure 4.2: Elastic-wave sensing setup (left), position of the cutting plane (middle), and "zebra" pattern of the fracture's heterogeneous contact condition (right).

mass density, and Poisson's ratio of the background solid are taken as $\mu = 1$, $\rho = 1$ and $\nu = 0.35$, whereby the shear and compressional wave speeds read $c_s = 1$ and $c_p = 2.08$, respectively. The interaction of Γ with incident (P- and S-) plane waves, propagating in direction $\boldsymbol{d}$, gives rise to the scattered wavefield $\boldsymbol{v}$ solving (4.2) – whose far-field pattern $\boldsymbol{v}^\infty$ is then computed on the basis of (4.21).

Far-field operator. For both illumination and sensing purposes, the unit sphere Ω is sampled by a uniform grid of $N_\theta \times N_\phi$ observation directions, specified by the polar (θ_j, $j = 1, \ldots N_\theta$) and azimuthal (ϕ_k, $k = 1, \ldots N_\phi$) angle values. With reference to (J1), note that both the polarization vector $\boldsymbol{q} = \boldsymbol{q}_p \oplus \boldsymbol{q}_s$ of an incident plane wave and the far-field pattern $\boldsymbol{v}_{\boldsymbol{q}}^\infty = \boldsymbol{v}_{\boldsymbol{q}_p}^\infty \oplus \boldsymbol{v}_{\boldsymbol{q}_s}^\infty$ of the scattered wave each have *only three* nontrivial components. In this setting, the discretized far-field operator $\mathbf{F}$ is represented as a $3N \times 3N$ matrix ($N = N_\theta N_\phi$) with components

$$\mathbf{F}(3k+1\!:\!3k+3,\ 3j+1\!:\!3j+3) \;=\; \mathbf{W}^\infty(\boldsymbol{d}_j, \hat{\boldsymbol{\xi}}_k), \qquad j, k = 0, \ldots N-1, \qquad (4.68)$$

where

$$\mathbf{W}^\infty(\boldsymbol{d}_j, \hat{\boldsymbol{\xi}}_k) \;=\; \begin{bmatrix} W_{11}^\infty & W_{12}^\infty & W_{13}^\infty \\ W_{21}^\infty & W_{22}^\infty & W_{23}^\infty \\ W_{31}^\infty & W_{32}^\infty & W_{33}^\infty \end{bmatrix} (\boldsymbol{d}_j, \hat{\boldsymbol{\xi}}_k), \qquad (4.69)$$

and W_{kj}^∞ ($j, k = 1, 2, 3$) are specified in (J1). Unless stated otherwise, we assume $N_\theta = 50$ and $N_\phi = 25$.

Noisy data. To account for the presence of noise in measurements, we consider the perturbed far-field operator

$$\mathbf{F}^{\delta} := (\boldsymbol{I} + \boldsymbol{N}_{\epsilon})\,\mathbf{F}, \tag{4.70}$$

where $\boldsymbol{I}$ is the $3N \times 3N$ identity matrix, and $\boldsymbol{N}_{\epsilon}$ is the noise matrix of commensurate dimension whose components are uniformly-distributed (complex) random variables in $[-\epsilon,\,\epsilon]^2$. On the basis of definition (4.53), one has $\delta = \|\boldsymbol{N}_{\epsilon}\mathbf{F}\|$ which in the sequel takes values of up to 20%. With reference to Remark 7, the region of interest

Trial far-field pattern. With reference to Remark 7, the GLSM indicator map (4.66) is constructed by solving (4.55) for the minimizer of (4.54) over a grid of trial infinitesimal fractures $L = \boldsymbol{z} + \mathsf{R}\mathsf{L}$, where $\boldsymbol{z}$ denotes the sampling point and R is a unitary rotation matrix. In what follows, this is accomplished by taking L to be a vanishing penny-shaped fracture with unit normal $\boldsymbol{n}_{\circ}$, i.e. by setting the FOD in (4.42) as $\boldsymbol{a}(\boldsymbol{y}) = \delta(\boldsymbol{y} - \boldsymbol{z})\mathsf{R}\boldsymbol{n}_{\circ}$. Writing for brevity $\mathbf{n} = \mathsf{R}\boldsymbol{n}_{\circ}$, one in particular finds that

$$\boldsymbol{\Phi}_L^{\infty}(\hat{\boldsymbol{\xi}}) \;=\; -\Big(\mathrm{i}k_p\,\hat{\boldsymbol{\xi}}\,[\lambda + 2\mu\,(\mathbf{n}\cdot\hat{\boldsymbol{\xi}})^2]\,e^{-\mathrm{i}k_p\hat{\boldsymbol{\xi}}\cdot\boldsymbol{z}} \;\oplus\; 2\mathrm{i}\mu\,k_s\,\hat{\boldsymbol{\xi}}\times(\mathbf{n}\times\hat{\boldsymbol{\xi}})\,(\mathbf{n}\cdot\hat{\boldsymbol{\xi}})\,e^{-\mathrm{i}k_s\hat{\boldsymbol{\xi}}\cdot\boldsymbol{z}}\Big). \tag{4.71}$$

Recalling (J1), one may note that for each observation direction $\hat{\boldsymbol{\xi}}_k$, (4.71) has only three non-trivial components in the reference $(\hat{\boldsymbol{\xi}}_k, \boldsymbol{\theta}_k, \boldsymbol{\phi}_k)$ orthonormal basis, which are for consistency with (4.69) arranged as a $3N \times 1$ vector

$$\boldsymbol{\Phi}_{\boldsymbol{z},\mathbf{n}}^{\infty}(3k+1\!:\!3k+3) \;=\; \begin{bmatrix} \mathrm{i}k_p[\lambda + 2\mu\,(\mathbf{n}\cdot\hat{\boldsymbol{\xi}}_k)^2]\,e^{-\mathrm{i}k_p\hat{\boldsymbol{\xi}}_k\boldsymbol{z}} \\ 2\mathrm{i}\mu\,k_s(\mathbf{n}\cdot\boldsymbol{\theta}_k)(\mathbf{n}\cdot\hat{\boldsymbol{\xi}}_k)\,e^{-\mathrm{i}k_s\hat{\boldsymbol{\xi}}_k\boldsymbol{z}} \\ 2\mathrm{i}\mu\,k_s(\mathbf{n}\cdot\boldsymbol{\phi}_k)(\mathbf{n}\cdot\hat{\boldsymbol{\xi}}_k)\,e^{-\mathrm{i}k_s\hat{\boldsymbol{\xi}}_k\boldsymbol{z}} \end{bmatrix}, \qquad k = 0,\ldots N-1. \tag{4.72}$$

Accordingly, the far-field equation (4.41) takes the discretized form

$$\mathbf{F}^{\delta}\boldsymbol{g}_{\boldsymbol{z},\mathbf{n}} \;=\; \boldsymbol{\Phi}_{\boldsymbol{z},\mathbf{n}}^{\infty}, \tag{4.73}$$

thus forming the basis for computing GLSM and LSM indicator functionals.

4.6.1 Fracture indicators

As shown in Fig. 4.2, the search area i.e. the sampling region is a *cube of side 2* where the featured (GLSM and LSM) indicator functionals are evaluated. The resulting distributions are plotted either in three dimensions, or in the mid-section of the "true" cylindrical fracture (see Fig. 4.2).

Sampling. In what follows, the search cube $[-1, 1]^3 \subset \mathbb{R}^3$ is probed by a uniform $40{\times}40{\times}40$ grid of sampling points $\boldsymbol{z}$, while the unit sphere – spanning possible fracture orientations – is sampled by a $24{\times}6$ grid of trial normal directions $\mathbf{n} = \mathbf{R}\boldsymbol{n}_\circ$. Accordingly, the fracture indicator map is constructed by solving (4.73) for a total of $M = 64000{\times}144$ trial pairs $(\boldsymbol{z}, \mathbf{n})$.

GLSM indicator. With reference to (4.55) and (4.68)-(4.73), a discretized version of the GLSM solution vector, $\boldsymbol{g}_{\boldsymbol{z},\mathbf{n}}^{\mathrm{GLSM}}$, is computed by solving the linear system

$$\left(\mathbf{F}^{\delta*}\mathbf{F}^\delta + \alpha_{\boldsymbol{z},\mathbf{n}}(\mathbf{F}_\sharp^\delta)^{\frac{1}{2}*}(\mathbf{F}_\sharp^\delta)^{\frac{1}{2}} + \alpha_{\boldsymbol{z},\mathbf{n}}\delta\,\boldsymbol{I}\right)\boldsymbol{g}_{\boldsymbol{z},\mathbf{n}}^{\mathrm{GLSM}} \;=\; \mathbf{F}^{\delta*}\boldsymbol{\Phi}_{\boldsymbol{z},\mathbf{n}}^\infty, \tag{4.74}$$

where $(\cdot)^*$ is the Hermitian operator; $\mathbf{F}_\sharp^\delta$ is evaluated on the basis of definitions (4.45) and (4.46); and, following [12],

$$\alpha_{\boldsymbol{z},\mathbf{n}} \;:=\; \frac{\eta_{\boldsymbol{z},\mathbf{n}}}{\|\,\mathbf{F}^\delta\| + \delta}. \tag{4.75}$$

Here $\eta_{\boldsymbol{z},\mathbf{n}}$ is a regularization parameter of the classical LSM solution (4.77), computed via the Morozov discrepancy principle [102]. With reference to (4.66), the GLSM indicator function is then obtained as

$$I^{\mathscr{G}_\sharp}(\boldsymbol{z}) \;=\; \frac{1}{\sqrt{\|(\mathbf{F}_\sharp^\delta)^{\frac{1}{2}}\boldsymbol{g}_{\boldsymbol{z}}^{\mathrm{GLSM}}\|^2 + \delta\,\|\boldsymbol{g}_{\boldsymbol{z}}^{\mathrm{GLSM}}\|^2}},$$

$$\boldsymbol{g}_{\boldsymbol{z}}^{\mathrm{GLSM}} \;:=\; \mathrm{argmin}_{\boldsymbol{g}_{\boldsymbol{z},\mathbf{n}}^{\mathrm{GLSM}}} \|\boldsymbol{g}_{\boldsymbol{z},\mathbf{n}}^{\mathrm{GLSM}}\|_{L^2(\Omega)}^2, \quad \mathbf{n} \in \Omega. \tag{4.76}$$

LSM indicator. To gain better insight into the effectiveness of the proposed approach, the GLSM reconstruction is compared to a corresponding LSM map. The latter is computed on the basis of a Tikhonov-regularized solution $\boldsymbol{g}_{\boldsymbol{z},\mathbf{n}}^{\mathrm{LSM}}$ to (4.73), namely

$$\boldsymbol{g}_{\boldsymbol{z},\mathbf{n}}^{\mathrm{LSM}} \;:=\; \mathrm{argmin}_{\boldsymbol{g}_{\boldsymbol{z},\mathbf{n}}}\Big\{\,\|\mathbf{F}^\delta\boldsymbol{g}_{\boldsymbol{z},\mathbf{n}} - \boldsymbol{\Phi}_{\boldsymbol{z},\mathbf{n}}^\infty\|_{L^2(\Omega)}^2 + \eta_{\boldsymbol{z},\mathbf{n}}\,\|\boldsymbol{g}_{\boldsymbol{z},\mathbf{n}}\|_{L^2(\Omega)}^2\,\Big\}, \tag{4.77}$$

where the regularization parameter $\eta_{z,\mathbf{n}}$ is obtained by way of Morozov discrepancy principle [102]. On the basis of (4.77), the LSM indicator functional is constructed following [46] as

$$I^{\mathscr{L}}(\boldsymbol{z}) \; := \; \frac{1}{\|\boldsymbol{g}_{\boldsymbol{z}}^{\mathrm{LSM}}\|^2}, \qquad \boldsymbol{g}_{\boldsymbol{z}}^{\mathrm{LSM}} \; := \; \mathrm{argmin}_{\boldsymbol{g}_{\boldsymbol{z,n}}^{\mathrm{LSM}}} \, \|\boldsymbol{g}_{\boldsymbol{z,n}}^{\mathrm{LSM}}\|^2_{L^2(\Omega)}, \; \mathbf{n} \in \Omega. \qquad (4.78)$$

4.6.2 Results

In the sequel, the arclength ($\ell = 0.55$) of a "true" cylindrical fracture in its mid-plane, see Fig. 4.2, is used as a reference length to gauge the illuminating shear wavelength $\lambda_s = 2\pi/k_s$.

Density of the sensing grid. Taking $\lambda_s/\ell = 0.7$, Fig. 4.3 illustrates the sensitivity of the GLSM indicator (4.76) to the spatial density of sensory data, given by $N_\theta \times N_\phi$ incident/observation directions over the unit sphere. This is done by gradual downsampling of the default 50×25 sensing grid. From the panels, it is apparent that for satisfactory geometric reconstruction, the sensing grid should carry at least 100 test directions over Ω. In what follows, the (full-aperture) reconstructions are implemented using a 50×25 grid.
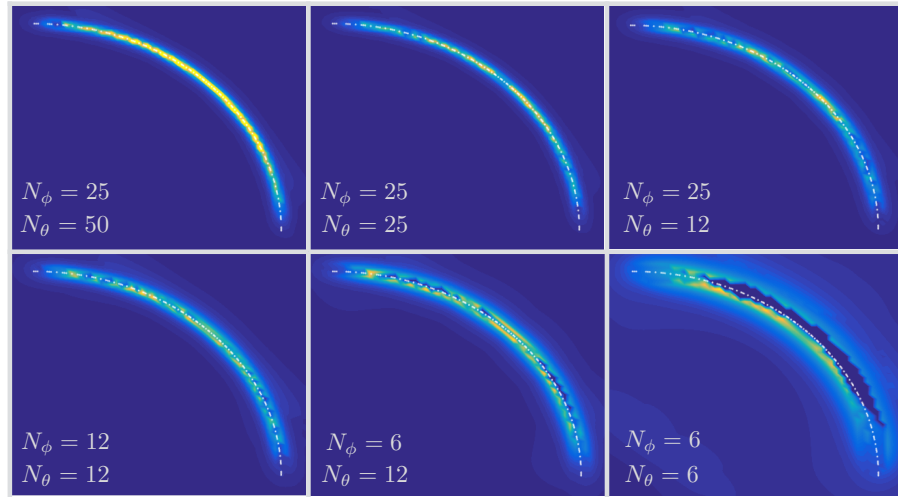
Figure 4.3: Full-aperture GLSM reconstruction of a cylindrical fracture in its mid-section, Π, for $\lambda_s/\ell = 0.7$: effect of density of the $N_\theta \times N_\phi$ sensing grid of illumination/observation directions spanning the unit sphere.

Sensitivity to measurement noise. Assuming full-aperture illumination and sensing, the GLSM and LSM indicators are next compared in terms of their robustness against noise in the far-field data. With reference to (4.70), the levels of "white" noise used to contaminate the boundary integral simulations of the forward scattering problem are taken $\delta = \|\boldsymbol{N}_\epsilon \mathbf{F}\| \in \{0, 0.1, 0.2\}\|\mathbf{F}\|$. On focusing the comparison on the mid-section Π of a "true" fracture, the results are shown in Figs. 4.4, 4.5, and 4.6 assuming the illuminating wavelengths of $\lambda_s/\ell = 1.3$, 0.7, and 0.3, respectively. Note that $\delta\% :=$ $\delta/\|\mathbf{F}\|$. As can be seen from the display, the GLSM indicator (4.76) inherits the superior localization ability of its LSM predecessor (4.78), while carrying far greater robustness to noise in the sensory data.
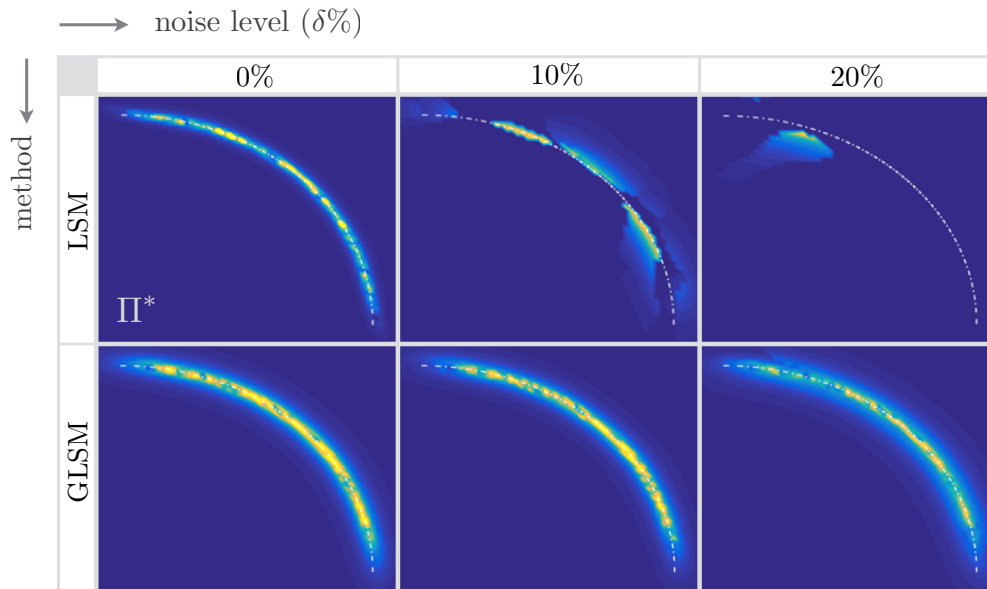
Figure 4.4: Sensitivity to measurement noise for $\lambda_s/\ell = 1.3$: Full-aperture reconstruction of a cylindrical fracture, mid-section Π, by the LSM indicator (top panels) and its GLSM counterpart (bottom panels).

Effect of the sensing aperture. The ramifications of an incomplete aperture on the quality of fracture reconstruction are illustrated in Figs. 4.7 and 4.8, where only *the "upper" half* of Ω in Fig. 4.2 is available for the purposes of illumination and observation. More specifically, Figs. 4.7 and 4.8 depict the GLSM and LSM fields in the mid-section of Γ at "long" ($\lambda_s/\ell = 1.3$) and "short" ($\lambda_s/\ell = 0.3$) excitation wavelengths, respectively,
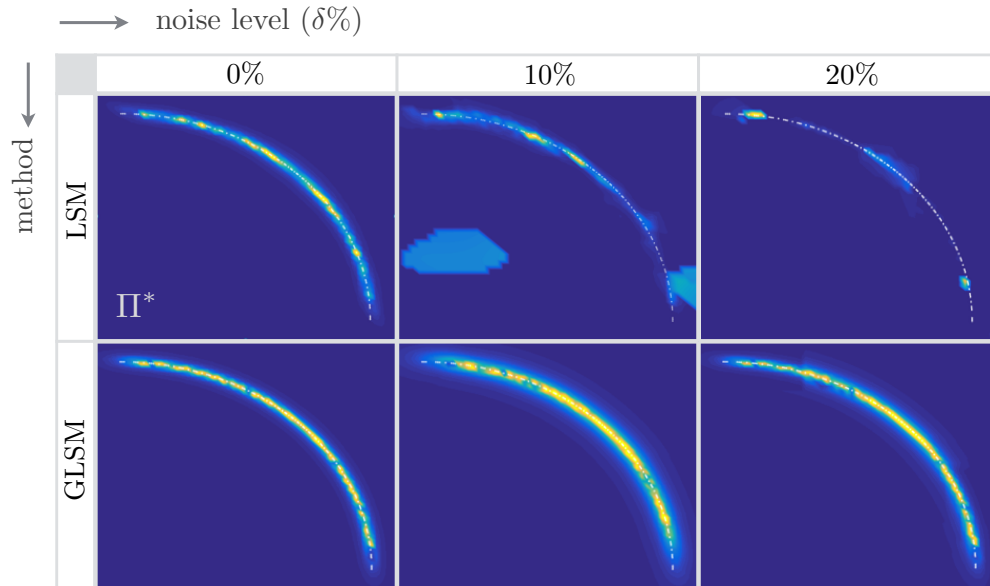
Figure 4.5: Sensitivity to measurement noise for $\lambda_s/\ell = 0.7$: Full-aperture reconstruction of a cylindrical fracture, mid-section Π, by the LSM indicator (top panels) and its GLSM counterpart (bottom panels).
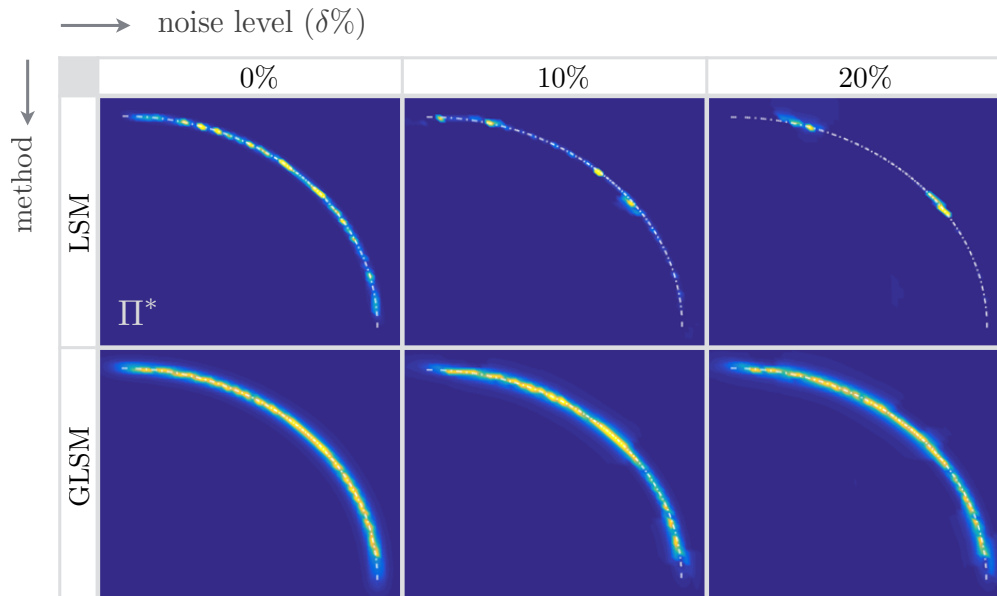
Figure 4.6: Sensitivity to measurement noise for $\lambda_s/\ell = 0.3$: Full-aperture reconstruction of a cylindrical fracture, mid-section Π, by the LSM indicator (top panels) and its GLSM counterpart (bottom panels).

noise level ($\delta\%$)

method

	0%	10%	20%
LSM			
GLSM			
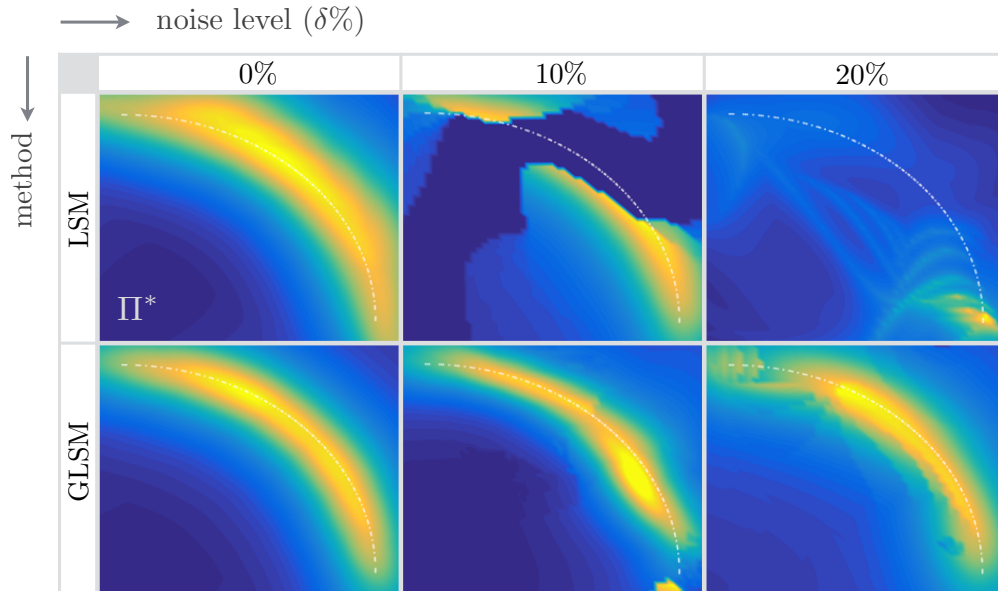
Figure 4.7: Half-aperture reconstruction of a cylindrical fracture, mid-section Π, for $\lambda_s/\ell = 1.3$: sensitivity of the LSM indicator (top panels) and its GLSM counterpart (bottom panels) to noise in the measurements.

noise level ($\delta\%$)

method

	0%	10%	20%
LSM			
GLSM			
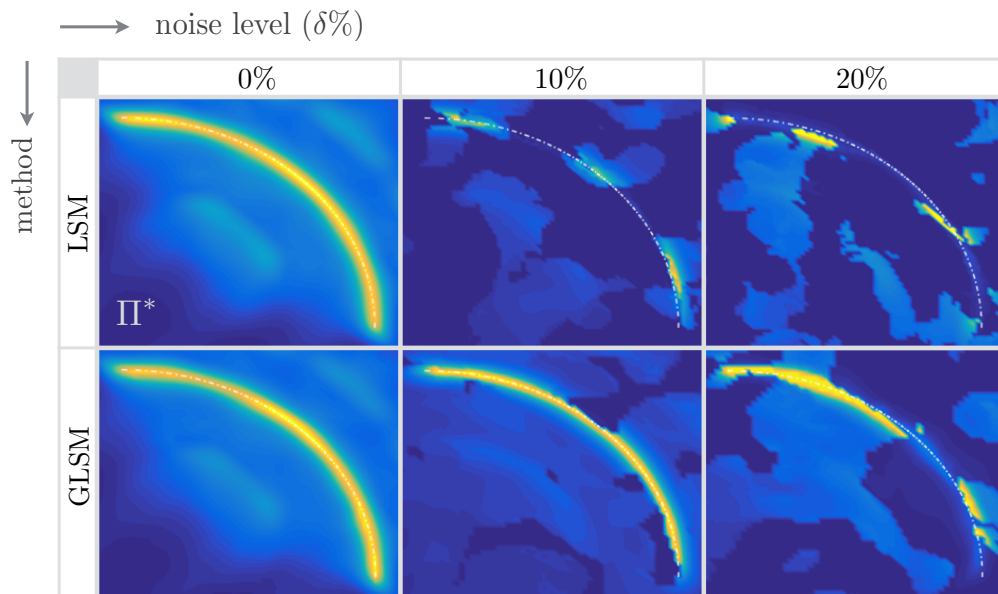
Figure 4.8: Half-aperture reconstruction of a cylindrical fracture, mid-section Π, for $\lambda_s/\ell = 0.3$: sensitivity of the LSM indicator (top panels) and its GLSM counterpart (bottom panels) to noise in the measurements.

constructed from the half-aperture sensory data. While the loss of resolution in both GLSM and LSM maps is clear relative to Figs. 4.4 and 4.6, it is noted that (for the problem under consideration) the GLSM indicator offers far better robustness to noise, providing acceptable reconstruction of Γ for δ as high as $0.1\|\mathbf{F}\|$.

3D reconstruction. For completeness, Fig. 4.9 illustrates the full-aperture GLSM reconstruction of Γ inside the sampling region $[-1,1]^3$, assuming $\lambda_s/\ell = 1.3$ and $\delta\% = 10$ (top panels) and $\lambda_s/\ell = 0.7$ and $\delta\% = 5$ (bottom panels). For clarity, the indicator maps are thresholded by 10%, i.e. only the sampling points whose $I^{\mathscr{G}_\sharp}(\boldsymbol{z})$ values are higher than ten percent of the global maximum value are shown (left panels). Then, a scattered interpolant is constructed based on thus obtained 3D cloud of points, giving an optimal reconstruction of the fracture surface. The latter is generated by (i) projecting the thresholded GLSM map onto a reference plane (the $X - Y$ plane in this example), and (ii) defining a suitable grid of points covering the projected area. This forms the sought-for input for the scattered interpolant providing a 3D reconstruction of the fracture interface, as shown in the middle panels of Fig. 4.9. Due in part to a scattered nature of the interpolant, thus obtained fracture surface will suffer from some artificial roughness – that depends for example on the density of sampling points and an ad-hoc thresholding parameter. This issue may be mitigated by implementing a suitable spatial (e.g. moving average) filter, as shown in the right panels of Fig. 4.9.
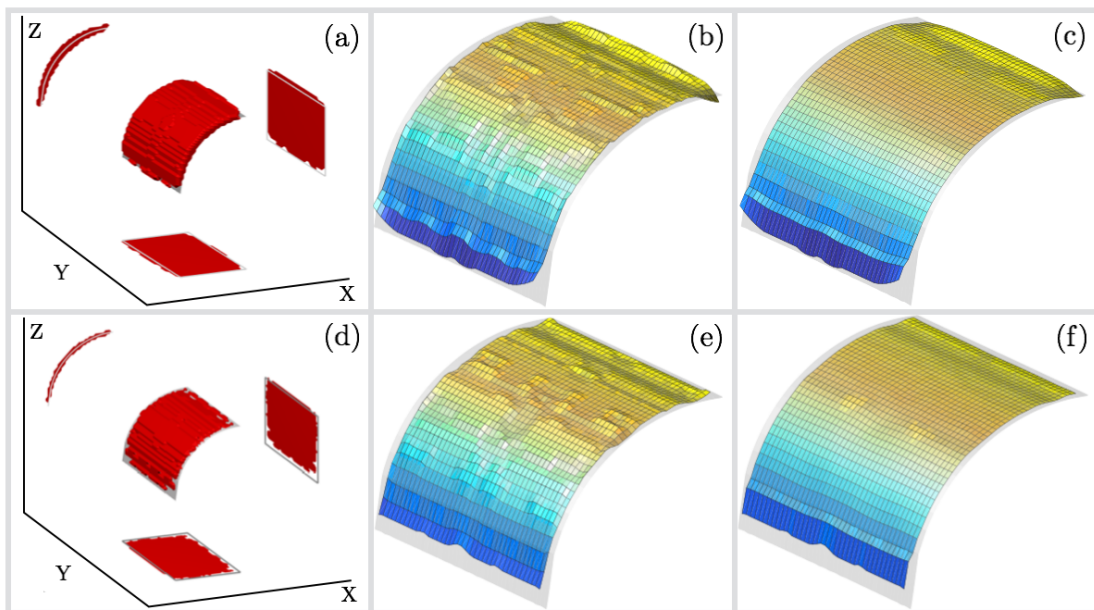
Figure 4.9: Full-aperture 3D GLSM reconstruction for $\{\lambda_s/\ell = 1.3, \delta\% = 0.1\}$ (top) and $\{\lambda_s/\ell = 0.7, \delta\% = 0.05\}$ (bottom): GLSM indicator (4.76) thresholded at 10% (left), fracture surface as reconstructed from the 3D cloud of points (middle), and fracture reconstruction after the application of a mean filter (right).

Chapter 5

From geometric reconstruction to interfacial characterization

This chapter integrates the robust imaging tools developed in Chapters 3 and 4 – for the *geometric* reconstruction of heterogeneous fractures from remote data, and the boundary integral equations to enable a quantitative identification of *interfacial condition* at the boundary of subsurface discontinuities. To this end, by taking advantage of the shape reconstruction capability of GLSM and TS – both agnostic with respect to the contact law at the boundary of hidden scatterers, the idea is to first reconstruct the (generally non-planar and unconnected) fracture geometry *without* the knowledge of its intefacial condition. Given a proper approximation of the fracture support, a boundary integrals map is constructed – on the basis of double layer potential, to recover the FOD profile, i.e. the displacement jump distribution, along the fracture surface from the measured waveforms. This is then utilized as an input to solve the traction boundary integral equation – defined over the (recovered) fracture surface, for the unknown contact parameters i.e. heterogeneous specific stiffness profile in shear and normal directions. To facilitate a high-fidelity inversion of interfacial stiffness, a 3-step regularization algorithm is devised aiming at minimizing the error associated with the recovered fracture geometry and FOD profile. The performance of the proposed hybrid algorithm is illustrated in a set of numerical experiments where (curved) fractures endowed with two sets of interfacial stiffness patterns are reconstructed – in terms of both geometry and interfacial condition, from far-field data.

5.1 Non-iterative imaging and characterization of fractures

Preliminaries. Consider a fracture of generally non-planar and unconnected support $\Gamma \subset \mathbb{R}^3$, endowed with inhomogeneous specific stiffness matrix $\boldsymbol{K}(\boldsymbol{\xi})$. The fracture is embedded in an elastic domain Ω with (known) shear modulus μ, Poisson's ratio ν, and mass density ρ. As illustrated in Fig. 5.1 – describing a generic seismic experiment, the fracture can be "illuminated" by either boundary (i.e. surface) excitation, subterranean point sources, or plane waves of density $\boldsymbol{g}$ defined over the source grid (namely the union of germane source locations or directions), which gives rise to the incident field $\boldsymbol{u}^i$. Thus induced scattered field $\tilde{\boldsymbol{u}}$ is measured over a generic sensing array S^{obs} in that $\boldsymbol{u}^{\mathrm{obs}} = \tilde{\boldsymbol{u}} + \boldsymbol{u}^i$, where $\boldsymbol{u}^{\mathrm{obs}}$ are the experimental waveforms captured on S^{obs}. The seismic excitation is *time-harmonic* with frequency ω, whereby the field equations and boundary conditions governing $\tilde{\boldsymbol{u}}$ are given by

$$
\begin{aligned}
\nabla \cdot [\boldsymbol{C} \colon \nabla \tilde{\boldsymbol{u}}](\boldsymbol{\xi}) &= -\rho(\boldsymbol{\xi}) \omega^2 \tilde{\boldsymbol{u}}(\boldsymbol{\xi}), & \boldsymbol{\xi} \in \Omega \backslash \Gamma, \\
\tilde{\boldsymbol{t}}(\boldsymbol{\xi}) &= \boldsymbol{K}(\boldsymbol{\xi}) \cdot [\![\tilde{\boldsymbol{u}}]\!](\boldsymbol{\xi}) - \boldsymbol{t}_f(\boldsymbol{\xi}), & \boldsymbol{\xi} \in \Gamma, \\
\tilde{\boldsymbol{t}}(\boldsymbol{\xi}) &= \boldsymbol{0}, & \boldsymbol{\xi} \in S,
\end{aligned}
\tag{5.1}
$$
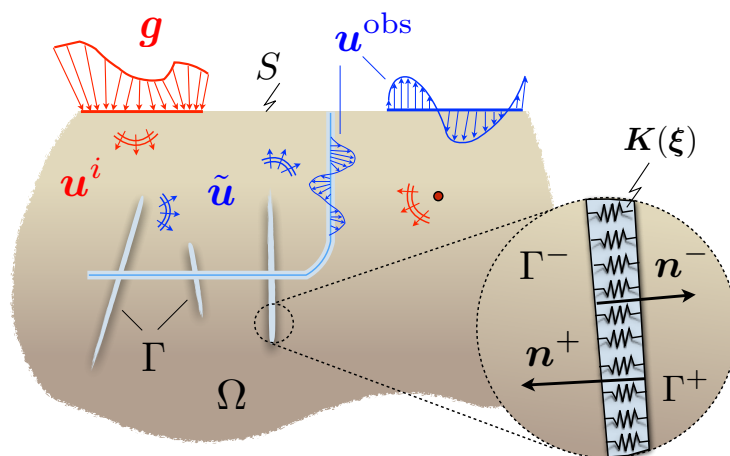
Figure 5.1: A generic seismic experiment: Fracture $\Gamma \in \Omega$ with heterogeneous specific stiffness $\boldsymbol{K}(\boldsymbol{\xi})$ is illuminated by a set of surface excitations over S (or point sources in Ω) of density profile $\boldsymbol{g}$, generating the free field $\boldsymbol{u}^i$ in Ω; The interaction of $\boldsymbol{u}^i$ with Γ gives rise to the scattered wavefield $\tilde{\boldsymbol{u}}$ in $\Omega \backslash \Gamma$ which is measured over the observation surface as $\boldsymbol{u}^{\mathrm{obs}}$.
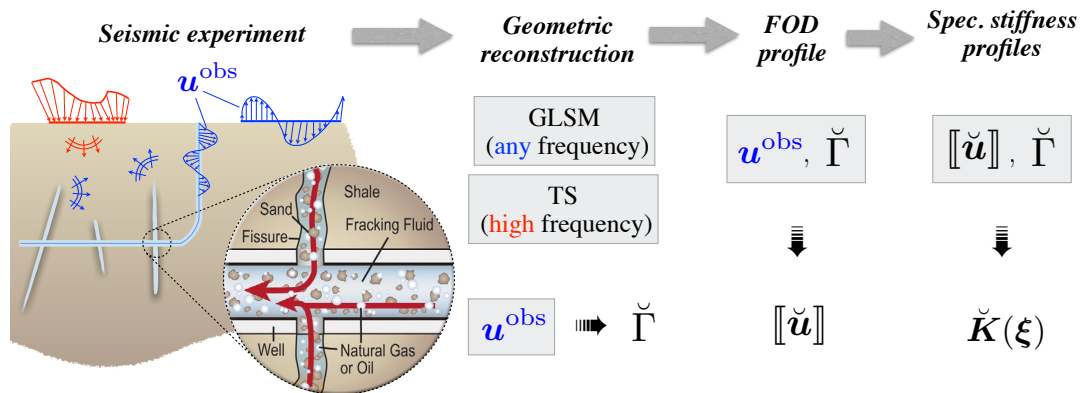
Figure 5.2: Three-step approach to non-iterative reconstruction and characterization of heterogeneous fractures.

complemented by the exterior boundary (or radiation) conditions as applicable [2, 88]. Here, $\tilde{\boldsymbol{t}} = \boldsymbol{n} \cdot \boldsymbol{C} : \nabla \tilde{\boldsymbol{u}}$ and $\boldsymbol{t}_f = \boldsymbol{n} \cdot \boldsymbol{C} : \nabla \boldsymbol{u}^i$ denote respectively the scattered- and free-field tractions on Γ with unit normal $\boldsymbol{n} = \boldsymbol{n}^-(\boldsymbol{\xi})$; $\boldsymbol{C}$ is the elasticity tensor, and $[\![\tilde{\boldsymbol{u}}]\!]$ is the fracture opening displacement (FOD), i.e. the displacement jump across Γ.

Inverse solution. Taking advantage of the developments in Chapters 2–4, a unique 3-step approach is proposed as in Fig. 5.2 for the non-iterative waveform sensing of heterogeneous subsurface fractures (e.g. hydraulic fractures) where:

- The *fracture geometry* $\breve{\Gamma}$ is reconstructed in 3D irrespective of its (heterogeneous) contact condition via the TS and GLSM methods;

- The *FOD profile* $[\![\breve{\boldsymbol{u}}]\!]$ over the reconstructed fracture support $\breve{\Gamma}$ is recovered from the germane boundary integral representation of the scattered field, and

- The distribution of *specific stiffness* $\breve{\boldsymbol{K}}(\boldsymbol{\xi})$ (given e.g. by its normal and shear components) is recovered from the knowledge of $[\![\breve{\boldsymbol{u}}]\!]$ and $\breve{\Gamma}$.

These basic steps are elucidated in the sequel.

5.1.1 3D geometric reconstruction

In light of the Topological Sensitivity (TS) framework established in Chapter 2 and Chapter 3 for the shape reconstruction of fractures – corroborated by the numerical and laboratory results (see Figs. 2.1 and 3.9–3.10), the idea is to make use of the TS as

a non-iterative (inverse scattering) tool for the *high-frequency* reconstruction of fracture surfaces, applicable to situations where the illuminating wavelength is shorter than the characteristic fracture size. In situations where such illumination is not possible due to e.g. heterogeneity of rock (which inherently scatters and thus attenuates high-frequency seismic waves), the GLSM approach developed Chapter 4 can be used as a robust imaging companion which inherently works in *both* high- and "low"- frequency regimes. Note that in cases where high-frequency data are available, both TS and GLSM schemes may be deployed toward elevated robustness of geometric fracture reconstruction.

Remark 12. *Both GLSM and TS techniques are generic in that they apply to finite, semi-infinite, or infinite (homogeneous or piecewise-homogeneous) background domains Ω – whose elastic and density properties are known beforehand.*

Remark 13. *For generality, it should be noted that geometric fracture reconstruction may also be accomplished via other application-specific inversion schemes, e.g. microseismic imaging – which deploys travel time inversion or migration of seismic events generated during fracking [112]. The proposed TS and GLSM techniques are, however, part of a more general waveform inversion platform which is both (i) computationally efficient due to its non-iterative nature; (ii) self-contained for it uses the common set of sensory data for both geometric reconstruction and interfacial characterization, and (iii) robust by providing significant flexibility in terms of the sensing configuration and requiring no a priori knowledge on the fracture geometry nor its boundary condition.*

5.1.2   Inversion of the FOD profile

Given a suitable approximation of the fracture geometry $\breve{\Gamma}$ – obtained as described in Section 5.1.1, the integral representation of the scattered field [33] serves as *a map* $\boldsymbol{M} \colon \tilde{H}^{1/2}(\breve{\Gamma}) \to H^{1/2}(S^{\mathrm{obs}})$ relating the sought FOD $[\![\breve{\boldsymbol{u}}]\!]$ to the sensory data $\tilde{\boldsymbol{u}}^{\mathrm{obs}} = \boldsymbol{u}^{\mathrm{obs}} - \boldsymbol{u}^i$, namely

$$\boldsymbol{M}[\![\breve{\boldsymbol{u}}]\!](\boldsymbol{\xi}) \;=\; [\boldsymbol{u}^{\mathrm{obs}} - \boldsymbol{u}^i](\boldsymbol{\xi}), \qquad \boldsymbol{M}[\![\breve{\boldsymbol{u}}]\!] \;:=\; \int_{\breve{\Gamma}} ([\![\breve{\boldsymbol{u}}]\!] \otimes \breve{\boldsymbol{n}}) \colon \boldsymbol{\Sigma} \; \mathrm{d}S_{\boldsymbol{x}}, \qquad \boldsymbol{\xi} \in S^{\mathrm{obs}} \quad (5.2)$$

where $\boldsymbol{x} \in \breve{\Gamma}$; $\breve{\boldsymbol{n}} = \breve{\boldsymbol{n}}(\boldsymbol{x})$ denotes the unit normal on $\breve{\Gamma}$; and, $\boldsymbol{\Sigma} = \boldsymbol{\Sigma}(\boldsymbol{\xi}, \boldsymbol{x}, \omega)$ is the elastodynamic stress Green's function for a given reference domain – namely the Cauchy stress tensor at $\boldsymbol{\xi} \in \Omega$ due to a point load applied in the three coordinate directions

at $\boldsymbol{x} \in \breve{\Gamma}$, see Appendix F when $\Omega = \mathbb{R}^3$ and [88] when Ω is a layered half-space (as in seismic experiments). Note that the kernel $\boldsymbol{\Sigma}$ is regular for all $\boldsymbol{x} \in \breve{\Gamma}$ since one may reasonably assume that $\breve{\Gamma} \cap S^{\mathrm{obs}} = \emptyset$, i.e. that the fracture surface does not intersect the sensing array.

Discretization. Considering S^{obs} as a union of discrete sensing points – as is typically the case in seismic experiments (see Fig. 5.2), and allowing the reconstructed fracture surface $\breve{\Gamma}$ to be arbitrarily complex, a discrete version of $\boldsymbol{M}[\![\breve{\boldsymbol{u}}]\!]$ may be obtained via suitable discretization of $\breve{\Gamma}$ and FOD in terms of surface (i.e. boundary) elements, see Appendix G and [33]. As a result, (5.2) can be recast using the collocation method as

$$\mathbf{M}[\![\breve{\mathbf{u}}]\!] \;=\; \tilde{\mathbf{u}}^{\mathrm{obs}}, \tag{5.3}$$

where $\mathbf{M}$ is a $3N^{\mathrm{obs}} \times 3N^{\mathrm{nds}}$ coefficient matrix; $[\![\breve{\mathbf{u}}]\!]$ is a vector sampling the FOD at N^{nds} geometric nodes over $\breve{\Gamma}$ (see the middle panel in Fig. 8.6), and $\tilde{\mathbf{u}}^{\mathrm{obs}}$ collects the triaxial scattered field $(\mathbf{u}^{\mathrm{obs}} - \mathbf{u}^i)$ at N^{obs} sensing points over S^{obs}. Note that the components of $\mathbf{M}$ can be evaluated without regularization thanks to the regularity of kernel $\boldsymbol{\Sigma}$ in (5.2).

Solution. In this setting, the idea is to have $N^{\mathrm{nds}} < N^{\mathrm{obs}}$ and to compute the FOD profile on $\breve{\Gamma}$ from the measurements $\tilde{\mathbf{u}}^{\mathrm{obs}}$ by solving the *overdetermined* linear system (5.3). Accordingly, the *resolution* of the FOD reconstruction will inherently be controlled by the number of (triaxial) sensors on S^{obs}. Note that for every seismic excitation $p = 1, \ldots P$, over the incident grid (see Fig. 5.2), (5.3) can be solved anew for each right-hand side $(\mathbf{u}^{\mathrm{obs}} - \mathbf{u}^i)_p$ where $\mathbf{M}$ is invariant i.e. source-independent.

Regularization. A critical point in recovering the FOD – which directly affects the inversion of specific stiffness via singular value decomposition (SVD) – is that (5.3) is typically *ill-posed* in that $\mathbf{M}$ contains *zero or near-zero singular values*. This problem may arise due to either a *limited "viewing" aperture* furnished by S^{obs}, or the emergence of *interfacial scattered waves* – propagating along the fracture surface [138] – that cannot be sensed on S^{obs} (see Section 5.2). Accordingly, (5.3) can be solved via suitable regularization, e.g. Tikhonov regularization aided by the Morozov discrepancy principle (which takes the regularization parameter to be commensurate with the level of noise

in the data) [99]. As examined next, the span of eigenvectors corresponding to unacceptably small singular eigenvalues of $\mathbf{M}$ (eliminated by regularization) determines the FOD subspace *to be avoided* when reconstructing the profile of specific stiffnesses.

5.1.3   Inversion of heterogeneous specific stiffnesses

The last step in the proposed inverse scheme is to substitute the identified FOD $[\![\breve{\boldsymbol{u}}]\!]$ into the fracture's *boundary condition* on $\breve{\Gamma}$, namely

$$\breve{\boldsymbol{t}}(\boldsymbol{\xi}) \; = \; \breve{\boldsymbol{K}}(\boldsymbol{\xi})\,[\![\breve{\boldsymbol{u}}]\!](\boldsymbol{\xi}) - \breve{\boldsymbol{t}}_f(\boldsymbol{\xi}), \qquad \boldsymbol{\xi} \in \breve{\Gamma}, \tag{5.4}$$

to be solved for specific stiffness $\breve{\boldsymbol{K}}(\boldsymbol{\xi})$. Here, $\breve{\boldsymbol{t}}_f = \breve{\boldsymbol{n}} \cdot \boldsymbol{C} : \nabla \boldsymbol{u}^i$ is the incident-field traction over $\breve{\Gamma}$, while $\breve{\boldsymbol{t}}$ is the scattered-field traction on $\breve{\Gamma}$ expressed in terms of $[\![\breve{\boldsymbol{u}}]\!]$ by invoking the Traction Boundary Integral Equation (TBIE) [134, 33] as a map $\boldsymbol{T} \colon \tilde{H}^{1/2}(\breve{\Gamma}) \to H^{-1/2}(\breve{\Gamma})$ such that

$$\boldsymbol{T}[\![\breve{\boldsymbol{u}}]\!](\boldsymbol{\xi}) := \breve{\boldsymbol{t}}(\boldsymbol{\xi}) \; = \; -\breve{\boldsymbol{n}} \cdot \boldsymbol{C} : \fint_{\breve{\Gamma}} \boldsymbol{\Sigma} : \boldsymbol{D}_{\boldsymbol{x}}[\![\breve{\boldsymbol{u}}]\!](\boldsymbol{x})\,\mathrm{d}S_{\boldsymbol{x}} \; +$$
$$\rho\omega^2 \breve{\boldsymbol{n}} \cdot \boldsymbol{C} : \int_{\breve{\Gamma}} \boldsymbol{U} \cdot ([\![\breve{\boldsymbol{u}}]\!] \otimes \breve{\boldsymbol{n}})(\boldsymbol{x})\,\mathrm{d}S_{\boldsymbol{x}}, \qquad \boldsymbol{\xi} \in \breve{\Gamma}, \tag{5.5}$$

where $\boldsymbol{U} = \boldsymbol{U}(\boldsymbol{\xi}, \boldsymbol{x}, \omega)$ and $\boldsymbol{\Sigma} = \boldsymbol{\Sigma}(\boldsymbol{\xi}, \boldsymbol{x}, \omega)$, arranged as tensors, denote respectively the elastodynamic displacement and stress Green's function at $\boldsymbol{\xi}$ due to point force acting at $\boldsymbol{x} \in \Omega$ (see Appendix F and [88, 33]); $\fint$ signifies the Cauchy-principal-value integral, and $\boldsymbol{D}_{\boldsymbol{x}}$ is the *tangential differential operator* (3.14) on $\breve{\Gamma}$.

Remark 14. *Given the FOD $[\![\breve{\boldsymbol{u}}]\!]$ over $\breve{\Gamma}$, the scattered-field traction $\breve{\boldsymbol{t}}(\boldsymbol{\xi})$ in (5.4) may also be computed without the knowledge of $\breve{\boldsymbol{K}}$ in an FEM platform. This is accomplished by imposing $[\![\breve{\boldsymbol{u}}]\!]$ as a Dirichlet boundary condition on $\breve{\Gamma}$ and solving the resulting boundary value problem in $\Omega \backslash \breve{\Gamma}$ for the associated traction $\breve{\boldsymbol{t}}(\boldsymbol{\xi})$ over $\breve{\Gamma}$.*

Discretization.   By deploying the collocation method as discussed in Section 5.1.2, a discretized version of $\boldsymbol{T}[\![\breve{\boldsymbol{u}}]\!]$ can be obtained as

$$\mathbf{T}[\![\breve{\mathbf{u}}]\!] \; = \; \breve{\mathbf{t}}, \tag{5.6}$$

where $\mathbf{T}$ is a $3N^{\mathrm{col}} \times 3N^{\mathrm{nds}}$ coefficient matrix, and $\check{\mathbf{t}}$ is a vector sampling the scattered-field traction at N^{col} collocation points (see the middle panel in Fig. 8.6) over $\check{\Gamma}$. For clarity, let us recall that owing to the smoothness requirement by the TBIE (imposed by presence of the tangential differential operator $\boldsymbol{D_x}$), the FOD $[\![\check{\mathbf{u}}]\!](\boldsymbol{x})$ in (5.5) is parametrized via *non-conforming* interpolation where the collocation points are situated *inside* the boundary elements (see Appendix G for details). As discussed in the sequel, the number of collocation points N^{col} – carrying the parametrization of the unknown interfacial stiffness – can be either smaller or larger than the number of geometric nodes N^{nds} used to describe $\check{\Gamma}$. It should also be noted that, since the collocation points in the TBIE belong to the fracture surface i.e. $\boldsymbol{\xi} \in \check{\Gamma}$, the first boundary integral on the right-hand-side of (5.5) is singular and must be regularized as discussed in Appendix G. Given (5.4) and (5.6), the discretized contact condition on $\check{\Gamma}$ reads

$$\check{\mathbf{K}}[\![\check{\mathbf{u}}]\!] \;=\; \mathbf{T}[\![\check{\mathbf{u}}]\!] + \check{\mathbf{t}}_f, \tag{5.7}$$

where $\check{\mathbf{K}}$ is a $3N^{\mathrm{col}} \times 3N^{\mathrm{nds}}$ stiffness matrix, and $\check{\mathbf{t}}_f$ is the free-field traction vector sampled at N^{col} collocation points over $\check{\Gamma}$.

Solution. To solve (5.7) for the entries of $\check{\mathbf{K}}$, one may consider the following parameterizations:

1. Assuming $\check{\boldsymbol{K}}$ to be diagonal in the fracture's local coordinates, namely $\check{\boldsymbol{K}} = \mathrm{diag}(\check{k}_n, \check{k}_{s_1}, \check{k}_{s_2})$, the specific stiffness distribution can be directly parametrized in terms of the values at collocation points. In particular, the left hand side of (5.7) can be recast as

$$\check{\mathbf{K}}[\![\check{\mathbf{u}}]\!] \;=\; \check{\mathbf{F}}_1 \check{\mathbf{k}}, \qquad \check{\mathbf{F}}_1 \;:=\; \check{\mathbf{F}}_1[\![\check{\mathbf{u}}]\!], \tag{5.8}$$

where $\check{\mathbf{F}}_1$ is a $3N^{\mathrm{col}} \times 3N^{\mathrm{col}}$ coefficient matrix affiliated with a given FOD profile $[\![\check{\mathbf{u}}]\!]$, and $\check{\mathbf{k}}$ is a $3N^{\mathrm{col}}$-vector sampling the normal and shear stiffness coefficients, i.e. $\{\check{k}_n, \check{k}_{s_1}, \check{k}_{s_2}\}$ at N^{col} collocation nodes over $\check{\Gamma}$. Assuming m internal collocation points per boundary element in the evaluation of (5.6), one accordingly has $N^{\mathrm{col}} = mN^{\mathrm{el}} \gtreqless N^{\mathrm{nds}}$, where N^{el} denotes the number of boundary elements, see Fig. 8.6. On substituting (5.8) into (5.7), one may now solve for the three components of the unknown interfacial stiffness profile $\check{\mathbf{k}}$.

2.   In situations where $\check{\boldsymbol{K}}(\boldsymbol{\xi})$ is *fully populated* whereby the number of unknowns per contact point is six, the specific stiffness distribution is parametrized using the previously established *geometric interpolation* – so that the unknowns are evaluated at N^{nds} geometric nodes. In this setting, one finds

$$\check{\mathbf{K}}[\![\check{\mathbf{u}}]\!] \;=\; \check{\mathbf{F}}_2\check{\mathbf{k}}, \qquad \check{\mathbf{F}}_2 \;:=\; \check{\mathbf{F}}_2[\![\check{\mathbf{u}}]\!], \tag{5.9}$$

where $\check{\mathbf{F}}_2$ is a $3N^{\mathrm{col}} \times 6N^{\mathrm{nds}}$ coefficient matrix, and $\check{\mathbf{k}}$ is a $6N^{\mathrm{nds}}$-vector collecting the six entries of the symmetric stiffness matrix $\check{\mathbf{K}}$ sampled at N^{nds} geometric nodes over $\check{\Gamma}$. Accordingly, by taking m internal collocation points per element so that $N^{\mathrm{col}} = mN^{\mathrm{el}} \geqslant 2N^{\mathrm{nds}}$, one obtains the sufficient of equations to solve (5.7) for $\check{\mathbf{k}}$.

Regularization.   To help construct a robust solution to (5.7), a *3-step* regularization algorithm is devised aiming at minimizing the error due to: 1) the local FOD modes e.g. interface waves, 2) the differentiation of FOD according to $\boldsymbol{D_x}$ in (5.5), and 3) the presence of areas on $\check{\Gamma}$ with near-zero FOD values. These three steps of regularization are elucidated in the sequel. To aid the ensuing discussion, let us introduce the singular value decomposition (SVD) of the matrices $\mathbf{M}$ and $\mathbf{T}$ as follows

$$\mathbf{M} = \mathbf{U}_{\mathrm{M}}\boldsymbol{\Lambda}_{\mathrm{M}}\mathbf{V}_{\mathrm{M}}^*, \qquad \mathbf{T} = \mathbf{U}_{\mathrm{T}}\boldsymbol{\Lambda}_{\mathrm{T}}\mathbf{V}_{\mathrm{T}}^*, \tag{5.10}$$

where $\mathbf{U}$ (resp. $\mathbf{V}$) collects the left (resp. right) eigenvectors of a given matrix, while $\boldsymbol{\Lambda}$ signifies its singular values.

"Unrecoverable" modes contributing to FOD.   Recalling the solution procedure of (5.3) and assuming multiple seismic excitations ($p = 1, \ldots P$), the idea is to *synthetically recombine* the available scattered field data $\tilde{\mathbf{u}}^{\mathrm{obs},p}$ (associated to every seismic excitation) in order to minimize the participation of "local" modes (e.g. surface waves) in the associated FOD profile $[\![\check{\mathbf{u}}]\!]$. To do so, let us denote by $\mathbf{U}_{\mathrm{M,q}}$ ($\mathrm{q}=1, 2, \ldots Q$) the *left eigenvectors* affiliated with the Q *smallest singular values* of $\mathbf{M}$ that are suppressed

by the regularization of (5.3). Now, by solving

$$\Big(\sum_{p=1}^{P} g_p\, \tilde{\mathbf{u}}^{\mathrm{obs},p}\Big) \cdot \mathbf{U}_{\mathrm{M,q}} \;=\; 0, \qquad q = \overline{1,Q}, \tag{5.11}$$

for the (synthetic) source density $\boldsymbol{g} = (g_1, g_2, \ldots, g_P)$, one may reduce the participation of "undesired" left eigenvectors of $\mathbf{M}$, i.e. $\mathbf{U}_{\mathrm{M,q}}$, in the right-hand-side of (5.3) that is a weighted summation of sensory data. This, on one hand, helps circumvent the ill-posedness, if any, of (5.3), and on the other hand, decreases the contribution of local modes – which are difficult to retrieve due to their "weak" signature in measurements – to the solution of (5.3). The resulting FOD profile, thanks to the linearity of the forward problem, can be recast as

$$\llbracket \breve{\mathbf{u}} \rrbracket \;=\; \sum_{p=1}^{P} g_p\, \llbracket \breve{\mathbf{u}} \rrbracket^p,$$

where $\llbracket \breve{\mathbf{u}} \rrbracket^p$ represents the FOD associated with the pth seismic source, as reconstructed in Section 5.1.2. At this point, one may proceed with solving (5.7) for the specific stiffness profile $\breve{\mathbf{k}}$ by setting $\breve{\mathbf{t}}^{\mathrm{f}} = \sum_{p=1}^{P} g_p\, \breve{\mathbf{t}}_p^{\mathrm{f}}$ where $\breve{\mathbf{t}}_p^{\mathrm{f}}$ is the free-field traction on $\breve{\Gamma}$ due to the pth incident field.

Remark 15. *Assuming $P < Q$ in solving (5.11), the "density" g_p of each seismic source can be computed via least squares. When $P > Q$, however, one can take Q out of P available sets of sensory data to construct an even-determined problem.*

Regularizing T. This step deals with the smoothing of $\mathbf{T}$, see (5.5) and (5.6), that is constructed on the basis of the recovered fracture support $\breve{\Gamma}$ and entails tangential derivation. As a result, $\mathbf{T}$ may contain large eigenvalues, e.g. due to the approximate nature of $\breve{\Gamma}$ and its roughness, leading to amplification of small errors in $\llbracket \breve{\mathbf{u}} \rrbracket$ while computing the right-hand-side of (5.7). To resolve this, let us denote by $\mathbf{V}_{\mathrm{T,i}}$ ($i = 1, 2, \ldots N$) the *right eigenvectors* of $\mathbf{T}$ contributing to the construction of $\llbracket \breve{\mathbf{u}} \rrbracket$ beyond a designated threshold δ (a measure of error in the reconstructed FOD), namely

$$\Big\| \llbracket \breve{\mathbf{u}} \rrbracket - \sum_{i=1}^{N} (\llbracket \breve{\mathbf{u}} \rrbracket \cdot \mathbf{V}_{\mathrm{T,i}}) \mathbf{V}_{\mathrm{T,i}} \Big\| \;<\; \delta.$$

In this setting, $\check{\mathbf{t}} = \mathbf{T} \, [\![\check{\mathbf{u}}]\!]$ in (5.7) may be regularized via the following approximation

$$\check{\mathbf{t}} \simeq \sum_{i=1}^{N} \left(\mathbf{T} \, [\![\check{\mathbf{u}}]\!] \cdot \mathbf{U}_{\mathrm{T},i}\right) \mathbf{U}_{\mathrm{T},i},$$

where $\mathbf{U}_{\mathrm{T},i}$ $(i=1,2,\ldots N)$ are the left eigenvectors of $\mathbf{T}$.

Boundary points of vanishing FOD. Solving (5.7) for the interfacial stiffness profile $\check{\mathbf{k}}$, one may find that the coefficient matrix $\check{\mathbf{F}}_1$ in (5.8) or $\check{\mathbf{F}}_2$ in (5.9) is singular. To interpret this, one may recall (5.8) and observe that the near-zero eigenvalues of $\check{\mathbf{F}}_1$ are affiliated to those collocation points on $\check{\Gamma}$ where $[\![\check{\mathbf{u}}]\!] \to \mathbf{0}$. In this case, (5.7) can be solved via suitable regularization e.g. by invoking Tikhonov regularization or truncated SVD.

5.2 Numerical implementation and results

This section examines the effectiveness of the 3-step inversion approach summarized in Fig. 5.2 with particular focus on the *inversion of specific stiffness* at the surface of heterogeneous fractures. The numerical experiments presented in the sequel aim to complement those of Section 4.6 on the *geometric fracture reconstruction*; accordingly, both sections feature the same testing configuration in $\mathbb{R}^3$ as shown in Fig. 4.2. For clarity of discussion, let us recall that the "true" subsurface fracture Γ is a cylindrical discontinuity of width $L = 0.7$, arclength $\ell = 0.55$, and radius $R = 0.35$ embedded in a linear, isotropic and homogeneous background domain with shear and compressional wave speeds $c_s = 1$ and $c_p = 2.08$, respectively. As before, the frequency of illumination is such that the ratio between the shear wavelength and the arclength of the cylindrical fracture is $\lambda_s/\ell = 0.7$.

With reference to Fig. 5.3, the fracture is endowed with two sets of "true" (diagonal and orthotropic) interfacial stiffness profiles $\boldsymbol{K}(\boldsymbol{\xi})$ on Γ, namely: 1) a piecewise-constant *zebra* distribution in both shear and normal directions, and 2) a distributed *cheetah* pattern defined in the fracture's local coordinates. In both scenarios, the specific stiffness distribution is assumed to be complex-valued, indicating dissipation (due to e.g. friction) at the fracture interface.

The fracture is illuminated by a set of plane (P- and S-) waves and thus induced
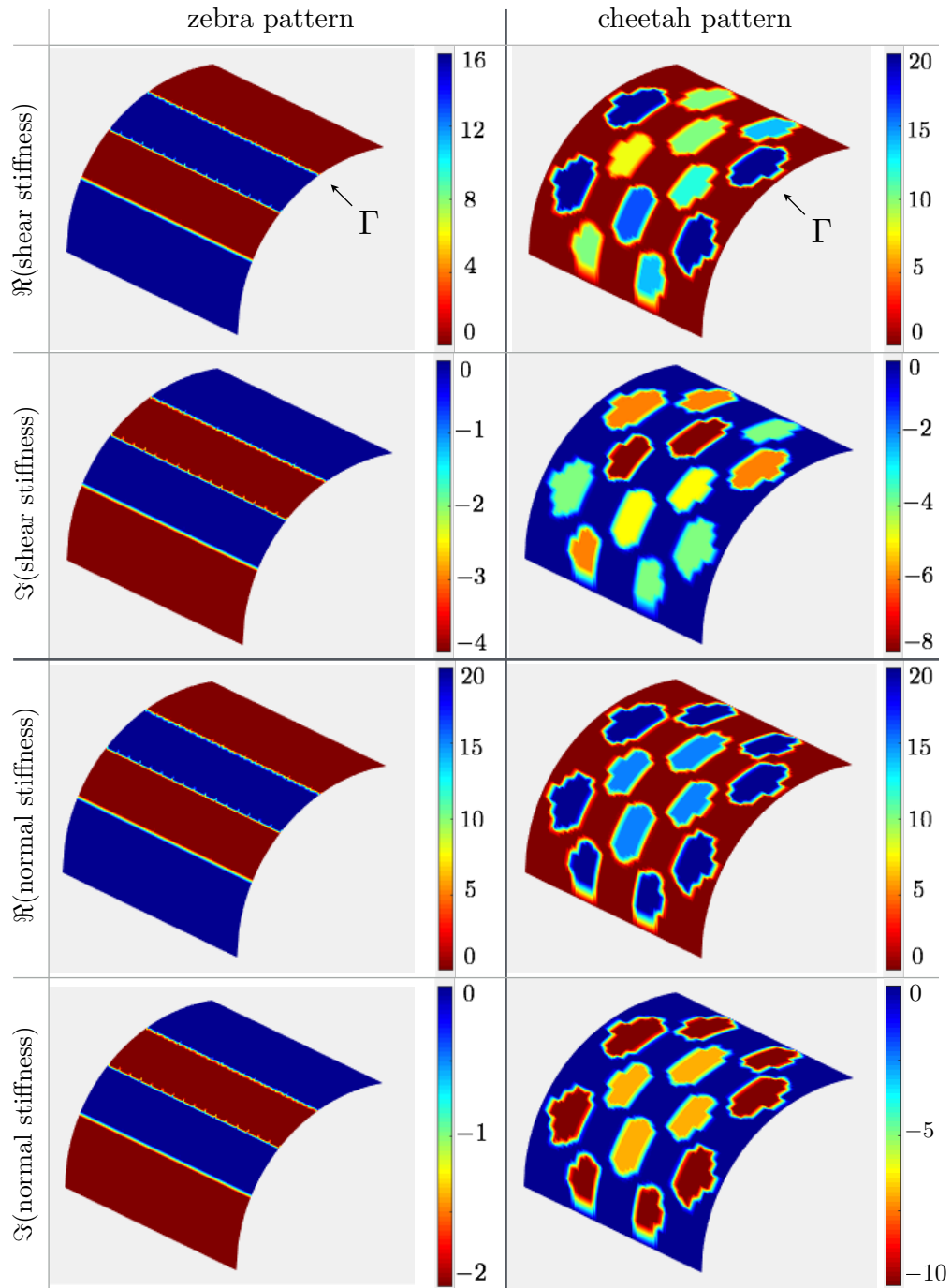
Figure 5.3: Two interface scenarios: Zebra (left) and cheetah (right) patterns representing the true distribution of complex interfacial stiffness in shear and normal directions.
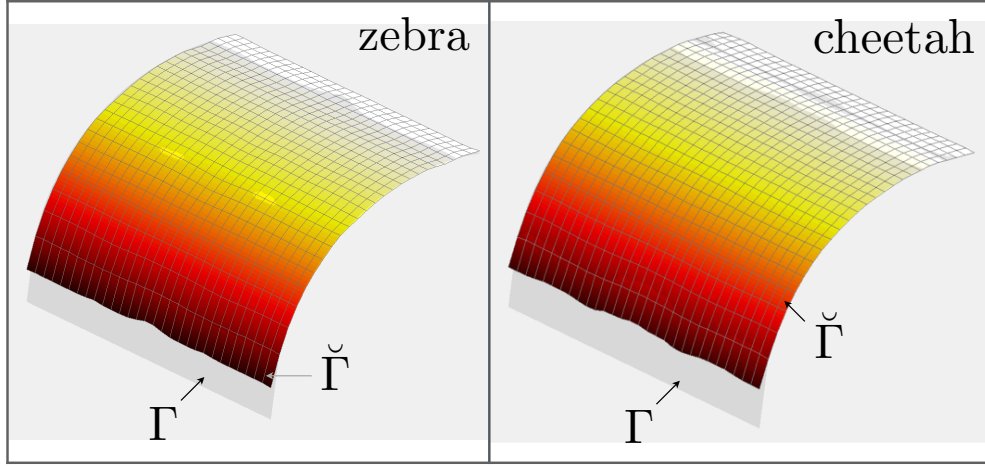
Figure 5.4: Geometric reconstruction: "True" geometry Γ *vs.* the *recovered* fracture support $\breve{\Gamma}$ for the zebra and cheetah interface scenarios.

scattered field is measured in terms of its far-field pattern, see also Chapter 4. The spatial density of sensory data, for both illumination and sensing purposes, is given by $N_\theta \times N_\phi = 25 \times 12$ according to the polar (θ_j, $j = 1, \ldots N_\theta$) and azimuthal (ϕ_k, $k = 1, \ldots N_\phi$) angle values on the unit sphere of incident/observation directions.

Geometric reconstruction. For each interface scenario the fracture support $\breve{\Gamma}$ is recovered, by way of GLSM, from the corresponding far-field data as shown in Fig. 5.4 (see Section 4.6 for details of the implementation).

FOD reconstruction. Given $\breve{\Gamma}$, one may construct the operator $\mathbf{M}$ according to (5.2) and (5.3) which maps the sought FOD $[\![\breve{\mathbf{u}}]\!]$ to the observed far-field pattern $\tilde{\mathbf{u}}^{\mathrm{obs}}$. As examined in Section 5.1.2, $\mathbf{M}$ is typically ill-posed due to the presence of interface waves and/or the limited aperture of observation. The former source of ill-posedness is illustrated in Fig. 5.5 where the "true" FOD over Γ – obtained by simulating the direct scattering problem (4.2) subject to a single S-wave excitation, is decomposed into two components, namely: i) the *retrievable* part computed by solving (5.3) for $[\![\breve{\mathbf{u}}]\!]$ over Γ via regularization, and ii) the *residual* part, including local modes, obtained by subtracting the jump profile recovered in i) from the "true" FOD. Note that $\mathbf{M}$ used to recover FOD in Fig. 5.5 is intentionally constructed on the basis of the *"true"* fracture geometry Γ, so that the computed residual part is not polluted by errors due to geometric fracture

reconstruction $\breve{\Gamma}$. With this remark, Fig. 5.7 compares the total FOD over Γ – induced by the interaction of a single illuminating P-wave with the "zebra" interface on Γ, with the recovered displacement jumps, according to (5.3), over Γ and $\breve{\Gamma}$. For a robust inversion of the interfacial stiffness, however, one should deploy the FOD profile obtained by the first step of regularization in Section 5.1.3 – where the observed wavefield data from multiple incidents are *synthetically recombined* to minimize, or eliminate, the contribution of the local modes in the total FOD. This is shown in Fig. 5.7, which compares the "true" FOD over Γ – due to recombined incident fields – with the corresponding reconstruction $[\![\breve{\mathbf{u}}]\!]$ over $\breve{\Gamma}$.

Inversion of stiffness profiles. In the ensuing numerical results, it is assumed that the specific stiffness matrix is *diagonal* and *orthotropic* ($k_{s1} = k_{s2}$) in the fracture's local coordinates, so that the sought heterogeneous distributions in the shear and normal directions are obtained by solving

$$\breve{\mathbf{F}}_1[\![\breve{\mathbf{u}}]\!]\,\breve{\mathbf{k}} \;=\; \sum_{i=1}^{N} \left(\mathbf{T}[\![\breve{\mathbf{u}}]\!]\cdot\mathbf{U}_{\mathrm{T},i}\right)\mathbf{U}_{\mathrm{T},i} \;+\; \breve{\mathbf{t}}_f,$$

for $\breve{\mathbf{k}}$. Here, $\breve{\mathbf{t}}_f$ is the discretized free-field traction over $\breve{\Gamma}$ affiliated with $[\![\breve{\mathbf{u}}]\!]$ (see *Regularization* in Section 5.1.3 for details); and $\mathbf{U}_{\mathrm{T},i}$ ($i=1,2,\ldots N$) are the *left eigenvectors* of $\mathbf{T}$ selected according to the second step of regularization in Section 5.1.3 to minimize the effect of errors due to imperfect geometric reconstruction. In this setting, Fig. 5.8 shows the reconstructed *zebra* pattern over Γ – assuming prior knowledge of the "true" fracture geometry Γ, while Fig. 5.9 (*resp.* Fig. 5.10) compares the "true" zebra (*resp.* cheetah) $\boldsymbol{K}$-distributions over Γ with their recovered $\breve{\boldsymbol{K}}$-counterparts on $\breve{\Gamma}$. As can be seen from both displays, the fidelity of the specific stiffness reconstruction is rather *remarkable* given (i) *no prior information* about the fracture geometry nor its contact condition, and (ii) *multiple steps of regularization* used to obtain the sequential geometric reconstruction and interfacial characterization.
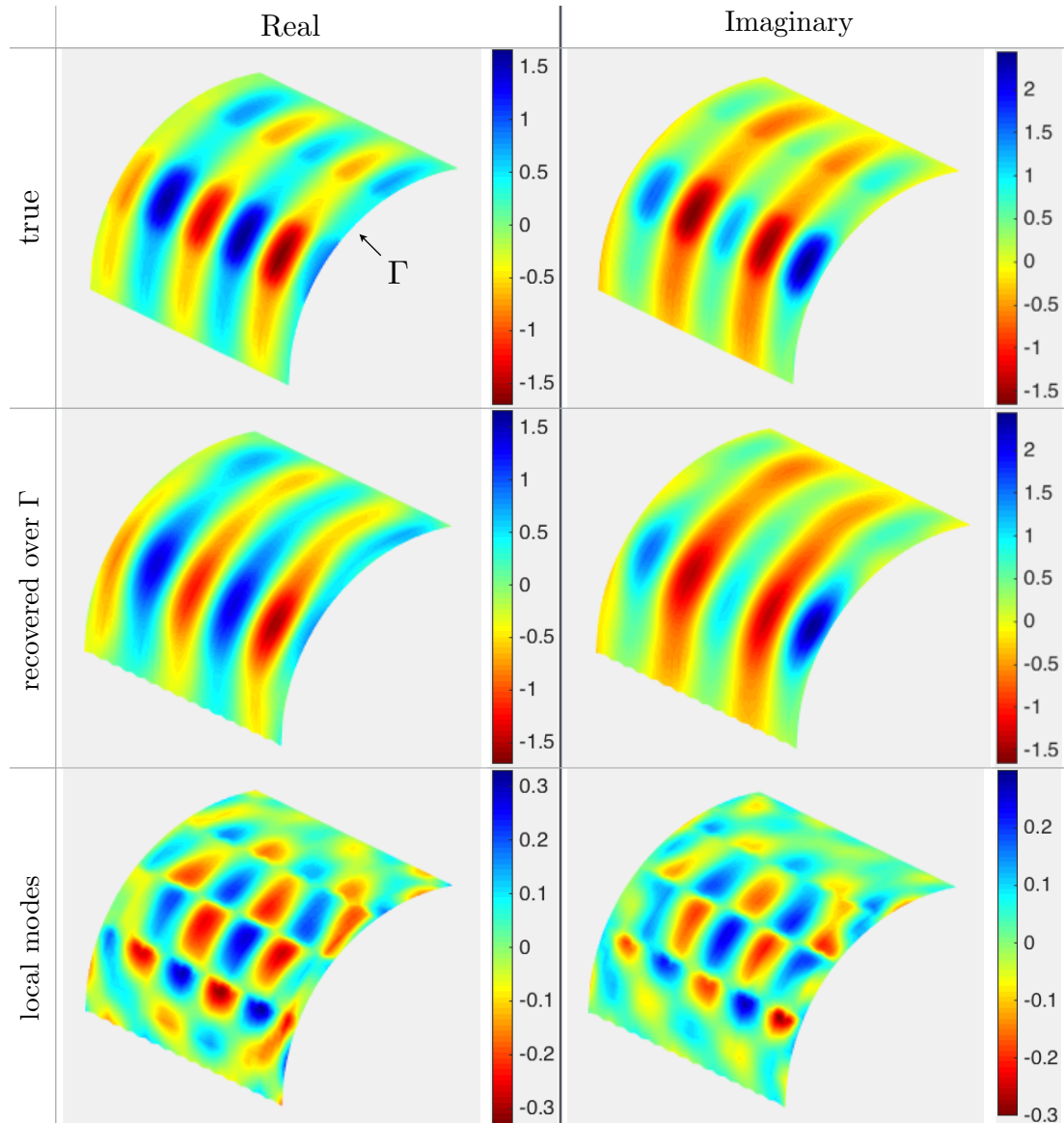
Figure 5.5: Recovery of the FOD distribution assuming prior knowledge of the "true" fracture surface Γ, shear component of $[\![\check{\mathbf{u}}]\!]$ (along the width of Γ), zebra interface scenario, single illuminating wave: the total FOD (top row) consists of i) the trace of propagating waves (middle row) – whose clear fingerprint in the far-field data allows for their robust reconstruction, and ii) the residual part (bottom row), including the trace of local modes i.e. interface waves – whose vanishing signature in the far-field data prevents their recovery.
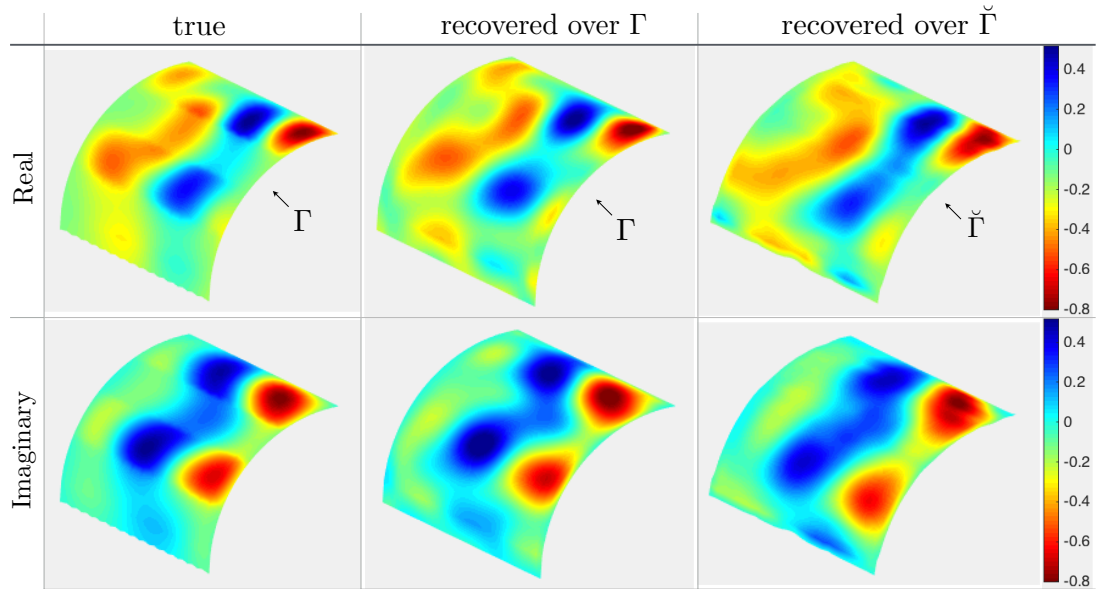
Figure 5.6: FOD reconstruction from the sensory data collected for a single P-wave incident, normal component of $[\![\breve{\mathbf{u}}]\!]$, zebra interface scenario: true FOD on Γ (left column); the recovered FOD over the true fracture geometry Γ (middle column); the recovered FOD over the reconstructed fracture geometry $\breve{\Gamma}$ (right column).
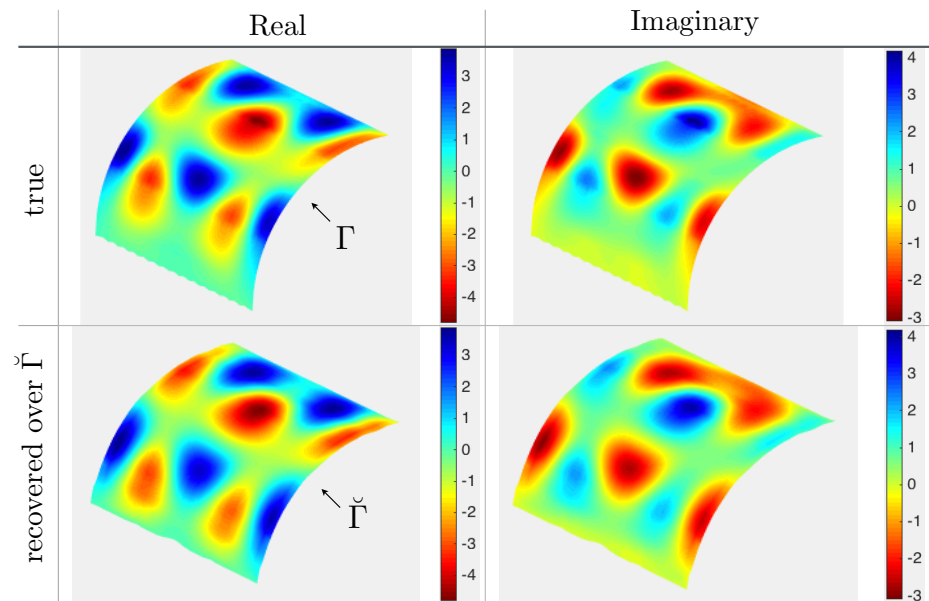
Figure 5.7: FOD reconstruction from the sensory data collected for multiple incident waves, normal component of $[\![\breve{\mathbf{u}}]\!]$, zebra interface scenario: true FOD on Γ (top row) induced by a set of incident plane waves whose density is obtained via (5.11) vs. the recovered FOD over the reconstructed fracture surface $\breve{\Gamma}$ (bottom row).
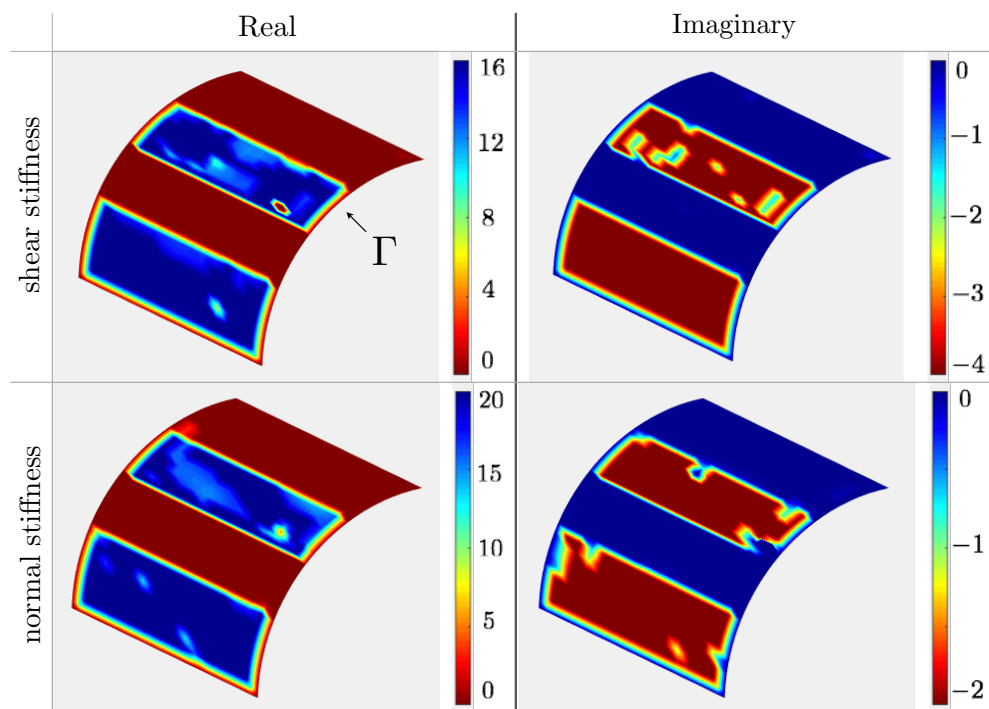
Figure 5.8: Recovered distribution of the specific stiffness, assuming prior knowledge of the "*true*" fracture geometry Γ, from the sensory data collected for multiple incident waves: normal and shear components of $\breve{\boldsymbol{K}}(\boldsymbol{\xi})$, zebra interface scenario.
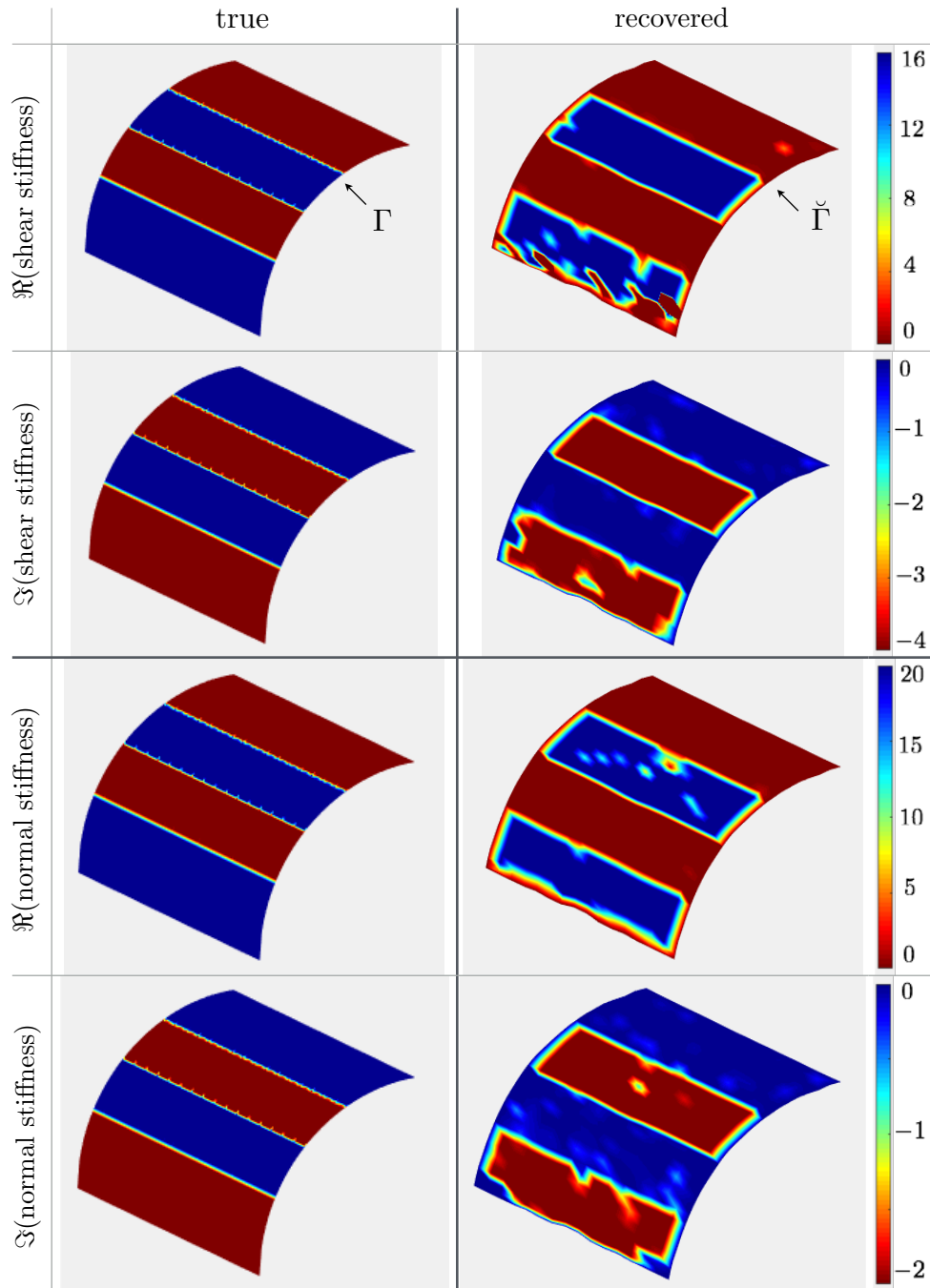
Figure 5.9: Recovered distribution of the specific stiffness, over the *reconstructed* fracture surface $\breve{\Gamma}$, from the sensory data collected for multiple incident waves: "true" (zebra) pattern $\boldsymbol{K}(\boldsymbol{\xi})$ over Γ (left) vs. the recovered distribution $\breve{\boldsymbol{K}}(\boldsymbol{\xi})$ over $\breve{\Gamma}$ (right).
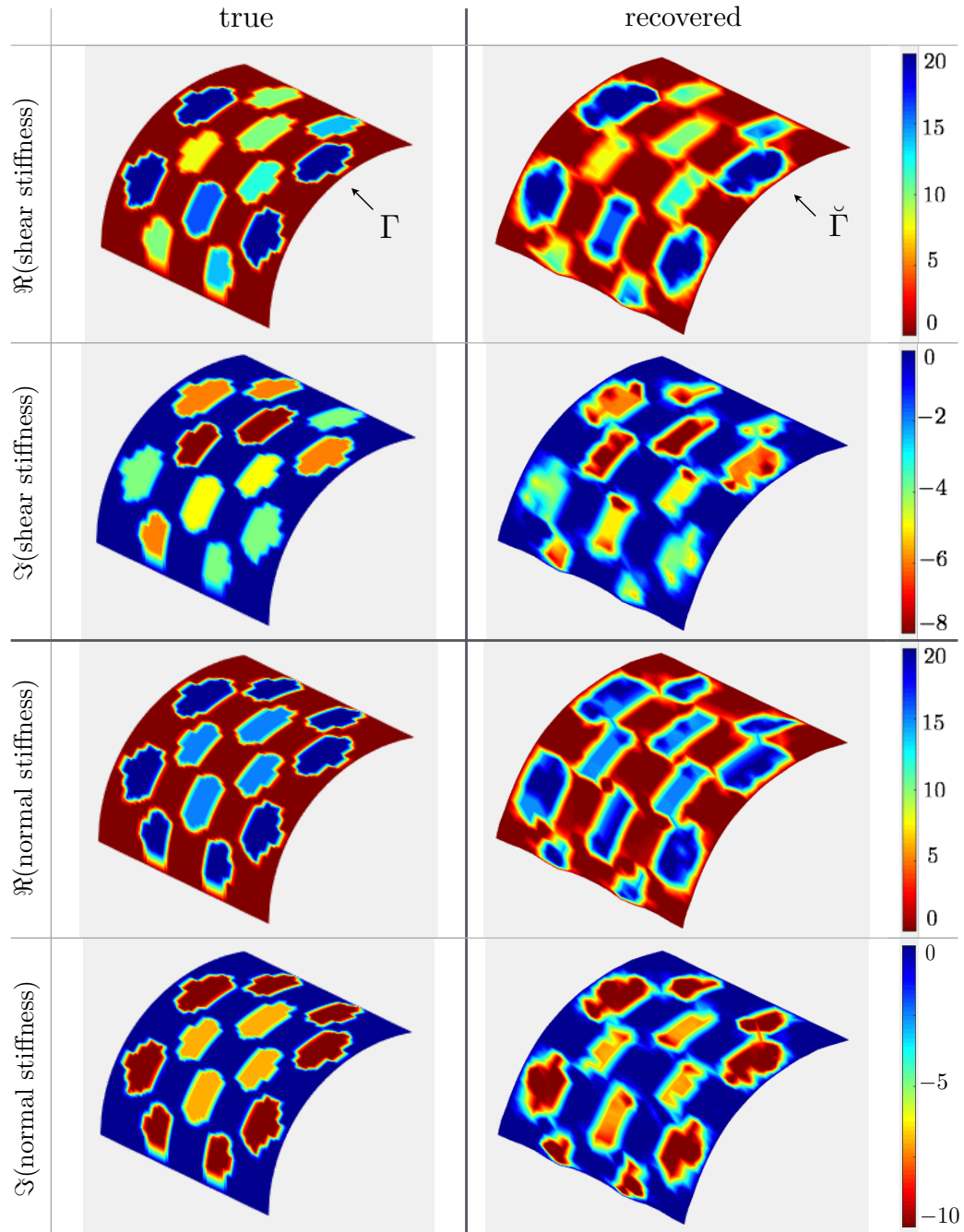
Figure 5.10: Recovered distribution of the specific stiffness, over the *reconstructed* fracture surface $\breve{\Gamma}$, from the sensory data collected for multiple incident waves: "true" (cheetah) pattern $\boldsymbol{K}(\boldsymbol{\xi})$ over Γ (left) vs. the recovered distribution $\breve{\boldsymbol{K}}(\boldsymbol{\xi})$ over $\breve{\Gamma}$ (right).

Chapter 6

Active ultrasonic imaging and interfacial characterization of stationary and evolving fractures in rock

The aim of this chapter, describing the *laboratory ultrasonic experiments* on fractured rock specimens, is to: 1) non-parametrically expose the true contact law and its spatiotemporal variations along the surface of stationary and propagating fractures in rock, and 2) extract the linearized contact properties in terms of the shear and normal specific stiffness – together with their heterogeneous distribution along the fracture. This is accomplished in a laboratory setting by monitoring the full-field interaction of ultrasonic shear waves (propagating through granite specimens) with stationary and advancing fractures via the 3D Scanning Laser Doppler Vibrometer (SLDV) that is capable of monitoring triaxial particle velocity, with frequencies up to 1MHz, over the surface of rock specimens with 0.1mm spatial resolution and O(nm) displacement accuracy. Experiments are performed on slab-like granite specimens featuring either stationary or evolving fractures where the fracturing, in the latter case, occurs in 3-point bending configuration. The rock specimens are excited, under the plane stress condition, by a piezoelectric transducer at 20-30kHz, while the in-plane velocity response of the sample

is monitored over a rectangular region covering the fracture. Thus obtained full-field data are next used to recover both the fracture geometry, and to expose its nonlinear contact behavior. The latter is then approximated point-wise in terms of the linearized contact properties i.e. specific (shear and normal) stiffness, whose recovered spatial variations for stationary and advancing fractures are found to conform with expected trends. Looking forward, the full-field seismic observations such as those presented herein may not only help decipher the true physics of a fracture interface and shine light on the fidelity of classical interface models, but may also provide the *ground truth* toward validating the next generation of seismic imaging tools for simultaneous geometric reconstruction and interfacial characterization of fractures in rock from remote seismic data [72, 134].

6.1 Experimental setup

Experiments are performed on two slab-like prismatic specimens of charcoal and Rockville granite with dimensions 0.96m ×0.3m ×0.03m, designed such that: a) the largest specimen dimension is almost one meter in order to enable the propagation of low-frequency (i.e. long-wavelength) waves through the sample; and b) the 0.03m slab thickness is at least decade-smaller than the remaining characteristic dimensions of the problem in order to approximate the plane-stress condition at lower excitation frequencies, where the shear-wavelength-to- slab-thickness ratio is $\lambda_s/h > 5$. Note that in this frequency range, the phase error committed by the plane stress approximation is less than 3% [160]. Under such conditions, the SLDV-captured surface motion can be taken as being uniform throughout the thickness of a granite slab. For further reference, the nominal material properties of the featured rock types are listed in Table 6.1 [171] where c_p and c_s are the P- and S- wave velocities, respectively. With reference to Fig. 6.1, the geometric reconstruction and interfacial characterization of an evolving fracture is pursued by fracturing a Rockville-granite slab in a three-point bending (3PB) configuration and sensing the fracture surface periodically during the loading process. This is accomplished by (i) generating the shear waves by an ultrasonic transducer, emitting a modulated five-cycle burst with the center frequency of 20kHz, and (ii) scanning the induced wave motion over the surface of a granite slab via SLDV. The tests were performed in the 1000kN
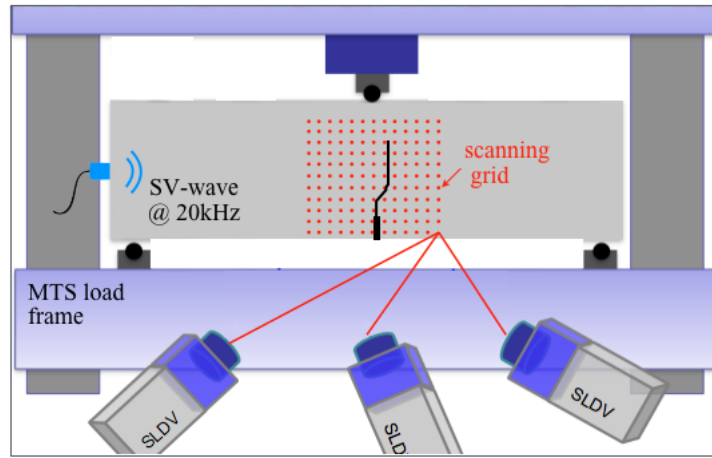
Figure 6.1: Schematic of the SLDV sensing configuration for imaging and characterization of an evolving fracture.

MTS load frame (see Fig. 6.2), which has one meter clearance between columns, providing an unimpeded SLDV vantage of the specimen. In this approach, the crack initiation and propagation is controlled by a closed-loop, servo-hydraulic system with the crack mouth opening displacement (CMOD) as the feedback signal. Note that the 3PB testing with an eccentric notch gives rise to a mixed-mode loading, resulting in fracture propagation along a curved path. The target SLDV scan is performed at approximately 70% of the maximum load (post-peak regime) while keeping the CMOD constant.

For the experimental study of stationary fractures, a through-fracture is induced in the charcoal-granite slab via 3PB in an MTS load frame; the pieces are then reconnected by applying a very small normal load (O(10kPa)) to the opposite sides of the specimen using clamps, see Fig. 6.3. As in the case of an advancing fracture, the sample was excited by elastic shear waves at 20kHz, while monitoring the full-field surface motion is via SLDV. For further reference, it is noted that the dominant shear wave length, at 20kHz, in the charcoal (resp. Rockville) granite is $\lambda_s \sim 16$cm (resp. $\lambda_s \sim 10$cm).

Table 6.1: Nominal properties of the featured rock materials.

Rock	E [GPa]	ν	ρ [kg/m^3]	c_p [m/s]	c_s [m/s]
Rockville	25	0.2	2720	3196	1955
Charcoal	70	0.24	2800	5428	3175
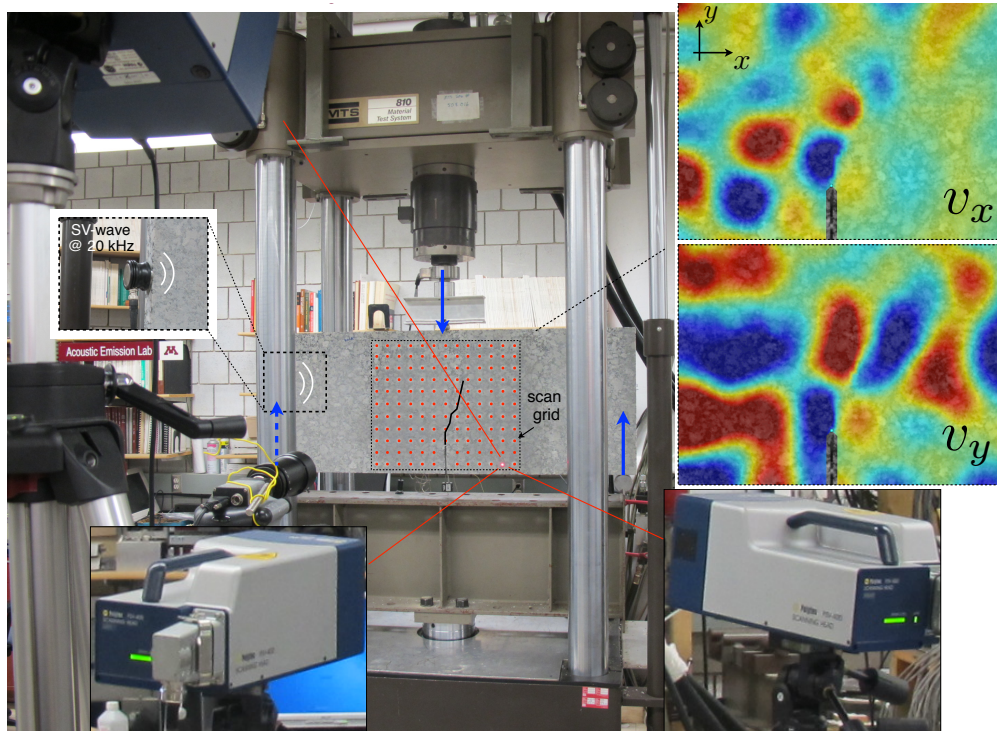
Figure 6.2: Full-field ultrasonic sensing of an advancing fracture: the specimen is fractured in the 3-point bending configuration; at a fixed CMOD, plane-stress ultrasonic waves are induced in the sample while monitoring the surface particle velocities (in the x- and y-directions) over the scanning grid via SLDV.
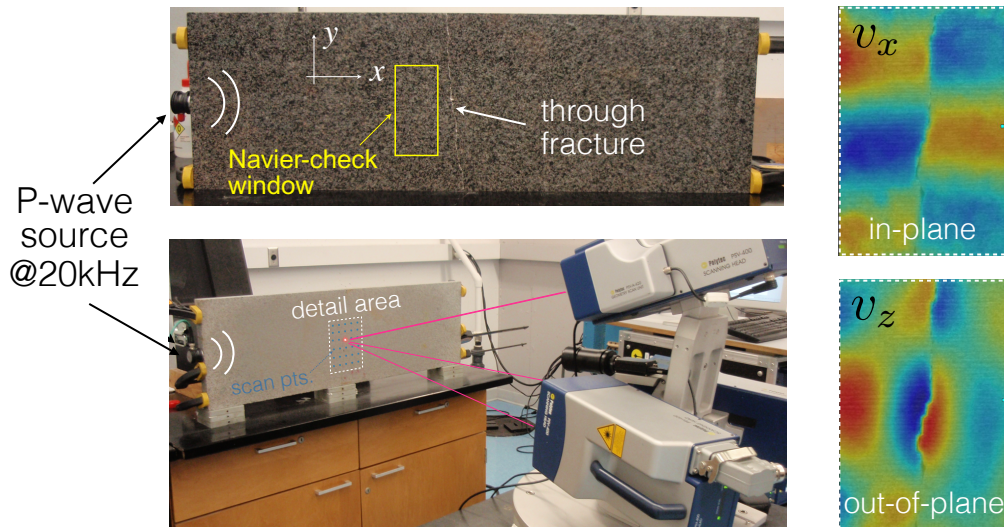
Figure 6.3: Fractured granite slab (top right), SLDV testing configuration (bottom right), and snapshot in time of the particle velocity field across the fracture (left). The experimental wavefield is constructed via a rectangular grid of 37×48 scan points with the mean spacing of 4 mm.

6.2 Results and discussion

With reference to Fig. 6.4, the SLDV-measured velocity fields in the neighborhood of a fracture are processed to recover the fracture's geometry and interfacial behavior as described in the sequel.

Geometric reconstruction. It is apparent from Fig. 6.2 and Fig. 6.3 that the interaction of ultrasonic shear waves with a fracture gives rise to discontinuity in the wavefield across the interface. Thus, to obtain the fracture geometry, one may (at every snapshot in time) compute the jump in both (v_x and v_y) velocity distributions in the x- and y-directions. Then, by integrating the absolute value of thus obtained jump fields over the entire time span, one finds the plots as in Fig. 6.5 over the scanned area where the points of highest cumulative jump expose the fracture's true geometry.

Contact law. The idea behind non-parametric identification of the fracture's contact behavior is to extract (i) the profile of fracture opening displacement (FOD), and (ii) the distribution of tractions along the fracture from particle-velocity measurements on both sides of the discontinuity. Then, by plotting in time the (shear and normal) traction versus affiliated FOD – for every point along the fracture edge, one may retrieve the "true" spatiotemporal variation of the interfacial behavior.

Signal Processing. A suitable band-pass filter, with cut-off frequencies of 10kHz and 30kHz (catering for the spectrum of the source wavelet), is applied to the raw particle velocity signals measured at every scan point. Thus obtained smooth velocity signals are then numerically integrated, and high-pass filtered to eliminate the low-frequency
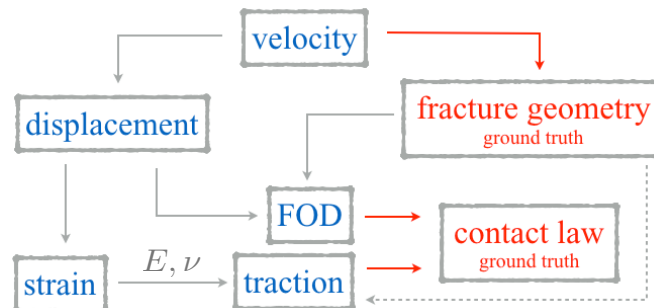
Figure 6.4: Roadmap for the geometric reconstruction and non-parametric interfacial characterization of fractures from full- field SLDV data.
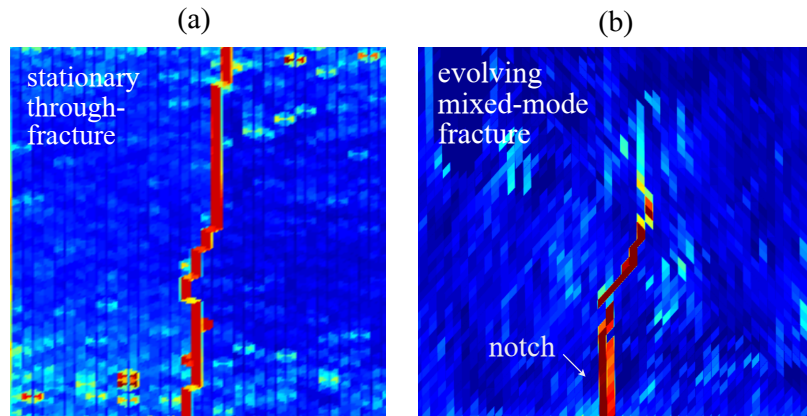
Figure 6.5: Reconstructed fracture geometries from SLDV wavefields (0.4m×0.3m scanning window): a) stationary fracture in charcoal granite, and b) advancing fracture in Rockville granite at 70% post-peak load.

drift due to integration. In this way, one obtains the "raw" displacement fields shown in the left panel of Fig. 6.6, which are smooth and differentiable in time, yet non-smooth in space. However, with reference to Fig. 6.4, these fields must provide the basis for the computation of strain and stress fields in the rock slab. To resolve the problem, a two-step spatial smoothing is applied to such "raw" displacements at every snapshot in time. First, a median-based moving average filter (with the spatial extent of $\lambda_s/8$) is applied to eliminate bad scan points i.e. sudden spikes in the data, and to stabilize the next (interpolation) step. Second, the resulting displacement distributions are then approximated by double Fourier series (including up to seven harmonics) in x- and y-directions. This gives birth to the smooth displacement fields shown in the right panel of Fig. 6.6, which are now differentiable both in time and space, and can thus be used to compute the strain components as needed.

Given the (previously recovered) fracture geometry, one may further compute the FOD profile along the fracture mid-section by extending the smooth displacement fields from both sides to this line, see Fig. 6.6 (b). For the purpose of calculating the stress fields from the available strain distributions, one needs to implement the Hooke's law which requires knowledge of the specimens' elastic moduli. While the nominal values of the latter are reported in Table 6.1, one may alternatively take advantage of the full-field SLDV data to recover the (generally heterogeneous) distribution of the Young's modulus
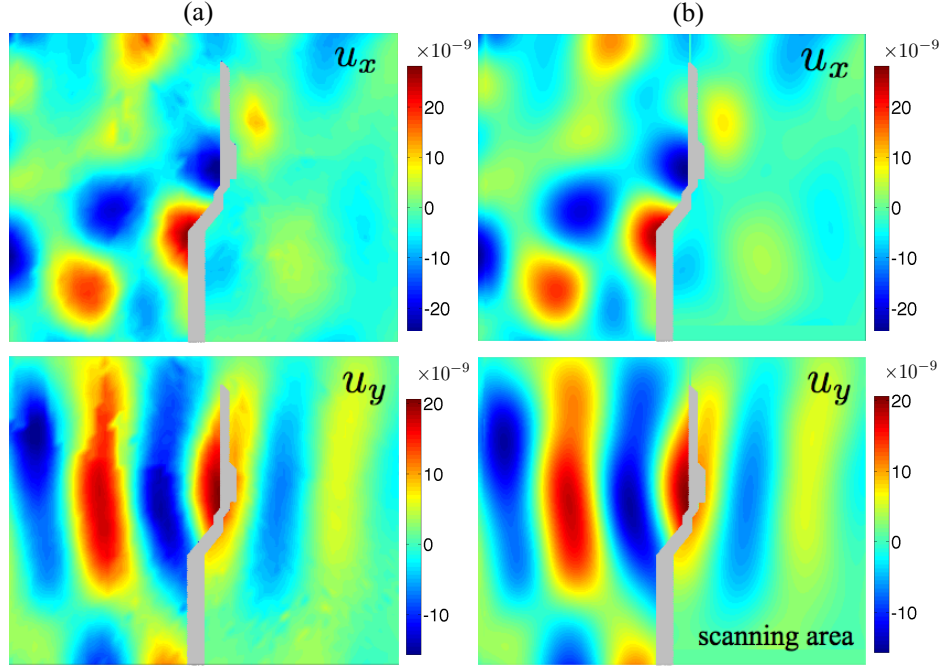
Figure 6.6: Snapshot in time of the displacement fields in the x- and y-directions (0.4m×0.3m window containing the advancing fracture at 70% post-peak load): a) raw waveforms, and b) smooth fields obtained after signal processing.

and Poisson's ratio over the scanned area, which carries the potential of furnishing a more robust stress estimation.

Elastography. This concept was first introduced in the context of biomedical imaging [124], and the core idea, adapted for the purpose of this study, is as follows: given smooth and differentiable displacement fields u_x and u_y over the scanning region (see Fig. 6.6 (b)) during certain time interval, the distribution of elastic moduli in this area may be obtained by pointwise solving the 2D Navier equation in terms of the sought-for material properties. More specifically, the Navier equation is recast, under the plane stress assumption, as

$$\begin{bmatrix} \ddot{u}_x & \frac{1}{2}(u_{x,yy} + u_{y,xy}) - u_{y,yx} \\ \ddot{u}_y & \frac{1}{2}(u_{y,xx} + u_{x,yx}) - u_{x,xy} \end{bmatrix} \begin{bmatrix} \frac{\rho}{E'} \\ \nu \end{bmatrix} = \begin{bmatrix} \frac{1}{2}(u_{x,yy} + u_{y,xy}) + u_{x,xx} \\ \frac{1}{2}(u_{y,xx} + u_{x,yx}) + u_{y,yy} \end{bmatrix}, \qquad (6.1)$$
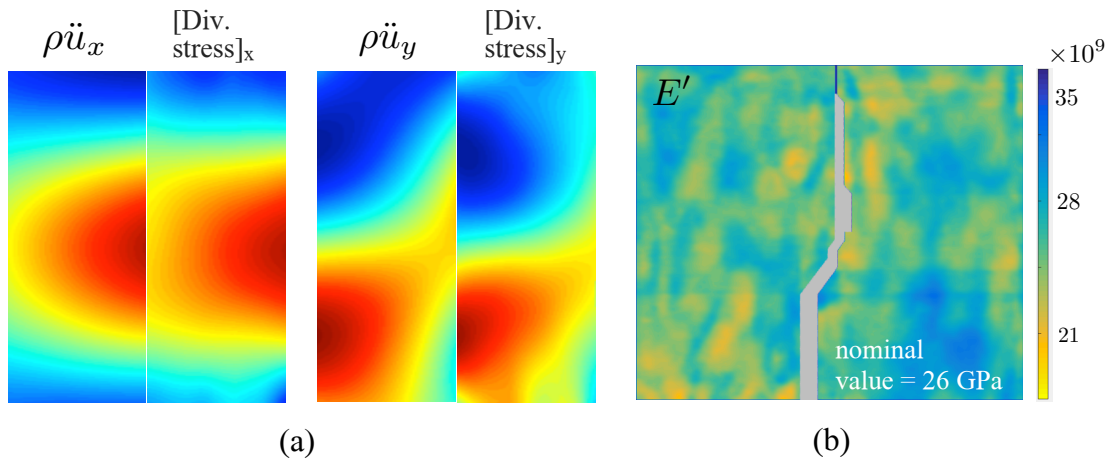
Figure 6.7: a) SLDV-observed balance (x- and y-directions) of the plane-stress Navier equations over the 0.05m × 0.15m window shown in the top-right panel in Fig. 6.3, and b) recovered distribution of the Young's modulus over the scanning area using elastography (0.4m×0.3m window).

where $E' = E/(1 - \nu^2)$ is the plane-stress Young's modulus, and over-dots indicate temporal differentiation. Note that the implicit postulate in (6.1) is that both Young's modulus and Poisson's ratio are assumed to be locally constant. Otherwise, (6.1) takes a much more complex form that also includes the spatial derivatives of the elastic parameters [19]. In this setting, one may first assess the validity of the plane-stress assumption by substituting the nominal elastic parameters from Table 6.1 into (6.1), and visually comparing the left-hand side (divergence of the stress tensor) and the right-hand side (mass density times the acceleration vector) in the Navier equation. One example of such verification is shown in Fig. 6.7 (a), which shows a reasonable agreement between the two sides of the Navier equation. Next, returning to the principle of elastography, one may solve (6.1) for the elastic parameters at every scan point and average the resulting field over the entire time interval to obtain their spatial distribution, see Fig. 6.7 (b) for an example of his recovered distribution of the Young's modulus. With such result in place, one may now compute the stress fields, and consequently the distribution of tractions along the fractures mid-section.

At this point, the true contact behavior at every point along the fracture may be exposed by plotting the shear and normal traction versus respective FOD over a given time interval T_i, $i = 1, 2, \cdots$ (whose duration is comparable to the dominant period of

ultrasonic excitation), see Fig. 6.8. Phenomenologically, the traction – FOD plots in shear direction resembles the frictional hysteresis loops obtained by [4, 133]. However, one should bear in mind that in this study the illuminating wavelet is transient – and thus it possesses a much wider frequency spectrum than the conventional steady-state and single-frequency excitations that are typically used for the dynamic analysis of frictional interfaces. Hence, one may not assume equivalence between the results of Fig. 6.8 – involving transient and multi-scale dynamics – with that of a steady-state behavior. On the other hand, the traction-FOD plots in normal direction feature a distinct cusp as FOD increases. This phenomenon may be affiliated with the well-known bi-linear behavior of frictional contacts in the normal direction e.g. [94].

At a given time window T_i, one may replace the complex and possibly nonlinear behavior at the interface with a linearized approximation by computing the average slope of the traction-FOD diagrams in the normal and shear directions to obtain the respective (normal and shear) specific stiffness coefficients, given by the slopes of the dotted lines in Fig. 6.8. By recovering these values for every point along the fracture, one arrives at the heterogeneous distribution of interfacial stiffness in shear and normal directions, as shown in Fig. 6.9 for the respective cases of propagating and stationary fractures. As expected, both normal and shear specific stiffness generally increase toward fracture tip in the case of an advancing fracture, while the stationary fracture is characterized by a rather uniform distribution of the pair of specific stiffnesses.
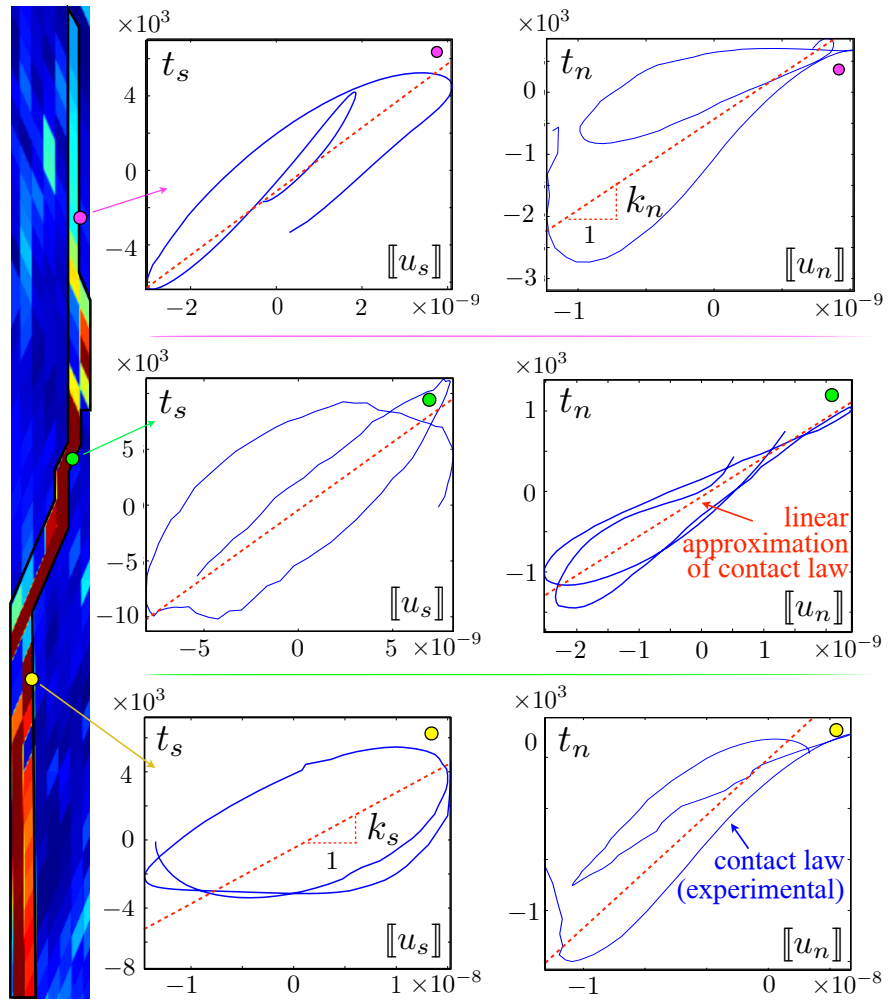
Figure 6.8: Apparent interfacial behavior in the shear (t_s vs. $\llbracket u_s \rrbracket$) and normal ($t_n$ vs. $\llbracket u_n \rrbracket$) directions at three points along the mixed-mode fracture (70% post-peak load).
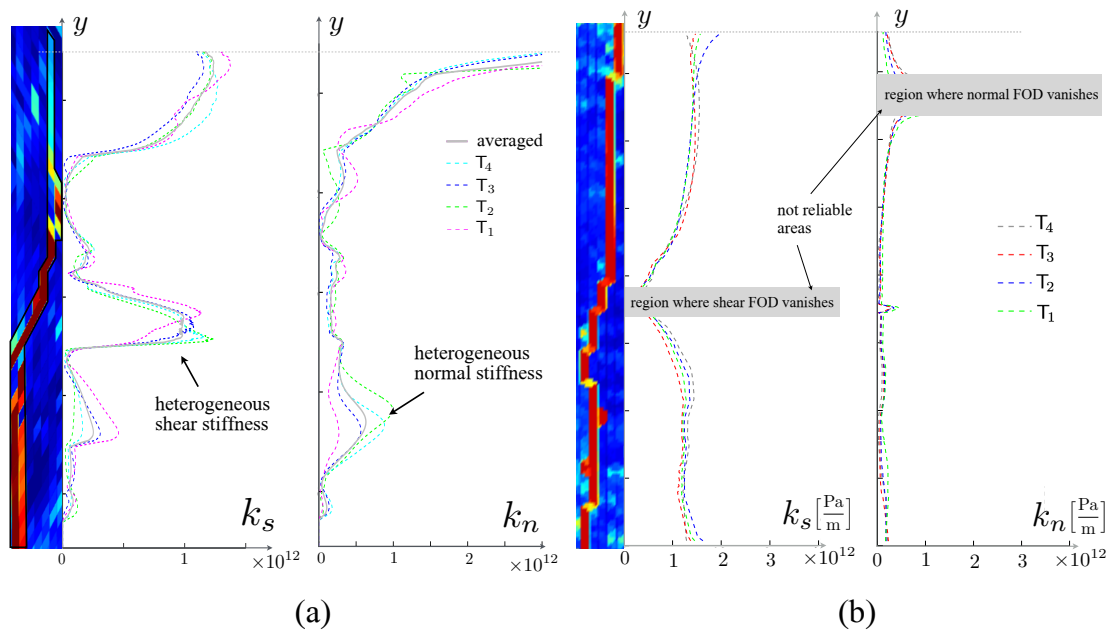
Figure 6.9: Heterogeneous distribution of normal and shear specific stiffness – as recovered from the analysis of transient waveforms during 5 different time subintervals (T_i, $i = 1, 2, \cdots, 5$), along the boundary of (a) a mixed-mode evolving fracture in Rockville granite (70% post-peak load) where the vertical extent of the fracture (including the notch) is 25cm ≈ $2.5\lambda_s$ at 20kHz, and (b) a stationary through fracture in Charcoal granite where the fracture is subjected to a very small (O(10kPa)) normal stress, and that the vertical extent of the fracture (including the notch) is 30cm ≈ $2\lambda_s$ at 20kHz.

Chapter 7

Summary and outlook

This work, focused on the seismic imaging and characterization of fractures in rock, entails both analytical, computational, and experimental developments – arranged as a collection of complementary yet self-contained works. The main contributions of this dissertation include: (I) two inverse scattering solutions, entailing respectively the methods of Topological Sensitivity and Linear Sampling, for *non-iterative* 3D waveform tomography of curved fracture surfaces *irrespective* of their (unknown) contact condition; (II) an inverse solution – established within the framework of boundary integral formulations – that enables, for the first time, *quantitative* 3D recovery of the (shear and normal) *specific stiffness distributions* along fractures with abitrary (curved) geometry; and (III) next-generation *experimental results and analysis*, making use of the Scanning Laser Doppler Vibrometer, that pave the way toward exposing the *true* contact behavior of fractures in rock under ultrasonic (seismic) excitation. In this spirit, the ensuing discussion summarizes the specific contributions as deliberated in each chapter.

Chapter 2. In this work, it is shown *why the topological sensitivity (TS) works* as a non-iterative tool for the waveform tomography of finite-sized anomalies in the *short wavelength* regime. The analysis confirms previous numerical and experimental findings to this effect, that have so far eluded rigorous justification. To establish the claim, it is assumed that an anomaly is convex and impenetrable, and that the measurements of the scattered wavefield are taken away the interrogated region. Making use of the multipole expansion, Kirchhoff approximation, and *theory of diffraction catastrophes*, the TS indicator function is – under the premise of high-frequency excitation – pruned

to three asymptotic essentials, namely i) the near-boundary approximation for sampling points within few wavelengths from the illuminated surface of an anomaly; ii) diffraction catastrophes (of codimension less then four) for sampling points near caustic surfaces, lines, and points; and iii) stationary phase approximation in the remainder of the sampled region. In the case of the full aperture of illuminating plane waves, it is shown via catastrophe theory that the TS is asymptotically dominated by the explicit near-boundary term. This result in particular unveils the *new reconstruction logic* at short wavelengths, where the boundary of an anomaly is obtained as a *zero level set* of the TS field separating its extreme negative and extreme positive values. Extensions of the study may include better understanding of related concepts such as time reversal and other techniques for non-iterative waveform tomography.

Chapter 3. This chapter investigates the utility of the TS approach as a non-iterative tool for the seismic waveform tomography of fractures with specific stiffness, e.g. hydraulic fractures. On postulating the nucleation of an infinitesimal penny-shaped fissure with trial (normal and shear) interfacial stiffnesses at a sampling point, the elastodynamic TS formula is derived and expressed in closed form. In this setting, it is shown via numerical simulations that the TS carries the capacity of approximating the *fracture location* and its *unit normal* from the long-wavelength scattered field measurements, regardless of the assumption on the (trial) interfacial parameters of a vanishing fracture. Given thus obtained geometric information, it is further shown that the interfacial condition of nearly-planar fractures can be *qualitatively* identified at virtually no added computational cost. In particular, the analysis shows that such scheme allows for *the ratio* between the shear and normal specific stiffness – representative of a hidden fracture – to be exposed as either i) near-zero, ii) on the order of unity, or iii) exceeding unity by a large amount. In terms of energy applications, such information can potentially be used (on the basis of a recent field evidence) to discriminate between the old mineralized, newly created, and proppant-filled fractures. Through preliminary simulations at "short" incident wavelengths which demonstrate both enhanced TS resolution and elevated sensitivity to the fracture's interfacial condition, this study further provides an impetus for studying the *high-frequency* TS sensing of fractures with specific stiffness.

Chapter 4. This work draws from the recent developments in the mathematical theory of inverse scattering to formulate a *non-iterative* approach to the seismic waveform

tomography of partially-closed fractures, that embodies both *top-tier spatial resolution* (irrespective of the illumination frequency), *minimal sensitivity to fracture's contact condition*, and *robustness to measurement errors.* In particular, the Generalized Linear Sampling Method (GLSM) is combined with the Kirsch's factorization technique to form a fast, yet robust, platform for the seismic reconstruction of heterogeneous (and dissipative) discontinuity surfaces from scattered wavefield data. It is shown that the GLSM indicator possesses little sensitivity to measurement noise – that compares in terms of robustness to that of the TS approach, while inheriting the superior localization property of the classical linear sampling method, which nearly guarantees high-fracture reconstruction over a broad range of illuminating wavelengths and contact stiffness profiles $\boldsymbol{K}(\boldsymbol{x})$. Such attributes form a basis for the establishment of a *holistic seismic sensing* approach presented in Chapter 5 that is capable of not only the geometric reconstruction of hidden fractures, but also the quantitative identification of their heterogenous contact condition. Here it should be noted that the GLSM reconstruction algorithm does not require the fracture surface to be connected, thus in principle allowing for the simultaneous reconstruction of *multiple fractures* in the subsurface, e.g. systems of hydraulic fractures.

Chapter 5. Existing approaches to the seismic characterization of fractures with specific stiffness are, by and large, limited to sensing configurations where the fracture is planar, while the seismic sources and receivers are placed on the opposite sides of a discontinuity. The sensing paradigm proposed in this chapter is unique in that it allows for the imaging and characterization of *arbitrary-shaped* fractures, and caters for significant *flexibility* in terms of the sensing arrangement (location of sources and receivers). With reference to Fig. 7.1, this is made possible by a novel *3-step approach* where:

1. The *fracture geometry* is reconstructed in 3D *irrespective* of its specific stiffness via the TS approach – given the availability of high-frequency seismic data (as discussed in Chapters 2 and 3), or by the GLSM paradigm – in a more general setting with no limitations on the illumination frequency (as described in Chapter 4);

2. The fracture's *fracture opening displacement (FOD) profile* is computed using thus obtained fracture reconstruction (denoted by $\check{\Gamma}$) via a boundary integral representation of the seismic field scattered by the fracture, and

3. The distribution of *specific stiffness* $\boldsymbol{K}(\boldsymbol{x})$ – given by its normal and shear components k_n and k_s – is computed from the knowledge of $FOD(\boldsymbol{x})$, making use of the (elastodynamic) traction boundary integral equation written for $\breve{\Gamma}$.
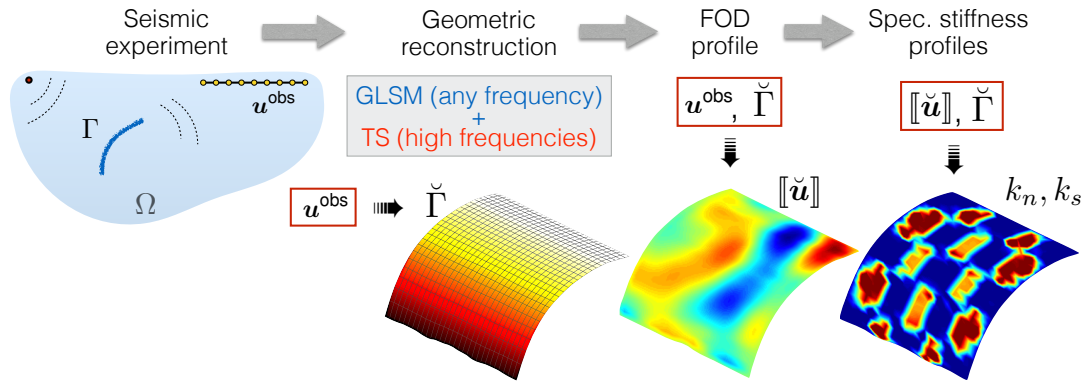
Figure 7.1: A hybrid approach to non-iterative reconstruction and characterization of heterogeneous fractures.

Chapter 6. This work describes the *initial laboratory study* on the full-field ultrasonic investigation of stationary and advancing fractures in rock, effected via a 3D Scanning Laser Doppler Vibrometer (SLDV). The experiments are performed on slab-like granite specimens at ultrasonic wavelengths significantly exceeding the thickness of a slab, thus allowing for approximation of the underpinning wave propagation problem in terms of the *plane stress* assumption. With suitable smoothing of the observed waveforms, it is shown that the proposed experimental procedure carries the potential of both (i) reconstructing the curvilinear fracture geometry, and (ii) point-wise identifying its true contact behavior, which can then be approximated in terms of customary linearized parameters of shear and normal specific stiffness.

Outlook. From a broader perspective, the research presented in this dissertation is intended to provide an initial spur toward the development of a field technique for active seismic imaging and characterization of subsurface fractures – with application to e.g. hydrocarbon harvesting and mining operations. The follow-up studies building upon this work are expected to include (i) application of the 3-step inverse solution to, and verification by way of, laboratory ultrasonic data, (ii) consideration of medium and measurement uncertainties (via e.g. Bayesian framework) geared toward elevating the

robustness of the inverse solution, and (iii) trial field applications of the proposed technique under increasing levels of subsurface complexity (e.g. stratified and/or multiphase rock volumes, fracture networks).

References

[1] M. J. Ablowitz and Z. H. Musslimani. Inverse scattering transform for the integrable nonlocal nonlinear schrodinger equation. *Nonlinearity*, 29:915, 2016.

[2] J. D. Achenbach. *Reciprocity in Elastodynamics*. Cambridge Univ. Press, Cambridge, UK, 2003.

[3] A. Acosta-Colon, L.J. Pyrak-Nolte, and D.D Nolte. Laboratory-scale study of field of view and the seismic interpretation of fracture specific stiffness. *Geophys. Prosp.*, 57:209–224, 2009.

[4] H. Ahmadian, H. Jalali, and F. Pourahmadian. Nonlinear model identification of a frictional contact support. *Mech. Syst. Signal Pr.*, 24:2844–2854, 2010.

[5] H. Ammari, J. Garnier, V. Jugnon, and H. Kang. Stability and resolution analysis for a topological derivative based imaging functional. *SIAM J. Contr. Opt.*, 50:48–76, 2012.

[6] H. Ammari and H. Kang. *Reconstruction of small inhomogeneities from boundary measurements*. Springer-Verlag, Berlin, 2004.

[7] H. Ammari and H. Kang. *Reconstruction of the Small Inhomogeneities from Boundary Measurements*. Springer, New York, 2004.

[8] H. Ammari and H. Kang. *Polarization and moment tensors with application to inverse problems and effective medium theory*. Springer, 2007.

[9] A. Asheim and D. Huybrechs. Extraction of uniformly accurate phase functions across smooth shadow boundaries in high frequency scattering problems. *SIAM J. Appl. Math.*, 74:454–476, 2014.

[10] L. Audibert. *Full-wave Nonlinear Inverse Scattering for Acoustic and Electromagnetic Breast Imaging.* PhD thesis, University of Michigan, 2012.

[11] L. Audibert. *Qualitative methods for heterogeneous media.* PhD thesis, Ecole Doctorale Polytechnique, 2015.

[12] L. Audibert and H. Haddar. A generalized formulation of the linear sampling method with exact characterization of targets in terms of farfield measurements. *Inverse Problems*, 30:035011, 2014.

[13] A. F. Baird, J.-M. Kendall, J. P. Verdon, A. Wuestefeld, T. E. Noble, Y. Li, M. Dutko, and Q. J. Fisher. Monitoring increases in fracture connectivity during hydraulic stimulations from temporal variations in shear wave splitting polarization. *Geophys. J. Int.*, 2013.

[14] A. F. Baird, J.-M. Kendall, J. P. Verdon, A. Wuestefeld, T. E. Noble, Y. Li, M. Dutko, and Q. J. Fisher. Monitoring increases in fracture connectivity during hydraulic stimulations from temporal variations in shear wave splitting polarization. *Geophysical Journal International*, 2013.

[15] S. K. Bakku, M. Fehler, and D. Burns. Fracture compliance estimation using borehole tube waves. *Geophysics*, 78:D249–D260, 2013.

[16] A. Bakulin, V. Grechka, and I. Tsvankin. Estimation of fracture parameters from reflection seismic data – part I: HTI model due to a single fracture set. *Geophysics*, 65:1788–1802, 2000.

[17] D. Bakun-Mazor, Y. H. Hatzor, and S. D. Glaser. Dynamic sliding of tetrahedral wedge: the role of interface friction. *Int. J. Num. Anal. Meth. Geomech.*, 36:249 – 390, 2011.

[18] H. P. Baltes. *Inverse Scattering Problems in Optics.* Springer-Verlag, 1980.

[19] P.E. Barbone and N.H. Gokhale. Elastic modulus imaging: on the uniqueness and nonuniqueness of the elastography inverse problem in two dimensions. *Inverse Problems*, 20:238, 2004.

[20] G. I. Barenblatt. *Scaling (Cambridge texts in applied mathematics)*. Cambridge University Press, Cambridge, UK, 2003.

[21] N. Barton. The shear strength of rock and rock joints. *Int. J. Rock. Mech. Min. Sci.*, 13:255–279, 1976.

[22] C. Bellis. *Qualitative methods for inverse scattering in solid mechanics*. PhD thesis, Ecole Polytechnique, 2010.

[23] C. Bellis and M. Bonnet. Crack identification by 3d time-domain elastic or acoustic topological sensitivity. *C. R. Mecanique*, 337:124–130, 2009.

[24] C. Bellis and M. Bonnet. Crack identification by 3d time-domain elastic or acoustic topological sensitivity. *C. R. Mecanique*, 337:124–130, 2009.

[25] C. Bellis and M. Bonnet. A FEM-based topological sensitivity approach for fast qualitattive identification of buried cavities from elastodynamic overdetermined boundary data. *Int. J. Solids Struct.*, 47:1221–1242, 2010.

[26] C. Bellis and M. Bonnet. Qualitative identification of cracks using 3d transient elastodynamic topological derivative: formulation and fe implementation. *Comput. methods Appl. Mech. Engrg*, 253:89–105, 2013.

[27] C. Bellis, M. Bonnet, and F. Cakoni. Acoustic inverse scattering using topological derivative of far-field measurements-based L^2 cost functionals. *Inverse Problems*, 29:075012, 2013.

[28] M. V. Berry, J. F. Nye, and F. J. Wright. The elliptic umbilic diffraction catastrophe. *Philos. Trans. R. Soc. London*, 291:453–484, 1979.

[29] M. V. Berry and C. Upstill. Catastrophe optics: Morphologies of caustics and their diffraction patterns. *Progress in Optics*, 18:257–346, 1980.

[30] L. Bjerrum. Progressive failure in slopes of over-consolidated plastic clay and clay shales. *J. Soil Mech. Found. Div. (ASCE)*, 93:141–187, 1967.

[31] N. Bleistein. *Mathematical Methods for Wave Phenomena*. Academic Press, London, 1984.

[32] N. Bleistein, J.K. Cohen, and J.W. Stockwell, Jr. *Mathematics of Multidimensional Seismic Imaging, Migration, and Inversion.* Springer, New York, 2001.

[33] M. Bonnet. *Boundary integral equation methods for solids and fluids.* John Wiley & Sons, 1999.

[34] M. Bonnet. Inverse acoustic scattering by small-obstacle expansion of a misfit function. *Inverse Problems*, 24:035022, 2008.

[35] M. Bonnet. Fast identification of cracks using higher-order topological sensitivity for 2-d potential problems. *Eng. Anal. Bound. Elem.*, 35:223–235, 2011.

[36] M. Bonnet. Topological sensitivity for 3D elastodynamic and acoustic inverse scattering in the time domain. *Eng. Anal. Bound. Elem.*, 35:223–235, 2011.

[37] M. Bonnet and B. B. Guzina. Sounding of finite solid bodies by way of topological derivative. *Int. J. Numer. Meth. Engng*, 61, 2004.

[38] M. Bonnet and B. B. Guzina. Topological derivative for the inverse scattering of elastic waves. *Int. J. Num. Meth. Eng.*, 57:161–179, 2004.

[39] V. A. Borovikov. *Uniform Stationary Phase Method.* Instit. Electrical Engineers, London, 1994.

[40] Y. Boukari and H. Haddar. The factorization method applied to cracks with impedance boundary conditions. *Inverse Probl. Imag.*, 7:1123–1138, 2013.

[41] Y. Boukari and H. Haddar. The factorization method applied to cracks with impedance boundary conditions. *Inverse Probl Imag*, 7:1123–1138, 2013.

[42] L Bourgeois and E LunAville. On the use of the linear sampling method to identify cracks in elastic waveguides. *Inverse Problems*, 29(2):025017, 2013.

[43] W.F. Brace and E.G. Bombolakis. A note on brittle crack growth in compression. *J. Geophys. Res.*, 68:3709–3713, 1963.

[44] James H. Bramble and Joseph E. Pasciak. A note on the existence and uniqueness of solutions of frequency domain elastic wave problems: a priori estimates in $\boldsymbol{H}^1$. *J. Math. Anal. Appl.*, 345(1):396–404, 2008.

[45] O. P. Bruno and C. A. Geuzaine. An o(1) integration scheme for three-dimensional surface scattering problems. *Comp. Appl. Math.*, 204(2):463–476, 2007.

[46] F. Cakoni and D. Colton. The linear sampling method for cracks. *Inverse Problems*, 19:279–295, 2003.

[47] F. Cakoni and D. Colton. *A Qualitative Approach to Inverse Scattering Theory.* Springer, New York, 2014.

[48] F. Cakoni and R. Kress. Integral equation methods for the inverse obstacle problem with generalized impedance boundary condition. *Inverse problems*, 29, 2013.

[49] F. Cakoni and P. Monk. The determination of anisotropic surface impedance in electromagnetic scattering. *Meth. App. Analy.*, 17:379–394, 2010.

[50] A. Carpio and M. L. Rapun. Topological derivatives for shape reconstruction. *Lect. Not. Math.*, 1943:85–131, 2008.

[51] P. L. Castrigiano and S. A. Hayes. *Catastrophe Theory.* Addison-Wesley, 1993.

[52] M. Chamaillard, N. Chaulet, and H. Haddar. Analysis of the factorization method for a general class of boundary conditions. *J. Inverse Ill-posed Probl.*, 22:643 – 670, 2014.

[53] C. Chester, B. Friedman, and F. Ursell. An extension of the method of steepest descents. *Proc. Camb. Phil. Soc.*, 53(599–611), 1957.

[54] I. Chikichev and B. B. Guzina. Generalized topological derivative for the Navier equation and inverse scattering in the time domain. *Comp. Meth. Appl. Mech. Eng.*, 197:4467–4484, 2008.

[55] M.-K. Choi, A. Bobet, and L. J. Pyrak-Nolte. The effect of surface roughness and mixed-mode loading on the stiffness ratio k_x/k_z for fractures. *Geophysics*, 79:319–331, 2014.

[56] D. Colton and F. Cakoni. The determination of the surface impedance of a partially coated obstacle from far-field data. *SIAM J. Appl. Math.*, 64:709–723, 2004.

[57] D. Colton, J. Coyle, and P. Monk. Recent developments in inverse acoustic scattering theory. *SIAM Review*, 42:369–414, 2000.

[58] D. Colton and R. Kress. *Inverse acoustic and electromagnetic scattering theory.* Springer, Berlin, 1992.

[59] J. N. L. Connor. Asymptotic evaluation of multidimensional integrals for the S matrix in the semiclassical theory of inelastic and reactive molecular collisions. *Mol. Phys.*, 25:181–191, 1973.

[60] J. N. L. Connor. Catastrophes and molecular collisions. *Mol. Phys.*, 31:33–55, 1976.

[61] J. N. L. Connor, P. R. Curtis, and D. Farrelly. The uniform asymptotic swallowtail approximation: practical methods for oscillating integrals with four coalescing saddle points. *Phys. A: Math. Gen.*, 17:283–310, 1984.

[62] N.G.W. Cook. Natural joints in rock: Mechanical, hydraulic and seismic behaviour and properties under normal stress. *Int. J. Rock Mech. Min. Sci.*, 29:198–223, 1992.

[63] G. Dassios, K. Kiriaki, and D. Polyzos. On the scattering amplitudes for elastic waves. *Z. Angew. Math. Phys.*, 38:856–873, 1987.

[64] G. Dassios and Z. Rigou. Elastic herglotz functions. *SIAM J Appl Math*, 55:1345–1361, 1995.

[65] Michel Demazure. *Bifurcations and Catastophes.* Springer, Berlin, 2000.

[66] A.J. Devaney. *Mathematical Foundations of Imaging, Tomography and Wavefield Inversion.* Cambridge Univ. Press, Cambridge, UK, 2012.

[67] N. Dominguez and V. Gibiat. Non-destructive imaging using the time domain topological energy method. *Ultrasonics*, 50:367–372, 2010.

[68] N. Dominguez, V. Gibiat, and Y. Esquerre. Time domain topological gradient and time reversal analogy: an inverse method for ultrasonic target detection. *Wave Motion*, 42:31–52, 2005.

[69] E. Eberhardt, D. Stead, and J.S. Coggan. Numerical analysis of initiation and progressive failure in natural rock slopes ? the 1991 randa rockslide. *Int. J. Rock Mech. Min. Sci.*, 41:69–87, 2004.

[70] A. Erdelyi, editor. *Bateman Manuscript Project, Tables of Integral Transforms Volume II.* McGraw-Hill, New York, 1954.

[71] F. Esu, D. Distefano, M. Grisolia, and G. Tancredi. Stability of a high cut in overconsolidated lacustrine deposits. In *Proc. IV Int. Symp. Landslides*, volume 2, pages 63–68, Ontario, Canada, 1984.

[72] Pourahmadian F., B. B. Guzina, and H. Haddar. Generalized linear sampling method for elastic-wave sensing of heterogeneous fractures. *submitted to Inverse Problems: arXiv preprint arXiv:1605.08743*, 2016.

[73] V. I. Fabrikant. Flat crack of arbitrary shape in an elastic body: analytical approach. *Philos. Mag.*, 56:175–189, 1987.

[74] X. Fang, M. C. Fehler, Z. Zhu, Y. Zheng, and D. R. Burns. Reservoir fracture characterization from seismic scattered waves. *Geophysical Journal International*, 196:481–492, 2014.

[75] G. R. Feijoo. A new method in inverse scattering based on the topological derivative. *Inverse Problems*, 20:1819–1840, 2004.

[76] M. E. French, H. Kitajima, J. S. Chester, F. M. Chester, and T. Hirose. Displacement and dynamic weakening processes in smectite-rich gouge from the central deforming zone of the San Andreas fault. *J. Geoph. Res. Solid Earth*, 119:1777 – 1802, 2014.

[77] R. Gallego and G. Rus. Identification of cracks and cavities using the topological sensitivity boundary integral equation. *Comp. Mech.*, 33:154–163, 2004.

[78] T. H. W. Goebel, D. Schorlemmer, T. W. Becker, G. Dresen, and C. G. Sammis. Acoustic emissions document stress changes over many seismic cycles in stick-slip experiments. *Geophys. Res. Lett.*, 40:2049–2054, 2013.

[79] W.H. Gu, N.R. Morgenstern, and P.K. Robertson. Progressive failure of lower san fernando dam. *J. Geotech. Eng.*, 119:333–349, 1993.

[80] B. Guzina and D. Kunerth. *Three-dimensional NDE of VHTR core components via simulation-based testing.* NEUP (US Department of Energy), 2014. `http://www.osti.gov/scitech/servlets/purl/1183651`.

[81] B. B. Guzina. *Seismic response of foundations in multilayered media.* PhD thesis, Univ. of Colorado at Boulder, 1996.

[82] B. B. Guzina and M. Bonnet. Topological derivative for the inverse scattering of elastic waves. *Quart. J. Mech. Appl. Math.*, 57:161–179, 2004.

[83] B. B. Guzina and M. Bonnet. Topological derivative for the inverse scattering of elastic waves. *Quart. J. Mech. Appl. Math.*, 57:161–179, 2004.

[84] B. B. Guzina and M. Bonnet. Small-inclusion asymptotic of misfit functionals for inverse problems in acoustics. *Inverse Problems*, 22:1761–1785, 2006.

[85] B. B. Guzina and Pourahmadian F. Why the high-frequency inverse scattering by topological sensitivity may work. *Proc. R. Soc. A*, 471:20150187, 2015.

[86] B. B. Guzina and Chikichev I. From imaging to material identification: a generalized concept of topological sensitivity. *J. Mech. Phys. Solids*, 55:245–279, 2007.

[87] B. B. Guzina and A. Madyarov. A linear sampling approach to inverse elastic scattering in piecewise-homogeneous domains. *Inverse Problems*, 11:1467–93, 2007.

[88] B. B. Guzina and Pak R.Y.S. On the analysis of wave motions in a multi-layered solid. *Q J Mechanics Appl Math*, 54:13–37, 2001.

[89] A. Hedayat, Pyrak-Nolte, L. J., and A. Bobet. Precursors to the shear failure of rock discontinuities. *Geophys. Res. Lett.*, 41:5467–5475, 2014.

[90] F. Hernandez-Valle, A.R. Clough, and R.S. Edwards. Stress corrosion cracking detection using non-contact ultrasonic techniques. *Corrosion Science*, 78:335–342, 2014.

[91] C. Hobday and M. H. Worthington. Field measurements of normal and shear fracture compliance. *Geophysical Prospecting*, 60:488–499, 2012.

[92] Chikichev I. and B. B. Guzina. Generalized topological derivative for the navier equation and inverse scattering in time domain. *Comp. Meth. Appl. Mech. Eng.*, 197:4467?84, 2007.

[93] J.C. Jaeger, N.G.W. Cook, and R. Zimmerman. *Fundamentals of Rock Mechanics.* John Wiley & Sons, 2009.

[94] H. Jalali, H. Ahmadian, and F. Pourahmadian. Identification of micro-vibro-impacts at boundary condition of a nonlinear beam. *Mech. Syst. Signal Pr.*, 25:1073–1085, 2011.

[95] P. A. Johnson, B. Ferdowsi, B. M. Kaproth, M. Scuderi, M. Griffa, J. Carmeliet, R. A. Guyer, P-Y. Le Bas, D. T. Trugman, and C. Marone. Acoustic emission and microslip precursors to stick-slip failure in sheared granular material. *Geophys. Res. Lett.*, 40:5627–5631, 2013.

[96] Park W. K. Music-type imaging of small perfectly conducting cracks with an unknown frequency. *J Phys Conf Ser*, 633(1):012005, 2015.

[97] J. B. Keller. Geometrical theory of diffraction. *J. Opt. Soc. Amer.*, 52:116–130, 1962.

[98] A. Kirsch and N. Grinberg. *The factorization methods for inverse problems.* Oxford University Press, Oxford, 2008.

[99] Andreas Kirsch. *An Introduction to the Mathematical Theory of Inverse Problems*, volume 120. Springer, 2011.

[100] R. Knight, L. J. Pyrak-Nolte, L. Slater, E. Atekwana, A. Endres, J. Geller, D. Lesmes, S. Nakagawa, A. Revil, M. M. Sharma, and C. Straley. Geophysics at the interface: response of geophysical properties to solid-fluid, fluid-fluid, and solid-solid interfaces. *Reviews of Geophysics*, 48, 2010.

[101] R. Kress. Inverse scattering from an open arc. *Math. Methods Appl. Sci.*, 18:267–293, 1995.

[102] R. Kress. *Linear integral equation.* Springer, Berlin, 1999.

[103] E. Kreyszig. *Differential Geometry.* Dover, 1991.

[104] V. D. Kupradze, T. G. Gegelia, M. O. Basheleishvili, and T. V. Burchuladze. *Three-dimensional problems of the mathematical theory of elasticity and thermoelasticity.* North-Holland Publishing, Netherlands, 1979.

[105] B. R. Levy and J. B. Keller. Diffraction by a smooth object. *Comm. Pure Appl. Math.*, 12:159–209, 1959.

[106] D. Lockner. The role of acoustic emission in the study of rock fracture. *Int. J. Rock. Mech. Min. Sci.*, 30:883–899, 1993.

[107] R. Lubbe, J. Sothcott, M. H. Worthington, and C. McCann. Laboratory estimates of normal and shear fracture compliance. *Geophysical Prospecting*, 56:239–247, 2008.

[108] S. J. Martel and D. D. Pollard. Mechanics of slip and fracture along small faults and simple strike-slip fault zones in granitic rock. *J. Geophys. Res.*, 94:9417–9428, 1989.

[109] P. A. Martin and G. Dassios. Karpos theorem in elastodynamic inverse scattering. *Inverse Problems*, 9:97–111, 1993.

[110] P. A. Martin and G. R. Wickham. *Wave Asymptotics.* Cambridge University Press, 1992.

[111] M. Masmoudi, J. Pommier, and B. Samet. The topological asymptotic expansion for the Maxwell equations and some applications. *Inverse Problems*, 21:547–564, 2005.

[112] S. Maxwell. *Microseismic Imaging of Hydraulic Fracturing.* Society of Exploration Geophysicists, 2014.

[113] G.C. McLaskey, A.M. Thomas, S.D. Glaser, and R.M. Nadeau. Fault healing promotes high-frequency earthquakes in laboratory experiments and on natural faults. *Nature*, 491:101–104, 2012.

[114] W. McLean. *Strongly Elliptic Systems and Boundary Integral Equations.* Cambridge University Press, Cambridge, 2000.

[115] R. B. Melrose and M. E. Taylor. Near peak scattering and the corrected kirchhoff approximation for a convex obstacle. *Advances in Mathematics*, 55:242–315, 1985.

[116] S. Minato and R. Ghose. Inverse scattering solution for the spatially heterogeneous compliance of a single fracture. *Geophys. J. Int.*, 195:1878–1891, 2013.

[117] S. Minato and R. Ghose. Imaging and characterization of a subhorizontal non-welded interface from point source elastic scattering response. *Geophys. J. Int.*, 197:1090–1095, 2014.

[118] P. Monk. *Finite Element Methods for Maxwell's Equations.* Clarendon Press, Oxford, 2003.

[119] M. Motamed and O. Runborg. A fast phase space method for computing creeping rays. *J. Comp. Phys.*, 219:276–295, 2006.

[120] O. Mutlu and A. Bobet. Slip initiation on frictional fractures. *Eng. Frac. Mech.*, 72:729–747, 2005.

[121] A. H. Nayfeh. *Introduction to Perturbation Techniques.* John Wiley & Sons, 1993.

[122] S. Nintcheu Fata and B. B. Guzina. A linear sampling method for near-field inverse problems in elastodynamics. *Inverse Problems*, 20:713–736, 2004.

[123] F. W. J. Olver, D. W. Lozier, R. F. Boisvert, and C. W. Clark, editors. *NIST Handbook of Mathematical Functions.* Cambridge Univ. Press, New York, 2010.

[124] J. Ophir, S.K. Alam, B. Garra, F. Kallel, E. Konofagou, T. Krouskop, and T. Varghese. Elastography: ultrasonic estimation and imaging of the elastic properties of tissues. *Proc. Inst. Mech. Eng. H J. Eng.*, 213:203–233, 1999.

[125] A. Osborne. *Nonlinear Ocean Waves and the Inverse Scattering Transform.* Academic Press, 2010.

[126] R. Y. S. Pak and B. B. Guzina. Seismic soil-tructure interaction analysis by direct boundary element methods. *Int. J. Solids Struct.*, 26:4743–4766, 1999.

[127] W-K. Park. *Diffraction inverse par des inclusions minces et des fissures.* PhD thesis, Ecole Polytechnique, 2009.

[128] W-K. Park. Topological derivative strategy for one-step iteration imaging of arbitrary shaped thin, curve-like electromagnetic inclusions. *J. Comp. Phys.*, 231:1426–1439, 2012.

[129] W. K. Park. Multi-frequency subspace migration for imaging of perfectly conducting, arc-like cracks in full- and limited-view inverse scattering problems. *J comp phys*, 283:52 – 80, 2015.

[130] R. Pike and P. Sabatier, editors. *Scattering: scattering and inverse scattering in pure and applied science*, volume 1 & 2. Academic Press, San Diego, 2002.

[131] J. Place, O. Blake, D. Faulkner, and A. Rietbrock. wet fault or dry fault? a laboratory approach to remotely monitor the hydro-mechanical state of a discontinuity using controlled-source seismics. *Pure Appl. Geophys.*, 2014.

[132] T. Poston and I. Stewart. *Catastrophe Theory and its Applications.* Pitman, London, 1981.

[133] F. Pourahmadian, H. Ahmadian, and H. Jalali. Modeling and identification of frictional forces at a contact interface experiencing micro-vibro-impacts. *J. Sound Vib.*, 331:2874–2886, 2012.

[134] F. Pourahmadian and B. B. Guzina. On the elastic-wave imaging and characterization of fractures with specific stiffness. *int. J Solids Struct.*, 71:126–140, 2015.

[135] F. Pourahmadian and B. B. Guzina. Active ultrasonic imaging and interfacial characterization of stationary and evolving fractures in rock. *ARMA2016*, pages 16–803, 2016.

[136] C. Prada and M. Fink. Eigenmodes of the time reversal operator: A solution to selective focusing in multiple-target media. *Wave Motion*, 20:151–163, 1994.

[137] L. Pyrak-Nolte and D. Nolte. Frequency dependence of fracture stiffness. *Geophysical Research Letters*, 19:325–328, 1992.

[138] L. J. Pyrak-Nolte and N. G. W. Cook. Elastic interface waves along a fracture. *Geophys. Res. Let.*, 14:1107–1110, 1987.

[139] L. J. Pyrak-Nolte and D. D. Nolte. Approaching a universal scaling relationship between fracture stiffness and fluid flow. *Nature Communications*, 7:10663, 2016.

[140] L.J. Pyrak-Nolte and J.P. Morris. Single fractures under normal stress: The relation between fracture specific stiffness and fluid flow. *Int. J. Rock. Mech. Min. Sci.*, 37:245–262, 2000.

[141] L.J. Pyrak-Nolte, L.R. Myer, and N.G.W. Cook. Transmission of seismic waves across single natural fractures. *J. Geophys. Res.*, 95:8617–8638, 1990.

[142] L.J. Pyrak-Nolte and D.D. Nolte. Frequency dependence of fracture stiffness. *Geophys. Res. Let.*, 19:325–328, 1992.

[143] S. Rodriguez, P. Sahuguet, V. Gibiat, and X. Jacob. Fast topological imaging. *Ultrasonics*, 52:1010–1018, 2012.

[144] C. M. Sayers and L. D. den Boer. Characterizing production-induced anisotropy of fractured reservoirs having multiple fracture sets. *Geophysical Prospecting*, 60:919–939, 2012.

[145] M. Schoenberg. Elastic interface waves along a fracture. *J. Acoust. Soc. Am.*, 68:1516–1521, 1980.

[146] J. P. Seidel and C. M. Haberfield. Towards an understanding of joint roughness. *Rock Mech. Rock Engng.*, 28:69–92, 1995.

[147] K.R. Shah and J.F. Labuz. Damage mechanisms in stressed rock from acoustic emission. *J. Geophys. Res.*, 100:15527–15539, 1995.

[148] F. Simonetti and L. Huang. Synthetic aperture diffraction tomography for three-dimensional imaging. *Proc. Roy. Soc. A*, 465:2877–2895, 2009.

[149] A. W. Skempton. Long-term stability of clay slopes. *Geotechnique*, 14:77–102, 1964.

[150] J. Sokolowski and A. Zochowski. On the topological derivative in shape optimization. *SIAM J. Control Optim.*, 37:1251–1272, 1999.

[151] J. Sokolowski and A. Zochowski. On the topological derivative in shape optimization. *SIAM J. Control Optim.*, 37:1251–1272, 1999.

[152] J. J. Stamnes. *Waves in Focal Regions.* Taylor & Francis, New York, 1986.

[153] I. Stewart. Catastrophe theory in physics. *Rep. Prog. Phys.*, 45:185–221, 1982.

[154] H. Tabatabai, D. E. Oliver, J. W. Rohrbaugh, and C. Papadopoulos. Novel applications of laser doppler vibration measurements to medical imaging. *Sens Imaging*, 14:13–28, 2013.

[155] J. Taron and D. Elsworth. Coupled mechanical and chemical processes in engineered geothermal reservoirs with dynamic permeability. *Int. J. Rock. Mech. Min. Sci.*, 47:1339–1348, 2010.

[156] R. Thom. *Stabilité Structurelle et Morphogénèse.* Benjamin, New York, 1972.

[157] R. Thom. Structural stability, catastrophe theory, and applied mathematics: the John von Neumann Lecture, 1976. *SIAM Review*, 19:189–201, 1977.

[158] Andrew L Thomas and David D Pollard. The geometry of echelon fractures in rock: implications from laboratory and numerical experiments. *J. Struct. Geol*, 15:323–334, 1993.

[159] R. Tokmashev. *Experimental validation of the Topological Sensitivity approach to elastic-wave imaging.* PhD thesis, University of Minnesota, 2015.

[160] R.D. Tokmashev, A. Tixier, and B.B. Guzina. Experimental validation of the topological sensitivity approach to elastic-wave imaging. *Inverse Problems*, 29:125005, 2013.

[161] V. Twersky. Multiple scattering by arbitrary configuration in three dimensions. *J. Math. Phys.*, 3:83, 1962.

[162] S. Ueda, S. Biwa, K. Watanabe, R. Heuer, and C. Pecorari. On the stiffness of spring model for closed crack. *Int. J. Eng. Sci.*, 44:874–888, 2006.

[163] J. P. Verdon and A. Wustefeld. Measurement of the normal/tangential fracture compliance ratio (z_N/z_T) during hydraulic fracture stimulation using s-wave splitting data. *Geophysical Prospecting*, 61:461–475, 2013.

[164] J Virieux and S Operto. An overview of full-waveform inversion in exploration geophysics. *Geophysics*, 74:WCC1–WCC26, 2009.

[165] M. Willis, D. Burns, R. Rao, B. Minsley, M. Toksoz, and L. Vetri. Spatial orientation and distribution of reservoir fractures from scattered seismic energy. *Geophysics*, 71:O43–O51, 2006.

[166] J. Wookey. Direct probabilistic inversion of shear-wave data for anisotropy. *Geophysical Journal International*, 189:1025–1037, 2012.

[167] R. A. W. Young. *The Uniform Hyperbolic Umbilic Approximation*. ProQuest, UMI Dissertations Publishing, 1986.

[168] E. C. Zeeman. The geomery of catastrophe. *Times Literary Supplement*, Dec. 10:1556–7, 1971.

[169] D. Zhao. *Multiscale Seismic Tomography*. Springer, 2015.

[170] Y. Zheng, X. Fang, M. C. Fehler, and D. R. Burns. Seismic characterization of fractured reservoirs by focusing Gaussian beams. *Geophysics*, 78:A23–A28, 2013.

[171] W.K. Zietlow and J.F. Labuz. Measurement of the intrinsic process zone in rock using acoustic emission. *Int. J. Rock Mech. Min. Sci.*, 35:291–299, 1998.

Chapter 8

Appendix

A Hessian of the phase function

A.1 Determinant of the Hessian matrix

At the stationary points of $\boldsymbol{\zeta}\cdot\boldsymbol{d}\pm r$, one finds via (2.27) and (2.25) its Hessian to read

$$A_{pq}(\boldsymbol{\zeta}) \;=\; \pm\frac{1}{r}\left[\frac{\partial\boldsymbol{\zeta}}{\partial\eta^p}\cdot\frac{\partial\boldsymbol{\zeta}}{\partial\eta^q} - \left(\boldsymbol{d}\cdot\frac{\partial\boldsymbol{\zeta}}{\partial\eta^p}\right)\left(\boldsymbol{d}\cdot\frac{\partial\boldsymbol{\zeta}}{\partial\eta^q}\right)\right] \;+\; \begin{cases} 0, & \boldsymbol{\zeta}=\boldsymbol{\zeta}_{\mathrm{I}}^{\pm} \\ -2|\boldsymbol{d}\cdot\boldsymbol{n}|\,\boldsymbol{n}\cdot\frac{\partial^2\boldsymbol{\zeta}}{\partial\eta^p\partial\eta^q}, & \boldsymbol{\zeta}=\boldsymbol{\zeta}_{\mathrm{II}}^{\pm} \end{cases},$$

$$\text{(A1)}$$

where $r = |\boldsymbol{\zeta}-\boldsymbol{x}^{\circ}| > 0$. On selecting the curvilinear coordinates (η^1,η^2) so that their tangents coincide with the *principal directions* $\boldsymbol{a}_p$ $(p{=}1,2)$ of S^{f} at the stationary point, (A1) reduces to

$$A_{pq}(\boldsymbol{\zeta}) \;=\; \pm\frac{1}{r}\left[g_{pq} - \sqrt{g_{pp}g_{qq}}\,(\boldsymbol{d}\cdot\boldsymbol{a}_p)(\boldsymbol{d}\cdot\boldsymbol{a}_q)\right] \;+\; \begin{cases} 0, & \boldsymbol{\zeta}=\boldsymbol{\zeta}_{\mathrm{I}}^{\pm} \\ 2|\boldsymbol{d}\cdot\boldsymbol{n}|\,\frac{g_{pq}}{\rho_p}, & \boldsymbol{\zeta}=\boldsymbol{\zeta}_{\mathrm{II}}^{\pm} \end{cases} \quad \text{(no sum)},$$

$$\text{(A2)}$$

where $\boldsymbol{n}$ is the unit outward normal on S^{f}; $\rho_1 \geqslant \rho_2 > 0$ denote the principal radii of curvature of S^{f}; g_{pq} are the components of the (diagonal) first fundamental form, and b_{pq} stand for the second fundamental form. From (A2) and the first of (2.29), one finds that

$$\det(A_{pq}) \;=\; \det g_{pq}\,\frac{(\boldsymbol{d}\cdot\boldsymbol{n})^2}{r^2} > 0, \qquad \mathrm{sgn}(A_{pq}) = \pm 2, \qquad \boldsymbol{\zeta}=\boldsymbol{\zeta}_{\mathrm{I}}^{\pm}, \quad \boldsymbol{x}^{\circ}\in \mathrm{I}^{\pm}, \qquad \text{(A3)}$$

where the signature of the Hessian matrix, $\mathrm{sgn}(A_{pq})$, equals the difference between the number of positive and negative eigenvalues of A_{pq}. The strict positivity of $\det(A_{pq})$ in (A3) demonstrates that the stationary-phase approximation (2.24) is valid for all sampling points $\boldsymbol{x}^\circ \notin \mathcal{N}_\epsilon$ along the $\mathrm{I}^\pm$ loci. The situation along the $\mathrm{II}^\pm$ loci is, however, more complicated since

$$\det(A_{pq}) \;=\; \frac{4(\boldsymbol{d}\cdot\boldsymbol{n})^2}{\rho_1\rho_2\, r^2}\, \det g_{pq}\, (r \pm r_1)(r \pm r_2), \qquad \boldsymbol{\zeta} = \boldsymbol{\zeta}^\pm_{\mathrm{II}}, \quad \boldsymbol{x}^\circ \in \mathrm{II}^\pm, \tag{A4}$$

where

$$\begin{aligned}
r_{1/2} &\;=\; \frac{1}{4|\boldsymbol{d}\cdot\boldsymbol{n}|}\Big[h \pm \sqrt{h^2 - 4(\boldsymbol{d}\cdot\boldsymbol{n})^2\rho_1\rho_2}\,\Big], \\
h &\;=\; \rho_1(1-(\boldsymbol{d}\cdot\boldsymbol{a}_1)^2) + \rho_2(1-(\boldsymbol{d}\cdot\boldsymbol{a}_2)^2).
\end{aligned} \tag{A5}$$

Assuming $\boldsymbol{x}^\circ \notin \mathcal{N}_\epsilon$, (A4) infers that the stationary-phase approximation (2.24) holds for all sampling points along ray II^+, and those along ray II^- whose distance to the stationary point, $r=|\boldsymbol{x}^\circ - \boldsymbol{\zeta}^-|$, is sufficiently separated from the caustic values (A5). In this case, one has

$$\begin{aligned}
\det(A_{pq}) &> 0, & \mathrm{sgn}(A_{pq}) &= 2, & \boldsymbol{\zeta} &= \boldsymbol{\zeta}^+_{\mathrm{II}}, & \boldsymbol{x}^\circ &\in \mathrm{II}^+, \\
\det(A_{pq}) &\gtrless 0 & \mathrm{sgn}(A_{pq}) &\in \{-2, 0, 2\}, & \boldsymbol{\zeta} &= \boldsymbol{\zeta}^-_{\mathrm{II}}, & \boldsymbol{x}^\circ &\in \mathrm{II}^-.
\end{aligned} \tag{A6}$$

A.2 Nature of the roots r_1 and r_2

In light of the facts that $0 < \rho_2 \leqslant \rho_1$ and $(\boldsymbol{d}\cdot\boldsymbol{n})^2 = 1 - (\boldsymbol{d}\cdot\boldsymbol{a}_1)^2 - (\boldsymbol{d}\cdot\boldsymbol{a}_2)^2$, one finds that the discriminant in (A5) is, for any given triplet $\{\rho_1, \rho_2, \boldsymbol{d}\cdot\boldsymbol{a}_1\}$, a monotonically decreasing function of $(\boldsymbol{d}\cdot\boldsymbol{n})^2$. Accordingly, the latter is (given $\boldsymbol{d}\cdot\boldsymbol{a}_1$) minimized by setting $\boldsymbol{d}\cdot\boldsymbol{a}_2 = 0$, in which case

$$h^2 - 4(\boldsymbol{d}\cdot\boldsymbol{n})^2\rho_1\rho_2 \;=\; (\rho_1(\boldsymbol{d}\cdot\boldsymbol{n})^2 - \rho_2)^2 \begin{cases} = 0, & \boldsymbol{d}\cdot\boldsymbol{a}_2 = 0 \quad \text{and} \quad |\boldsymbol{d}\cdot\boldsymbol{n}|^2 = \rho_2/\rho_1 \\ > 0, & \text{otherwise} \end{cases}. \tag{A7}$$

As a result, the roots r_1 and r_2 are real-valued, positive, and distinct unless $\boldsymbol{d}\cdot\boldsymbol{a}_2 = 0$ and $|\boldsymbol{d}\cdot\boldsymbol{n}|^2 = \rho_2/\rho_1$ (in which case $r_1 = r_2 = \sqrt{\rho_1\rho_2}/2$). From (A5), it is also seen that for fixed $\{\rho_1, \rho_2, \boldsymbol{d}\cdot\boldsymbol{n}\}$, h is a monotonically decreasing function of $(\boldsymbol{d}\cdot\boldsymbol{a}_1)^2$. Accordingly the lower (r_j^ℓ) and upper (r_j^u) bounds on $r_{1/2}$ can be obtained from (A5) by setting $(\boldsymbol{d}\cdot\boldsymbol{a}_1)^2$

to either zero or $1-(\boldsymbol{d}\cdot\boldsymbol{n})^2$; in particular, one finds that

$$
\begin{aligned}
r_2^\ell &= \frac{\rho_2}{2}|\boldsymbol{d}\cdot\boldsymbol{n}| \\
r_1^u &= \frac{\rho_1}{2|\boldsymbol{d}\cdot\boldsymbol{n}|}
\end{aligned}, \quad
r_2^u = \begin{cases} \frac{\rho_1}{2}|\boldsymbol{d}\cdot\boldsymbol{n}|, & |\boldsymbol{d}\cdot\boldsymbol{n}| \leqslant \sqrt{\frac{\rho_2}{\rho_1}} \\ \frac{\rho_2}{2|\boldsymbol{d}\cdot\boldsymbol{n}|}, & \text{otherwise} \end{cases}, \quad
r_1^\ell = \begin{cases} \frac{\rho_2}{2|\boldsymbol{d}\cdot\boldsymbol{n}|}, & |\boldsymbol{d}\cdot\boldsymbol{n}| \leqslant \sqrt{\frac{\rho_2}{\rho_1}} \\ \frac{\rho_1}{2}|\boldsymbol{d}\cdot\boldsymbol{n}| & \text{otherwise} \end{cases},
$$

$$\tag{A8}$$

where r_1^ℓ is obtained by substituting the upper bound on r_2 into identity $r_1 r_2 = \rho_1 \rho_2/4$. The above result is illustrated in Fig. 8.1 via the polar plots of $r_2^\ell, r_2^u, r_1^\ell$ and r_1^u for the example ratio $\rho_2/\rho_1 = 0.7$. For completeness it can be also shown that, consistent with Fig. 8.1,

$$
\lim_{|\boldsymbol{d}\cdot\boldsymbol{n}|\to 0} r_1 = \frac{\rho_1 - (\rho_1 - \rho_2)(\boldsymbol{d}\cdot\boldsymbol{a}_1)^2}{2|\boldsymbol{d}\cdot\boldsymbol{n}|}, \quad
\lim_{|\boldsymbol{d}\cdot\boldsymbol{n}|\to 0} r_2 = \frac{\frac{1}{2}\rho_1\rho_2 |\boldsymbol{d}\cdot\boldsymbol{n}|}{\rho_1 - (\rho_1 - \rho_2)(\boldsymbol{d}\cdot\boldsymbol{a}_1)^2}, \quad
\lim_{|\boldsymbol{d}\cdot\boldsymbol{n}|\to 1} r_k = \frac{\rho_k}{2}.
$$
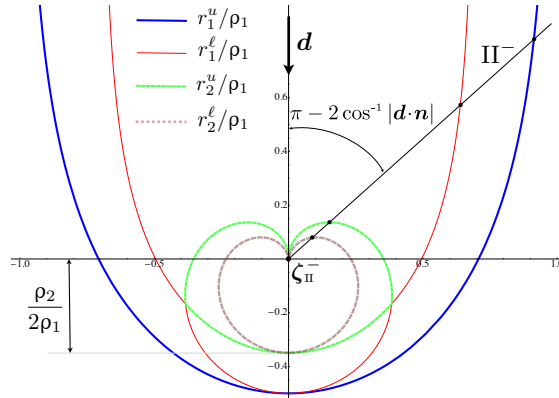
Figure 8.1: Upper and lower bounds on r_1 and r_2 along ray II^-, computed for $\rho_2/\rho_1 = 0.7$.

A.3 Behavior of the Hessian for near-caustic sampling points

For the purpose of this study, it is instructive to examine the limiting behavior of (A2) for sampling points $\boldsymbol{x}^\circ \in \mathrm{II}^-$ such that $r = |\boldsymbol{x}^\circ - \boldsymbol{\zeta}_{\mathrm{II}}^-| = r_k + \epsilon$, $\epsilon \to 0$. In this setting, consider first the situations when either $\boldsymbol{d}\cdot\boldsymbol{a}_1 = 0$ or $\boldsymbol{d}\cdot\boldsymbol{a}_2 = 0$, i.e. when A_{pq} in (A2) is diagonal.

Case $d \cdot a_1 = 0$ $(\zeta = \zeta_\text{II}^-)$. For this configuration, one finds from (A2) and (A5) that the mixed derivative vanishes at the stationary point (i.e. $A_{12} = A_{21} = 0$) for any $r > 0$, while

$$A_{11} \stackrel{\epsilon^2}{=} g_{11}\frac{4|d \cdot n|^2}{\rho_1^2}\epsilon, \qquad A_{22} \stackrel{\epsilon}{=} 2g_{22}\left(\frac{|d \cdot n|}{\rho_2} - \frac{|d \cdot n|^3}{\rho_1}\right), \qquad r = r_1 + \epsilon,$$

$$A_{22} \stackrel{\epsilon^2}{=} \frac{4g_{22}}{\rho_2^2}\epsilon, \qquad A_{11} \stackrel{\epsilon}{=} \frac{2g_{11}}{|d \cdot n|}\left(\frac{|d \cdot n|^2}{\rho_1} - \frac{1}{\rho_2}\right), \qquad r = r_2 + \epsilon, \tag{A9}$$

when $\epsilon \to 0$. From (A9) it is clear that the corank of the Hessian matrix (A2) equals *one* in the limit as $r \to r_{1/2}$, except when $|d \cdot n|^2 = \rho_2/\rho_1 = 1$.

Case $d \cdot a_2 = 0$ $(\zeta = \zeta_\text{II}^-)$. In this situation, one again finds that $A_{12} = A_{21} = 0$ for any $r > 0$. On the other hand, it follows from (A2) and (A5) that

$$A_{11} \stackrel{\epsilon^2}{=} \frac{4g_{11}}{\rho_1^2}\epsilon, \qquad A_{22} \stackrel{\epsilon}{=} \frac{2g_{22}}{|d \cdot n|}\left(\frac{|d \cdot n|^2}{\rho_2} - \frac{1}{\rho_1}\right), \qquad \begin{cases} r = r_1 + \epsilon, \ \frac{\rho_2}{\rho_1} < |d \cdot n|^2 \\ r = r_2 + \epsilon, \ \frac{\rho_2}{\rho_1} \geqslant |d \cdot n|^2 \end{cases}$$

$$A_{22} \stackrel{\epsilon^2}{=} \frac{4g_{22}|d \cdot n|^2}{\rho_2^2}\epsilon, \quad A_{11} \stackrel{\epsilon}{=} 2g_{11}\left(\frac{|d \cdot n|}{\rho_1} - \frac{|d \cdot n|^3}{\rho_2}\right), \qquad \begin{cases} r = r_1 + \epsilon, \ \frac{\rho_2}{\rho_1} \geqslant |d \cdot n|^2 \\ r = r_2 + \epsilon, \ \frac{\rho_2}{\rho_1} < |d \cdot n|^2 \end{cases} \tag{A10}$$

when $\epsilon \to 0$. For sampling points x° along ray II$^-$, (A10) accordingly demonstrates that the corank of (A2) equals one in the limit as $r \to r_{1/2}$, except when $|d \cdot n|^2 = \rho_2/\rho_1$.

Case $(d \cdot a_1)(d \cdot a_2) \neq 0$ $(\zeta = \zeta_\text{II}^-)$. For this class of configurations, $r_1 \neq r_2$ due to (A5) and (A7). As a result the corank of the Hessian matrix (A2) at $\zeta = \zeta_\text{II}^-$ equals one, regardless of $d \cdot n$, in the limit as $r \to r_{1/2}$. To examine the problem in more detail, take $r = r_j + \epsilon$, $\epsilon \to 0$ where $j = 1, 2$. According to the Splitting Lemma [132], for each j there exists a local diffeomorphism $(\eta^1, \eta^2) \to (\vartheta^1, \vartheta^2)$ in a neighborhood of the critical point under which the phase function (2.36) is approximated by the second of (2.39). In this case one has $A_{\vartheta^1\vartheta^2} = A_{\vartheta^2\vartheta^1} = 0$ and, thanks to the invariance of (A4) with respect to the choice of local coordinates,

$$A_{\vartheta^1\vartheta^1} = O(1), \qquad A_{\vartheta^2\vartheta^2} = O(\epsilon), \qquad r = r_j + \epsilon, \qquad \epsilon \to 0. \tag{A11}$$

B Asymptotic expansion in the caustic region

For completeness, this section summarizes the asymptotic evaluation of a two-dimensional Fourier integral (2.23) in situations when the phase function $\phi = \boldsymbol{\zeta} \cdot \boldsymbol{d} - r$ is affiliated with any of the diffraction catastrophes listed in Table 2.1. The analysis implicitly makes use of the Van der Corput neutralizers [31, 39] that are described at the end of the section.

B.1 Hessian matrix of corank one

With the caveat of two degenerate configurations discussed in Appendix A.3, the corank of the Hessian of (2.36) within the bifurcation set (2.37) equals *one* which allows for the separation of ϕ into a non-degenerate Morse piece and a single-argument degenerate part according to the second of (2.39). In this setting (2.23) can be first integrated along the non-degenerate direction ϑ^1, thereby allowing the contribution of nearby (or coalescing) stationary points to be investigated in the context of a one-dimensional integral

$$k^{-\frac{1}{2}} \int_{-\infty}^{\infty} \mathscr{F}(\vartheta)\, e^{ik\psi(\vartheta)}\, \mathrm{d}\vartheta, \qquad \vartheta = \vartheta^2, \qquad \psi(\vartheta) = (\boldsymbol{\zeta} \cdot \boldsymbol{d} - r)|_{\vartheta^1 = 0}, \qquad \text{(B1)}$$

where

$$\mathscr{F}(\vartheta) = \frac{\sqrt{2\pi}\, e^{i\delta\pi/4}\, f(\boldsymbol{\zeta})|_{\vartheta^1 = 0}}{\sqrt{|\partial^2\phi/\partial(\vartheta^1)^2|_{\vartheta^1 = 0}}} \times \left.\frac{\mathrm{d}S_\eta}{\mathrm{d}S_\vartheta}\right|_{\vartheta^1 = 0}, \qquad \delta = \mathrm{sign}\left(\frac{\partial^2\phi}{\partial(\vartheta^1)^2}\right)\bigg|_{\vartheta^1 = 0}. \qquad \text{(B2)}$$

Following Table 2.1, the codimension of the phase function is assumed not to exceed three, which in the context of (B1) allows for structurally-stable caustics that are of either type *fold*, *cusp* or *swallowtail* [29] depending on the geometry of S^{f} in the neighborhood of $\boldsymbol{\zeta}_{\mathrm{II}}^{-}$.

One particular phenomenon that is common to all caustics, as elucidated by the catastrophe theory, is a dramatic shift in the character of the phase function due to smooth variation of its parameters. This may be interpreted as the suppression of propagating waves across the caustic: on the so-called *bright side* [152] of the bifurcation set B_ϕ, the diffraction pattern is formed by propagating waves stemming from the interaction of real-valued stationary points; however as $\boldsymbol{x}^\circ$ moves across B_ϕ into the *dark side* of the caustic, at least one pair of the interacting stationary points become

complex conjugate, leading to a diffraction pattern that is formed (at least in part) by evanescent waves. Due to the fact that the ensuing asymptotic models apply uniformly throughout the neighborhood of B_ϕ (and beyond), however, the remainder of this section makes little distinction between its bright and dark regions.

The procedure for developing *uniform* asymptotic approximation for a given type of diffraction catastrophe was first proposed in [53], and entails the following three steps. First, the degeneracy of the phase function is categorized, in terms of the topology of its stationary points, as a particular type of universal unfolding according to Thom's classification theorem. Second, a diffeomorphism is specified that maps the given phase function into a *normal form* representing the featured class of caustics. In particular, parameters of the so-called (minimal) *control space*, given by the coefficients of the normal form, are computed by solving a set of nonlinear equations. Third, depending upon the type of the caustic, a suitable expansion of the non-exponential part of the integrand is introduced – by which one arrives at the sought asymptotic approximation of an oscillatory integral. Here one should note that in the immediate vicinity of the bifurcation set B_ϕ (where stationary points coalesce), the uniform approximation breaks down. In this case the required mapping is computed stably, albeit locally, via Taylor series expansion of both the phase function and sought diffeomorphism, leading to the so-called *transitional* asymptotic approximation. A comprehensive asymptotic analysis of the fold and cusp diffraction catastrophes (both in terms of uniform and transitional approximations) can be found in [152], while the uniform asymptotic approximation of the swallowtail catastrophe is obtained in [61]. To facilitate the main presentation, the remainder of this section summarizes the uniform asymptotic treatment of the fold, cusp, and swallowtail catastrophes. Their transitional counterparts retain the same functional form, except that the germane control parameters and coefficients of approximation are computed locally.

Fold catastrophe. This type of caustics is affiliated with two coalescing stationary points that, on the dark side B_ϕ, become complex conjugate. The local behavior of the phase function around the "halfway" inflection point $\psi^{(2)}(0) = 0$ follows, up to a diffeomorphism, the fold *normal form* $t^3/3 + ct$. Following the aforementioned procedure, uniform asymptotic approximation of the one-dimensional integral (B1) due to

fold-type degeneracy of the phase function can be computed as

$$
k^{-1/2} \int_{-\infty}^{\infty} \mathcal{F}(\vartheta)\, e^{ik\psi(\vartheta)}\, \mathrm{d}\vartheta \;=\;
$$
$$
e^{ik\psi_\circ} \left[k^{-5/6} f_1\, Ai(-ck^{\frac{2}{3}}) \;+\; k^{-7/6} f_2\, Ai'(-ck^{\frac{2}{3}}) \right] \;+\; O(k^{-3/2}),
\tag{B3}
$$

in terms of the Airy function and its derivative

$$
Ai(b) \;=\; \frac{1}{2\pi} \int_{-\infty}^{\infty} e^{i(\tau^3/3 + b\tau)}\, \mathrm{d}\tau, \qquad
Ai' \;=\; \frac{\mathrm{d}Ai}{\mathrm{d}b},
\tag{B4}
$$

see e.g. [39]. Through a diffeomorphism $\vartheta \to t = k^{-1/3}\tau$ transforming $\psi(\vartheta)$ into $t^3/3 + ct + \psi_\circ$, the control parameter c and phase offset can be computed explicitly as

$$
c \;=\; \left[\tfrac{3}{4}\left(\psi(\vartheta_2) - \psi(\vartheta_1) \right) \right]^{2/3}, \qquad
\psi_\circ \;=\; \tfrac{1}{2}\left[\psi(\vartheta_1) + \psi(\vartheta_2) \right],
$$

where ϑ_1 and ϑ_2 are the adjacent stationary points of $\psi(\vartheta)$, arranged so that $\psi(\vartheta_2) > \psi(\vartheta_1)$. The remaining quantities in (B3) are the coefficients of the expansion given by

$$
f_1 = \pi g^+ \quad f_2 = -\frac{i\pi}{\sqrt{c}} g^-, \quad g^{\pm} = \mathcal{F}(\vartheta_1)\left[2\sqrt{c}/\psi^{(2)}(\vartheta_1)\right]^{1/2} \pm \mathcal{F}(\vartheta_2)\left[-2\sqrt{c}/\psi^{(2)}(\vartheta_2)\right]^{1/2}.
$$

As ϑ_1 and ϑ_2 move apart, uniform approximation (B3) reduces to the sum of the contributions of two isolated stationary points. It is also worth mentioning that the featured asymptotic model remains valid on the dark side of B_ϕ provided that c is replaced by $|c|e^{i\pi}$, where $|c| = (\tfrac{3}{4}\,\mathrm{Im}[\psi(\vartheta_1) - \psi(\vartheta_2)])^{2/3}$. Further details on (B3), along with a full account of the transitional approximation, can be found in [152].

Cusp catastrophe. In diffraction terms, this type of degeneracy occurs at the point contact of two fold caustics, and is characterized by three coalescing stationary points as the sampling point $\boldsymbol{x}^\circ$ approaches B_ϕ from the bright side. Specifically, the cusp catastrophe is the universal unfolding of *germ* t^4 with codimension two and normal form $t^4 + c_2 t^2 + c_1 t$. Assuming $\psi^{(3)}(0) = 0$ and $\psi^{(4)}(0) > 0$, uniform asymptotic approximation

of (B1) in the cusp region is given by

$$k^{-1/2} \int_{-\infty}^{\infty} \mathscr{F}(\vartheta) e^{ik\psi(\vartheta)} \, d\vartheta \;=\;$$

$$e^{ik\psi_{\circ}} \sum_{m=0}^{2} k^{-(3+m)/4} f_m \, P_{,m}(c_1 k^{\frac{3}{4}}, c_2 k^{\frac{1}{2}}) \;+\; O(k^{-3/2}), \tag{B5}$$

in terms of the Pearcey function and its derivatives

$$P(b_1, b_2) \;=\; \int_{-\infty}^{\infty} e^{i(\tau^4 + b_2 \tau^2 + b_1 \tau)} \, d\tau, \qquad P_{,0} \;=\; P, \qquad P_{,m} \;=\; \frac{1}{i} \frac{\partial P}{\partial b_m} \;\; (m=1,2),$$

see for instance [152]. Through an implicit diffeomorphism $\vartheta \to t = k^{-1/4}\tau$, the phase function $\psi(\vartheta)$ is mapped onto $t^4 + c_2 t^2 + c_1 t + \psi_{\circ}$. Accordingly, the control parameters (c_1, c_2) and phase offset $\psi_{\circ}$ featured in (B5) can be computed by solving the set of nonlinear equations enforcing one-to-one correspondence between the stationary points in the ϑ and t spaces, namely

$$\psi_{\circ} + c_1 t_m + c_2 t_m^2 + t_m^4 \;=\; \psi(\vartheta_m), \qquad m = 1, 2, 3$$

where the stationary points of $\psi(\vartheta)$ are denoted by ϑ_m, and their counterparts in the t-space are t_m which satisfy $4 t_m^3 + 2 c_2 t_m + c_1 = 0$. The coefficients f_m of the uniform expansion (B5) are obtained by solving

$$f_0 + f_1 t_m + f_2 t_m^2 \;=\; \mathscr{F}(\vartheta_m) \left. \frac{d\vartheta}{dt} \right|_{t=t_m}, \qquad \left. \frac{d\vartheta}{dt} \right|_{t=t_m} = \left[\frac{12 t_m^2 + 2 c_2}{\psi^{(2)}(\vartheta_m)} \right]^{1/2}, \qquad m = 1, 2, 3.$$

The transitional Pearcey approximation, that applies in the immediate vicinity of the cusp caustic, can be found in [152]. Note that the above analysis applies equally to the bright and dark side of B_ϕ, the key difference being that the triplets ϑ_m and t_m are each comprised of one real and two (complex-conjugate) roots in the latter case. In situations where $\psi^{(4)}(0) < 0$, the problem is resolved by applying (B5) to the complex conjugate of (B1).

Swallowtail catastrophe. In this case that is affiliated with four (real or complex) stationary points, two cusped edges, known as *ribs*, meet at a point. This type of

catastrophe is classified as the universal unfolding of germ t^5 with codimension three and normal form $t^5 + c_3 t^3 + c_2 t^2 + c_1 t$. The uniform asymptotic approximation of the diffraction integral (B1) endowed with this type of caustics can be written as

$$
\begin{aligned}
k^{-1/2} \int_{-\infty}^{\infty} \mathscr{F}(\vartheta)\, e^{ik\psi(\vartheta)}\, \mathrm{d}\vartheta \ &= \\
e^{ik\psi_\circ} \sum_{m=0}^{3} k^{-(7+2m)/10} \, f_m \, S_{,m}&(c_1 k^{\frac{4}{5}}, c_2 k^{\frac{3}{5}}, c_3 k^{\frac{2}{5}}) \ + \ O(k^{-3/2}),
\end{aligned}
\tag{B6}
$$

in terms of the swallowtail function and its derivatives

$$
S(b_1, b_2, b_3) \ = \ \int_{-\infty}^{\infty} e^{i(\tau^5 + b_3 \tau^3 + b_2 \tau^2 + b_1 \tau)}\, \mathrm{d}\tau,
$$

$$
S_{,0} \ = \ S, \qquad S_{,m} \ = \ \frac{1}{i} \frac{\partial S}{\partial b_m} \qquad (m = 1, 2, 3)
$$

see [60]. By invoking the same strategy as in the cusp case, the control parameters (c_1, c_2, c_3) and phase offset $\psi_\circ$ are obtained by solving the system of nonlinear equations

$$
\psi_\circ + c_1 t_m + c_2 t_m^2 + c_3 t_m^3 + t_m^5 \ = \ \psi(\vartheta_m), \qquad m = 1, 2, 3, 4,
$$

where ϑ_m are the stationary points of $\psi(\vartheta)$, and t_m are their counterparts in the t-space satisfying $5 t_m^4 + 3 c_3 t_m^2 + 2 c_2 t_m + c_1 = 0$. The remaining coefficients in (B6) are determined from the linear set of equations

$$
f_0 + f_1 t_m + f_2 t_m^2 + f_3 t_m^3 \ = \ \mathscr{F}(\vartheta_m) \left[\frac{20 t_m^3 + 6 c_3 t_m + 2 c_2}{\psi^{(2)}(\vartheta_m)} \right]^{1/2}, \qquad m = 1, 2, 3, 4,
$$

In the immediate vicinity of B_ϕ (where two or more stationary points coalesce), the above solution breaks down and is replaced by the transitional approximation, see [60, 61].

B.2 Hessian matrix of corank two

From the results in Appendix A.3, one finds that the rank of the Hessian matrix (A1) vanishes only for two nested degenerate configurations, namely i) $\boldsymbol{d}\cdot\boldsymbol{a}_2 = 0$ and $|\boldsymbol{d}\cdot\boldsymbol{n}|^2 = \rho_2/\rho_1 < 1$, and ii) $|\boldsymbol{d}\cdot\boldsymbol{n}|^2 = \rho_2/\rho_1 = 1$. In both cases, the corank-two degeneracy occurs

for sampling points where

$$r = |\boldsymbol{x}^{\circ} - \boldsymbol{\zeta}_{\text{II}}^{-}| \to r_1, \qquad r_1 = r_2 = \tfrac{1}{2}\rho_1|\boldsymbol{d}\cdot\boldsymbol{n}|, \qquad \boldsymbol{x}^{\circ} \in \text{II}^{-}.$$

To identify the class of catastrophes describing each case, it is necessary to expose the germ of the phase function $\phi = \boldsymbol{\zeta} \cdot \boldsymbol{d} - r$ in (2.23), characterizing its behavior when all nearby stationary points coalesce [29] as $r \to r_1$. To this end, consider first the third-order expansion of $\phi(\eta^1, \eta^2)$ for the case when $\rho_2/\rho_1 < 1$. Assuming the principal curvatures ρ_1 and ρ_2 to be locally constant, (2.36) can be expanded in Taylor series as

$$\phi(\eta^1, \eta^2) \simeq \phi_{\circ} + \frac{\boldsymbol{d}\cdot\boldsymbol{a}_1}{\rho_1}\left[\frac{g_{11}}{\rho_1}(\eta^1)^3 + \frac{g_{22}}{\rho_2}\eta^1(\eta^2)^2\right](g_{11})^{1/2}, \qquad \rho_2/\rho_1 < 1, \qquad \text{(B7)}$$

where $\phi_{\circ} = \phi(\boldsymbol{\zeta}_{\text{II}}^{-})$. On introducing the linear mapping $(\eta^1, \eta^2) \to (s, t)$ by way of

$$\eta^1 = \frac{1}{\sqrt{g_{11}}}\left(\frac{4\,\boldsymbol{d}\cdot\boldsymbol{a}_1}{\rho_1{}^2}\right)^{-\frac{1}{3}}(t + s), \qquad \eta^2 = \frac{|\boldsymbol{d}\cdot\boldsymbol{n}|\sqrt{3}}{\sqrt{g_{22}}}\left(\frac{4\,\boldsymbol{d}\cdot\boldsymbol{a}_1}{\rho_1{}^2}\right)^{-\frac{1}{3}}(t - s), \qquad \text{(B8)}$$

one obtains (up to a constant) the normal cubic form $s^3 + t^3$ of the phase function at $r = r_1$ which is of codimension three [51]. This particular germ corresponds to the *hyperbolic umbilic* catastrophe listed in Table 2.1, and is geometrically described by a cusp line touching a fold surface at the focus. In this case there are four interacting (real or complex) stationary points whose coalescence entails three control parameters (c_1, c_2, c_3), and their topology is such that the phase function can be transformed, in the neighborhood of $r = r_1$, into the normal form $s^3 + t^3 + c_3\,st + c_2\,t + c_1\,s$ via a diffeomorphism. The uniform asymptotic approximation of (2.23) due to this type of diffraction catastrophe [59] can be computed as

$$\int_{S^{\text{f}}} f(\boldsymbol{\zeta})\,e^{\text{i}k\phi(\eta^1,\eta^2)}\,\text{d}S_{\eta} =$$

$$e^{\text{i}k\phi_{\circ}}\sum_{m=0}^{2} k^{-(2+m)/3}f_m\,H_{,m}(c_1 k^{\frac{2}{3}}, c_2 k^{\frac{2}{3}}, c_3 k^{\frac{1}{3}}) + O(k^{-5/3}), \qquad \text{(B9)}$$

in terms of the hyperbolic-umbilic canonical integral and its derivatives

$$H(b_1, b_2, b_3) = \int_{-\infty}^{\infty} \int_{-\infty}^{\infty} e^{\mathrm{i}(\sigma^3 + \tau^3 + b_3 \sigma \tau + b_2 \tau + b_1 \sigma)} \, \mathrm{d}\sigma \, \mathrm{d}\tau,$$

$$H_{,0} = H, \qquad H_{,1} = \frac{1}{\mathrm{i}} \sum_{j=1}^{2} \alpha_j \frac{\partial H}{\partial b_j}, \qquad H_{,2} = \frac{1}{\mathrm{i}} \frac{\partial H}{\partial b_3}.$$

The procedure for computing the control parameters (c_1, c_2, c_3) follows the same logic as that outlined in the previous section and entails transforming $\phi(\eta^1, \eta^2)$ to the hyperbolic-umbilic normal form, see [59, 110] for details. Further, the coefficients $f_0, f_1\alpha_1, f_1\alpha_2$ and f_2 in (B9) are obtained [167] by expanding the non-exponential part of the integrand as

$$f(\boldsymbol{\zeta}) \frac{\mathrm{d}S_\eta}{\mathrm{d}s \, \mathrm{d}t} \simeq f_0 + f_1(\alpha_1 s + \alpha_2 t) + f_2 \, s t, \qquad \boldsymbol{\zeta} = \boldsymbol{\zeta}(\eta^1, \eta^2). \tag{B10}$$

As examined earlier, the remaining configuration from Appendix A.3 resulting in a corank-two Hessian of the phase function is given by $|\boldsymbol{d} \cdot \boldsymbol{n}|^2 = \rho_2/\rho_1 = 1$ and $r = r_1 = r_2$. In this case, the apex of S^{f} is also an umbilic point of the exposed boundary, and the third-order derivatives in (B7) uniformly vanish. Accordingly, the class of caustics involved in this case is at least of codimension four, i.e. $\mathrm{cod}(\phi) \geqslant 4$ which is beyond the scope of present investigation.

For completeness the reader is reminded that depending on the shape of S^{f}, the corank-two Hessian of the phase function may further be affiliated with "global" caustics, which involve third- and higher-order surface properties – and thus (possibly) additional types of degeneracy. Within the framework of this study which is limited to $\mathrm{cod}(\phi) \leqslant 3$, the only remaining class of catastrophes meeting this requirement is that of the *elliptic umbilic*, see Table 2.1. In this case, the leading asymptotic behavior of the diffraction integral is $O(k^{-2/3})$ [28], i.e. the same as that for the hyperbolic umbilic catastrophe.

As an illustration, example behavior of the canonical integrals featured in this section is plotted in Fig. 8.2, including their large-argument asymptotics as applicable.
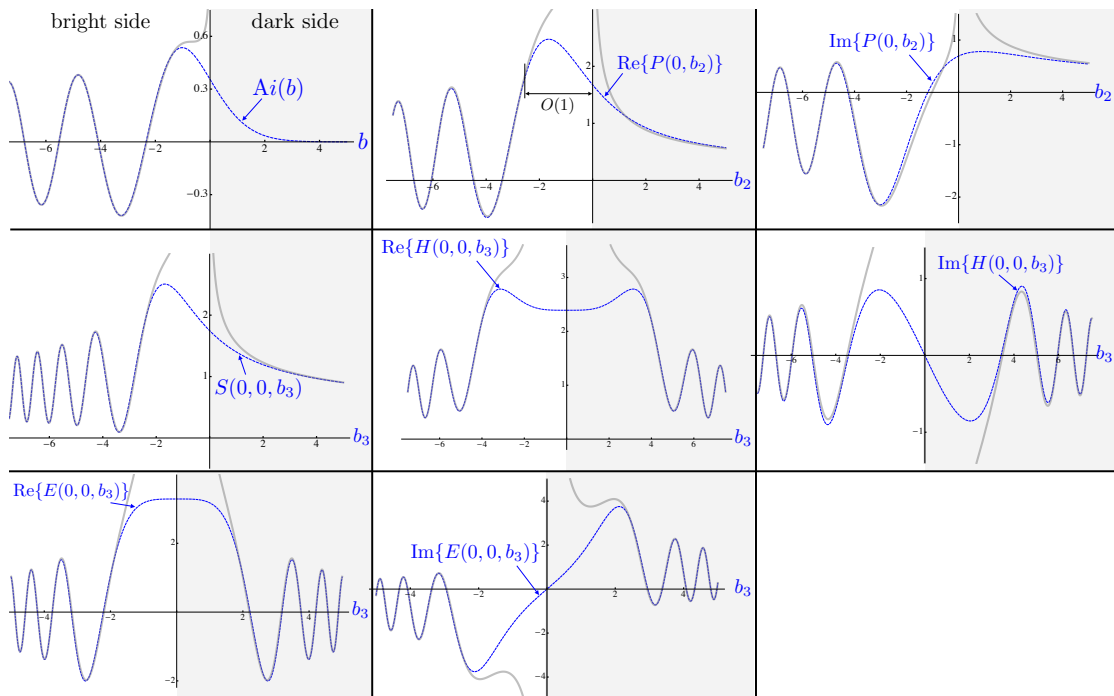
Figure 8.2: Elements of diffraction patterns (dashed lines) in the normalized control space $\boldsymbol{b}$ along with their large-argument asymptotic expansion (solid grey lines) for catastrophes of codimension less than four: fold, cusp, swallowtail, hyperbolic umbilic, end elliptic umbilic (left-to-right, top-to-bottom).

B.3   Neutralizer functions

For generic $\mathscr{F}$ and ψ, the contribution of a given set of coalescing stationary points of ψ to the one-dimensional integral in (B1) is evaluated via the partition of unity, namely

$$1 = \sum_j g_j(\vartheta) + \tilde{g}(\vartheta) \qquad \Rightarrow \qquad \mathscr{F}(\vartheta) = \sum_j \mathscr{F}_j(\vartheta) + \tilde{\mathscr{F}}(\vartheta), \qquad \vartheta \in \mathbb{R},$$

where $\mathscr{F}_j = \mathscr{F} g_j$, and g_j (called the Van der Corput neutralizers) isolate the individual clusters of interacting stationary points. Assuming that the given cluster is enclosed by g_m, the sought contribution is accordingly computed as

$$k^{-\frac{1}{2}} \int_{-\infty}^{\infty} \mathscr{F}_m(\vartheta)\, e^{ik\psi(\vartheta)}\, \mathrm{d}\vartheta. \tag{B11}$$

As examined for instance in [31], g_j are designed to: i) be infinitely differentiable, ii) equal unity over the support of germane (stationary point) interaction, and iii) vanish over the support of the remaining clusters. One example of a function meeting these requirements [39] is given by $g(\vartheta) = h(\vartheta)h(-\vartheta)/h_0^2$, where

$$h(x) = \int_x^\infty e(\delta - s)\,e(s - \epsilon)\,\mathrm{d}s, \qquad e(s) = \begin{cases} 0, & s \leqslant 0 \\ e^{-1/s}, & s > 0 \end{cases}, \qquad 0 < \epsilon < \delta$$

and

$$h_0 = \int_\epsilon^\delta e(\delta - s)\,e(s - \epsilon)\,\mathrm{d}s.$$

In particular, it is trivial to show that such infinitely differentiable function equals unity (resp. zero) for $|\vartheta| < \epsilon$ (resp. $|\vartheta| > \delta$).

Note that the concept of neutralizer functions extends naturally to surface (and in general higher-dimensional) integrals, see e.g. [45].

C   Existence and uniqueness of the stationary point ζ_II^+

Consider a convex domain $D \subset \mathbb{R}^3$ bounded by a smooth closed surface $S = \partial D$. As examined e.g. in [31], for each $\boldsymbol{x} \in \mathbb{R}^3 \backslash \overline{D}$ there exists a unique normal projection on S, $\boldsymbol{x}^*$, such that

$$\widehat{\boldsymbol{x}^* - \boldsymbol{x}} \;=\; -\boldsymbol{n}(\boldsymbol{x}^*), \qquad \boldsymbol{x}^* \in S. \tag{C1}$$

Next, consider the perturbation of $\boldsymbol{x}$ by $\mathrm{d}\boldsymbol{x}$ as shown in Fig. 8.3, where

$$\mathrm{d}_\mathrm{T}\boldsymbol{x} \;=\; \mathrm{d}\boldsymbol{x} - (\mathrm{d}\boldsymbol{x} \cdot \boldsymbol{n})\,\boldsymbol{n}(\boldsymbol{x}^*)$$

signifies the "tangential" component of $\mathrm{d}\boldsymbol{x}$ that is perpendicular to $\boldsymbol{n}$. Letting further $\mathrm{d}\boldsymbol{x}^* \perp \boldsymbol{n}$ denote the perturbation of the affiliated projection point, one finds that

$$\mathrm{d}\boldsymbol{n} \;=\; \boldsymbol{n}(\boldsymbol{x}^* + \mathrm{d}\boldsymbol{x}^*) - \boldsymbol{n}(\boldsymbol{x}^*) \;=\; \alpha\,(\mathrm{d}_\mathrm{T}\boldsymbol{x} - \mathrm{d}\boldsymbol{x}^*), \tag{C2}$$

where $\alpha > 0$ is the scaling coefficient dependent on distance $|\boldsymbol{x}^* - \boldsymbol{x}|$. With reference to the orthonormal basis $(\boldsymbol{a}_1, \boldsymbol{a}_2, \boldsymbol{n})$ where $\boldsymbol{a}_1$ and $\boldsymbol{a}_2$ are the principal directions of S

at $\boldsymbol{x}^*$, the formulae of Rodrigues [103] demonstrate that for a convex domain

$$\mathrm{d}\boldsymbol{n} = \rho_1^{-1}(\mathrm{d}\boldsymbol{x}^* \cdot \boldsymbol{a}_1)\,\boldsymbol{a}_1 + \rho_2^{-1}(\mathrm{d}\boldsymbol{x}^* \cdot \boldsymbol{a}_2)\,\boldsymbol{a}_2, \tag{C3}$$

where ρ_1 and ρ_2 denote the principal radii of curvature. On contracting the difference between (C2) and (C3) by $\boldsymbol{a}_p$ ($p=1,2$) one finds that

$$\mathrm{d}\boldsymbol{x}^* \cdot \boldsymbol{a}_p = \frac{\alpha\,\rho_p}{1+\alpha\rho_p}\,(\mathrm{d}_{\mathrm{T}}\boldsymbol{x} \cdot \boldsymbol{a}_p), \quad \Longrightarrow \quad \mathrm{d}\boldsymbol{x}^* \cdot \mathrm{d}\boldsymbol{x} = \sum_{p=1}^{2} \frac{\alpha\,\rho_p}{1+\alpha\rho_p}\,(\mathrm{d}_{\mathrm{T}}\boldsymbol{x} \cdot \boldsymbol{a}_p)^2 > 0, \tag{C4}$$

as long as $\mathrm{d}\boldsymbol{x} \nparallel \boldsymbol{n}$. Here it is also noted that

$$\mathrm{d}r = \tfrac{1}{2} r\,\mathrm{d}\boldsymbol{n} \cdot \mathrm{d}\boldsymbol{n} + \mathrm{d}\boldsymbol{x} \cdot \boldsymbol{n} > 0 \qquad \text{when} \qquad \mathrm{d}\boldsymbol{x} \cdot \boldsymbol{n} > 0, \qquad r = |\boldsymbol{x}^* - \boldsymbol{x}|. \tag{C5}$$
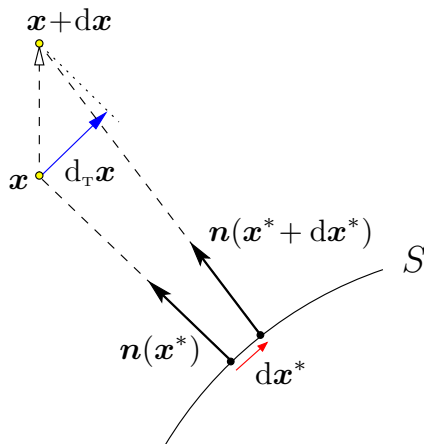
Figure 8.3: Perturbation of the normal projection, $\boldsymbol{x}^*$, of $\boldsymbol{x} \in \mathbb{R}^3 \backslash \overline{D}$ on S.

Proposition C.1. For each sampling point $\boldsymbol{x}^\circ \in \mathbb{R}^3 \backslash \bar{\mathscr{L}}^\pm$ where $\mathscr{L}^\pm(\boldsymbol{d})$ are open "half" cylinders defined in (2.28), there exists a unique stationary point $\boldsymbol{\zeta}_{\mathrm{II}}^+ \in S^{\mathrm{f}}$ given by the second of (2.27).

Proof. With reference to Fig. 8.4, consider the line L parallel to $\boldsymbol{d}$ passing through $\boldsymbol{x}^\circ$, and let $\boldsymbol{z}$ be the reference point on this line such that $(\boldsymbol{z} - \boldsymbol{z}^*) \perp \boldsymbol{d}$, where $\boldsymbol{z}^*$ is the normal projection of $\boldsymbol{z}$ on S according to (C1). In this setting, it is instructive to

examine the set of trial points $\boldsymbol{x} \in L$ "above" $\boldsymbol{z}$ specified by

$$\boldsymbol{x} \in L^{\mathrm{f}}, \qquad L^{\mathrm{f}} = \{\boldsymbol{\xi} \colon \boldsymbol{\xi} = \boldsymbol{z} + \chi(-\boldsymbol{d}), \ \chi > 0\}.$$

In light of the earlier discussion, for any $\boldsymbol{x} \in L^{\mathrm{f}}$ there exists a unique normal projection $\boldsymbol{x}^* \in S^{\mathrm{f}}$. In general, vectors $\boldsymbol{x}^* - \boldsymbol{x}$ are not coplanar when $\boldsymbol{x} \in L^{\mathrm{f}}$. On taking $\mathrm{d}\boldsymbol{x} = \mathrm{d}\chi(-\boldsymbol{d})$ and recalling that $\boldsymbol{n}{\cdot}\boldsymbol{d} < 0$ on S^{f}, one finds from (C6) that $r = |\boldsymbol{x}^* - \boldsymbol{x}|$ increases monotonically with $\chi > 0$. From Fig. 8.4, it is also seen that $\forall \boldsymbol{x} \in L^{\mathrm{f}}$ there is a *unique* "trailing" point, $\boldsymbol{x}' \in L$, with coordinates

$$\begin{aligned}
\boldsymbol{x}' &= \boldsymbol{x} - \frac{r}{2|\boldsymbol{n}{\cdot}\boldsymbol{d}|}(-\boldsymbol{d}) = \boldsymbol{z} + \chi'(-\boldsymbol{d}), \\
\chi' &= (\boldsymbol{x}^* - \boldsymbol{z}^*){\cdot}(-\boldsymbol{d}) + r\Big(|\boldsymbol{n}{\cdot}\boldsymbol{d}| - \frac{1}{2|\boldsymbol{n}{\cdot}\boldsymbol{d}|}\Big),
\end{aligned} \tag{C6}$$

where $\boldsymbol{n} = \boldsymbol{n}(\boldsymbol{x}^*)$. The key feature of $\boldsymbol{x}'$ is that the normal projection of $\boldsymbol{x}$ on S^{f}, $\boldsymbol{x}^*$, is the *stationary point* of type $\boldsymbol{\zeta}_{\mathrm{II}}^+$ for the integrals in (2.22) when the sampling point $\boldsymbol{x}^{\circ}$ coincides with $\boldsymbol{x}'$. Taking $\mathrm{d}\boldsymbol{x} = \mathrm{d}\chi(-\boldsymbol{d})$ as before, it follows from (C4) that the product $(\boldsymbol{x}^* - \boldsymbol{z}^*){\cdot}(-\boldsymbol{d})$ increases monotonically with $\chi > 0$. By virtue of the latter equality, one also finds that $|\boldsymbol{n}{\cdot}\boldsymbol{d}|$ steadily traverses the interval $(0,1)$ with increasing $\chi \in (0, \infty)$. As a result, $\chi'(\chi)$ is a *monotonically increasing* function that maps $(0, \infty)$ onto $(-\infty, \infty)$. On denoting the χ' coordinate of the given sampling point $\boldsymbol{x}^{\circ} \in L$ by $\chi'_{\circ} \gtreqless 0$, it follows that there exists a unique value $\chi_{\circ} > 0$, specified by the equality $\chi'(\chi_{\circ}) = \chi'_{\circ}$, such that $\boldsymbol{\zeta}_{\mathrm{II}}^+ = \boldsymbol{x}^* \in S^{\mathrm{f}}$ for $\boldsymbol{x} = \boldsymbol{z} + \chi_{\circ}(-\boldsymbol{d})$. $\qquad \square$

Proposition C.2. For each sampling point $\boldsymbol{x}^{\circ} \in \bar{\mathscr{L}}^- \backslash S^{\mathrm{f}}$ where $\mathscr{L}^-(\boldsymbol{d})$ is an open "half" cylinder defined in (2.28), there exists a unique stationary point $\boldsymbol{\zeta}_{\mathrm{II}}^+ \in S^{\mathrm{f}}(\boldsymbol{d})$ given by the second of (2.27).

Proof. The proof of this claim follows that of Proposition C.1 and is omitted for brevity. The only notable differences are that: i) the reference point $\boldsymbol{z}$ is taken as the projection of $\boldsymbol{x}^{\circ}$ along $\boldsymbol{d}$ on S^{f}, and ii) the function $\chi'(\chi)$, which is again monotonically increasing, maps $(0, \infty)$ onto itself. For completeness, it is noted that for $\boldsymbol{x}^{\circ} \in \partial \mathscr{L}^- \backslash S^{\mathrm{f}}$, $\boldsymbol{z}$ is the projection of $\boldsymbol{x}^{\circ}$ along $\boldsymbol{d}$ on ∂S^{f}. $\qquad \square$
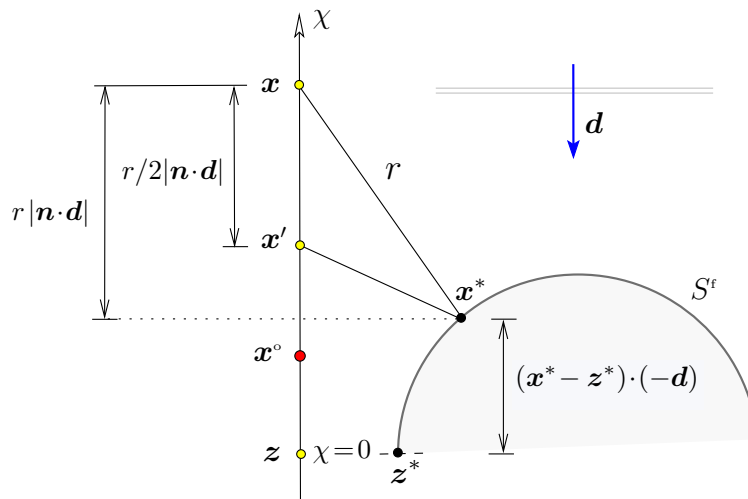
Figure 8.4: Geometrical platform for the identification of stationary point $\boldsymbol{\zeta}_{\mathrm{II}}^{+} \in S^{\mathrm{f}}$ affiliated with $\boldsymbol{x}^{\circ}$.

Proposition C.3. For any $\boldsymbol{x}^{\circ} \in \bar{\mathscr{L}}^{+} \backslash S^{\mathrm{f}}$ where $\mathscr{L}^{+}$ is an open "half" cylinder defined in (2.28), there are no stationary points $\boldsymbol{\zeta}_{\mathrm{II}}^{+} \in S^{\mathrm{f}}$ given by the second of (2.27).

Proof. This claim is a direct consequence of the facts that D is convex and that every ray II^{+} emanating from $\boldsymbol{\zeta} \in S^{\mathrm{f}}$ is oriented toward the exterior of D, see Fig. 2.3. $\quad\square$

Remark. For reasons detailed in Section 2.22.2.4, the stationary phase approximation (2.33) is superseded by the near-boundary expansion (2.52) for sampling points close to S^{f}. On the basis of this observation and Propositions C.1–C.3, one finds that the domain where (2.33) applies is contained within $\mathbb{R}^{3} \backslash \bar{\mathscr{L}}^{+}$.

D   On the accuracy of Kirchhoff approximation

To examine the ramifications of the Kirchhoff approximation (2.17) and (2.78) on the high-frequency TS analysis, consider the scattering by a convex Dirichlet obstacle as an example. Next, adopt the decomposition of obstacle's boundary $S = \partial D$ as

$$S = S_b \cup S_t \cup S_{ds},$$

where $S_b, S_t,$ and S_{ds} denote respectively the *bright, transitional,* and *deep shadow* region [9] schematically shown in Fig. 8.5. In the context of the present study one has $S^\mathrm{f} \subset S_b \cup S_t$, where $S^\mathrm{f}(\boldsymbol{d}) = \{\boldsymbol{x} \in S : \boldsymbol{n}(\boldsymbol{x}) \cdot \boldsymbol{d} < 0\}$ and S_t is a ring-like neighborhood of ∂S^f of width $O(k^{-1/3})$ [115]. With such premise, (2.17) can be written more precisely as

$$u = 0, \qquad u_{,n} = \begin{cases} 2\,\boldsymbol{u}^i_{,n} & \text{on} \quad S^\mathrm{f} \\ 0 & \text{otherwise} \end{cases} + E \qquad \text{on} \quad S, \tag{D1}$$

were E is the error of the Kirchhoff approximation. While *the phase* of E is obstacle-geometry-dependent [115] and remains an open research question [9], it can be shown [e.g. 105, 97, 115] that

$$u^i_{,n} = -\mathrm{i}k\,\boldsymbol{d}\cdot\boldsymbol{n}\,e^{-\mathrm{i}k\boldsymbol{\xi}\cdot\boldsymbol{d}} \quad \text{on } S^\mathrm{f} \quad \implies \quad E = \begin{cases} O(1) & \text{on } S_b \\ O(k^{2/3}) & \text{on } S_t \\ O(k^{2/3}) \times \exp\left(-\beta(k)s\right) & \text{on } S_{ds} \end{cases}, \tag{D2}$$

for scattering by a smooth Dirichlet obstacle, where s denotes a diffracted surface ray (the so-called creeping ray) path into the shadow region, and $\beta(k) \geqslant 0$ describes the amplitude decay of creeping rays due to tangential shedding of energy into the medium [119]. By virtue of this result, E can be shown to have no effect on the claim of Theorem 2.3.5 as elucidated below.
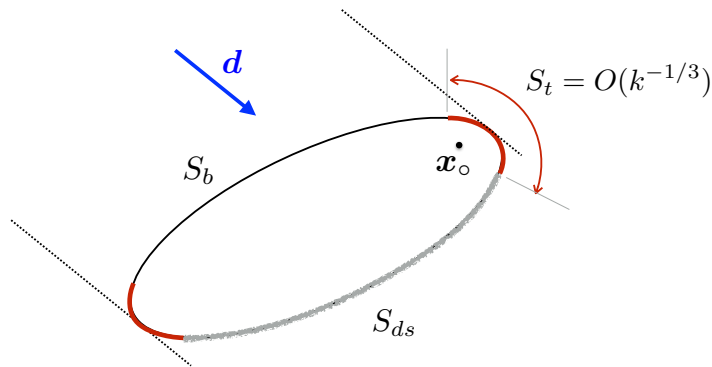
Figure 8.5: Schematics of the bright, transitional, and deep shadow regions comprising the surface of a scatterer.

- **Contribution of E to $\check{\mathsf{T}}$ via the boundary of the integration domain**. In the foregoing analysis, the contribution of critical points along the closed curve ∂S^{f} – the boundary of S^{f} – was neglected thanks to the fact that $u^i_{,n} = 0$ there. In the context of (D1), there is likewise no "boundary" contribution due to E since the integration must be performed over the entire (closed) surface S.

- **Contribution of E to $\check{\mathsf{T}}$ via the near-boundary term $\mathsf{T}^\star$**. From the analysis in Section 2.2.4.2 and (D2), it follows that the contribution of E over S to $\mathsf{T}^\star$ is $O(k^{2/3})$ in the case of illumination by a single plane wave. Accordingly the error in evaluating (2.75) and thus (2.77) due to E is at most $O(k^{2/3})$, which preserves the claim of Theorem 2.3.5.

- **Contribution of E to $\check{\mathsf{T}}$ via non-degenerate stationary points**. Thanks to (D2), one finds that the contribution of E to T in (2.53) via the stationary points (i.e. the contribution of E to $\mathsf{T}^{\mathrm{II}\pm}$) behaves at most as $O(k^{2/3})$ in the case of a single incident wave. As as a result, the claim of Theorem 2.3.5 remains unaltered by the stationary points of E – even if possible cancellation of their effect due to full-aperture illumination is altogether ignored.

- **Contribution of $E|_{S_b}$ to $\check{\mathsf{T}}$ via diffraction catastrophes**. From (2.54) and (D2), it can be seen that the single-indcident-wave contribution of E over S_b to T^c in (2.53) is at most $O(k^{1/3})$; accordingly it has no effect on the claim of Theorem 2.3.5.

- **Contribution of $E|_{S_t}$ to $\check{\mathsf{T}}$ via diffraction catastrophes**. In contrast to the previous case, (2.54) and (D2) demonstrate that the contribution of E over S_t to T^c may reach $O(k)$, which warrants further consideration. To this end, it can first be observed that the magnitude of E-catastrophes over the transitional region scales with wavenumber k as in Table 2.54 – diminished by a factor of $k^{-1/3}$. Next, one finds from the Melrose-Taylor corrected Kirchhoff approximation [115] underpinning (D2) that the neglected parts of integrands in (2.22) due to E contain rapidly-oscillating factors $e^{ik\phi_E(\zeta)}$ whose phase permits leading-order approximation

$$\phi_E(\boldsymbol{\zeta}) \;=\; \boldsymbol{\zeta}\cdot\boldsymbol{d} \pm r - \tfrac{1}{3}Z^3(\boldsymbol{\zeta}, \boldsymbol{d}). \tag{D3}$$

Here Z is a smooth function that reflects the geometry of a scatterer and vanishes, to the first order, on ∂S^{f} where $\boldsymbol{dn} = 0$. Continuing upon the full-aperture analysis of diffraction catastrophes according to Kirchhoff approximation, the discussion is hereon focused on the phase function in (D3) with the minus sign before r. In this setting, the developments in Sec. 2.3.2.2 can be extended to account for the leading-order correction $Z^3/3$, resulting in the analogue of (2.71) as

$$\phi_E(\boldsymbol{\zeta})\big|_{\boldsymbol{d}^\circ + \mathrm{d}\boldsymbol{d}} \; \simeq \; \tilde{\phi}_{E_\circ} + \tfrac{1}{2}\phi^{(2)}_{E_\circ}\sigma^2 + (\mathrm{d}\boldsymbol{d}{\cdot}\hat{\boldsymbol{s}})\sigma + \tfrac{1}{6}\,\phi'''_{E_\circ}\tau^3 + (\mathrm{d}\boldsymbol{d}{\cdot}\hat{\boldsymbol{t}})\tau - Z^2\frac{\partial Z}{\partial \boldsymbol{d}}{\cdot}\mathrm{d}\boldsymbol{d}, \;\; \text{(D4)}$$

where $Z = Z(\boldsymbol{\zeta}^* + \sigma\,\hat{\boldsymbol{s}} + \tau\,\hat{\boldsymbol{t}}, \boldsymbol{d}^\circ)$ and $\tilde{\phi}_{E_\circ}$, $\phi^{(2)}_{E_\circ}$ and $\phi'''_{E_\circ}$ are constants such that $\phi^{(2)}_{E_\circ} = O(1)$ and $\phi'''_{E_\circ} = O(1)$ under the premise of *fold catastrophe* at $\boldsymbol{\zeta}^* \in S_t$ when $\boldsymbol{d} = \boldsymbol{d}^\circ$. On recalling the framework of structural stability, the items of interest in (D4) are the *linear* and *cubic* terms in τ – which permit computation of the sought initial slope $V_E = |c|/\mathrm{dist}(\boldsymbol{d}, B^E_\phi)$ as $\boldsymbol{d}$ leaves the bifurcation set B^E_ϕ of ϕ_E, where c is the featured *fold* control parameter. Here it is noted, however, that the last term in (D4) behaves as

$$Z(\boldsymbol{\zeta}^* + \sigma\,\hat{\boldsymbol{s}} + \tau\,\hat{\boldsymbol{t}}, \boldsymbol{d}^\circ) \;\leqslant\; O(k^{-1/3}), \qquad \boldsymbol{\zeta}^* \in S_t$$

due to the facts that: i) Z vanishes smoothly to the first order on ∂S^{f}, and ii) $St \supset \partial S^{\mathrm{f}}$ is a ring-shaped surface of width $O(k^{-1/3})$. As a result, the contributions of $Z^2(\partial Z/\partial \boldsymbol{d}){\cdot}\mathrm{d}\boldsymbol{d}$ to both linear and cubic terms in τ are $O(k^{-2/3})$, whereby the E-counterpart of (2.72) reduces to

$$V_E \;\geqslant\; \left|\tfrac{1}{2}\phi'''_{E_\circ}\right|^{-\frac{1}{3}} \left(1 + O(k^{-2/3})\right)|\boldsymbol{d}^\circ{\cdot}\boldsymbol{n}| \;\simeq\; \left|\tfrac{1}{2}\phi'''_{E_\circ}\right|^{-\frac{1}{3}}|\boldsymbol{d}^\circ{\cdot}\boldsymbol{n}|, \qquad \text{(D5)}$$

noting that $\boldsymbol{n} = \boldsymbol{n}(\boldsymbol{\zeta}^*)$. When $\boldsymbol{\zeta}^* \in S_t$, it is clear from basic geometrical considerations that $|\boldsymbol{d}^\circ{\cdot}\boldsymbol{n}| \leqslant O(k^{-1/3})$, see Fig. 8.5. The question, however, is to determine the *lower bound* on $|\boldsymbol{d}^\circ{\cdot}\boldsymbol{n}|$ and thus that on V_E. To this end, one can show from (2.26), (2.27) and (D3) that

$$\boldsymbol{\zeta}^* - \boldsymbol{x}^\circ \;=\; |\boldsymbol{\zeta}^* - \boldsymbol{x}^\circ|\left[\boldsymbol{d}^\circ + 2|\boldsymbol{d}^\circ{\cdot}\boldsymbol{n}|\,\boldsymbol{n}(\boldsymbol{\zeta}^*)\right] + O(k^{-2/3}), \qquad \boldsymbol{\zeta}^* \in S_t \cap S^{\mathrm{f}}, \quad \text{(D6)}$$

which again makes use of the fact that $Z(\boldsymbol{\zeta}^*, \boldsymbol{d}^\circ) \leqslant O(k^{-1/3})$ in the transitional region. Assuming $|\boldsymbol{d}^\circ \cdot \boldsymbol{n}(\boldsymbol{\zeta}^*)| = O(k^{-\alpha})$ for some $0 < \alpha < 2/3$, (D6) can be used to show – via tangent-plane approximation of S at $\boldsymbol{\zeta}^*$ – that the distance between $\boldsymbol{x}^\circ$ and its normal projection on S behaves as $|\ell| \simeq (\boldsymbol{\zeta}^* - \boldsymbol{x}^\circ) \cdot \boldsymbol{n}(\boldsymbol{\zeta}^*) = O(k^{-\alpha} |\boldsymbol{\zeta}^* - \boldsymbol{x}^\circ|)$. Under the same hypothesis, one finds that $Z(\boldsymbol{\zeta}^*) = O(k^{-\alpha})$ and consequently, following the developments in Appendix A.1, that

$$|\boldsymbol{\zeta}^* - \boldsymbol{x}^\circ| = r_2 + O(Z(\boldsymbol{\zeta}^*)) = O(k^{-\alpha}) \quad \text{when } |\boldsymbol{d}^\circ \cdot \boldsymbol{n}(\boldsymbol{\zeta}^*)| = O(k^{-\alpha}),\ 0 < \alpha < 2/3,$$

where r_2 is given by (A5) and behaves asymptotically as $r_2 = O(|\boldsymbol{d}^\circ \cdot \boldsymbol{n}|)$ for $|\boldsymbol{d}^\circ \cdot \boldsymbol{n}| \ll 1$. In this setting one finds that for $|\boldsymbol{d}^\circ \cdot \boldsymbol{n}| = O(k^{-\alpha})$, the normal distance from $\boldsymbol{x}^\circ$ to the boundary is $|\ell| = O(k^{-2\alpha})$. As examined in Section 2.2.4, however, for sampling points with $|\ell| \leqslant O(k^{-1})$ the contribution of nearby critical points on S is universally computed via the near-boundary approximation (2.52). As a result, one obtains the lower bound $|\boldsymbol{d}^\circ \cdot \boldsymbol{n}| > O(k^{-1/2})$ for (D5), whereby the E-analogue of (2.73) reads

$$|\tilde{B}_\phi^E|_{\mathrm{cod}(\phi)=1} \ \leqslant \ O(|\boldsymbol{d}^\circ \cdot \boldsymbol{n}|^{-1} k^{-\sigma_m^{\min}}) \ = \ O(k^{1/2} k^{-2/3}) \ = \ O(k^{-1/6}). \quad \text{(D7)}$$

On the basis of Table 2.54, (D2), and (D8), it immediately follows that the full-aperture contribution of the fold catastrophes ($\mathrm{cod}(\phi_E) = 1$) of E over S_t scales, at most, as $O(k^{7/6} k^{-1/3} k^{-1/6}) = O(k^{2/3})$ which leaves the claim of Theorem 2.3.5 unaffected. As argued earlier in Section 2.3.2.2, the contribution of higher-order catastrophes in the transitional region is precluded by the regularity of the scattering surface S.

- **Contribution of $E|_{S_{ds}}$ to $\widܫ{\mathrm{T}}$ via diffraction catastrophes**. In this case one concludes, following the argument in Section 2.3.2.2, that $V_E = O(1)$ owing to the absence of vanishing length scales (namely the vanishing distance $|\ell|$ from $\boldsymbol{x}^\circ$ to S) there. As a result, the E-counterpart of (2.74) takes the form

$$|\tilde{B}_\phi^E|_{\mathrm{cod}(\phi_E) \geqslant 1} \ = \ \begin{cases} O(k^{-\sigma_m^{\min}}), & \mathrm{cod}(\phi_E) = 1 \\ O(k^{-2\sigma_m^{\min}}), & \mathrm{cod}(\phi_E) > 1 \end{cases} \quad \text{(D8)}$$

where $\sigma_m^{\min}$ are given in Table 2.1. From this result and (D2), it follows that the full-aperture contribution of catastrophes with $\text{cod}(\phi_E) \leqslant 3$ due to E over S_{ds} scales, at most, as $O(k^{1/3})$ – which again preserves the claim of Theorem 2.3.5.

E   Reconstruction of a Neumann obstacle

E.1   Single plane-wave incidence

Taking advantage of the ideas presented in Section 2.2 for a sound-soft obstacle, the proof of Theorem 2.3.6 is outlined in more detail with the aim of deriving (2.79). To this end, the use in (2.6) of the physical optics approximation for a *sound-hard* obstacle (2.78) yields

$$\mathsf{T}(\boldsymbol{x}^\circ, \beta, \gamma) = -2\operatorname{Re}\bigg\{ (1{-}\beta)\,\nabla \boldsymbol{u}^i(\boldsymbol{x}^\circ){\cdot}\boldsymbol{A}{\cdot}\int_{S^{\mathrm{f}}} \overline{\boldsymbol{u}^i}(\boldsymbol{\zeta})\,\boldsymbol{n}(\boldsymbol{\zeta}){\cdot}\int_{\Gamma^{\mathrm{obs}}} \nabla \overline{G}(\boldsymbol{\xi}, \boldsymbol{\zeta}) \otimes \nabla G(\boldsymbol{\xi}, \boldsymbol{x}^\circ)\, \mathrm{d}\Gamma_\xi\, \mathrm{d}S_\zeta$$

$$+ (1{-}\beta\gamma^2)\,k^2\,\boldsymbol{u}^i(\boldsymbol{x}^\circ) \int_{S^{\mathrm{f}}} \overline{\boldsymbol{u}^i}(\boldsymbol{\zeta})\,\boldsymbol{n}(\boldsymbol{\zeta}){\cdot}\int_{\Gamma^{\mathrm{obs}}} \nabla \overline{G}(\boldsymbol{\xi}, \boldsymbol{\zeta})\,G(\boldsymbol{\xi}, \boldsymbol{x}^\circ)\, \mathrm{d}\Gamma_\xi\, \mathrm{d}S_\zeta \bigg\}. \quad \text{(E1)}$$

Thanks to (2.13) and (2.15), one accordingly finds that

$$\mathsf{T}(\boldsymbol{x}^\circ, \beta, \gamma) = 2k^2 \operatorname{Re}\bigg\{ \frac{3(1{-}\beta)}{2+\beta}\,(\mathrm{i}\,e^{-\mathrm{i}k\boldsymbol{x}^\circ\cdot\boldsymbol{d}})\,(J_3 - J_4) - (1 - \beta\gamma^2)(e^{-\mathrm{i}k\boldsymbol{x}^\circ\cdot\boldsymbol{d}})\,J_5 \bigg\}, \quad \text{(E2)}$$

where

$$J_3 = \int_{S^{\mathrm{f}}} e^{\mathrm{i}k\boldsymbol{\zeta}\cdot\boldsymbol{d}}\,\frac{\varkappa}{kr}\left[3\operatorname{Re}(G(\boldsymbol{x}^\circ, \boldsymbol{\zeta})) + \left(\frac{3}{kr} - kr\right)\operatorname{Im}(G(\boldsymbol{x}^\circ, \boldsymbol{\zeta})) \right] \mathrm{d}S_\zeta,$$

$$J_4 = \int_{S^{\mathrm{f}}} e^{\mathrm{i}k\boldsymbol{\zeta}\cdot\boldsymbol{d}}\,\frac{1}{kr}\left[\operatorname{Re}(G(\boldsymbol{x}^\circ, \boldsymbol{\zeta})) + \frac{1}{kr}\operatorname{Im}(G(\boldsymbol{x}^\circ, \boldsymbol{\zeta})) \right] \boldsymbol{d}\cdot\boldsymbol{n}(\boldsymbol{\zeta})\, \mathrm{d}S_\zeta, \quad \text{(E3)}$$

$$J_5 = \int_{S^{\mathrm{f}}} e^{\mathrm{i}k\boldsymbol{\zeta}\cdot\boldsymbol{d}}\left[\operatorname{Re}(G(\boldsymbol{x}^\circ, \boldsymbol{\zeta})) + \frac{1}{kr}\operatorname{Im}(G(\boldsymbol{x}^\circ, \boldsymbol{\zeta})) \right] \boldsymbol{n}(\boldsymbol{\zeta})\cdot\widehat{(\boldsymbol{x}^\circ{-}\boldsymbol{\zeta})}\, \mathrm{d}S_\zeta,$$

and $\varkappa = \widehat{(\boldsymbol{x}^\circ{-}\boldsymbol{\zeta})} \otimes \widehat{(\boldsymbol{x}^\circ{-}\boldsymbol{\zeta})} : \boldsymbol{d} \otimes \boldsymbol{n}(\boldsymbol{\zeta})$. For completenes, it is noted that the $O(\alpha^2)$ approximation error due to (2.13) and (2.15) is implicit in (E2).

Contribution of non-degenerate stationary points.   On substituting (2.3) into (E3), one finds that the Fourier-type surface integrals J_m ($m = 3, 4, 5$) feature the same phase

function $\boldsymbol{\zeta}\cdot\boldsymbol{d}\pm r$ as J_1 and J_2 in (2.20). Thus the *non-uniform* asymptotic approximation (2.24), specifying the contribution of isolated stationary points $\boldsymbol{\zeta}^*$ to T, remains valid. Further, the loci of $\boldsymbol{\zeta}^*$ according to (2.27) and the nature of the affiliated Hessian matrix $A_{pq}(\boldsymbol{\zeta}^*)$, examined in Appendix A.1, stay the same. As a result, the contribution of non-degenerate critical points to (E2) can be computed from (E3), (2.30), (2.32) and (2.34) as

$$\mathsf{T}^{\mathrm{I}\pm}(\boldsymbol{x}^{\circ},\beta,\gamma) \overset{k^{-1}}{=\!=} \pm\frac{1}{r}\Big(\frac{3(1-\beta)}{2+\beta} - \frac{1}{2}(1-\beta\gamma^2)\Big), \quad r = |\boldsymbol{x}^{\circ}-\boldsymbol{\zeta}_{\mathrm{I}}^{\pm}|, \quad \boldsymbol{x}^{\circ}\in\mathrm{I}^{\pm}\cap(\mathscr{B}_1\backslash\mathscr{N}_\epsilon); \tag{E4}$$

$$\mathsf{T}^{\mathrm{II}+}(\boldsymbol{x}^{\circ},\beta,\gamma) \overset{1}{=\!=} -\frac{k\sqrt{\rho_1\rho_2}}{\sqrt{(r+r_1)(r+r_2)}}\,\mathrm{Im}\Big[e^{2\mathrm{i}k(\boldsymbol{d}\cdot\boldsymbol{n})^2 r}\Big]\Big\{\frac{3(1-\beta)}{4(2+\beta)}\big(1-2(\boldsymbol{d}\cdot\boldsymbol{n})^2\big) - \frac{1-\beta\gamma^2}{4}\Big\},$$
$$r = |\boldsymbol{x}^{\circ}-\boldsymbol{\zeta}_{\mathrm{II}}^{+}|, \qquad \boldsymbol{x}^{\circ}\in\mathrm{II}^{+}\cap(\mathscr{B}_1\backslash\mathscr{N}_\epsilon), \qquad \boldsymbol{n}=\boldsymbol{n}(\boldsymbol{\zeta}_{\mathrm{II}}^{+}); \tag{E5}$$

and

$$\mathsf{T}^{\mathrm{II}-}(\boldsymbol{x}^{\circ},\beta,\gamma) \overset{1}{=\!=} -\frac{k\sqrt{\rho_1\rho_2}}{\sqrt{|(r-r_1)(r-r_2)|}}\,\mathrm{Re}\Big[e^{-2\mathrm{i}k(\boldsymbol{d}\cdot\boldsymbol{n})^2 r+\mathrm{i}(\mathrm{sgn}\,A_{pq})\pi/4}\Big]\times$$
$$\times\Big\{\frac{3(1-\beta)}{4(2+\beta)}\big(1-2(\boldsymbol{d}\cdot\boldsymbol{n})^2\big) - \frac{1-\beta\gamma^2}{4}\Big\}, \quad r = |\boldsymbol{x}^{\circ}-\boldsymbol{\zeta}_{\mathrm{II}}^{-}|, \quad \boldsymbol{x}^{\circ}\in(\mathrm{II}^{-}\backslash\mathscr{C}_{\mathrm{II}})\cap(\mathscr{B}_1\backslash\mathscr{N}_\epsilon), \tag{E6}$$

assuming the stationary points of type I, II^{+} and II^{-}, respectively.

Here it is worth noting that the contribution of $\mathsf{T}^{\mathrm{I}\pm} = O(1)$ can be neglected due to the fact that $\mathsf{T}^{\mathrm{II}\pm} = O(k)$. Moreover, apart from the sign difference, (E5) and (E6) carry exactly the same structure as their "sound-soft" counterparts (2.33) and (2.35).

Contribution of diffraction catastrophes. Owing to the fact that the TS formulas (2.20) and (E2) share the phase function $\phi = \boldsymbol{\zeta}\cdot\boldsymbol{d} - r$, the analysis in Section 2.2.3 concerning the contribution of degenerate stationary points to the TS, namely T^c, remains unchanged.

Asymptotic expansion for $\boldsymbol{x}^{\circ}\in\mathscr{N}_\epsilon$. At the stationary points $\boldsymbol{\zeta}^*$ of type $\mathrm{II}^{\pm}$, one has $|\boldsymbol{d}\cdot\boldsymbol{n}(\boldsymbol{\zeta}^*)| = |\boldsymbol{n}(\boldsymbol{\zeta}^*)\cdot(\widehat{\boldsymbol{x}^{\circ}-\boldsymbol{\zeta}^*})|$ so that the kernels in J_m ($m=3,4,5$), when *evaluated*

at $\boldsymbol{\zeta}^*$, are proportional to $|\boldsymbol{d}\cdot\boldsymbol{n}|$. With such remark, one may appeal to the argument as in Section 2.2.4.1 to find the appropriate threshold, $\epsilon \geqslant 2\pi/k$, for the extent of $\mathscr{N}_\epsilon$ according to (2.21).

When $\boldsymbol{x}^\circ \in \mathscr{N}_\epsilon$, the analyses in Sections 2.2.2 and 2.2.3 do not apply to the critical points on ∂S^{f} that are close to the point of normal projection, $\boldsymbol{x}^\star$. Further, the latter becomes a critical point itself as $\boldsymbol{x}^\circ \to \boldsymbol{x}^\star$ due to a lack of differentiability of the kernels in (E3). In this case, one may resort to the tangent-plane approximation as in Section 2.2.4.2 such that, by adopting the change of variables (2.46) with $\varepsilon = 0$, J_3 in (E3) can be approximated as

$$
\begin{aligned}
J_3^\star = \;& \frac{e^{\mathrm{i}k\boldsymbol{x}^\star\cdot\boldsymbol{d}}}{4\pi} \int_0^\infty \frac{\varrho}{(kr_0)^4}\Big[3\cos(kr_0) + (kr_0 - \frac{3}{kr_0})\sin(kr_0)\Big] k\ell \;\times \\
& \times \int_0^{2\pi} e^{\mathrm{i}k\varrho d_t \cos(\theta)}\big(\boldsymbol{d}\cdot\boldsymbol{n}\,k\ell \,-\, d_t\,k\varrho\,\cos(\theta)\big)\mathrm{d}\theta\,\mathrm{d}(k\varrho), \quad \boldsymbol{x}^\circ \in \mathscr{N}_\epsilon,
\end{aligned}
\tag{E7}
$$

where $\boldsymbol{n} = \boldsymbol{n}(\boldsymbol{x}^\star)$, $r_0 = \sqrt{\ell^2 + \varrho^2}$, and $d_t = \sqrt{1 - |\boldsymbol{d}\cdot\boldsymbol{n}|^2}$. Note that the outer integral in (E7) has been conveniently extended to infinity by the use of an implicit neutralizer function [e.g. 152, 39]. The inner integral with respect to θ, on the other hand, can be expressed explicitly in terms of the Bessel functions of the first kind, namely $\mathrm{J}_0(d_t k\varrho)$ and $\mathrm{J}_1(d_t k\varrho)$. Thanks to the identity $\ell^2 = r_0^2 - \varrho^2$, thus obtained integral over $k\varrho$ can be rewritten as

$$
\begin{aligned}
J_3^\star = \;& \frac{e^{\mathrm{i}k\boldsymbol{x}^\star\cdot\boldsymbol{d}}}{2} \int_0^\infty \frac{\varrho}{(kr_0)^4}\Big[3\cos(kr_0) + (kr_0 - \frac{3}{kr_0})\sin(kr_0)\Big] \times \\
& \times \Big\{\boldsymbol{d}\cdot\boldsymbol{n}(kr_0)^2\,\mathrm{J}_0(d_t k\varrho) - \boldsymbol{d}\cdot\boldsymbol{n}(k\varrho_0)^2\,\mathrm{J}_0(d_t k\varrho) - \mathrm{i}d_t\,k\varrho\,k\ell\,\mathrm{J}_1(d_t k\varrho)\Big\}\mathrm{d}(k\varrho), \quad \boldsymbol{x}^\circ \in \mathscr{N}_\epsilon.
\end{aligned}
\tag{E8}
$$

On integrating (E8) by parts and making use of the integral identities in [70], the leading-order contribution of $\boldsymbol{x}^\star$ to J_3 is found to read

$$
J_3^\star = \frac{e^{\mathrm{i}k\boldsymbol{x}^\star\cdot\boldsymbol{d}}}{2k}\Big[\mathrm{i}\,d_t^2\,\sin(|\boldsymbol{d}\cdot\boldsymbol{n}|k\ell) - |\boldsymbol{d}\cdot\boldsymbol{n}|^2\Big(\cos(|\boldsymbol{d}\cdot\boldsymbol{n}|k\ell) - \frac{\sin(|\boldsymbol{d}\cdot\boldsymbol{n}|k\ell)}{|\boldsymbol{d}\cdot\boldsymbol{n}|k\ell}\Big)\Big], \quad \boldsymbol{x}^\circ \in \mathscr{N}_\epsilon.
\tag{E9}
$$

In a similar fashion, the leading-order contribution of $\boldsymbol{x}^\star$ to J_4 and J_5 can be obtained

as

$$J_4^\star \;=\; \frac{|\boldsymbol{d}\cdot\boldsymbol{n}|}{2k^2\ell}\, e^{\mathrm{i}k\boldsymbol{x}^\star\cdot\boldsymbol{d}}\sin(|\boldsymbol{d}\cdot\boldsymbol{n}|k\ell), \quad J_5^\star \;=\; -\frac{1}{2k}\, e^{\mathrm{i}k\boldsymbol{x}^\star\cdot\boldsymbol{d}}\sin(|\boldsymbol{d}\cdot\boldsymbol{n}|k\ell), \quad \boldsymbol{x}^\circ\in\mathscr{N}_\epsilon. \quad \text{(E10)}$$

By substituting (E9) and (E10) into (E2), one finds

$$\mathsf{T}^\star(\boldsymbol{x}^\circ,\beta,\gamma) \overset{1}{=} -\frac{k}{2}\sin(2k\ell|\boldsymbol{d}\cdot\boldsymbol{n}|)\left\{\frac{3(1-\beta)}{2+\beta}\,(1-2|\boldsymbol{d}\cdot\boldsymbol{n}|^2)\,-\,(1-\beta\gamma^2)\right\}, \quad \boldsymbol{x}^\circ\in\mathscr{N}_\epsilon \quad \text{(E11)}$$

to be the leading asymptotic contribution of $\boldsymbol{x}^\star$ to T in the case of scattering by a Neumann obstacle.

Remark 16. *In situations where an extended (impenetrable) scatterer D is reconstructed by sampling with a physically-commensurate vanishing obstacle, (E11) and its sound-soft counterpart (2.52) produce dissimilar TS patterns near ∂D – in spite of their identical structure – owing to distinct choices of the trial material parameters ($\beta = \rho/\rho_{trial}, \gamma = c/c_{trial}$) characterizing the vanishing perturbation.*

On the basis of the above results, the "Neumann" contributions $\mathsf{T}^{\mathrm{II}\pm}$, T^c and $\mathsf{T}^\star$ to the TS are found to behave as in (2.54), and are incorporated in (2.53) for further analysis.

Contribution of the boundary of the integration domain, ∂S^{f}. In contrast to the case of a Dirichlet obstacle, the kernels of J_3 and J_5 in (E3) entering the "Neumann" TS formula (E2) do not vanish as $\boldsymbol{\zeta}\to\partial S^{\mathrm{f}}$, which warrants further consideration (recall that $J_2\to 0$ in this case thanks to the fact that $\boldsymbol{d}\cdot\boldsymbol{n}=0$ on S^{f}). Note, however, that if $\boldsymbol{\zeta}^*\in\partial S^{\mathrm{f}}$ is a stationary point of $\boldsymbol{\zeta}\cdot\boldsymbol{d}\pm r$, the kernels of J_m ($m=3,5$) both vanish there thanks to (2.27); thus, the contribution of such critical points can be ignored. On the basis of the high-frequency analysis of oscillatory integrals in [152] (Sec. 9.2.1 (a)), the contribution of ∂S^{f} to (E3) can accordingly be computed as

$$J_m^{\partial S^{\mathrm{f}}} \;=\; k^{-1}\sum_{\pm}\int_{\partial\widetilde{S^{\mathrm{f}}}}\frac{\mathrm{i}}{\phi_{,s}^\pm(t,0)}\,g_m^\pm(\boldsymbol{\zeta};\boldsymbol{d})\,e^{\mathrm{i}k\phi^\pm}\,\mathrm{d}t, \quad \phi^\pm(t,s)=\boldsymbol{\zeta}\cdot\boldsymbol{d}\pm r, \quad \boldsymbol{\zeta}=\boldsymbol{\zeta}(t,s), \quad \text{(E12)}$$

where $m = 3,5$; $\partial\widetilde{S^{\mathrm{f}}}\subset\partial S^{\mathrm{f}}$ excludes all $\boldsymbol{\zeta}^*$; t is the arclength parameter along ∂S^{f}; and $s\geqslant 0$ is a curvilinear surface coordinate on S^{f}, positive inward, that is orthogonal to t

($s = 0$ on S^{f}). The oscillatory line integrals in (E12) can be evaluated via techniques introduced earlier, assuming structurally-stable caustics – if any – of codimension less than three (recall that $\mathrm{cod}(\phi^\pm)$ cannot exceed two for 1D integrals). As a result the high-frequency asymptotic behavior of (E2), i.e. the "Neumann" counterpart of (2.53), is found to include an *additional boundary contribution*

$$\mathsf{T}^{\partial S^{\mathrm{f}}} = O(k^{1/2+\beta}), \qquad 0 \leqslant \beta \leqslant \tfrac{3}{10}, \tag{E13}$$

where the limits on β are established according to Table 2.1.

E.2   Full source aperture

On recalling that the TS integral representations (2.19) and (E2) share the *common* phase function pair $\boldsymbol{\zeta}\cdot\boldsymbol{d} \pm r$, one finds that the "Dirichlet" analysis in Sections 2.3.2.1 and 2.3.2.2 applies equally to the reconstruction of a sound-hard obstacle. As a result, one has

$$\breve{\mathsf{T}}(\boldsymbol{x}^\circ, \beta, \gamma) \overset{k^\nu}{=} 1_{\breve{\mathcal{N}_\epsilon}}(\boldsymbol{x}^\circ) \int_\Omega \mathsf{T}^\star \, \mathrm{d}\Omega_{\boldsymbol{d}} \; + \; \int_{\tilde{B}_\phi} \mathsf{T}^c \, \mathrm{d}\Omega_{\boldsymbol{d}} \; +$$
$$+ \int_{S^\pm} \frac{|\boldsymbol{d}^*\!\cdot\boldsymbol{n}|}{r^2} \, \mathsf{T}^{II^\pm} \mathrm{d}S_\zeta \; + \; \int_\Omega \mathsf{T}^{\partial S^{\mathrm{f}}} \, \mathrm{d}\Omega_{\boldsymbol{d}}, \tag{E14}$$

where $\nu \leqslant 1/2$ and

$$\int_{\tilde{B}_\phi} \mathsf{T}^c \, \mathrm{d}\Omega_{\boldsymbol{d}} \; = \; O(k^\alpha), \qquad \tfrac{1}{4} \leqslant \alpha \leqslant \tfrac{2}{3},$$
$$\int_{S^\pm} \frac{|\boldsymbol{d}^*\!\cdot\boldsymbol{n}|}{r^2} \, \mathsf{T}^{II^\pm} \, \mathrm{d}S_\zeta \; = \; O(k^\beta), \qquad 0 \leqslant \beta \leqslant \tfrac{1}{3}. \tag{E15}$$

To compute the contribution of nearby critical points to (2.55) when $\boldsymbol{x}^\circ \in \breve{\mathcal{N}_\epsilon}$, on the other hand, (E11) can be integrated over $\Omega_{\boldsymbol{d}}$ as in Section 2.3.2.3 to obtain

$$\int_\Omega \mathsf{T}^\star \, \mathrm{d}\Omega_{\boldsymbol{d}} \; = \; \frac{-\pi k}{(k\ell)^3} \left\{ \frac{3(1-\beta)}{2+\beta} \left(k\ell \cos(k\ell) - \sin(k\ell)\right)^2 - (1-\beta\gamma^2)\,(k\ell)^2 \sin(k\ell)^2 \right\}. \tag{E16}$$

With (E15) and (E16) in place, the last step in the analysis is to evaluate the contribution of the boundary term $\mathsf{T}^{\partial S^{\mathrm{f}}}$ to the full-source-aperture TS variation (E14). From the onset, it is seen that (E13) itself may exceed the $O(k^{2/3})$ residual stated in Theorem 2.3.6 – which can possibly cause problems. By way of (E3) and (2.3), however,

it can be shown that $g_m^\pm$ in (E12) carry the intrinsic properties

$$g_3^\pm(\cdot, \boldsymbol{d}) = -g_3^\pm(\cdot, -\boldsymbol{d}), \quad g_5^\pm(\cdot, \boldsymbol{d}) = g_5^\pm(\cdot, -\boldsymbol{d}), \quad g_m^+ = \bar{g}_m^-, \quad m = 3, 5 \qquad \text{(E17)}$$

where the overbar symbol denotes complex conjugation. Since the "bright" surfaces $S^f(\boldsymbol{d})$ and $S^f(-\boldsymbol{d})$ are complementary, one also finds that $s|_{\boldsymbol{d}} = -s|_{-\boldsymbol{d}}$ for all $\boldsymbol{\zeta} \in \widetilde{S^f}$, and thus

$$\phi^\pm(t, 0)|_{\boldsymbol{d}} = -\phi^\mp(t, 0)|_{-\boldsymbol{d}} \implies \phi_{,s}^\pm(t, 0)|_{\boldsymbol{d}} = \phi_{,s}^\mp(t, 0)|_{-\boldsymbol{d}}. \qquad \text{(E18)}$$

From (E12), (E17) and (E18), it follows that

$$J_3^{\partial S^f}|_{\boldsymbol{d}} = \bar{J}_3^{\partial S^f}|_{-\boldsymbol{d}}, \qquad J_5^{\partial S^f}|_{\boldsymbol{d}} = -\bar{J}_5^{\partial S^f}|_{-\boldsymbol{d}}.$$

On substituting the last result into (E2) and (2.55), one immediately finds that

$$\mathsf{T}^{\partial S^f}|_{\boldsymbol{d}} + \mathsf{T}^{\partial S^f}|_{-\boldsymbol{d}} = 0 \implies \int_\Omega \mathsf{T}^{\partial S^f} \, d\Omega_{\boldsymbol{d}} = 0$$

which, in conjunction with (E14)–(E16), completes the proof of Theorem 2.3.6.

F   Asymptotic behavior of the integrals in (3.34)

The aim of this section is to expose the leading-order behavior of the integrals in (3.34) for $R_2/R_1 \gg 1$, where the integrands are expressed as antilinear forms in terms of the components of the fundamental stress tensor.

Elastodynamic fundamental solution   Assuming time-harmonic excitation by the unit point force applied at $\boldsymbol{x} \in \mathbb{R}^3$ in direction k, the governing equation of motion for an infinite solid with shear modulus μ, mass density ρ and Poisson's ratio ν can be written as

$$\nabla_{\boldsymbol{\xi}} \cdot \boldsymbol{\Sigma}^k + \rho \omega^2 \boldsymbol{U}^k = \delta(\boldsymbol{\xi} - \boldsymbol{x}) \boldsymbol{e}_k, \qquad \boldsymbol{\xi} \in \mathbb{R}^3, \quad \boldsymbol{\xi} \neq \boldsymbol{x},$$

where $\boldsymbol{U}^k(\boldsymbol{\xi}, \boldsymbol{x}, \omega)$ and $\boldsymbol{\Sigma}^k(\boldsymbol{\xi}, \boldsymbol{x}, \omega)$ denote respectively the fundamental displacement vector and stress tensor, given in the component form by

$$
\begin{aligned}
U_i^k(\boldsymbol{\xi}, \boldsymbol{x}, \omega) &= \frac{1}{4\pi\mu r}\left(B_1(r)\,\delta_{ik} + B_2(r)\,r_{,i}r_{,k}\right), \\
\Sigma_{ij}^k(\boldsymbol{\xi}, \boldsymbol{x}, \omega) &= \frac{1}{4\pi r^2}\left(2\,B_3(r)\,r_{,i}r_{,j}r_{,k} + (\delta_{ik}\,r_{,j} + \delta_{jk}\,r_{,i})B_4(r) + B_5(r)\,\delta_{ij}r_{,k}\right).
\end{aligned}
\tag{F1}
$$

Here

$$
\begin{aligned}
B_1(r) &= \left(1 - \frac{\mathrm{i}}{\chi_s} - \frac{1}{\chi_s^2}\right)e^{-\mathrm{i}\chi_s} + \gamma^2\left(\frac{\mathrm{i}}{\chi_p} + \frac{1}{\chi_p^2}\right)e^{-\mathrm{i}\chi_p}, \\
B_2(r) &= \left(\frac{3}{\chi_s^2} + \frac{3\mathrm{i}}{\chi_s} - 1\right)e^{-\mathrm{i}\chi_s} - \gamma^2\left(\frac{3}{\chi_p^2} + \frac{3\mathrm{i}}{\chi_p} - 1\right)e^{-\mathrm{i}\chi_p}, \\
B_3(r) &= \left(6 - \frac{15}{\chi_s^2} - \frac{15\mathrm{i}}{\chi_s} + \mathrm{i}\chi_s\right)e^{-\mathrm{i}\chi_s} - \gamma^2\left(6 - \frac{15}{\chi_p^2} - \frac{15\mathrm{i}}{\chi_p} + \mathrm{i}\chi_p\right)e^{-\mathrm{i}\chi_p}, \\
B_4(r) &= -(1 + \mathrm{i}\chi_s)e^{-\mathrm{i}\chi_s} + 2B_2(r), \\
B_5(r) &= -(1 - 2\gamma^2)(1 + \mathrm{i}\chi_p)e^{-\mathrm{i}\chi_p} + 2B_2(r),
\end{aligned}
\tag{F2}
$$

and

$$
r = |\boldsymbol{\xi} - \boldsymbol{x}|, \quad \chi_s = \frac{r\omega}{c_s}, \quad \chi_p = \frac{r\omega}{c_p}, \quad \gamma = \frac{c_s}{c_p}, \quad r_{,i} = \frac{\partial r}{\partial \xi_i},
$$

where δ_{ij} denotes the Kronecker delta, $c_s = \sqrt{\mu/\rho}$, and $c_p = c_s\sqrt{(2-2\nu)/(1-2\nu)}$.

Integration For $\boldsymbol{x} \in \mathscr{B}_1$ and $\boldsymbol{\xi} \in S^{\mathrm{obs}}$ (see Fig. 3.1), the argument $r = |\boldsymbol{\xi} - \boldsymbol{z}|$ of the relevant coefficients in (F1) and (F2) describing $\Sigma_{ij}^k(\boldsymbol{\xi}, \boldsymbol{z}, \omega)$ can be approximated (assuming $R_2/R_1 \gg 1$) to the leading order as $r \simeq R_2$; as a result, the prevailing behavior of integrals in (3.34) can be written as

$$
\begin{aligned}
Q_1 : \quad & \int_{S^{\mathrm{obs}}} [\Sigma_{33}^{j*}\Sigma_{33}^j](\boldsymbol{\xi}, \boldsymbol{z}, \omega)\,\mathrm{d}S_{\boldsymbol{\xi}} \simeq \\
& \mathrm{X}_1 \int_0^\pi \int_0^{2\pi} \left(\mathrm{X}_2\,r_{,3}^4 + 4\,\mathrm{Re}(\mathrm{X}_3)\,r_{,3}^2 + |B_5(R_2)|^2\right)\sin(\phi)\,\mathrm{d}\theta\,\mathrm{d}\phi,
\end{aligned}
\tag{F3}
$$

$$
\begin{aligned}
Q_2 : \quad & \int_{S^{\mathrm{obs}}} [\Sigma_{33}^{j*}\Sigma_{3\beta}^j](\boldsymbol{\xi}, \boldsymbol{z}, \omega)\,\mathrm{d}S_{\boldsymbol{\xi}} \simeq \\
& \mathrm{X}_1 \int_0^\pi \int_0^{2\pi} r_{,3}\,r_{,\beta}\left(\mathrm{X}_2\,r_{,3}^2 + 2\,\mathrm{X}_3\right)\sin(\phi)\,\mathrm{d}\theta\,\mathrm{d}\phi = 0,
\end{aligned}
\tag{F4}
$$

$$\int_{S^{\text{obs}}} |\Sigma_{3\beta}^{j}(\boldsymbol{\xi}, \boldsymbol{z}, \omega)|^2 \, \mathrm{d}S_{\boldsymbol{\xi}} \simeq$$

$$X_1 \int_0^{\pi} \int_0^{2\pi} \left(X_2 \, r_{,\beta}^2 \, r_{,3}^2 + (r_{,3}^2 + r_{,\beta}^2)|B_4(R_2)|^2 \right) \sin(\phi) \, \mathrm{d}\theta \, \mathrm{d}\phi,$$

$Q3:$ \hfill (F5)

$$\int_{S^{\text{obs}}} [\Sigma_{31}^{j*} \, \Sigma_{32}^{j}](\boldsymbol{\xi}, \boldsymbol{z}, \omega) \, \mathrm{d}S_{\boldsymbol{\xi}} \simeq$$

$$X_1 \int_0^{\pi} \int_0^{2\pi} \left(X_2 \, r_{,1} \, r_{,2} \, r_{,3}^2 + |B_4(R_2)|^2 \, r_{,1} r_{,2} \right) \sin(\phi) \, \mathrm{d}\theta \, \mathrm{d}\phi \; = \; 0,$$

where $\beta = 1, 2$ and

$$X_1 = \frac{1}{(4\pi R_2)^2}, \quad X_2 = 4\text{Re}\left\{ \left[|B_3|^2 + 2B_3^* B_4 \right](R_2) \right\},$$

$$X_3 = \left[|B_4|^2 + (B_3 + B_4)B_5^* \right](R_2). \tag{F6}$$

Considering the unit vector $\nabla r = (r_{,1}, r_{,2}, r_{,3}) = \big(\sin(\phi)\cos(\theta), \sin(\phi)\sin(\theta), \cos(\phi) \big)$ used to define S^{obs} in spherical coordinates, the integrals of (F3)-(F5) are analytically evaluated which results in (3.36).

G BIE computational platform

This section summarizes the numerical scheme adopted to solve the elastodynamic traction BIE for a fractured three-dimensional solid. The approach borrows substantially from the ideas established in [33, 81] considering the regularization of the featured surface integrals. For brevity, the technique is described with reference to the elastostatic canonical problem (3.22). With slight modifications, however, this method is utilized in a more general setting of Section 3.4 to compute the scattering of elastic waves by an *arbitrarily-shaped* fracture. Accordingly, the auxiliary formulae are expressed in their most general form (as applicable). Unless stated otherwise, the Einstein summation convention is assumed over repeated coordinate indexes.

Regularization. To avoid evaluating the Cauchy principal value in (3.22), the featured integral equation can be conveniently rewritten as

$$\frac{1}{2}[e_i \otimes e_j + e_j \otimes e_i]_{k\ell} n'_\ell - [K_{\text{trial}}]_{k\ell} [\![V_\ell]\!]^{ij}(\bar{\boldsymbol{\xi}}) = n'_\ell C_{k\ell pq} D_{qs}[\![V_m]\!]^{ij}(\bar{\boldsymbol{\xi}}) \check{S}^p_{ms}(\bar{\boldsymbol{\xi}}, \Gamma_{\text{trial}}) +$$

$$n'_\ell C_{k\ell pq} \int_{\Gamma_{\text{trial}}} (D_{qs}[\![V_m]\!]^{ij}(\bar{\boldsymbol{x}}) - D_{qs}[\![V_m]\!]^{ij}(\bar{\boldsymbol{\xi}})) \check{\Sigma}^p_{ms}(\bar{\boldsymbol{\xi}}, \bar{\boldsymbol{x}}) \, \mathrm{d}S_{\bar{\boldsymbol{x}}}, \quad \bar{\boldsymbol{\xi}} \in \Gamma_{\text{trial}},$$

$$\text{(G1)}$$

where the dummy indexes are summed over $\overline{1,3}$, and the singularity is transferred to the auxiliary integrals

$$I_\ell(\bar{\boldsymbol{\xi}}, \Gamma_{\text{trial}}) = \fint_{\Gamma_{\text{trial}}} \frac{1}{\mathrm{r}^2} \mathrm{r}_{,\ell} \, \mathrm{d}S_{\bar{\boldsymbol{x}}},$$

$$J_{pq\ell}(\bar{\boldsymbol{\xi}}, \Gamma_{\text{trial}}) = \fint_{\Gamma_{\text{trial}}} \frac{1}{\mathrm{r}^2} \mathrm{r}_{,p} \mathrm{r}_{,q} \mathrm{r}_{,\ell} \, \mathrm{d}S_{\bar{\boldsymbol{x}}}, \qquad \bar{\boldsymbol{\xi}} \in \Gamma_{\text{trial}},$$

$$\text{(G2)}$$

comprising the third-order tensor

$$\check{S}^p_{ms}(\bar{\boldsymbol{\xi}}, \Gamma_{\text{trial}}) = \fint_{\Gamma_{\text{trial}}} \check{\Sigma}^p_{ms}(\bar{\boldsymbol{\xi}}, \bar{\boldsymbol{x}}) \, \mathrm{d}S_{\bar{\boldsymbol{x}}} =$$

$$-\frac{1}{8\pi(1-\nu)} \left[(1-2\nu)(\delta_{mp} I_s + \delta_{sp} I_m - \delta_{ms} I_p) + 3 J_{msp} \right].$$

$$\text{(G3)}$$

Here it is useful to recall that $\mathrm{r} = |\bar{\boldsymbol{\xi}} - \bar{\boldsymbol{x}}|$, $\mathrm{r}_{,\ell} = \partial \mathrm{r}/\partial \bar{x}_\ell$, and $\boldsymbol{K}_{\text{trial}} = \kappa_n(\bar{e}_3 \otimes \bar{e}_3) + \kappa_s(\bar{e}_1 \otimes \bar{e}_1) + \kappa_s(\bar{e}_2 \otimes \bar{e}_2)$ where $(\bar{e}_1, \bar{e}_2, \bar{e}_3)$ are the unit vectors along $(\bar{\xi}_1, \bar{\xi}_2, \bar{\xi}_3)$. Considering I_ℓ first, one finds [33] via integration by parts, taking advantage of the Stokes identity, and noting that $[\![\boldsymbol{V}]\!]^{ij} = \boldsymbol{0}$ on $\partial \Gamma_{\text{trial}}$, that the first in (G2) can be reduced as

$$I_\ell = \int_{\Gamma_{\text{trial}}} \frac{1}{\mathrm{r}} \left(\frac{1}{\mathrm{r}} n'_p \mathrm{r}_{,p} - w_q n'_q \right) n'_\ell \, \mathrm{d}S_{\bar{\boldsymbol{x}}} - \int_{\partial \Gamma_{\text{trial}}} \frac{1}{\mathrm{r}} \mathrm{v}_\ell \, \mathrm{d}s, \qquad \bar{\boldsymbol{\xi}} \in \Gamma_{\text{trial}}, \qquad \text{(G4)}$$

where Γ_{trial} is interpreted as an *open set* (excluding fracture's edge $\partial \Gamma_{\text{trial}}$); $p, q = 1, 2, 3$; $\mathbf{v}$ denotes the outward normal on $\partial \Gamma_{\text{trial}}$ lying within the tangent plane to Γ_{trial}, and $w_k(f) = f_{,k} - n'_k(f_{,p} n'_p)$ is the tangential derivative operator. In terms of $J_{pq\ell}$, on the

other hand, one similarly obtains

$$
\begin{aligned}
3J_{pq\ell} \ = \ & \delta_{p\ell}\,I_q + \delta_{q\ell}\,I_p + \int_{\Gamma_{\text{trial}}} \frac{1}{\text{r}}\big(\text{r}_{,q}\,\text{r}_{,s}\,D_{sp}n'_\ell - w_p(n'_q n'_\ell) - w_q(n'_p n'_\ell)\big)\,\mathrm{d}S_{\bar{\boldsymbol{x}}} \ + \\[2mm]
& \delta_{pq}\int_{\Gamma_{\text{trial}}} \frac{1}{\text{r}^2}\,n'_\ell n'_s \text{r}_{,s}\,\mathrm{d}S_{\bar{\boldsymbol{x}}} + \int_{\Gamma_{\text{trial}}} \frac{1}{\text{r}}\,n'_\ell(2n'_p n'_q - \text{r}_{,p}\text{r}_{,q})w_s n'_s\,\mathrm{d}S_{\bar{\boldsymbol{x}}} \ - \\[2mm]
& 2\int_{\Gamma_{\text{trial}}} \frac{n'_p}{\text{r}^2}\,n'_q n'_\ell n'_s \text{r}_{,s}\,\mathrm{d}S_{\bar{\boldsymbol{x}}} + \int_{\partial\Gamma_{\text{trial}}} \frac{1}{\text{r}}\big(\text{v}_p n'_\ell n'_q + \text{v}_q n'_\ell n'_p - \text{r}_{,p}\text{r}_{,q}\text{v}_\ell\big)\,\mathrm{d}s \ + \\[2mm]
& \int_{\partial\Gamma_{\text{trial}}} \frac{1}{\text{r}}\,n'_\ell \text{r}_{,q}\text{r}_{,s}\big(\text{v}_s n'_p - \text{v}_p n'_s\big)\,\mathrm{d}s, \qquad\qquad \bar{\boldsymbol{\xi}} \in \Gamma_{\text{trial}}.
\end{aligned}
\tag{G5}
$$

For further details on (G1)–(G5), the reader is referred to Chapter 13 in [33]. Here one should mention that, for the canonical problem in Section 3.2.2 where $\boldsymbol{n}' = \bar{\boldsymbol{e}}_3$, formulas (G4) and (G5) can be remarkably simplified (see Appendix 5.A in [33]). In this presentation, however, both formulae are kept in their general format for they also pertain to the scattering by arbitrarily-shaped fractures.

Parametrization. With reference to Fig. 8.6, the fracture boundary Γ_{trial} is discretized using a conformal mesh permitting surface parametrization $(\boldsymbol{y} \to \bar{\boldsymbol{x}})$ as

$$
\bar{\boldsymbol{x}}(y_1, y_2) \ = \ \psi_{\text{m}}(y_1, y_2)\,\bar{\boldsymbol{x}}^{\text{m}}, \qquad \text{m} \ = \ 1, \cdots, \text{N}_n, \qquad -1 \leqslant y_1, y_2 \leqslant 1.
\tag{G6}
$$

Here $\text{N}_n = 8$ designates the number of nodes per element, and $\bar{\boldsymbol{x}}^{\text{m}}$ denotes the global
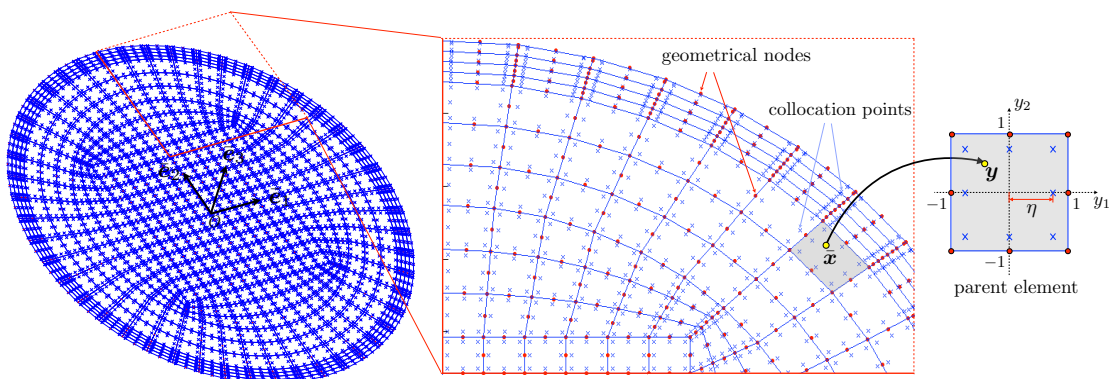
Figure 8.6: Geometric (dotes) and interpolation (crosses) nodes on Γ_{trial} in physical and parametric spaces.

coordinates of the element's $\mathrm{m^{th}}$ node – whose shape function $\psi_\mathrm{m}(\boldsymbol{y})$ is that of the standard eight-noded quadrilateral element. In this setting, one finds the natural basis $\boldsymbol{a}_{1,2}$ of the tangent plane and the surface differential as

$$\boldsymbol{a}_\beta(\boldsymbol{y}) \;=\; \frac{\partial\psi_\mathrm{m}}{\partial y_\beta}\,\bar{\boldsymbol{x}}^\mathrm{m}, \qquad \mathrm{d}S_{\bar{\boldsymbol{x}}} \;=\; \mathscr{G}(\boldsymbol{y})\,\mathrm{d}S_{\boldsymbol{y}}, \qquad \mathscr{G}(\boldsymbol{y}) \;=\; |\boldsymbol{a}_1\times\boldsymbol{a}_2|, \qquad \text{(G7)}$$

where $\beta = 1,2$ and the dummy index m is summed over $\overline{1,8}$. At this stage, one should note that all integrands in (G4) and (G5) – comprising $\check{S}^p_{ms}$ in (G1) – are *known* so that the boundary parametrization, given by (G6) and (G7), is the only necessary step prior to numerical integration.

In light of the smoothness requirement by the traction BIE (G1) and the adverse presence of the tangential derivative operator $D_{qs}(\cdot)$, the FOD $[\![\boldsymbol{V}]\!]^{ij}(\bar{\boldsymbol{x}})$ is discretized via *non-conforming* interpolation (see Section 3.2 of [33] for details). In particular, the interpolation i.e. collocation points are situated *inside* the boundary elements (see Fig. 8.6), and their position with respect to the geometrical nodes – in each element – is quantified via parameter η in the (y_1, y_2) space. In this setting, the FOD over the parent element can be approximated as

$$[\![V_\ell]\!]^{ij}(\bar{\boldsymbol{x}}) \;=\; \phi_\mathrm{m}(\boldsymbol{y})\,[\![V_\ell]\!]^{ij}_\mathrm{m}, \qquad \mathrm{m} \;=\; 1,\cdots,8, \qquad \text{(G8)}$$

where

$$[\![V_\ell]\!]^{ij}_\mathrm{m} \;=\; [\![V_\ell]\!]^{ij}(\bar{\boldsymbol{x}}^\mathrm{m}), \quad \phi_\mathrm{m}(\boldsymbol{y}) \;=\; \frac{1}{4\eta^3}(\eta + y^\mathrm{m}_1 y_1)(\eta + y^\mathrm{m}_2 y_2)(y^\mathrm{m}_1 y_1 + y^\mathrm{m}_2 y_2 - \eta), \quad \text{(G9)}$$

and $(y^\mathrm{m}_1, y^\mathrm{m}_2)$ is the position ofthe $\mathrm{m^{th}}$ collocation point in the parent element as shown in Fig. 8.6. Here it is important to mention that the surface elements adjacent to $\partial\Gamma_\mathrm{trial}$ are of *quarter-node type* (see e.g. Chapter 13 of [33]), designed to reproduce the square-root behavior of the FOD in the vicinity of $\partial\Gamma_\mathrm{trial}$. Note that for constant distribution of interfacial stiffness, i.e. for constant stiffness matrix $\boldsymbol{K}_\mathrm{trial}$, the asymptotic behavior of the FOD near $\partial\Gamma_\mathrm{trial}$ remains the same as that in the case of traction-free crack (see [162] for proof).

Given (G6)–(G9), it can be shown [33] that the tangential derivative operator

$D_{qs}[\![V_\ell]\!]^{ij}(\bar{\boldsymbol{x}})$ in (G1) permits the parameterization

$$D_{qs}[\![V_\ell]\!]^{ij}(\bar{\boldsymbol{x}}) = \Lambda_{qs}^{\mathrm{m}}(\boldsymbol{y})\,[\![V_\ell]\!]_{\mathrm{m}}^{ij},$$

$$\Lambda_{qs}^{\mathrm{m}}(\boldsymbol{y}) = \frac{\epsilon_{pqs}}{\mathscr{G}(\boldsymbol{y})}\big[(\boldsymbol{a}_2\cdot\bar{\boldsymbol{e}}_p)\phi_{\mathrm{m},1} - (\boldsymbol{a}_1\cdot\bar{\boldsymbol{e}}_p)\phi_{\mathrm{m},2}\big](\boldsymbol{y}), \quad \phi_{\mathrm{m},\beta} = \frac{\partial\phi_{\mathrm{m}}}{\partial y_\beta}, \tag{G10}$$

where the dummy indexes p and m are summed over $\overline{1,3}$, and $\overline{1,8}$, respectively; the basis unit vectors $\bar{\boldsymbol{e}}_p$ are shown in Fig. 8.6, and ϵ_{pqs} denotes the Levi-Civita symbol.

On substituting (G7) and (G10) into (G1), one arrives at the algebraic system for the values of $[\![\boldsymbol{V}]\!]^{ij}$ at the collocation nodes $\bar{\boldsymbol{\xi}} = \bar{\boldsymbol{x}}_{e^*}^{\mathrm{m}^*}$ as

$$
\begin{aligned}
\frac{1}{2}[\boldsymbol{e}_i\otimes\boldsymbol{e}_j &+ \boldsymbol{e}_j\otimes\boldsymbol{e}_i]_{k\ell}\,n'_\ell \;-\; [K_{\mathrm{trial}}]_{k\ell}\,[\![V_\ell]\!]_{\mathrm{m}^*e^*}^{ij} \;=\; n'_\ell\,C_{k\ell pq}\,\Lambda_{qs}^{\mathrm{m}e^*}(\boldsymbol{y}^{\mathrm{m}^*})\check{S}_{ms}^p(\bar{\boldsymbol{x}}_{e^*}^{\mathrm{m}^*},\Gamma_{\mathrm{trial}})[\![V_m]\!]_{\mathrm{m}e^*}^{ij} \\
&+ \sum_{e=1}^{\mathrm{N}_e}\sum_{\mathrm{m}=1}^{\mathrm{N}_n}\Big\{ n'_\ell\,C_{k\ell pq}\int_{S_{\boldsymbol{y}}}\big(\Lambda_{qs}^{\mathrm{m}e}(\boldsymbol{y}) - \delta_{ee^*}\,\Lambda_{qs}^{\mathrm{m}e}(\boldsymbol{y}^{\mathrm{m}^*})\big)\check{\Sigma}_{ms}^p(\bar{\boldsymbol{x}}_{e^*}^{\mathrm{m}^*},\bar{\boldsymbol{x}}(\boldsymbol{y}))\mathscr{G}_e(\boldsymbol{y})\,\mathrm{d}S_{\boldsymbol{y}}\Big\}[\![V_m]\!]_{\mathrm{m}e}^{ij} \\
&- \sum_{e=1}^{\mathrm{N}_e}(1-\delta_{ee^*})\sum_{\mathrm{m}=1}^{\mathrm{N}_n}\Big\{ n'_\ell\,C_{k\ell pq}\Big[\int_{S_{\boldsymbol{y}}}\check{\Sigma}_{ms}^p(\bar{\boldsymbol{x}}_{e^*}^{\mathrm{m}^*},\bar{\boldsymbol{x}}(\boldsymbol{y}))\mathscr{G}_e(\boldsymbol{y})\,\mathrm{d}S_{\boldsymbol{y}}\Big]\Lambda_{qs}^{\mathrm{m}e^*}(\boldsymbol{y}^{\mathrm{m}^*})\Big\}[\![V_m]\!]_{\mathrm{m}e^*}^{ij},
\end{aligned}
\tag{G11}
$$

where e^* is the element number; m^* denotes the local node number; no sum over e^* and m^* is implied; $N_n = 8$; N_e is the number of elements, and

$$[\![V_\ell]\!]_{\mathrm{m}e}^{ij} \;=\; [\![V_\ell]\!]^{ij}(\bar{\boldsymbol{x}}_e^{\mathrm{m}}), \quad \Lambda_{qs}^{\mathrm{m}e}(\boldsymbol{y}) \;=\; \frac{\epsilon_{pqs}}{\mathscr{G}_e(\boldsymbol{y})}\big[(\boldsymbol{a}_2^e\cdot\bar{\boldsymbol{e}}_p)\phi_{\mathrm{m},1} - (\boldsymbol{a}_1^e\cdot\bar{\boldsymbol{e}}_p)\phi_{\mathrm{m},2}\big](\boldsymbol{y}). \tag{G12}$$

Here it is worth noting that all integrals in (G4), (G5) and (G11) are numerically integrable. A specific mapping technique (in the case of weak singularity) along with the standard Gaussian quadrature method is employed to evaluate the aforementioned integrals (see Section 3.9 of [81] for details).

H Proof of equation (4.13)

As shown in [104], the irrotational ($\mathbf{u}^{\mathrm{p}}$) and solenoidal ($\mathbf{u}^{\mathrm{s}}$) parts of a radiating wavefield $\mathbf{u} = \mathbf{u}_\varphi$ solving (4.9) exhibit the following asymptotic behavior as $r := |\boldsymbol{\xi}| \to \infty$:

$$
\begin{aligned}
\frac{\partial \mathbf{u}^{\mathrm{p}}}{\partial r} - \mathrm{i}k_p \mathbf{u}^{\mathrm{p}} = O(r^{-2}), \qquad \mathbf{u}^{\mathrm{p}} = O(r^{-1}), \\
\frac{\partial \mathbf{u}^{\mathrm{s}}}{\partial r} - \mathrm{i}k_s \mathbf{u}^{\mathrm{s}} = O(r^{-2}), \qquad \mathbf{u}^{\mathrm{s}} = O(r^{-1}), \\
\hat{\boldsymbol{\xi}} \cdot \boldsymbol{C} : \nabla \mathbf{u}^{\mathrm{p}} - \mathrm{i}k_p (\lambda + 2\mu) \mathbf{u}^{\mathrm{p}} = O(r^{-2}), \\
\hat{\boldsymbol{\xi}} \cdot \boldsymbol{C} : \nabla \mathbf{u}^{\mathrm{s}} - \mathrm{i}k_s \mu \mathbf{u}^{\mathrm{s}} = O(r^{-2}), \qquad \mathbf{u}^{\mathrm{p}} \cdot \overline{\mathbf{u}^{\mathrm{s}}} = O(r^{-3})
\end{aligned} \tag{H1}
$$

For brevity, an auxiliary decomposition $\boldsymbol{t} = \hat{\boldsymbol{\xi}} \cdot \boldsymbol{C} : \nabla \mathbf{u} = \boldsymbol{t}^{\mathrm{p}} + \boldsymbol{t}^{\mathrm{s}}$ is adopted in the sequel, where $\boldsymbol{t}^{\mathrm{p}} = \hat{\boldsymbol{\xi}} \cdot \boldsymbol{C} : \nabla \mathbf{u}^{\mathrm{p}}$ and $\boldsymbol{t}^{\mathrm{s}} = \hat{\boldsymbol{\xi}} \cdot \boldsymbol{C} : \nabla \mathbf{u}^{\mathrm{s}}$. In this setting, one finds that

$$
\begin{aligned}
\Im \lim_{r \to \infty} \int_{\partial B_r} \overline{\mathbf{u}} \cdot \boldsymbol{t} \, \mathrm{d}S_{\boldsymbol{\xi}} &= \frac{1}{2\mathrm{i}} \lim_{r \to \infty} \int_{\partial B_r} \left\{ (\overline{\mathbf{u}^{\mathrm{p}}} + \overline{\mathbf{u}^{\mathrm{s}}}) \cdot (\boldsymbol{t}^{\mathrm{p}} + \boldsymbol{t}^{\mathrm{s}}) - (\mathbf{u}^{\mathrm{p}} + \mathbf{u}^{\mathrm{s}}) \cdot (\overline{\boldsymbol{t}^{\mathrm{p}}} + \overline{\boldsymbol{t}^{\mathrm{s}}}) \right\} \mathrm{d}S_{\boldsymbol{\xi}} \\
&= \lim_{r \to \infty} \int_{\partial B_r} \left\{ k_p (\lambda + 2\mu) \big(|\mathbf{u}^{\mathrm{p}}|^2 + \Re(\mathbf{u}^{\mathrm{p}} \cdot \overline{\mathbf{u}^{\mathrm{s}}}) \big) + k_s \mu \big(|\mathbf{u}^{\mathrm{s}}|^2 + \Re(\mathbf{u}^{\mathrm{p}} \cdot \overline{\mathbf{u}^{\mathrm{s}}}) \big) \right\} \mathrm{d}S_{\boldsymbol{\xi}}, \\
&= \lim_{r \to \infty} \int_{\partial B_r} \left\{ k_p (\lambda + 2\mu) |\mathbf{u}^{\mathrm{p}}|^2 + k_s \mu |\mathbf{u}^{\mathrm{s}}|^2 \right\} \mathrm{d}S_{\boldsymbol{\xi}},
\end{aligned} \tag{H2}
$$

which completes the proof.

I Elastodynamic fundamental stress tensor

In dyadic notation, the elastodynamic fundamental stress tensor [e.g. 2] can be written as

$$
\boldsymbol{\Sigma}(\boldsymbol{x}, \boldsymbol{y}) = \Sigma_{ij}^{\ell}(\boldsymbol{x}, \boldsymbol{y}) \, \boldsymbol{e}_i \otimes \boldsymbol{e}_j \otimes \boldsymbol{e}_\ell, \qquad \boldsymbol{x}, \boldsymbol{y} \in \mathbb{R}^3, \quad \boldsymbol{x} \neq \boldsymbol{y} \tag{I1}
$$

signifying the Cauchy stress tensor at $\boldsymbol{x}$ due to point force $\boldsymbol{e}_\ell$ acting at $\boldsymbol{y}$, where

$$
\Sigma_{ij}^{\ell}(\boldsymbol{x}, \boldsymbol{y}) = \frac{\lambda}{\lambda + 2\mu} [G(k_p r)]_{,\ell} \, \delta_{ij} - \frac{2}{k_s^2} [G(k_p r) - G(k_s r)]_{,ij\ell} + [G(k_s r)]_{,i} \, \delta_{j\ell} + [G(k_s r)]_{,j} \, \delta_{i\ell} \tag{I2}
$$

and

$$r = |\boldsymbol{x} - \boldsymbol{y}|, \qquad G(kr) := \frac{e^{\mathrm{i}kr}}{4\pi r}, \qquad [f]_{,i} := \frac{\partial f}{\partial x_i}.$$

As shown in [2], the far-field approximation of (I2) as $|\boldsymbol{x}| \to \infty$ reads

$$\Sigma_{ij}^{\ell,\infty}(\boldsymbol{x}, \boldsymbol{y}) \;=\; \Sigma_{ij}^{\ell,p}(\boldsymbol{x}, \boldsymbol{y}) \;+\; \Sigma_{ij}^{\ell,s}(\boldsymbol{x}, \boldsymbol{y}), \tag{I3}$$

where

$$
\begin{aligned}
\Sigma_{ij}^{\ell,p}(\boldsymbol{x}, \boldsymbol{y}) &= \mathrm{i}k_p A_{ij\ell}^p \frac{e^{\mathrm{i}k_p|\boldsymbol{x}|}}{4\pi|\boldsymbol{x}|} e^{-\mathrm{i}k_p \hat{\boldsymbol{x}} \cdot \boldsymbol{y}}, & A_{ij\ell}^p &= \left[\frac{2\mu}{\lambda+2\mu} \hat{x}_i \hat{x}_j + \frac{\lambda}{\lambda+2\mu} \delta_{ij} \right] \hat{x}_\ell, \\
\Sigma_{ij}^{\ell,s}(\boldsymbol{x}, \boldsymbol{y}) &= \mathrm{i}k_s A_{ij\ell}^s \frac{e^{\mathrm{i}k_s|\boldsymbol{x}|}}{4\pi|\boldsymbol{x}|} e^{-\mathrm{i}k_s \hat{\boldsymbol{x}} \cdot \boldsymbol{y}}, & A_{ij\ell}^s &= \delta_{i\ell} \hat{x}_j + \delta_{j\ell} \hat{x}_i - 2\hat{x}_i \hat{x}_j \hat{x}_\ell.
\end{aligned}
\tag{I4}
$$

J Proof of Lemma 4.3.1

Consider the orthonormal bases $(\boldsymbol{e}_1 := \hat{\boldsymbol{\xi}}, \boldsymbol{e}_2, \boldsymbol{e}_3)$ and $(\boldsymbol{h}_1 := \boldsymbol{d}, \boldsymbol{h}_2, \boldsymbol{h}_3)$, where $\hat{\boldsymbol{\xi}}$ and $\boldsymbol{d}$ denote respectively the directions of observation and plane-wave incidence. On representing the far-field pattern $\boldsymbol{v}_{\boldsymbol{q}}^\infty = \boldsymbol{v}_{\boldsymbol{q}_p}^\infty \oplus \boldsymbol{v}_{\boldsymbol{q}_s}^\infty$ (resp. the polarization vector $\boldsymbol{q} = \boldsymbol{q}_p \oplus \boldsymbol{q}_s$) in the $\boldsymbol{e}-$ (resp. $\boldsymbol{h}-$) basis, definition (4.23) of the far-field kernel $\boldsymbol{W}^\infty(\boldsymbol{d}, \hat{\boldsymbol{\xi}})$ can be written in matrix form as

$$
\boldsymbol{v}_{\boldsymbol{q}}^\infty(\boldsymbol{d}, \hat{\boldsymbol{\xi}}) =
\begin{bmatrix}
\boldsymbol{v}_{\boldsymbol{q}_p}^\infty \cdot \boldsymbol{e}_1 \\
0 \\
0 \\
0 \\
0 \\
\boldsymbol{v}_{\boldsymbol{q}_s}^\infty \cdot \boldsymbol{e}_2 \\
\boldsymbol{v}_{\boldsymbol{q}_s}^\infty \cdot \boldsymbol{e}_3
\end{bmatrix}
=
\begin{bmatrix}
W_{11}^\infty(\boldsymbol{d}, \hat{\boldsymbol{\xi}}) & 0 & 0 & 0 & W_{12}^\infty(\boldsymbol{d}, \hat{\boldsymbol{\xi}}) & W_{13}^\infty(\boldsymbol{d}, \hat{\boldsymbol{\xi}}) \\
0 & 0 & 0 & 0 & 0 & 0 \\
0 & 0 & 0 & 0 & 0 & 0 \\
0 & 0 & 0 & 0 & 0 & 0 \\
0 & 0 & 0 & 0 & 0 & 0 \\
W_{21}^\infty(\boldsymbol{d}, \hat{\boldsymbol{\xi}}) & 0 & 0 & 0 & W_{22}^\infty(\boldsymbol{d}, \hat{\boldsymbol{\xi}}) & W_{23}^\infty(\boldsymbol{d}, \hat{\boldsymbol{\xi}}) \\
W_{31}^\infty(\boldsymbol{d}, \hat{\boldsymbol{\xi}}) & 0 & 0 & 0 & W_{32}^\infty(\boldsymbol{d}, \hat{\boldsymbol{\xi}}) & W_{33}^\infty(\boldsymbol{d}, \hat{\boldsymbol{\xi}})
\end{bmatrix}
\begin{bmatrix}
\boldsymbol{q}_p \cdot \boldsymbol{h}_1 \\
0 \\
0 \\
0 \\
0 \\
\boldsymbol{q}_s \cdot \boldsymbol{h}_2 \\
\boldsymbol{q}_s \cdot \boldsymbol{h}_3
\end{bmatrix}.
\tag{J1}
$$

In this setting, the reciprocity statement (4.25) can be rewritten as

$$W_{ij}^\infty(\boldsymbol{d}, \hat{\boldsymbol{\xi}}) \;=\; W_{ji}^\infty(-\hat{\boldsymbol{\xi}}, -\boldsymbol{d}), \qquad i, j = 1, 2, 3. \tag{J2}$$

This section aims to extend Lemma 1 in [63] to cater for the scattering problem (4.2)-(4.6) with its particular boundary condition, (4.4), at the fracture interface Γ. With such result in place, the distilled reciprocity claim (J2) follows immediately as a consequence of Theorem 1 and its corollaries in [63]. To this end, consider two distinct *total fields*

$$\boldsymbol{\psi}_1 = \boldsymbol{u}_1^{\mathrm{f}} + \boldsymbol{v}_1, \qquad \boldsymbol{\psi}_2 = \boldsymbol{u}_2^{\mathrm{f}} + \boldsymbol{v}_2,$$

where $\boldsymbol{v}_j \in H^1_{\mathrm{loc}}(\mathbb{R}^3\backslash\Gamma)^3$ satisfies (4.2)-(4.6) with $\boldsymbol{u}^{\mathrm{f}} = \boldsymbol{u}_j^{\mathrm{f}}$ ($j = 1,2$). On adopting Twersky's notation [161]

$$\{\boldsymbol{\psi}_1, \boldsymbol{\psi}_2\}_S := \int_S \{\boldsymbol{\psi}_1 \cdot \boldsymbol{t}(\boldsymbol{\psi}_2) - \boldsymbol{\psi}_2 \cdot \boldsymbol{t}(\boldsymbol{\psi}_1)\}\, \mathrm{d}S_{\boldsymbol{\xi}},$$

Lemma 1 in [63] states that $\{\boldsymbol{\psi}_1, \boldsymbol{\psi}_2\}_{\partial B_R} = 0$, where B_R is a ball of radius R sufficiently large so that $\Gamma \subset B_R$. By substituting the Navier equation

$$\nabla(\boldsymbol{C}\!:\!\nabla\boldsymbol{\psi}_j) + \rho\omega^2\boldsymbol{\psi}_j = \boldsymbol{0} \quad \text{in} \quad \mathbb{R}^3\backslash\Gamma, \qquad j = 1,2$$

into Betti's third formula [104] written for domain $B_R\backslash\Gamma$, one finds that

$$\{\boldsymbol{\psi}_1, \boldsymbol{\psi}_2\}_{\partial\mathscr{B}_2\cup\Gamma} = \int_{\mathscr{B}_2\backslash\Gamma} \left\{\boldsymbol{\psi}_1 \cdot [\nabla\!\cdot\!(\boldsymbol{C}\!:\!\nabla\boldsymbol{\psi}_2)] - \boldsymbol{\psi}_2 \cdot [\nabla\!\cdot\!(\boldsymbol{C}\!:\!\nabla\boldsymbol{\psi}_1)]\right\} \mathrm{d}S_{\boldsymbol{\xi}} = 0 \quad \text{(J3)}$$

where, thanks to the jump condition on Γ in (4.2) and contact law (4.4), one has

$$\begin{aligned}
\{\boldsymbol{\psi}_1, \boldsymbol{\psi}_2\}_\Gamma &= \int_\Gamma \{[\![\boldsymbol{\psi}_1]\!] \cdot \boldsymbol{t}(\boldsymbol{\psi}_2) - [\![\boldsymbol{\psi}_2]\!] \cdot \boldsymbol{t}(\boldsymbol{\psi}_1)\}\, \mathrm{d}S_{\boldsymbol{\xi}} \\
&= \int_\Gamma \left\{[\![\boldsymbol{\psi}_1]\!]\!\cdot\!\boldsymbol{K}\!\cdot\![\![\boldsymbol{\psi}_2]\!] - [\![\boldsymbol{\psi}_2]\!]\!\cdot\!\boldsymbol{K}\!\cdot\![\![\boldsymbol{\psi}_1]\!]\right\} \mathrm{d}S_{\boldsymbol{\xi}}.
\end{aligned} \tag{J4}$$

Due to symmetry of $\boldsymbol{K}$, one has $\{\boldsymbol{\psi}_1, \boldsymbol{\psi}_2\}_\Gamma = 0$ and consequently $\{\boldsymbol{\psi}_1, \boldsymbol{\psi}_2\}_{\partial B_R} = 0$ thanks to (J3). ∎

K   Proof of Lemma 4.1

With reference to the Herglotz operator $\mathscr{H}\colon L^2(\Omega)^3 \to H^{-1/2}(\Gamma)^3$ given by (4.26) and a fracture opening displacement (FOD) profile $\boldsymbol{a} \in \tilde{H}^{1/2}(\Gamma)$, consider the duality product

$$\langle \mathscr{H}(\boldsymbol{g}), \boldsymbol{a} \rangle \;=\; \int_{\Gamma} \bar{\boldsymbol{a}} \cdot \boldsymbol{t}(\mathbf{u}_g) \, \mathrm{d}S_{\boldsymbol{y}}. \tag{K1}$$

Thanks to (4.18) and the linearity of $\boldsymbol{t}$, the right-hand side of (K1) can be recast as

$$\int_{\Gamma} \bar{\boldsymbol{a}} \cdot \boldsymbol{t}(\mathbf{u}_g) \, \mathrm{d}S_{\boldsymbol{y}} \;=\; \int_{\Omega} \int_{\Gamma} \bar{\boldsymbol{a}}(\boldsymbol{y}) \cdot \boldsymbol{t}\big(\boldsymbol{g}(\boldsymbol{d}) \cdot (\boldsymbol{d} \otimes \boldsymbol{d}) \, e^{\mathrm{i}k_p \boldsymbol{d} \cdot \boldsymbol{y}}\big) \, \mathrm{d}S_{\boldsymbol{y}} \, \mathrm{d}S_{\boldsymbol{d}}$$
$$+ \int_{\Omega} \int_{\Gamma} \bar{\boldsymbol{a}}(\boldsymbol{y}) \cdot \boldsymbol{t}\big(\boldsymbol{g}(\boldsymbol{d}) \cdot (\boldsymbol{I} - \boldsymbol{d} \otimes \boldsymbol{d}) \, e^{\mathrm{i}k_s \boldsymbol{d} \cdot \boldsymbol{y}}\big) \, \mathrm{d}S_{\boldsymbol{y}} \, \mathrm{d}S_{\boldsymbol{d}}.$$

On recalling that for arbitrary smooth surface S

$$\boldsymbol{t}(\boldsymbol{u}) \;=\; \boldsymbol{n} \cdot \boldsymbol{C} : \nabla \boldsymbol{u} \;=\; \lambda \, \boldsymbol{n} \nabla \cdot \boldsymbol{u} + 2\mu \, \boldsymbol{n} \cdot \nabla \boldsymbol{u} + \mu \, \boldsymbol{n} \times \nabla \times \boldsymbol{u} \quad \text{on} \quad S$$

where $\boldsymbol{C}$ is given by (4.3) and $\boldsymbol{n}$ is the unit normal on S, one finds that

$$\bar{\boldsymbol{a}} \cdot \boldsymbol{t}\big(\boldsymbol{g}(\boldsymbol{d}) \cdot (\boldsymbol{d} \otimes \boldsymbol{d}) \, e^{\mathrm{i}k_p \boldsymbol{d} \cdot \boldsymbol{y}}\big) \;=\; \boldsymbol{g}(\boldsymbol{d}) \cdot \overline{(-\mathrm{i}k_p) e^{-\mathrm{i}k_p \boldsymbol{d} \cdot \boldsymbol{y}} \big\{ 2\mu (\boldsymbol{a} \cdot \boldsymbol{d})(\boldsymbol{n} \cdot \boldsymbol{d}) + \lambda (\boldsymbol{a} \cdot \boldsymbol{n}) \big\} \boldsymbol{d}},$$

$$\bar{\boldsymbol{a}} \cdot \boldsymbol{t}\big(\boldsymbol{g}(\boldsymbol{d}) \cdot (\boldsymbol{I} - \boldsymbol{d} \otimes \boldsymbol{d}) \, e^{\mathrm{i}k_s \boldsymbol{d} \cdot \boldsymbol{y}}\big) \;=\;$$
$$=\; \boldsymbol{g}(\boldsymbol{d}) \cdot \overline{(-\mathrm{i}k_s) e^{-\mathrm{i}k_s \boldsymbol{d} \cdot \boldsymbol{y}} \, \boldsymbol{d} \times \big\{ \mu (\boldsymbol{a} \cdot \boldsymbol{d})(\boldsymbol{n} \times \boldsymbol{d}) + \mu (\boldsymbol{n} \cdot \boldsymbol{d})(\boldsymbol{a} \times \boldsymbol{d}) \big\}}.$$

As a result,

$$\int_{\Gamma} \bar{\boldsymbol{a}} \cdot \boldsymbol{t}(\mathbf{u}_g) \, \mathrm{d}S_{\boldsymbol{y}} \;=\;$$
$$\int_{\Omega} \boldsymbol{g}(\boldsymbol{d}) \cdot \overline{(-\mathrm{i}k_p) \, \boldsymbol{d} \int_{\Gamma} \big\{ \lambda (\boldsymbol{a} \cdot \boldsymbol{n}) + 2\mu (\boldsymbol{n} \cdot \boldsymbol{d})(\boldsymbol{a} \cdot \boldsymbol{d}) \big\} e^{-\mathrm{i}k_p \boldsymbol{d} \cdot \boldsymbol{y}} \, \mathrm{d}S_{\boldsymbol{y}}} \, \mathrm{d}S_{\boldsymbol{d}} \;+\;$$
$$\int_{\Omega} \boldsymbol{g}(\boldsymbol{d}) \cdot \overline{(-\mathrm{i}k_s) \, \boldsymbol{d} \times \int_{\Gamma} \big\{ \mu (\boldsymbol{a} \times \boldsymbol{d})(\boldsymbol{n} \cdot \boldsymbol{d}) + \mu (\boldsymbol{n} \times \boldsymbol{d})(\boldsymbol{a} \cdot \boldsymbol{d}) \big\} e^{-\mathrm{i}k_s \boldsymbol{d} \cdot \boldsymbol{y}} \, \mathrm{d}S_{\boldsymbol{y}}} \, \mathrm{d}S_{\boldsymbol{d}}.$$

By virtue of (4.16) and (4.20) which verify $\langle \boldsymbol{g}, \boldsymbol{v}^{\infty} \rangle = \langle \boldsymbol{g}_p, \boldsymbol{v}_p^{\infty} \rangle + \langle \boldsymbol{g}_s, \boldsymbol{v}_s^{\infty} \rangle$, one finds that

$$\langle \mathscr{H}(\boldsymbol{g}), \, \boldsymbol{a} \rangle \;=\; \langle \boldsymbol{g}, \, \mathscr{H}^*(\boldsymbol{a}) \rangle$$

which establishes (4.28). ∎

L   Proofs of Theorem 4.5.7 and Theorem 4.5.9

Proof. Consider the following:

- Let $\boldsymbol{\Phi}_L^\infty \in Range(\mathscr{H}^*)$. By definition, $\exists \psi \in \overline{Range(T)}$ such that $\mathscr{H}^*\psi = \boldsymbol{\Phi}_L^\infty$. Then, by recalling the continuity of T^{-1} (Lemma 4.4.6) and the range denseness of $\mathscr{H}$ (Lemma 4.4.2), one may find $\boldsymbol{g}_\circ \in L^2(\Omega)^3$ for every $\alpha > 0$ such that $\|\mathscr{H}\boldsymbol{g}_\circ - T^{-1}\psi\|^2 < \alpha$. Now, let us observe that

  i) by the continuity of $\mathscr{G} = \mathscr{H}^*T$ (Lemma 4.5.5), one has

  $$\|F\boldsymbol{g}_\circ - \boldsymbol{\Phi}_L^\infty\|^2 \;\leqslant\; \alpha\|\mathscr{G}\|^2;$$

  ii) the boundedness i.e. continuity of $\mathfrak{T}$ (see Lemma 4.4.4 and (4.48)) implies that

  $$|(\boldsymbol{g}_\circ, B\boldsymbol{g}_\circ)| \;\leqslant\; \|\mathfrak{T}\|\|\mathscr{H}\boldsymbol{g}_\circ\|^2 \;<\; 2\,\|\mathfrak{T}\|\,(\alpha + \|T^{-1}\psi\|^2);$$

  iii) thanks to the definitions of $\mathrm{j}_\alpha(\boldsymbol{\Phi}_L^\infty)$ and $\boldsymbol{g}_\alpha^L$, one has

  $$\mathfrak{J}_\alpha(\boldsymbol{\Phi}_L^\infty; \boldsymbol{g}_\alpha^L) - \mu\alpha \;\leqslant\; \mathrm{j}_\alpha(\boldsymbol{\Phi}_L^\infty) \;\leqslant\; \|F\boldsymbol{g}_\circ - \boldsymbol{\Phi}_L^\infty\|^2 + \alpha|(\boldsymbol{g}_\circ, B\boldsymbol{g}_\circ)|.$$

  As a result, it immediately follows that

  $$\alpha|(\boldsymbol{g}_\alpha^L, B\boldsymbol{g}_\alpha^L)| \;\leqslant\; \mathfrak{J}_\alpha(\boldsymbol{\Phi}_L^\infty; \boldsymbol{g}_\alpha^L) \;\leqslant\; \mu\alpha + \alpha\|\mathscr{G}\|^2 + 2\alpha\|\mathfrak{T}\|\,(\alpha + \|T^{-1}\psi\|^2), \quad \text{(L1)}$$

  whereby $\limsup\limits_{\alpha\to 0} |(\boldsymbol{g}_\alpha^L, B\boldsymbol{g}_\alpha^L)| < \infty$ which implies $\liminf\limits_{\alpha\to 0} |(\boldsymbol{g}_\alpha^L, B\boldsymbol{g}_\alpha^L)| < \infty$.

- Next, let $\boldsymbol{\Phi}_L^\infty \notin Range(\mathscr{H}^*)$. Let us by contradiction assume that $\liminf\limits_{\alpha\to 0} |(\boldsymbol{g}_\alpha^L, B\boldsymbol{g}_\alpha^L)| < \infty$; then, for some constant $c > 0$ independent of α, one has $|(\boldsymbol{g}_\alpha^L, B\boldsymbol{g}_\alpha^L)| < c$ for an extracted subsequence of $\boldsymbol{g}_\alpha^L$. The coercivity of $\mathfrak{T}$ then implies that $\mathscr{H}\boldsymbol{g}_\alpha^L$ is also bounded. As $H^{-1/2}(\Gamma)^3$ is reflexive, one may suppose that up to an extracted subsequence, $\mathscr{H}\boldsymbol{g}_\alpha^L$ weakly converges to some $T^{-1}\psi \in H^{-1/2}(\Gamma)^3$. In fact, $T^{-1}\psi \in \overline{Range(\mathscr{H})}$ since the latter set is convex. Now, since $\mathscr{G}$ is compact, $\mathscr{G}\mathscr{H}\boldsymbol{g}_\alpha^L$ strongly converges to $\mathscr{G}T^{-1}\psi = \mathscr{H}^*\psi$ as $\alpha \to 0$. Recalling the definition of $\mathfrak{J}_\alpha(\boldsymbol{\Phi}_L^\infty; \boldsymbol{g}_\alpha^L)$ and the fact that $\mathrm{j}_\alpha(\boldsymbol{\Phi}_L^\infty) \to 0$ as $\alpha \to 0$ thanks to the

range denseness of F, one may observe that $\| F\boldsymbol{g}_\alpha^L - \boldsymbol{\Phi}_L^\infty \|^2 \leqslant \mathfrak{J}_\alpha(\boldsymbol{\Phi}_L^\infty; \boldsymbol{g}_\alpha^L) \leqslant \mathfrak{j}_\alpha(\boldsymbol{\Phi}_L^\infty) + \mu\alpha \to 0$ as $\alpha \to 0$. Thus, $\mathscr{H}^*\boldsymbol{\psi} = \boldsymbol{\Phi}_L^\infty$ which is a contradiction. Accordingly, $\boldsymbol{\Phi}_L^\infty \notin Range(\mathscr{H}^*)$ necessitates $\liminf\limits_{\alpha\to0} |(\boldsymbol{g}_\alpha^L, B\boldsymbol{g}_\alpha^L)| = \infty$ which in turn implies $\limsup\limits_{\alpha\to0} |(\boldsymbol{g}_\alpha^L, B\boldsymbol{g}_\alpha^L)| = \infty$.

$\square$

Proof. The logic of this proof follows that of Theorem 4.5.7, and entails the following steps.

- Let $\boldsymbol{\Phi}_L^\infty \in Range(\mathscr{H}^*)$ so that $\mathscr{H}^*\boldsymbol{\psi} = \boldsymbol{\Phi}_L^\infty$ for some $\boldsymbol{\psi} \in \overline{Range(T)}$. Define for every $\alpha > 0$ independent of δ, density $\boldsymbol{g}_\circ \in L^2(\Omega)^3$ such that $\| \mathscr{H}\boldsymbol{g}_\circ - T^{-1}\boldsymbol{\psi} \|^2 < \alpha$, and set $\delta > 0$ sufficiently small so that

$$\delta\{2\alpha\|\boldsymbol{g}_\circ\|^2 + \delta\|\boldsymbol{g}_\circ\|^2 + 2\|F\boldsymbol{g}_\circ - \boldsymbol{\Phi}_L^\infty\|\,\|\boldsymbol{g}_\circ\|\} \leqslant \alpha.$$

  With reference to (4.64), one finds

$$\mathfrak{J}_\alpha^\delta(\boldsymbol{\Phi}_L^\infty; \boldsymbol{g}_{\alpha,\delta}^L) \ \leqslant \ \mathfrak{J}_\alpha^\delta(\boldsymbol{\Phi}_L^\infty; \boldsymbol{g}_\circ) \ \leqslant \ \mathfrak{J}_\alpha(\boldsymbol{\Phi}_L^\infty; \boldsymbol{g}_\circ) + \alpha. \tag{L2}$$

  On recalling the bound in (L1) on $\mathfrak{J}_\alpha$, this yields

$$\alpha\left(|(\boldsymbol{g}_{\alpha,\delta}^L, B^\delta\boldsymbol{g}_{\alpha,\delta}^L)| + \delta\|\boldsymbol{g}_{\alpha,\delta}^L\|^2\right) \leqslant \mathfrak{J}_\alpha^\delta(\boldsymbol{\Phi}_L^\infty; \boldsymbol{g}_{\alpha,\delta}^L) \leqslant$$
$$\leqslant (\mu+1)\alpha + \alpha\|\mathscr{G}\|^2 + 2\alpha\|\mathfrak{T}\|(\alpha + \|T^{-1}\boldsymbol{\psi}\|^2),$$

  which guarantees that $\limsup\limits_{\alpha\to0} \limsup\limits_{\delta\to0} \left(|(\boldsymbol{g}_{\alpha,\delta}^L, B^\delta\boldsymbol{g}_{\alpha,\delta}^L)| + \delta\|\boldsymbol{g}_{\alpha,\delta}^L\|^2\right) < \infty$.

- Let $\boldsymbol{\Phi}_L^\infty \notin Range(\mathscr{H}^*)$, and assume to the contrary that

$$\liminf\limits_{\alpha\to0} \liminf\limits_{\delta\to0} \left(|(\boldsymbol{g}_{\alpha,\delta}^L, B^\delta\boldsymbol{g}_{\alpha,\delta}^L)| + \delta\|\boldsymbol{g}_{\alpha,\delta}^L\|^2\right) < \infty.$$

  Using the coercivity of $\mathfrak{T}$ and triangle inequality, one finds

$$c\,\|\mathscr{H}\boldsymbol{g}_{\alpha,\delta}^L\|^2 \leqslant |(\boldsymbol{g}_{\alpha,\delta}^L, B\boldsymbol{g}_{\alpha,\delta}^L)| \leqslant |(\boldsymbol{g}_{\alpha,\delta}^L, B^\delta\boldsymbol{g}_{\alpha,\delta}^L)| + \delta\|\boldsymbol{g}_{\alpha,\delta}^L\|^2,$$

  whereby $\limsup\limits_{\alpha\to0} \limsup\limits_{\delta\to0} \|\mathscr{H}\boldsymbol{g}_{\alpha,\delta}^L\|^2 < \infty$. Then, there exists a subsequence $(\alpha', \delta(\alpha') <$

α') such that $\alpha' \to 0$ and $\|\mathscr{H}\boldsymbol{g}^L_{\alpha',\delta(\alpha')}\|^2$ is bounded independently from α'. In light of Lemma 4.5.8, one may design this subsequence such that $\mathfrak{J}^{\delta(\alpha')}_{\alpha'}(\boldsymbol{\Phi}^\infty_L; \boldsymbol{g}^L_{\alpha',\delta(\alpha')}) \to 0$ as $\alpha' \to 0$, and thus $\| F^\delta \boldsymbol{g}^L_{\alpha',\delta(\alpha')} - \boldsymbol{\Phi}^\infty_L \| \to 0$ as $\alpha' \to 0$. The compactness of $\mathscr{H}^*$ and boundedness of $\mathfrak{T}$ imply that a subsequence of $\mathscr{H}^* \mathfrak{T} \mathscr{H} \boldsymbol{g}^L_{\alpha',\delta(\alpha')}$ converges to some $\mathscr{H}^* \boldsymbol{\psi}$ in $L^2(\Omega)^3$. The uniqueness of this limit implies that $\mathscr{H}^* \boldsymbol{\psi} = \boldsymbol{\Phi}^\infty_L$, which is a contradiction.

$\square$